PROJECT SUMMARY REPORT 1422-3F

DEVELOPMENT OF A ROLLING DYNAMIC DEFLECTOMETER FOR CONTINUOUS DEFLECTION TESTING OF PAVEMENTS

James A. Bay and Kenneth H. Stokoe, II

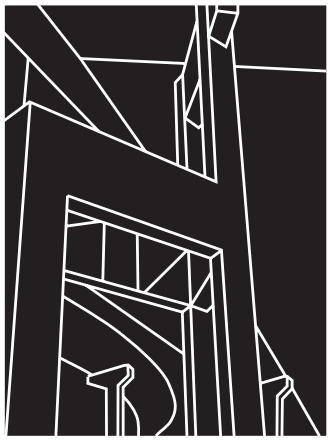

CENTER FOR TRANSPORTATION RESEARCH
BUREAU OF ENGINEERING RESEARCH
THE UNIVERSITY OF TEXAS AT AUSTIN

MAY 1998

Technical Report Documentation Page

1. Report No. FHWA/TX-99/1422-3F	2. Government Accession No.	3. Recipient's Catalog No.
4. Title and Subtitle DEVELOPMENT OF A ROLLING DYNAMIC DEFLECTOMETER FOR CONTINUOUS DEFLECTION TESTING OF PAVEMENTS		5. Report Date May 1998 6. Performing Organization Code Organization Code
7. Author(s) James A. Bay and Kenneth H. Stokoe, II		8. Performing Organization Report No. Research Report 1422-3F
9. Performing Organization Name and Address Center for Transportation Research The University of Texas at Austin 3208 Red River, Suite 200 Austin, Texas 78705-2650		10. Work Unit No. (TRAIS) 11. Contract or Grant No. Research Study 0-1422
12. Sponsoring Agency Name and Address Texas Department of Transportation Research and Technology Transfer Section/Construction Division P.O. Box 5051 Austin, Texas 78763-5051		13. Type of Report and Period Covered Project Summary Report (9/96-8/97) 14. Sponsoring Agency Code

15. Supplementary Notes

Project conducted in cooperation with the U.S. Department of Transportation, Federal Highway Administration.

16. Abstract

A rolling dynamic deflectometer (RDD) was developed as a nondestructive method for determining continuous deflection profiles of pavements. Unlike other commonly used pavement testing methods, the RDD performs continuous rather than discrete measurements. The ability to perform continuous measurements makes RDD testing very effective for quickly characterizing large sections of pavement while simultaneously providing a comprehensive picture of the pavement condition, with little danger of missing critical pavement features. RDD testing is performed while the RDD vehicle travels at speeds of up to 1.5 mph (2.4 km/hr).

Continuous deflection profiles determined with the RDD can be used to: 1) assess the overall stiffness of a pavement; 2) differentiate the relative stiffnesses of different regions; 3) detect cracks, joints, and weak regions; 4) assess the performance of cracked or jointed regions; 5) delineate the regions of the pavement influenced by joints and cracks; and 6) identify areas where additional discrete testing should be performed. The RDD is a powerful tool having the potential for: 1) designing pavement repairs and retrofits, 2) estimating the remaining life of pavements, and 3) functioning as a quality assurance and quality control system during the construction of new pavements.

The RDD was constructed by modifying the electrohydraulic loading system on a Vibroseis truck. The RDD applies large sinusoidal dynamic forces to the pavement through specially designed loading rollers. The resulting deflections are simultaneously measured by rolling sensors designed to minimize the influence of noise caused by rough pavement surfaces. Distance measuring and data acquisition systems were designed to record the forces applied to the pavement and the resulting dynamic displacements; these systems also track the position of the RDD.

The RDD was used to determine continuous deflection profiles at two sites on Interstate Highway 10 over a total length of 21 mi (33.5 km). These results were used to assess the condition of the pavement and to design an overlay. The RDD was also used to test runway and taxiway airport pavements at the Dallas-Fort Worth International Airport as part of a project to predict the remaining life of the airport pavements. Finally, the RDD was used in a stationary mode to dynamically load bridges and bridge foundations. All testing except the bridge project is presented in this report.

17. Key Words	18. Distribution Statement
Rolling dynamic deflector (RDD), pavement testing, highway pavement testing, airport pavement testing, deflection testing, nondestructive testing, pavement predictions	No restrictions. This document is available to the public through the National Technical Information Service, Springfield, Virginia 22161.

19. Security Classif. (of this report)	20. Security Classif. (of this page)	21. No. of pages	22. Price
Unclassified	Unclassified	252	

Form DOT F 1700.7 (8-72) Reproduction of completed page authorized

DEVELOPMENT OF A ROLLING DYNAMIC DEFLECTOMETER FOR CONTINUOUS DEFLECTION TESTING OF PAVEMENTS

by

Dr. James A. Bay

Dr. Kenneth H. Stokoe, II

Project Summary Report 1422-3F

and

Geotechnical Engineering Report GR98-7

Research Project 0-1422

Project Title: “Stationary and Continuous Measurements with the Heavy-Load Profiler”

Conducted for the

TEXAS DEPARTMENT OF TRANSPORTATION

in cooperation with the

U.S. Department of Transportation

Federal Highway Administration

by the

CENTER FOR TRANSPORTATION RESEARCH

Bureau of Engineering Research

THE UNIVERSITY OF TEXAS AT AUSTIN

May 1998

DISCLAIMERS

The contents of this report reflect the views of the authors, who are responsible for the facts and the accuracy of the data presented herein. The contents do not necessarily reflect the official views or policies of the Federal Highway Administration (FHWA) or the Texas Department of Transportation (TxDOT). This report does not constitute a standard, specification, or regulation.

There were modifications to an invention first applied in practice in the course of this contract, namely, modifications to the Rolling Dynamic Deflectometer. Some of these modifications may be patentable under the patent laws of the United States of America and in various foreign countries.

NOT INTENDED FOR CONSTRUCTION, BIDDING, OR PERMIT PURPOSES

Kenneth H. Stokoe, P.E. (Texas No. 49095)
Research Supervisor

IMPLEMENTATION STATEMENT

The results from the experimental studies conducted on this project have demonstrated the ability of the Rolling Dynamic Deflectometer (RDD) to determine continuous deflection profiles along pavements. Unlike other commonly used pavement testing methods, the RDD performs continuous rather than discrete measurements. This ability to perform continuous measurements makes RDD testing very effective for quickly characterizing sections of pavement while simultaneously providing a comprehensive picture of the pavement condition, with little danger of missing critical pavement features. RDD testing is performed while the RDD vehicle travels at speeds of up to 1.5 mph (2.4 km/hr). This type of testing can be implemented by TxDOT to assist it in locating other discrete tests on the pavement, as well as to use in direct characterization of pavements in project-level studies. Specific, enumerated recommendations are provided in Chapter 11.

ACKNOWLEDGMENTS

This project required substantial financial resources. The United States Air Force Office of Sponsored Research provided funds for the purchase of the Vibroseis truck under Grant No. AFOSR-87-0056. TxDOT funded the initial modifications required to transform the Vibroseis into the RDD under TxDOT Project No. 3/10-18-90/2-1243. The University of Texas Physical Plant provided much of the skilled labor required, constructing major components of the RDD during the initial transformation. The work presented in this report was funded by four different sources. Initially, TxDOT Project No. 0-1422 funded modifications and upgrades to the RDD from September 1995 through August 1996. The subsequent two years were funded in part by testing performed for 1) the Houston District of TxDOT under Project No. LOA96-05, 20 the Dallas–Fort Worth Airport Authority, 3) the Center for Transportation Research (CTR), and 4) the Geotechnical Engineering Center. Olson Engineering also supported research associated with this project as part of Project FHWA, Contract No. DTFH61-96-C-00030.

The researchers acknowledge the assistance provided by Mark McDaniel (DES), the TxDOT project director for this study. Also appreciated is the guidance provided by the other members of the project monitoring committee, which included K. Alkier (CMD), Carl Bertrand (DES), and D. Chen (DES).

ABSTRACT

An RDD was developed as a nondestructive method for determining continuous deflection profiles of pavements. Unlike other commonly used pavement testing methods, the RDD performs continuous rather than discrete measurements. The ability to perform continuous measurements makes RDD testing very effective in quickly characterizing large sections of pavement while simultaneously providing a comprehensive picture of the pavement condition, with little danger of missing critical pavement features. RDD testing is performed while the RDD vehicle travels at speeds of up to 1.5 mph (2.4 km/hr).

Continuous deflection profiles determined with the RDD can be used to: 1) assess the overall stiffness of a pavement; 2) differentiate the relative stiffnesses of different regions; 3) detect cracks, joints, and weak regions; 4) assess the performance of cracked or jointed regions; 5) delineate the regions of the pavement influenced by joints and cracks; and 6) identify areas where additional discrete testing should be performed. The RDD is a powerful tool with the potential for use: 1) designing pavement repairs and retrofits, 2) estimating the remaining life of pavements, and 3) functioning as a quality assurance and quality control system during the construction of new pavements.

The RDD was constructed by modifying the electrohydraulic loading system on a Vibroseis truck. The RDD applies large sinusoidal dynamic forces to the pavement through specially designed loading rollers. The resulting deflections are simultaneously measured by rolling sensors designed to minimize the influence of noise caused by rough pavement surfaces. Distance measuring and data acquisition systems were designed to record the forces applied to the pavement and the resulting dynamic displacements; these systems also track the position of the RDD.

The RDD was used to determine continuous deflection profiles at two sites on Interstate Highway 10 over a total length of 21 mi (33.5 km). These results were used to assess the condition of the pavement and to design an overlay. The RDD was also used to test runway and taxiway airport pavements at the Dallas–Fort Worth International Airport as part of a project to predict the remaining life of the airport pavements. Finally, the RDD was used in a stationary mode to dynamic load bridges and bridge foundations. All testing except the bridge project is presented in this report.

TABLE OF CONTENTS

CHAPTER 1. INTRODUCTION TO THE ROLLING DYNAMIC DEFLECTOMETER

1.1 INTRODUCTION

Nondestructive testing is an important tool in infrastructure management. The present combination of decaying infrastructure plus limited government expenditures in the United States calls for new nondestructive testing methods to assess more completely and accurately the condition of the nation's infrastructure and how it is changing with time. Better assessments and improved tracking with time from nondestructive testing will result in better decisions regarding where to expend effort and money on infrastructure, and can lead to better designs for repair and remediation.

The rolling dynamic deflectometer (RDD), developed at The University of Texas at Austin, is an improved method for nondestructive testing of highway and airport pavements. This report details the evolution in the development and present design of the RDD, the methods used for RDD testing, and the procedures used to analyze RDD measurements.

RDD testing has one major advantage over other nondestructive testing methods: RDD testing provides a continuous profile of pavement behavior, while most nondestructive (and destructive) testing techniques provide information only at discrete pavement locations. The problem with discrete testing methods is that there is no assurance that critical, or even typical, pavement locations will be tested. With continuous methods, the entire pavement is characterized. Thus, poor, average, and good sections of pavement can rapidly be delineated with the RDD. Additionally, a continuous profile gives a very informative picture of the performance of the pavement system. The behavior of every joint and crack is easily determined. The regions affected by joints and cracks are distinguishable from regions of intact pavement. Continuous deflection profiles of pavements are quickly measured with the RDD, and these measurements can be readily performed in the presence of traffic.

The RDD is a mobile, truck-mounted device. It generates and measures large dynamic forces, which are applied to the pavement through loading rollers as the truck moves along the pavement. The deflections induced by the dynamic loads are measured with multiple, specially designed rolling sensors. These measured deflections are indicators of the mechanical properties of the pavement system.

In this chapter, we introduce the RDD and RDD testing so as to make more meaningful subsequent discussions of this new technology. The following chapters contain detailed descriptions of the RDD that the reader will more fully understand if familiar with the basic RDD ideas and concepts presented in this chapter.

1.2 PURPOSE OF RESEARCH

The purpose of this research is to develop the technology for achieving robust measurements of continuous dynamic deflection profiles of pavements. Continuous deflection profiles are a powerful tool for assessing the quality and mechanical properties of a pavement system.

1.2.1 Nondestructive Testing in Pavement Management

Nondestructive testing plays an important role in pavement management. Various methods have been developed over the last several decades for testing pavements. These methods can generally be categorized as either seismic-based or deflection-based methods. Seismic-based methods measure the velocities at which low-strain ($< 10^{-4}\%$) stress waves propagate through the pavement. Deflection-based methods involve applying a large force to the pavement and measuring the induced deflections. Both methods are used to determine the elastic properties of the pavement. These elastic properties are then used to predict the pavement capacity and remaining life.

One additional nondestructive testing technique used to evaluate pavement is ground penetrating radar. This technique involves measuring the velocity of reflected electromagnetic waves propagating within the pavement. The product of these measurements is the dielectric properties of the pavement materials. Even though these results are often very useful, they do not directly measure engineering properties that affect pavement performance (as do seismic-based or deflection-based methods).

All seismic-based and deflection-based nondestructive methods commonly used in the U.S. are performed at discrete points along a pavement. These results are then used to characterize the entire pavement. The more tests performed, the better the predictions, though there is never complete assurance that all critical locations have been tested. Another weakness of discrete measurements is that it is difficult to separate the effects of the elastic properties of the pavement from the pavement geometry. For example, larger deflections will be measured near a joint or free edge. However, in discrete tests it is difficult to differentiate increased deflections created by joints and edges from increased deflections created by a softer pavement.

1.2.2 Advantages of Continuous Measurements

The RDD was developed to overcome the weaknesses inherent in discrete pavement testing techniques. The variability inherent in pavements, which nearly always traverse various geological formations, cuts, and fills, ranks among the highest degrees of variability encountered in an engineering design. Statistics provide a useful tool for estimating pavement properties from discrete measurements, but the ideal approach is to measure continuous properties of the entire pavement. The RDD rapidly measures continuous deflection profiles of a pavement.

At the present state of development, the continuous deflection profiles measured with the RDD do not provide as complete a picture of the individual layers composing a given pavement profile as do discrete methods such as the spectral-analysis-of-surface-waves (SASW) technique or the falling weight deflectometer (FWD) test with backcalculation of pavement properties. However, the advantages of a continuous profile make up for this weakness to some extent. Continuous deflection profiles can be used to locate precisely the softest pavement locations for remedial actions, quantify the extent of various pavement conditions, and determine the pavement performance at cracks, joints, and intact sections. Even greater benefits can be achieved by using the RDD in conjunction with discrete testing methods. Instead of randomly selecting locations for discrete tests, critical locations can be

selected from the continuous deflection profile. A few detailed discrete tests can be used to characterize larger areas of the pavement system that exhibit similar deflections.

There are several applications that are especially well suited for RDD testing. One of these is quality assurance and quality control (QA/QC). With continuous profiles, all sections of the pavement system not conforming to specifications are readily identified. Another application is load rating of pavements. RDD testing can be performed along the entire pavement to be load rated to identify critical sections. The RDD can quickly and completely characterize a length of pavement. This makes it very well suited to determine temporal variations in pavements caused by environmental conditions and number of loading cycles. Additional testing can then be performed at the critical sections to determine the pavement capacity. One additional test that might be performed with the RDD is a stationary fatigue test to measure directly the number of load cycles the pavement can withstand.

1.3 OVERVIEW OF THE ROLLING DYNAMIC DEFLECTOMETER

1.3.1 Description of the Rolling Dynamic Deflectometer

The RDD was constructed by modifying a Vibroseis truck. Vibroseis trucks are used in exploration geophysics to apply large dynamic forces to the ground in order to generate seismic waves for oil prospecting. The RDD requires similar dynamic forces. Thus, the Vibroseis was an ideal beginning point in the development of the RDD. Photographs of the Vibroseis truck and the RDD are shown in Figure 1.1.

a) Photograph of Vibroseis Truck

Figure 1.1 Photographs of the Vibroseis truck and the RDD

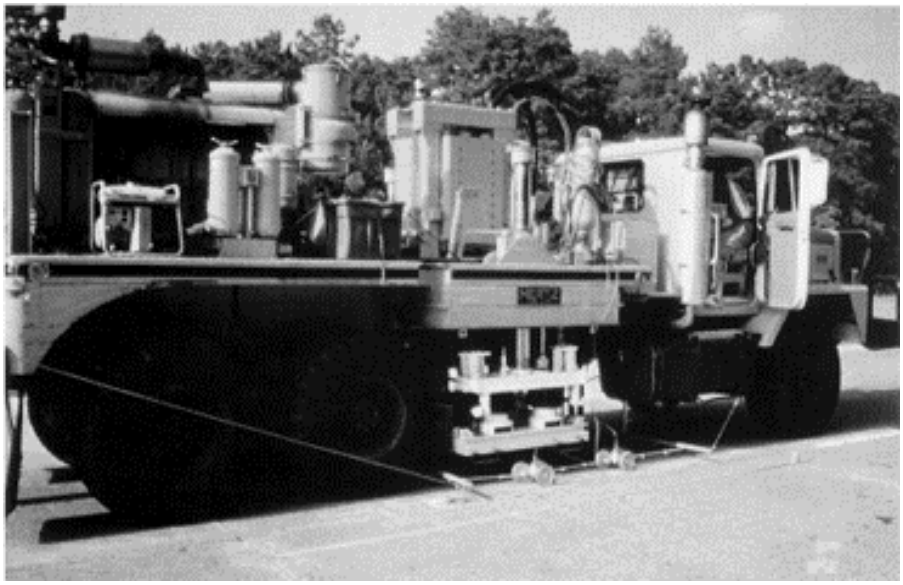

b) Photograph of the RDD

Figure 1.1 (Cont.) Photographs of the Vibroseis truck and the RDD

A line drawing of the RDD that identifies important components is shown in Figure 1.2. The truck has a gross weight of about 195 kN (44 kip). A large diesel engine on the rear of the truck powers a hydraulic pump. This hydraulic system powers the loading system, which applies a combined static and dynamic force to the pavement through two loading rollers. The displacements induced by the applied dynamic force are sensed with multiple rolling sensors that are pulled along with the truck.

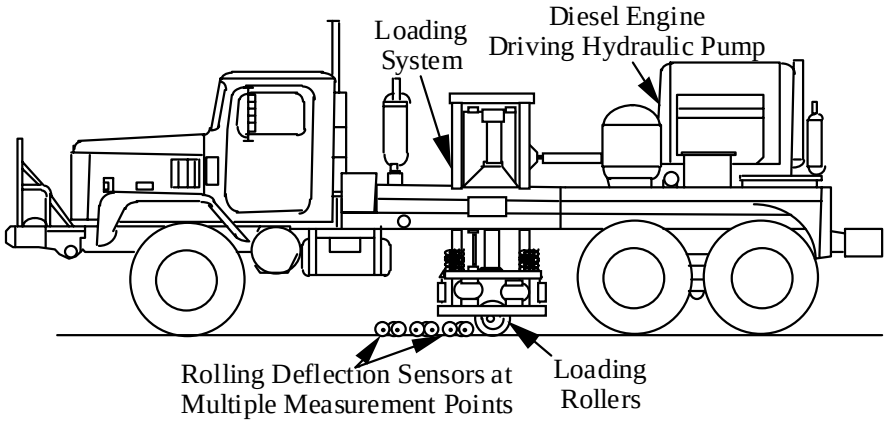

Figure 1.2 Drawing of the RDD Showing Important Components

Details of the RDD loading system are shown in Figure 1.3. Dynamic forces are generated by cycling hydraulic fluid in and out of the top and bottom chambers of the hydraulic actuator inside the reaction mass. The hydraulic pressure in the actuator accelerates the 33.4 kN (7.5 kip) reaction mass up and down. This system is capable of generating dynamic forces up to 154 kN (34.7 kip) peak at frequencies from 5 to 100 Hz. The dynamic forces are transferred down the stilt structure, to the loading frame, and then through the loading rollers to the pavement. The force applied to the pavement is measured with load cells located between the loading frame and the bearings of the loading rollers.

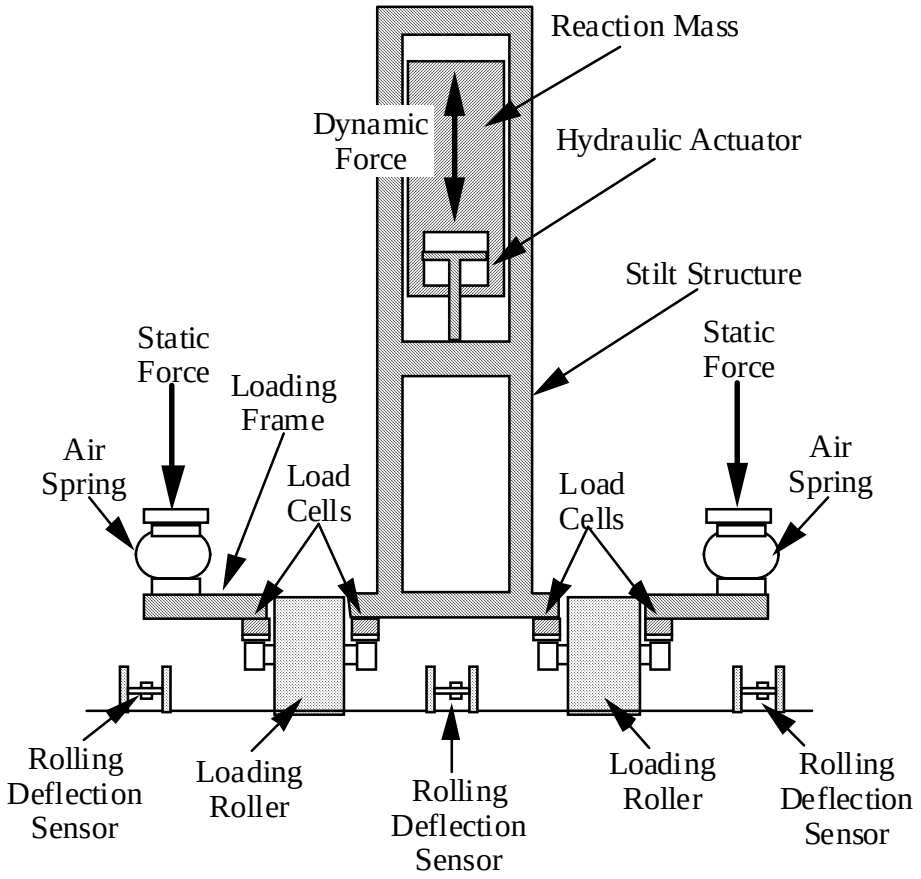

Figure 1.3 Front Cross-Sectional View of the RDD Loading System

The dynamic loading system is capable of generating forces much greater than the dead weight of the loading system. This could cause the entire loading system to momentarily lift off the pavement and then slam back down to the pavement. To prevent the loading rollers from lifting off the pavement, a static loading system is also provided. The static loading system is comprised of two hydraulic cylinders, one on either side of the truck.

These cylinders apply a static force to the loading system through two pairs of air springs. The air springs provide for compliance in the static loading system and act as isolators, reducing the vibrations in the truck caused by the dynamic forces.

An example of combined static and dynamic forces applied by the RDD in operation is shown in Figure 1.4. This figure shows a static force of 62.3 kN (14.0 kip) combined with a 40-Hz dynamic force of 53.4 kN (12.0 kip) peak-to-peak. This results in the total force cycling between 35.6 kN and 89.0 kN (8 to 20 kip). These force levels would be typical for RDD operation on a highway pavement.

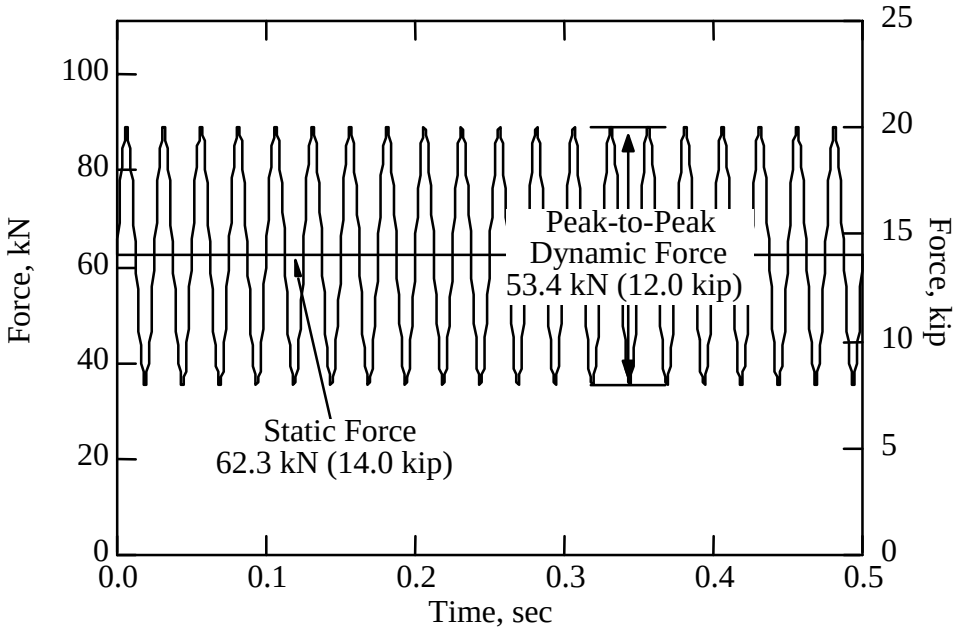

Figure 1.4 Example of Combined Static and Dynamic Forces Applied by the RDD

A number of rolling sensors were shown in Figures 1.2 and 1.3. These rolling sensors are used to measure the dynamic displacements induced by the RDD loading. The sensors can be positioned in any number of locations relative to the loading rollers, and they are pulled along with the truck by a vibration-isolated towing system. The locations of the rolling sensors are selected to meet the requirements of the particular study. The most important sensor location is the midpoint between the two loading rollers.

The outputs from the load cells, the loading rollers, and a distance-measuring device, which tracks the RDD position, are recorded on a PC-based data acquisition system. This data acquisition system incorporates filters and amplifiers to provide for high-quality measurements.

1.3.2 Operation of the Rolling Dynamic Deflectometer

Several operating parameters affect the performance of the RDD and must be selected prior to testing. These include: 1) the testing velocity along the pavement, 2) the operating frequency, 3) the applied force levels, 4) data acquisition sampling rate and filter settings, and 5) the rolling sensor positions. These parameters are discussed in greater detail in Chapter 7, where the criteria used to determine the parameters are presented. In general, RDD testing is performed at speeds of 0.3–0.6 m/s (1–2 ft/sec). Slower testing speeds are used for high-resolution testing, and higher testing speeds are used for low-resolution testing. The operating frequency is selected based on the site subgrade conditions, the pavement roughness and operating velocity, and on sensor contact considerations. Generally, the operating frequency is between 20 and 80 Hz. Force levels are selected based primarily on the estimated strength of the pavement to be tested. The possible range in dynamic forces is 13–300 kN (3–70 kip) peak-to-peak. A static force level is selected that will keep the loading rollers in contact with the pavement. The sample rate and filter settings are dependent on the selected operating frequency. The positions of the rolling sensors and the position of the loading rollers on the pavement are selected according to the purpose of the study. For instance, the loading rollers can be positioned near pavement edges, along longitudinal joints, or at the centerline of the slab to evaluate support in those areas. The rolling sensors can be positioned in a linear array to characterize the deflection basin, or they can straddle a longitudinal joint to evaluate the load transfer across the joint.

Testing is commenced by positioning the RDD at a known reference point, applying the combined loading, and then slowly driving over the pavement. The applied forces and the displacements at each rolling sensor are constantly monitored during testing. Additionally, the position of the RDD is constantly calculated based on the known starting position and using a distance encoding device. Ideally, testing will continue for approximately one hour, or until the RDD arrives at the next reference point.

Additional stationary tests can be performed with the RDD. The procedures used for these tests are outlined in Chapter 7. These tests are used to estimate the depth to bedrock, to measure the site response, and to measure the fatigue resistance of the pavement.

1.3.3 Rolling Dynamic Deflectometer Measurement Results

An example section of a continuous displacement profile measured with the RDD is shown in Figure 1.5. This testing was performed on runway 17R-35L at the Dallas-Fort Worth International Airport. This displacement profile was measured with the rolling sensor positioned at the midpoint between the two loading rollers. The results of this testing are presented in greater detail in Chapter 11.

The runway pavement shown as an example profile in Figure 1.5 is a reinforced, jointed concrete pavement, with dowelled and keyed joints spaced every 15.2 m (50 ft). The large displacement peaks in Figure 1.5 coincide with the location of these construction joints, as indicated in the figure. Additionally, smaller displacement peaks appear between the construction joints. These peaks correspond to the locations of sawn joints. This interpretation has been verified by matching the location of the joints with a survey of the runway.

Variations in the performance of construction joints, sawn joints, and midslab regions are readily observable in Figure 1.5. Additionally, the regions of the pavement where the displacements are influenced by each joint are discernible. It is immediately evident in Figure 1.5 that continuous results give a better representation of the performance of the pavement than could possibly be obtained with discrete results at few locations.

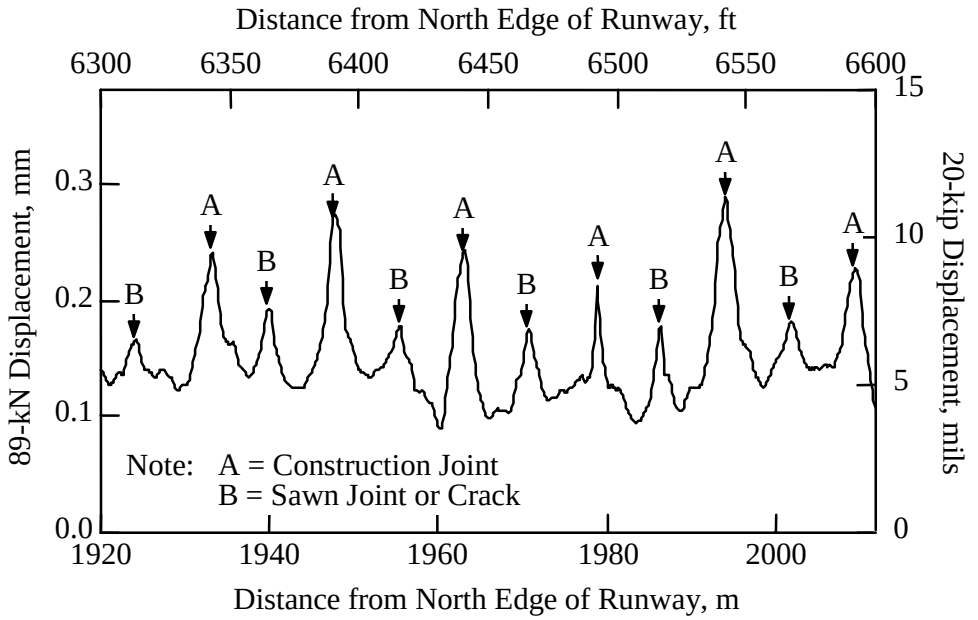

Figure 1.5 Example Section of a Continuous Displacement Profile; Example Section Measured on Runway 17R-35L at the Dallas-Fort Worth International Airport

1.4 ORGANIZATION OF THE REPORT

This chapter (Chapter 1) serves as an introduction to the RDD and presents the benefits of continuous deflection testing in pavement management. It is intended to familiarize the reader with the ideas and concepts behind the RDD.

Chapter 2 is a literature review. The chapter has two parts: The first discusses the various methods and devices historically and currently used to perform deflection testing on pavements. These different methods, along with the RDD, are compared and categorized according to the type of loading used, the methods of measuring deflection, and the efficiency of the method. The second section provides a brief history of the development of the Vibroseis method in exploration geophysics. As previously mentioned, the RDD uses Vibroseis technology for much of its loading system.

Chapter 3 discusses the RDD loading system. It begins with an explanation of the Vibroseis loading system, with subsequent sections presenting the details of structural,

mechanical, hydraulic, and electronic modifications that were made to the Vibroseis to obtain the RDD loading system.

Chapter 4 discusses the RDD force measurement system. Two different approaches have been used to measure the dynamic forces on the RDD: an inertial approach and load cells. This chapter presents the details of both approaches and the advantages of using load cells. The details of the design and construction of RDD load cells are presented.

Chapter 5 discusses the rolling sensors used to measure the deflections induced by the RDD loading. The influence of various rolling sensor parameters on rolling noise and sensor contact are presented. Two different rolling sensors have been used with the RDD. The designs and calibrations of both systems are presented.

Chapter 6 discusses the RDD data acquisition and distance measurement systems. These systems measure and record the forces applied by the RDD and the deflections induced by the dynamic loading. A distance encoding system is used to monitor the location of the RDD during testing.

Chapter 7 discusses the RDD testing procedures. The RDD testing parameters are discussed and criteria for selecting appropriate testing parameters are presented.

Chapter 8 presents the RDD data analysis procedures. The approach presented uses the principles of amplitude demodulation. The design of digital filters to use with this method are presented. The relationship between spatial resolution and the accuracy of displacement measurements is discussed. A statistical approach for predicting the confidence interval of RDD measurements is also given.

Chapter 9 presents the results of RDD measurements performed on two different rigid highway pavements. The first is an unreinforced, jointed concrete pavement on Interstate Highway 10 (IH-10) near Orange, Texas. The second is a reinforced, jointed concrete pavement on IH-10 in Houston, Texas.

Chapter 10 presents the results of RDD measurements taken on airport pavements at the Dallas-Fort Worth International Airport. RDD testing was performed on an operating runway, on an operating taxiway, and on a newly constructed runway. These different pavements are compared.

Chapter 11 contains the conclusions of this research. It discusses the strengths and weaknesses of the existing RDD, and identifies several improvements that can be made to the device.

1.5 SUMMARY

The RDD is a valuable new tool in pavement management. The RDD can quickly measure continuous displacement profiles of extended lengths of pavements (typically, 6.4–14.4 km [4–9 mi] can be profiled in a working day). With these continuous profiles, all poorly performing sections of the pavement can be identified, and the performance of every region can be quantified. With a continuous profile, regions influenced by cracks, joints, and free edges of the pavement are distinguishable from the intact midslab regions.

The RDD was developed by making extensive modifications to a Vibroseis truck that was purchased in 1988 with funding from the U.S. Air Force, the College of Engineering at The University of Texas at Austin, and Teledyne, Inc. The RDD makes use of the dynamic loading system of the Vibroseis, but adds the capability to apply dynamic forces to the

pavement while the truck is moving. The RDD has load cells to measure the forces applied to the pavement and a number of rolling sensors to measure the dynamic deflections induced by the loading system.

An example of a continuous deflection profile measured with the RDD on a rigid airport pavement is presented to familiarize the reader with the typical measurements that are performed. This profile illustrates the value of obtaining continuous profiles in differentiating the performance of different sections of pavement.

CHAPTER 2. LITERATURE REVIEW

2.1 INTRODUCTION

Engineers have recognized the value of pavement deflection measurements for more than 40 years. Several approaches have been used to measure these deflections. In the first part of this chapter, these approaches and the equipment that has been developed for pavement deflection testing are briefly discussed, and a perspective is offered on how these different methods of pavement testing compare.

The rolling dynamic deflectometer (RDD) makes use of Vibroseis technology developed in the field of oil-exploration geophysics. In the second part of this chapter, the development of wave sources for oil exploration, particularly the Vibroseis, is discussed.

2.2 PAVEMENT DEFLECTION TESTING

2.2.1 Static and Pseudostatic Deflection Measurements

A number of static or pseudostatic deflection testing methods have been developed. Static tests use a stationary, nontime-variant force to induce the measured displacement. Pseudostatic measurements use time-variant loadings that approximate a static loading. Typically, pseudostatic loads for deflection testing are slowly moving wheel loads.

2.2.1.1 The Benkelman Beam — In 1953, A. C. Benkelman of the U.S. Bureau of Public Roads developed this device that bears his name. The Benkelman beam was first used on the 1953 WASHO Road Test (Zube and Forsyth 1966). The Benkelman beam is a simple device used to measure pavement deflections induced by a stationary truck wheel. A simplified drawing of side and plan views of the Benkelman beam is shown in Figure 2.1.

The Benkelman beam consists of a reference frame supported by three legs. A probe arm pivots at the reference frame. The probe arm extends forward from the pivot 244 cm (8 ft) to a probe point, which rests on the pavement at the point where deflections are to be measured. The probe arm also extends 122 cm (4 ft) behind the pivot, where a dial gauge measures the relative vertical distance between the pivot arm and the reference frame.

Benkelman beam testing is usually performed during the unloading of the pavement. To perform the tests, a truck with dual rear wheels and a known wheel load is positioned on the pavement with one set of dual wheels at the measurement point. The Benkelman beam probe point is then positioned between the dual wheels. The reference frame is next leveled, and an initial dial gauge reading is made. The truck is moved forward more than 244 cm (8 ft) and a second dial gauge reading is made. The pavement rebound is equal to twice the difference between the final and initial dial gauge readings. Testing can also be performed by making an initial dial gauge reading with the pavement unloaded, and then loading the pavement for a final reading. Additional measurements can be made with the load at various locations relative to the probe.

To obtain accurate results with the Benkelman beam, the deflected region of a pavement must be limited to a radius of less than 244 cm (8 ft) around the loading point. Otherwise, the reference frame portion of the Benkelman beam will not remain fixed during the course of the test, resulting in a measurement that under-represents the total deflection.

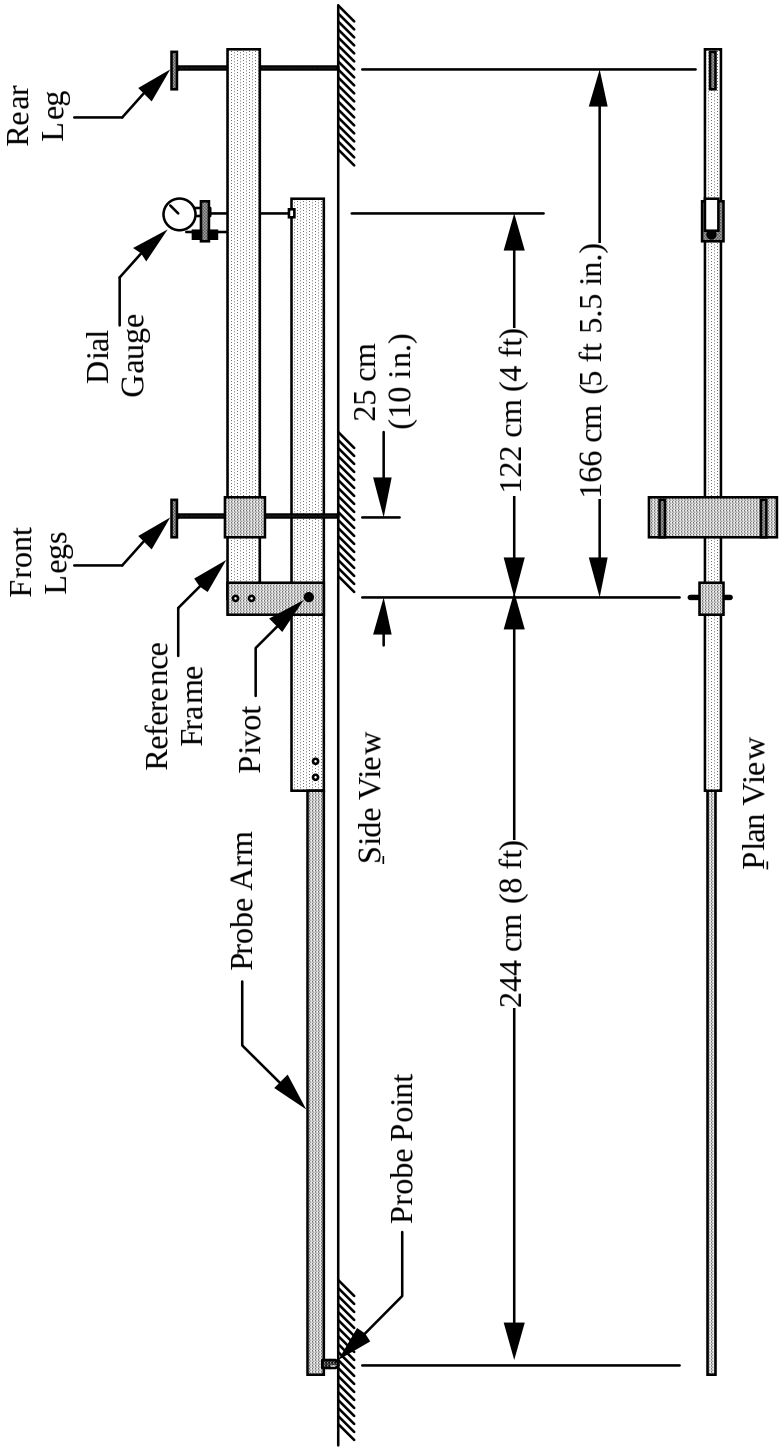

Figure 2.1 Simplified Drawing of Benkelman Beam (after Carneiro 1966)

Thick rigid pavements are very likely to have deflected regions larger than what the Benkelman beam is capable of measuring (Scrivner et al. 1966). In these cases, one or two additional Benkelman beams can be used. The additional devices are used to measure the deflections at the front legs — and perhaps the rear leg — of the primary Benkelman beam.

The equipment required for Benkelman beam testing is simple and inexpensive. Testing can be easily performed by a crew of three technicians. Typical daily production for such a crew is 50–100 test points per day (Smith and Lytton 1985).

2.2.1.2 The Traveling Deflectometer — Between 1955 and 1960, the California Division of Highways developed a device based on the Benkelman beam called the traveling deflectometer (Zube and Forsyth 1966). This one-of-a-kind device was a truck-trailer unit having dual probes to simultaneously measure the deflection between each set of dual wheels. With this device, deflection measurements were performed at 3.8-m (12.5-ft) intervals while traveling at a steady rate of 0.8 km/hr (0.5 mph). A total production of 1,500–2,000 test points per day by a crew of one technician has been reported (Smith and Lytton 1985).

Few details about this device are available, however. The fact that it was not more widely produced may indicate that it did not live up to its expectations or initial performance.

2.2.1.3 The CEBTP Curviameter — Another device that operates on principles similar to those of the Benkelman beam is the *Centre Experimental de Recherches et d'Ettudes du Batiment et des Travaux Public* (CEBTP) Curviameter (Paquet 1978). This French vehicle measures not only pavement deflections, but also the radius of curvature of the pavement deflection bowl. Testing is performed at discrete points every 11.45 m (37.6 ft) as the vehicle moves at a constant speed of 18 km/hr (11.2 mph).

The CEBTP Curviameter has a continuous chain that moves at the same velocity as the vehicle. The chain is positioned on the ground about 2.5 m (8 ft) in front of a pair of dual rear wheels of the truck. The chain passes back between the dual wheels and behind the wheels for more than 1.5 m (5 ft), and then back up over the rear wheel. As the truck moves forward, it constantly places the chain down in front of the rear wheels. The chain remains at a fixed location on the pavement as the truck wheels roll over it. One or more geophones are attached to this chain. The translated literature is not clear on the number of geophones used.

Testing proceeds in the following manner. When the geophone arrives at a position on the ground 2 m (6.6 ft) in front of the rear axle, a recording device begins to record the output from the geophone. The geophone remains at the same position on the pavement as the dual rear wheels roll over it, deforming the pavement. The measurement continues until the geophone is 1 m (3.3 ft) behind the rear axle. The vehicle continues forward until the geophone (or another geophone) is again in position for another test.

The geophone makes a measurement of vertical particle velocity, *d(t)*, at the pavement surface. The pavement deflection is calculated by simply integrating the geophone output. The pavement curvature, *C(x)*, is equal to:

$$C(x) = \frac{1}{R(x)} = d''(x) \qquad \text{(Equation 2.1)}$$

where $R(x)$ is the radius of curvature
$d''(x)$ is the second derivative of displacement with respect to distance

To calculate the curvature, the geophone output is first differentiated to obtain the vertical acceleration, $\ddot{d}(t)$. The curvature is then determined using the following relationship:

$$C(x) = \frac{\ddot{d}(t)}{V^2} \qquad \text{(Equation 2.2)}$$

where V is the vehicle forward velocity

The production rates and testing interval are dependent upon the number of geophones on the continuous chain. With one geophone on the chain, the testing interval would be about 5 m (16.4 ft) and the daily production would be about 2,500 test locations per day.

2.2.1.4 The Rolling Weight Deflectometer — Quest Integrated, Inc., is developing a rolling weight deflectometer (RWD) (Johnson and Rish 1996). This is a trailer-mounted device that makes continuous deflection measurements. The pavement is loaded with a single 76-cm (30-in.) diameter pneumatic tire mounted on the rear of the trailer. The static loading force is provided by removable weights and can be varied from 76.3 kN to 89 kN (17.1 to 20 kip). Testing is performed while pulling the RWD at a velocity of 10 km/hr (6 mph), and an average deflection is determined over every 0.3-m (1-ft) interval. The device uses exactly the same principles as the Benkelman beam to measure deflections.

The RWD consists of a support beam about 10 m (33 ft) long with the loading wheel at its rear, and four optical sensors that measure the distance to the pavement surface. The configuration of these sensors, designated A, B, C, and D, is shown in Figure 2.2.

The RWD deflection measurement is a two-step process, with such process illustrated in Figure 2.2 for a deflection measurement at point P_3. The first step in determining this deflection is to determine the distance, *h*, between the undeflected pavement surface at P_3 and the line defined by points P_2 and P_1. This analysis is conducted at time T_1 when the loading wheel is at point P_4, 2.74 m (9 ft) from point P_3. Using the geometry of similar triangles, the distance, *h*, is calculated as follows:

$$\text{at time } T_1\text{: } h = A - 2B + C \qquad \text{(Equation 2.3)}$$

where *A* is the distance from the optical distance sensor A to the pavement
B is the distance from the optical distance sensor B to the pavement
C is the distance from the optical distance sensor C to the pavement

The next step is to determine the distance, *h'*, between the deflected pavement surface at P_3 and the line defined by points P_2 and P_1. This analysis is conducted at time T_2 when the loading wheel is at point P_2. The equation for *h'* is:

$$\text{at time } T_2\text{: } h' = B - 2C + D \qquad \text{(Equation 2.4)}$$

where *B* is the distance from the optical distance sensor B to the pavement
C is the distance from the optical distance sensor C to the pavement
D is the distance from the optical distance sensor D to the pavement

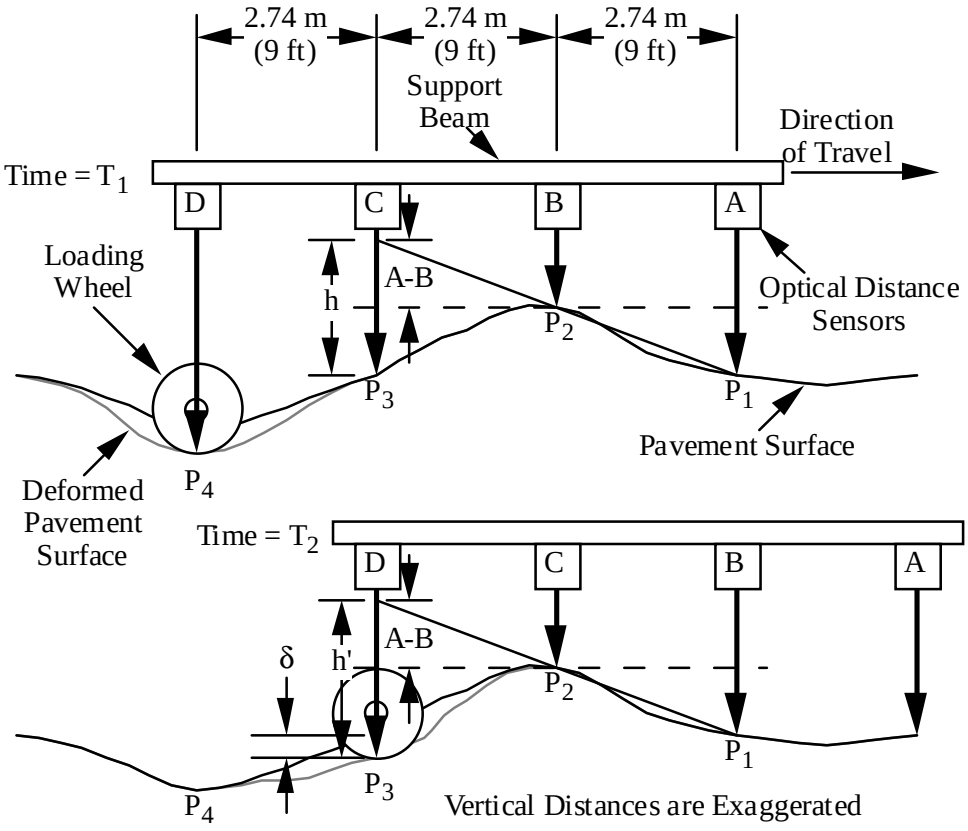

Figure 2.2 Configuration of Optical Distance Sensors on RWD Support Beam and Pictorial Representation of RWD Two-Step Deflection Measurement

The pavement deflection when the loading wheel is at point P_3 is:

$$\delta = h - h', \qquad \text{(Equation 2.5)}$$

where δ is the pavement deflection

In the first version of the RWD, the distances from the optical distance sensors were measured relative to the support beam. However, it was discovered that beam bending owing to thermal gradients and vibrations caused excessive errors in the deflection measurements. To solve this problem, a hollow support with a laser beam aimed down the length of the support beam was used. The laser beam, rather than the structural support beam, is used as the measurement datum.

The optical distance sensors emit a laser beam vertically downward to the pavement surface. Two lateral-effect photodiodes (LEPs) measure the distance to the pavement surface using triangulation and the parallax principle. The accuracy of this measurement depends on

the diameter of the spot of laser light on the pavement surface, with smaller spots yielding higher accuracy. Johnson and Rish (1996) report that spot diameters of a few millimeters are preferred for measurements of this sort.

Using small spot diameters leads to complications in RWD testing. To obtain accurate deflection measurements, it is essential that identical locations be measured by subsequent optical distance sensors. For example, in Figure 2.2, sensor C first measures the distance to point P_3. The RWD then rolls forward 2.74 m (9 ft) and sensor D must measure the distance to exactly the same point. If the RWD turns slightly and sensor D measures a point other than P_3, an error about equal to the difference in elevation of point P_3 and the point actually measured will be introduced into the deflection measurement. This error could easily be several orders of magnitude higher than the actual deflection. Johnson and Rish (1996) report that adequate results are obtained if there is at least 50 percent overlap in the regions scanned by subsequent sensors.

Johnson and Rish (1996) have presented the results of RWD measurements on about 230 m (750 ft) of an airport taxiway. Additionally, falling weight deflectometer (FWD) tests were performed on the same pavement at intervals of 15.2 m (50 ft). The RWD results show a reasonable agreement with the FWD results. The RWD was able to identify pavement features that were missed in the FWD testing. The testing, therefore, illustrates the value of continuous measurements over discrete measurements.

This testing was performed using a laser spot diameter of 6.3 mm (0.25 in.). Johnson and Rish's (1996) criteria of 50 percent overlap between the regions scanned by subsequent sensors would have required that the minimum curvature of the RWD path be less than 1,190 m (3,900 ft). To this writer, that seems a prodigious feat of driving skill. With very careful driving, the RDD can remain in a path about 2.5 cm (1 in.) wide at speeds of up to 1.6 km/hr (1 mph). RWD operation would require driving a vehicle pulling a long trailer at speeds of up to 10 km/hr (6 mph) within a path 0.63 cm (0.25 in.) wide. This leads this writer to question the robustness of the measurement technique as currently implemented. Also, the required straight testing path makes testing on curved highway pavements impossible. Furthermore, there is no way to verify that the testing was actually performed with an acceptable overlap in scanned areas.

2.2.2 Dynamic Deflection Testing

Another class of deflection testing methods uses a dynamic force to generate pavement deflections. There are two different types of dynamic forces that can be applied to the pavement. The first is a steady-state sinusoidal excitation. With this monochromatic type of excitation, all of the dynamic force is at a single frequency. The second type of dynamic force is a broadband excitation, where the force energy is distributed over a range of frequencies. A broadband force can be obtained in a number of ways, but the means employed in pavement deflection testing is an impulsive force generated with a drop weight.

2.2.2.1 The Dynaflect — The first dynamic displacement measurement technique was the Dynaflect. The Dynaflect was first developed in 1964 by the Lane-Wells Company (Scrivner et al. 1966). The Dynaflect is a trailer-mounted device that uses two eccentric rotating masses to generate a monochromatic vertical force. This dynamic force is applied to the pavement through two steel wheels. The force is applied at a fixed frequency of 8 Hz

with a force level of 4.45 kN (1 kip) peak. The trailer has a dead weight of 7.12 kN (1.6 kip), which supplies the hold-down force required to keep the loading wheels in contact with the ground. The displacements induced by this force are measured with five geophones.

A plan view of the typical arrangement of the loading wheels and the geophones for Dynaflect testing is shown in Figure 2.3. One geophone is positioned at the midpoint between the loading wheels, and the other four geophones extend out in a linear array to measure the deflection basin. No measurement of pavement deflection is made at the points of load application.

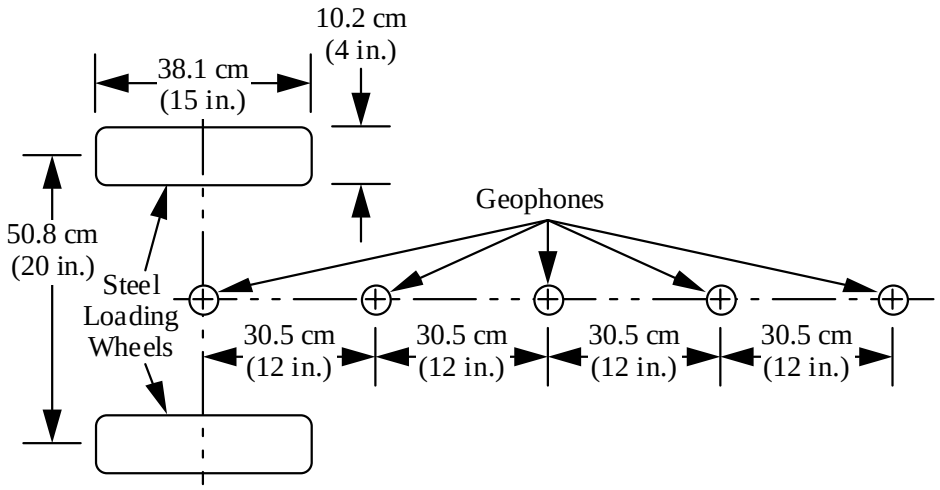

Figure 2.3 Plan View of the Typical Loading Wheel/Geophone Arrangement Used for Dynaflect Testing (after Scrivner et al. 1966)

The testing is conducted by positioning the device at the testing location. A motorized lift system then lowers the steel loading wheels and, in the process, raises the trailer's pneumatic wheels off the pavement. The geophones are then lowered into contact with the pavement. A motor begins spinning the eccentric masses. The rate of rotation of the spinning masses is monitored. When the spinning rate has come to equilibrium at 8 Hz, the output from each geophone is recorded. Deflections are determined from these outputs. If the next test location is a short distance away, the geophones are raised off the pavement and the Dynaflect is rolled to the next location on the steel loading wheels at speeds less than 16 km/hr (10 mph). If higher towing speeds are required, then the steel loading wheels are raised and the trailer is pulled on the pneumatic wheels.

The Dynaflect has been used fairly widely around the world. A typical production rate for a crew of two technicians is 100–400 test locations per day (Smith and Lytton 1985).

2.2.2.2 The Road Rater — The Road Rater is a device functionally similar to the Dynaflect. Both devices are trailer-mounted. They both apply monochromatic dynamic forces to the pavement, and they measure the induced deflections with an array of geophones.

The Road Rater uses a hydraulic system to accelerate a reaction mass up and down, generating the vertical dynamic force. Unlike the Dynaflect, the frequency and magnitude of

the dynamic force can be varied on the Road Rater. Various sizes of Road Raters have been built. The smallest can generate peak dynamic force levels of 2.22 kN–8.9 kN (0.5 kip–2 kip). The largest device can generate peak dynamic forces from 4.45 kN to 35.6 kN (1 kip to 8 kip). The hold-down force is supplied by the weight of the trailer. Loading frequencies from 5 to 70 Hz can be used (Smith and Lytton 1985). The force is applied to the pavement through a rectangular or circular steel plate. Plates of various sizes and shapes have been used with the Road Rater. All plates have a hole in the center, through which a deflection measurement is made. The applied vertical force magnitude is measured with a load cell.

The Road Rater uses a linear array of four or five geophones extending away from the loading plate. One geophone is positioned at the center of the plate, and a spacing of 30.5 cm (1 ft) between geophones is typically used.

Testing can be performed at various force and frequency levels with the Road Rater (Hoffman and Thompson 1982). This testing can be used to study nonlinear behavior and frequency effects of pavement systems.

Typical production for the Road Rater operated by a crew of one or two technicians is 100–400 test locations per day (Smith and Lytton 1985).

2.2.2.3 The Falling Weight Deflectometer — The FWD was first developed in Europe (Bohn et al. 1972), but is now used widely in the United States. The FWD is a trailer-mounted device used to apply an impulsive dynamic force to the pavement and measure the induced deflections. Three different FWDs have been developed: the Dynatest FWD, the Phoenix FWD, and the KUAB FWD. The Dynatest is the FWD device most commonly used within the United States. All three devices apply a broadband impulsive force to the pavement by dropping a weight on a spring-loaded pad and recording inertially referenced deflection measurements of the induced deflections (Smith and Lytton 1985).

The FWD was designed to apply a force pulse to the pavement in an action similar to the loading applied by moving vehicular traffic. Research with transducers buried in pavement indicates that the wheel loads of a truck traveling 80 km/hr (50 mph) will load the pavement with a force pulse about 120 msec wide (Hoffman and Thompson 1982). The force level and duration of FWD loading can be varied by changing the mass of the drop weight, the drop height, and the stiffness of the pad that the drop weight strikes. The stiffness of the pavement also influences the level and duration of FWD force pulses. Force levels of 4.45 kN–156 kN (1 kip–35 kip) and force pulse durations of 30 msec–40 msec can be achieved with various FWD devices.

The frequency content of an FWD impulse is determined by the shape and duration of the force pulse. For example, synthesized FWD time records with durations of 120, 60, 30 and 15 msec are shown in Figure 2.4a. These force pulses are haversine shaped, which is a good approximation for the shape of traffic or FWD force pulses. All of the force pulses have a peak value of 1 kN (0.225 kip). Frequency spectra for the four force pulses are shown in Figure 2.4b. The spectral amplitudes for all of the pulses are lower than the peak values in the time domain, because the force energy is distributed over a range of frequencies. The longest duration force pulse (120 msec) has the highest spectral amplitude at low frequencies, but its amplitude drops most quickly with frequency. On the other hand, the shortest duration force pulse (15 msec) has the lowest spectral amplitude at low frequencies, but the highest spectral amplitude at high frequencies. The 120-msec force pulse roughly

approximates traffic moving at highway speeds. FWD loading would generally fall somewhere between the 30- and 60-msec force pulses.

All three types of FWDs apply the dynamic force to the pavement through a 30-cm diameter (11.8-in. diameter) circular pad. The KUAB FWD uses an oil-filled hydraulic device to distribute the force equally between four segments in its loading plate (Thollen et al. 1985). All the devices use a hole in the center of the loading plate to measure the pavement deflections at the point of load application. Load cells are employed to measure the vertical dynamic force applied to the pavement.

A linear array of transducers is used to measure the deflection basin from the imposed dynamic loading for all three types of FWDs. All the devices employ one deflection sensor at the loading point. The Dynatest FWD uses as many as seven geophones — located at any position in a linear array — to measure displacements. The Phoenix FWD uses three geophones to measure deflections: one at the center of the load pad, and the others at 30 cm and 75 cm (11.8 in. and 29.5 in.) from the center of the loading pad (Smith and Lytton 1985). The KUAB uses five specially designed, inertially referenced displacement transducers to measure the induced deflections (Thollen et al. 1985). These sensors measure the distance between the pavement surface and a spring-mass reference using linear variable displacement transducers (LVDTs). Again, one transducer is positioned at the center of the loading pad. The remaining transducers can be positioned at arbitrary locations from 20 cm to 250 cm (7.9 in. to 100 in.) from the center of the loading pad.

FWD testing is conducted by positioning the FWD at the desired testing location. The loading pad and the deflection sensors are then lowered to contact the pavement. The drop weight is then raised hydraulically. When the drop weight is at the selected drop height, an electrical release drops it onto the loading pad. A data acquisition system measures the load cell and deflection transducer outputs. Typically, the test is repeated several times and the results averaged. Tests can also be performed using different drop heights and, hence, different force levels at each testing location. After the testing is completed, the loading pad and sensors are raised, and the device is towed to the next test location. Typical daily production for the FWD operated by a crew of one or two technicians is 100–300 test locations per day (Smith and Lytton 1985).

2.2.3 Summary of Pavement Deflection Testing Methods

Many researchers have attempted to make empirical correlations between the deflections measured with the dynamic devices discussed above (Scrivner et al. 1966, Thollen et al. 1985, and Hoffman and Thompson 1982). These attempts are complicated by the fact that each of the devices applies a different loading function to the pavement. The induced deflection is determined by the force magnitude and the frequency content of the forcing function. The frequency dependencies vary from site to site because of pavement and subgrade conditions. Given the site dependency of these comparisons, they are of limited value and are not presented herein. This discussion is limited to the mechanistic differences between the various testing methods.

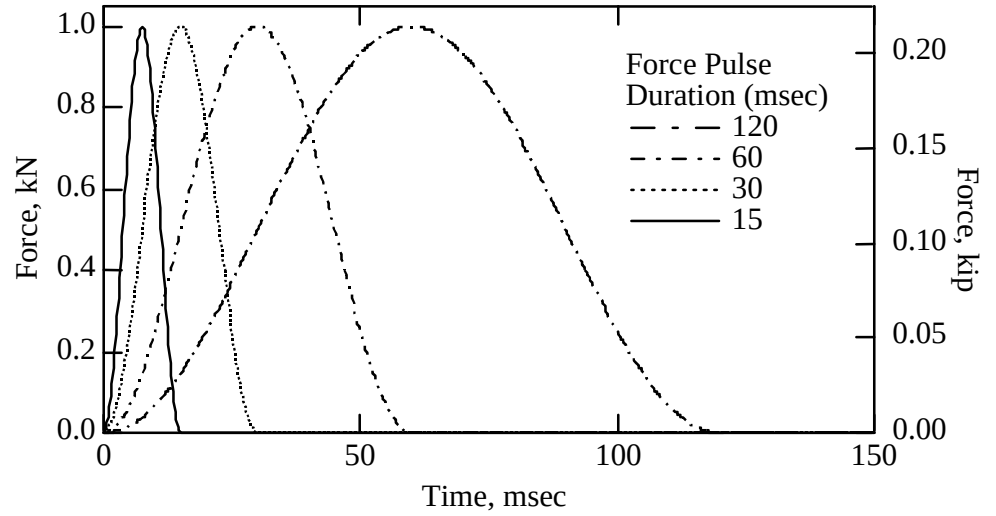

a) Synthesized FWD Time Records

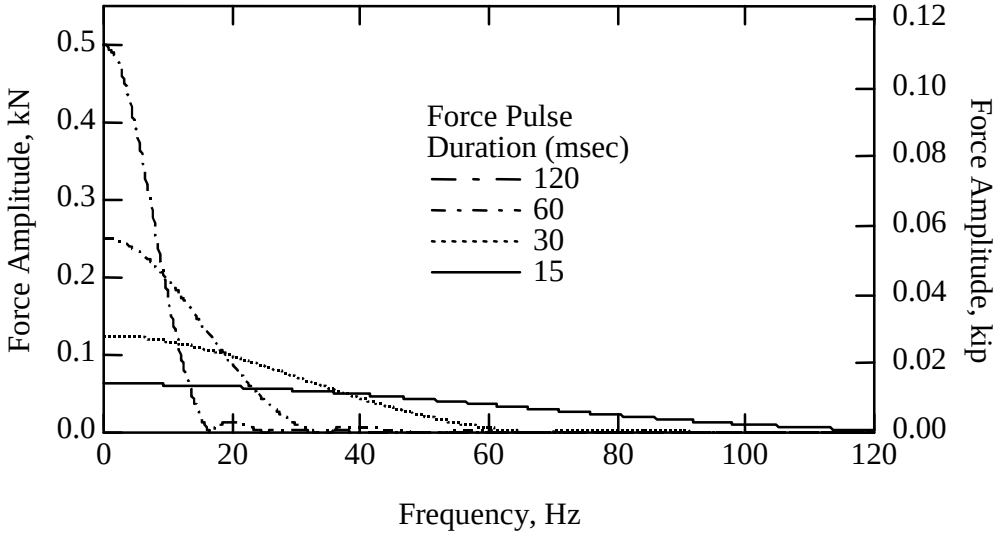

b) Amplitude Spectra from Synthesized FWD Time Records

Figure 2.4 Time Domain Records and Amplitude Spectra for Synthesized FWD Force Pulses

The first way the different methods can be compared is by the type of forcing function they apply to the pavement. The applied forces for all of the methods discussed are summarized in Table 2.1 (the traveling deflectometer is not included because few details about it are available in the literature). The RDD is also included in this comparison.

The static and pseudostatic methods have the advantage of being easier to model analytically than the dynamic methods. On the other hand, actual vehicular pavement loading is dynamic, so the dynamic method may simulate actual loading conditions better than the static methods. There is a significant advantage to using monochromatic dynamic

forces for pavement loading. The monochromatic signal can be separated from the background noise caused by traffic and other noise sources using filters.

The next way to compare the different deflection methods is by the methods used to measure the deflections. Table 2.2 contains a comparison of deflection testing methods.

Table 2.1 Summary of Forcing Functions Applied to the Pavement by Various Deflection Testing Methods

Deflection Testing Method	Type of Applied Force	Force Level	Frequency Range	Force Measurement Method
Benkelman Beam	Static	≈ 23–45 kN (5–10 kip)	0 Hz	Dead Weight on Wheels
CEBPT Curviameter	Pseudostatic	≈ 23–45 kN (5–10 kip)	< 4 Hz*	Dead Weight on Wheels
RWD	Pseudostatic	76–89 kN (17–20 kip)	< 4 Hz*	Dead Weight on Wheels
Dynaflect	Monochromatic Dynamic	8.9 kN (2 kip) peak-to-peak	8 Hz	Inertial
Road Rater	Monochromatic Dynamic	2.2–36 kN (0.5–8 kip) peak-to-peak	5–70 Hz	Load Cell
FWD	Broadband Dynamic	4.45–156 kN (1–35 kip)	≈ 0–60 Hz Distributed	Load Cell
RDD	Monochromatic Dynamic	13.3–310 kN (3–70 kip) peak-to-peak	20–100 Hz	Load Cells

*Frequency range could not be found in literature and was simply estimated.

Table 2.2 Summary of Deflection Measurement Methods Employed by Various Deflection Testing Methods

Deflection Testing Method	Deflection Reference	Deflection Measured at Point of Force Application?	Number of Measurement Points
Benkelman Beam	Elevation Datum	Yes	1
CEBPT Curviameter	Inertial	Yes	Continuous for 3 m*
RWD	Elevation Datum	Yes	1
Dynaflect	Inertial	No	Up to 5
Road Rater	Inertial	Yes	Up to 5
FWD	Inertial	Yes	Up to 7
RDD	Inertial	No	Up to 4

*Sensor monitors deflection as loading wheel rolls by.

Two different approaches are used to measure deflections. One is to use an elevation datum as a reference, and the other is to use an inertial reference. Using an inertial reference is a simpler, more robust measurement. The geophones employed for most of these devices are simple, inexpensive, and reliable transducers. These geophones are technically called vertical velocity transducers, which means vertical displacements are obtained with a single integration, and vertical accelerations with a single differentiation.

For the pavement deflection methods using an elevation reference, the reference is established on the pavement some distance from the loading point (about 2.4 m [8 ft]). This is troublesome because sometimes the reference point is in the region of deflected pavement. Extending the reference point further from the loading point is not usually a practical solution. In the case of the RWD, the elevation datum is further complicated by vibrations from the moving test and a constantly changing datum position. The RWD requires involved laser sensors to minimize these problems.

A deflection measurement at the loading point is very valuable. This is the point with the largest deflections and the easiest point to model. All of these methods allow for this measurement except the Dynaflect and the RDD.

Moreover, measuring deflections at multiple points has substantial benefits. The shape of the deflection basin contains important information about the pavement system. The shape of the deflection basin can be obtained from all the methods except for the Benkelman beam and the RWD.

The last way to compare the different methods is by their coverage and testing efficiency. Table 2.3 compares the different methods with regard to their coverage and efficiency.

The very high daily production of the CEBPT Curviameter illustrates the value of a continuously moving measurement. Unlike the other discrete testing methods, the CEBPT Curviameter does not stop for each test. Consequently, the CEBPT Curviameter quickly performs a very large number of discrete measurements over a large distance.

Table 2.3 Summary of Coverage and Efficiency of Deflection Measurement Methods

Deflection Testing Method	Coverage (Discrete or Continuous)	Crew Size	Maximum Daily Production
Benkelman Beam	Discrete	3	50–100 Points
CEBPT Curviameter	Discrete (but moving)	No Data	2,500 Points over 144 km (90 mi)
RWD	Continuous	No Data	60 km (36 mi)*
Dynaflect	Discrete	1–2	100–400 Points
Road Rater	Discrete	1–2	100–400 Points
FWD	Discrete	1–2	100–300 Points
RDD	Continuous	1–2	14.4 km (9 mi)**

*10 km/hr × 6 hr/day = 60 km/day **2.4 km/hr × 6 hr/day = 14.4 km/day

The only two methods that make a continuous measurement are the RWD and the RDD. Continuous measurements have the production advantage of being a continuously moving measurement. Much more pavement is evaluated with continuous measurements than with discrete methods. Perhaps more important, the entire pavement can be tested. There is no need to predict pavement properties statistically, and all critical sections of pavement will be detected.

The RWD's operational speeds are higher than those for the RDD, making it somewhat more efficient. The RDD, however, is more robust because it utilizes an inertial displacement measurement rather than the difficult elevation-referenced measurement used on the RWD; moreover, there is no need to drive the RDD along an extremely straight path as with the RWD.

Among the discrete methods, the Benkelman beam is the most labor intensive and least efficient. The CEBPT Curviameter is by far the most efficient. There is little difference among the other methods.

2.3 DEVELOPMENT OF THE VIBROSEIS FOR OIL EXPLORATION

The RDD utilizes technology that was developed for the Vibroseis method in exploration geophysics. This section reviews the history of the exploration methods leading up to the Vibroseis method, and then discusses the Vibroseis method in some detail.

2.3.1 Brief History of Sources for Seismic Exploration

Geophysicists have used seismic waves to characterize geological strata since the early part of this century. The primary approach used is a reflection survey. A detailed discussion of this approach is given by Waters (1981). The following brief discussion of reflection seismology deals only with a few aspects that are of interest in the development of the Vibroseis method.

Generally, a reflection survey involves generating waves on or near the earth's surface and monitoring the wave reflections off deep strata, with a number of surface receivers arranged at various distances from the source. The depths to various geological layers are determined from the times required for the reflections to arrive at the receivers.

Reflection surveys present a few major challenges. First, most of the energy generated from a source at or near the earth's surface does not propagate into the earth as body waves. Most of the energy propagates along the ground surface in the form of surface waves (Richart et al. 1970), or what geophysicists generally call *ground roll*. This distribution in energy means that much of the motion sensed by the surface receivers contains no information about the deep strata. The second challenge is associated with weathered, unlithified near-surface strata. Generally, this near-surface material is quite variable, both in terms of its stiffness and its depth. Because of the relatively slow wave velocities associated with this material, vertical waves spend a relatively long time propagating through the near-surface strata. This material can be viewed as a lens that distorts the geophysicist's view of deep strata. When more time is required for a reflection off a deep layer of interest to reach the surface, it is difficult to determine whether that is because the layer is deeper at that location or because the wave spent more time propagating through the near-surface material. Third, it is often a challenge to obtain a wave source with enough energy to guarantee that sufficient reflected energy will be generated to be detectable at the ground surface.

2.3.1.1 Buried Dynamite Source — The first wave source used extensively in reflection seismology was a dynamite charge buried in a borehole (Anstey 1991). Dynamite provides large amounts of energy and, because it burns very rapidly, it provides sharp reflections that are easy to detect. Initially, dynamite was buried to constrain the blast, minimize the danger of deadly shrapnel, and minimize air-blast waves. It was discovered that buried dynamite also reduced the amount of energy that propagated as surface waves. By burying the dynamite below the weathered near-surface material, the distortion caused by the weathered layer is also reduced. The wave propagates through the distorting material only once, instead of twice, as with a source at the surface.

Because buried dynamite provided very good results, it is still used as the wave source in almost half the seismic surveys conducted worldwide (Baeten and Ziolkowski

1990). With buried dynamite, however, the time and labor involved in drilling shot holes severely limits the production of a seismic crew and increases the cost of the survey. Dynamite also is not a suitable source for testing close to developed areas, where the substantial vibrations from the blast can cause damage to structures.

2.3.1.2 Surface Dynamite Source — Another seismic source is dynamite on the ground surface or poles a short distance above the ground surface. This is known as air shooting (Anstey 1991). It was first used in the early 1950s in seismic exploration of Antarctica, where boring was not possible. The method is very dangerous and has never been widely used. However, it is of interest because it led to the development of surface source arrays.

Geophysicists using air shooting found that their results were complicated by the presence of more surface wave energy than was obtained with buried shoots. They found that the surface wave energy could be decreased by setting off a number of charges simultaneously. These charges were arranged in an array in line with the receiver line. The surface wave energy from each charge in the source array tended to cancel the energy from adjacent charges as it propagated in the horizontal direction. The vertically propagating energy from all the charges added constructively, increasing the total body wave energy. By clever arrangement of a surface array, critical wavelength ranges of surface waves could be highly attenuated (Waters 1981).

2.3.1.3 The Thumper Source — The thumper, another class of surface sources, was also developed in the early 1950s (Anstey 1991). Many different versions of the thumper have been developed, but they are all essentially heavy drop weights mounted on trucks. In some cases, the drop weight is propelled downward with large elastic bands, as much to prevent the drop weight from rebounding as to increase the energy.

There are many problems with thumpers. Thumpers do not provide sharp pulses like dynamite does. When successive drops from thumpers are averaged (stacked), problems arise owing to variability between successive drops. It is impossible to synchronize multiple units to use thumpers in a source array. In spite of these problems, testing with the thumper is very fast and convenient. Because of the ease associated with a nonexplosive, mobile, surface source, the thumper was used quite widely for about 20 years, despite its limitations.

2.3.1.4 The Dinoseis Source — The thumper demonstrated the advantages of having a highly mobile, surface source. The Dinoseis source was developed to gain the advantages of the thumper while overcoming some of its weaknesses. The Dinoseis source is a truck-mounted source consisting of a large cylindrical chamber with a flexible diaphragm on the bottom. To operate the source, the diaphragm is lowered to the ground. The chamber is filled with a mixture of oxygen and propane. This mixture is ignited with a spark, generating a sharp explosive force pulse in the earth (Anstey 1991).

The Dinoseis source has the advantage of creating a sharp explosive force, like dynamite. Furthermore, the sparks igniting the fuel mixture of a number of these devices can be synchronized, allowing the Dinoseis to be used in a source array. The Dinoseis was a major advance in surface seismic sources.

2.3.2 Development of the Vibroseis Source

The technological advancements that led to the Vibroseis method were made during World War II through radar and sonar research (Anstey 1991). Efforts to extend the range of radar were failing, because putting more electrical power into antennas resulted in arcing rather than electromagnetic wave transmission. Similarly, further increases in power in sonar sources resulted in cavitation rather than in acoustic wave propagation. To solve these problems, researchers found a means of increasing the energy in propagating waves without increasing the source power. Energy is power multiplied by time. Therefore, wave energy can be increased by increasing the time the source is driven, rather than increasing the power driving it. Unfortunately, long wave trains are not conducive to accurately measuring travel times, as is required in radar and sonar. However, long wave trains can be analytically compressed into a pulse using cross-correlation if there is no repetition within the wave train. One type of wave train that fits this requirement is a chirp or sweep (Waters 1981). A chirp or sweep has a constantly changing frequency and, hence, no repetitive segments. The general equation for a linear sweep is:

$$F(t) = F_D \sin 2\pi\left(at + \frac{bt^2}{2}\right)(0 < t < T) \qquad \text{(Equation 2.6)}$$

where $F(t)$ is the sweeping force function
F_D is the peak dynamic force
T is the duration of the sweep
a and b control the sweep beginning and ending frequencies

The beginning frequency of the sweep (f_o), and the ending frequency of the sweep are calculated as follows:

$$f_o = a \qquad \text{(Equation 2.7)}$$

$$f_f = (a + bT) \qquad \text{(Equation 2.8)}$$

A plot of a linear sweep from 1 Hz to 10 Hz with a peak dynamic force of 44.5 kN (10 kip) is shown in Figure 2.5.

These advancements led to the development of chirp radar and chirp sonar, but remained classified until 1952. In 1952, Bill Doty, a Conoco researcher, attended a seminar at MIT on advanced echo-ranging systems. He recognized the potential value of chirped sources in geophysical exploration. Bill Doty and his supervisor, John Crawford, convinced Conoco of the value of this approach and put together a team of Conoco researchers to develop the Vibroseis method (Anstey 1991).

There were three major challenges to overcome in developing the Vibroseis method. The first was to develop a source that could impart a controlled force-sweep to the ground. The second was the development of a control system capable of driving several of these sources simultaneously, such that all the sources would remain in phase throughout the sweep. The use of several sources together is important because it allows the use of source array. The final challenge was the development of a system to cross-correlate the receiver

outputs with the applied forcing function (Waters 1981). This last step is nearly trivial today, given our current digital technology. To researchers in 1952, however, it was a daunting task, and one that they deserve great credit for solving using only analog tools.

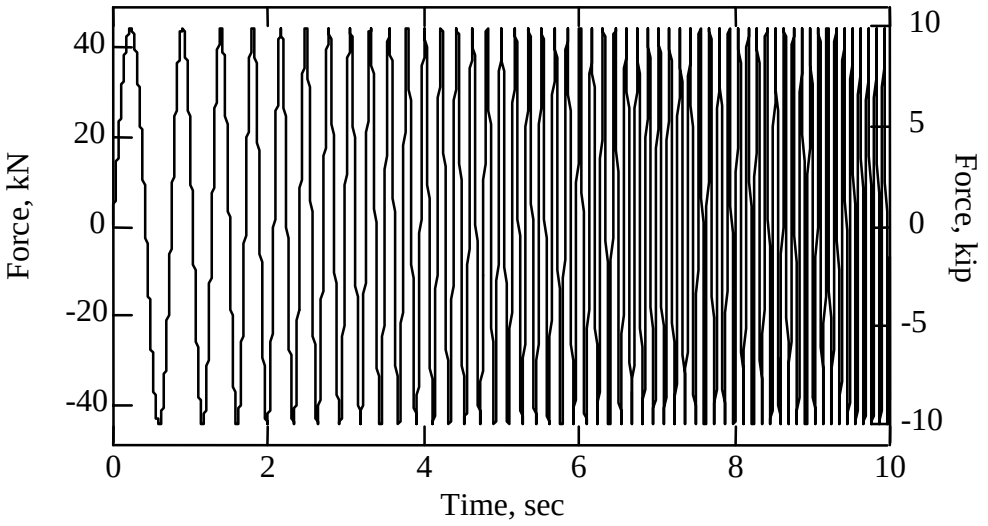

Figure 2.5 Linear Force Sweep from 1 Hz to 10 Hz with Peak Dynamic Force of 44.5 kN (10 kip)

Conoco researchers developed the Vibroseis truck as the seismic source for imparting a known forcing function into the ground. The RDD also requires a highly controllable source to apply high forces to the pavement. The Vibroseis loading system is discussed in depth in Section 3.2. The RDD has a superior dynamic loading system because it benefits from the years of research that went into Vibroseis development and from the experience obtained through millions of hours of Vibroseis operation.

2.4 SUMMARY

Over the past 40 years, pavement engineers have recognized the value of pavement deflection measurements for assessing the quality of pavement systems. Several methods to make these measurements have been developed using static, pseudostatic, and dynamic forces. In this chapter the major methods have been discussed and compared. Only two methods have been developed for measuring deflections continuously. These are the RWD and the RDD, the latter being the subject of this report.

The creation of the RDD was aided significantly by technology that was developed as part of the Vibroseis method used in exploration geophysics. This chapter contained a brief discussion of the history of the development of surface sources in exploration geophysics, and especially the development of the Vibroseis method.

CHAPTER 3. DEVELOPMENT OF THE ROLLING DYNAMIC DEFLECTOMETER LOADING SYSTEM

3.1 INTRODUCTION

The Vibroseis was chosen as the moving platform for the rolling dynamic deflectometer (RDD) because its loading system already has many of the features required for an RDD, and because this type of vehicle is readily available. Nonetheless, the unique function of the RDD requires a number of modifications to the Vibroseis. This chapter discusses the various components of the Vibroseis loading system and the modifications that were required to convert a Vibroseis to an RDD.

3.2 THE VIBROSEIS LOADING SYSTEM

The Vibroseis is used to apply combined static and dynamic forces to the ground surface through a reinforced loading plate while the truck is stationary. A schematic representation of the loading plate in operation is shown in Figure 3.1. The dynamic vertical force generated by moving the reaction mass is transferred to the loading plate through four stilts. This operation does not impose lateral forces on the Vibroseis loading system. Also, tipping is prevented by the large contact area of the plate relative to the small central area where the force from the reaction mass is delivered to the plate. The only requirement of the static hold-down force on the Vibroseis is that it must be larger than the peak dynamic force to keep the plate in contact with the ground while vibrating. The fact that the bearing area of the plate (about 3 m^2 [32 ft^2]) is much larger than the bearing area of the truck wheels (about 0.39 m^2 [4.2 ft^2]) means that the plate will always be able to support the total weight of the Vibroseis. Thus, normal Vibroseis operation involves applying a static force nearly equal to the total vehicle weight. Moreover, in normal Vibroseis operation, there is no need to carefully regulate the static hold-down force on the plate or to provide for low static and/or dynamic forces.

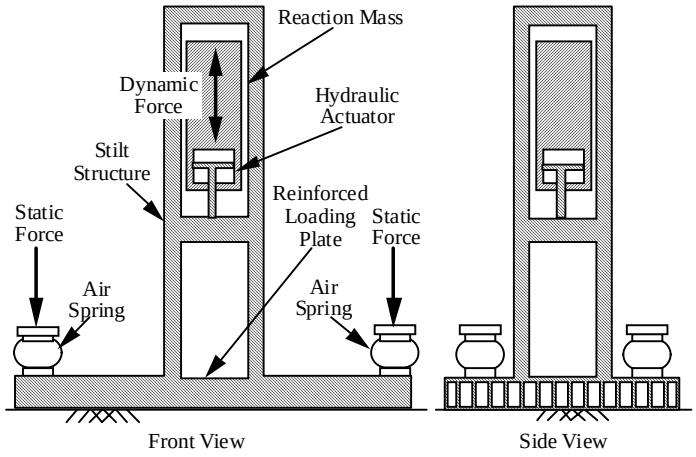

Figure 3.1 Front and Side Views of the Loading System of the Vibroseis as Used in Oil Exploration

3.3 ROLLING DYNAMIC DEFLECTOMETER LOADING SYSTEM REQUIREMENTS

The RDD is used to apply combined static and dynamic forces to a pavement surface through two loading rollers while the truck is moving, as shown in Figure 3.2. The same stilt structure is used to transfer the dynamic forces to the loading rollers. However, the RDD requires the addition of components to the loading system that can react to any lateral forces imposed by rolling and that can also resist any tipping forces in the reaction mass system. The forces the RDD applies through the loading roller are much more concentrated than the forces applied through the plate of the Vibroseis. The loading roller and associated components are designed to withstand these concentrated forces. Furthermore, it is very important to be able to carefully control the force level so that the applied forces do not damage the pavements. These additional requirements necessitated the addition of a lateral support system and the replacement of the portions of the hydraulic control system that regulates the applied static force.

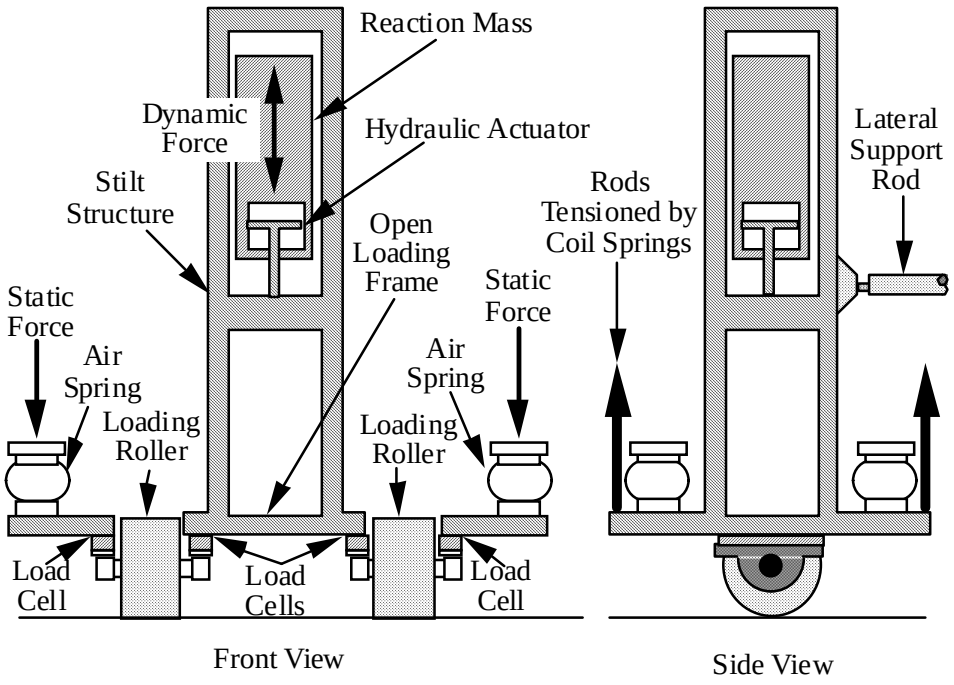

Figure 3.2 Front and Side Views of the Loading System of the RDD as Used in Testing Pavements

3.4 ROLLING DYNAMIC DEFLECTOMETER STRUCTURAL AND SUPPORT SYSTEMS

3.4.1 Design of an Open Loading Frame

The first step taken in converting the Vibroseis into the RDD was replacing the reinforced loading plate with an open loading frame capable of supporting the loading rollers and allowing room for the required sensors. The design of the open loading frame is complicated by the large forces that the static and dynamic loading systems are capable of generating, and the limited space available for the structural elements owing to ground clearance requirements. A combination of composite rolled steel sections and composite solid steel sections were employed in the final design. A plan view of the open loading frame is shown in Figure 3.3. The frame is composed of two longitudinal wide-flanged (WF) beams and two transverse WF beams. All WF sections are WF 5×16. There are also four bearing supports and two stilt supports running in the transverse direction. These beams are a composite of 4.9×15.2 cm (2×6 in.) and 4.9×10.2 cm (2×4 in.) solid steel rectangular bars. The critical structural members are the longitudinal beams and the bearing supports.

3.4.1.1 Structural Design of Longitudinal Beams — The design of the structural components of the RDD used the criteria of the American Institute of Steel Construction (AISC) (AISC 1980) with large strength reduction factors to account for the uncertain nature of the loading. The AISC design criteria are presented in English units rather than in SI units. Therefore, English units will be used as the primary units in the following two sections.

The assumed critical loading along the longitudinal beams is shown in Figure 3.4. Figure 3.4a shows the assumed loading for the combination of maximum static force, the dead weight of the loading system, and the maximum downward dynamic force. Figure 3.4b shows the assumed loading for the combination of maximum static force, the dead weight of the system, and the maximum upward dynamic force. These loadings assume that the force is distributed equally between the two longitudinal beams. The dead weight of the loading system (80 kN [18 kip]) is positioned at the stilt supports. The loading is statically indeterminate and dependent on the distribution of forces between the four bearings supporting the loading rollers. Because of the complexity in determining the actual force distribution, a conservative assumption of an equal force distribution between bearings was used. The shear and moment diagrams for two critical loading conditions are also shown in Figure 3.4. The loading in Figure 3.4a represents the maximum downward dynamic force and the maximum static hold-down force. The loading in Figure 3.4b represents the maximum upward dynamic force and the maximum static hold-down force.

The loading condition that gives the critical moment for the longitudinal beam is the maximum static force plus the maximum upward dynamic force. This loading condition gives a maximum moment of 196.8 kip-in. (22.2 kN-m). Using mild A36 hot-rolled steel sections and a strength reduction factor of 0.25, the required section modulus, *S*, for this beam is:

$$S = \frac{196.8\,\text{kip-in.}}{0.25 \times 36\,\text{ksi}} = 21.9\ \text{in.}^3\ (359\ \text{cm}^3) \qquad \text{(Equation 3.1)}$$

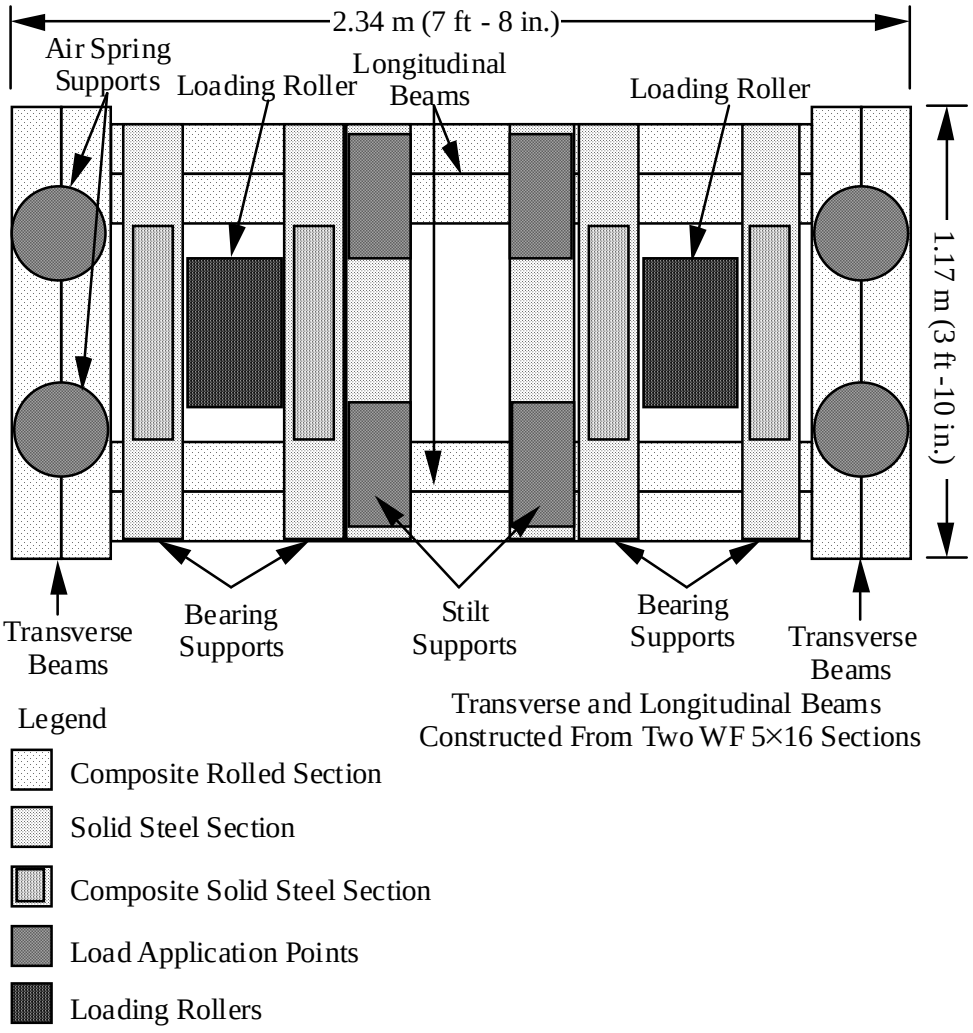

Figure 3.3 Plan View of Open Loading Frame for RDD

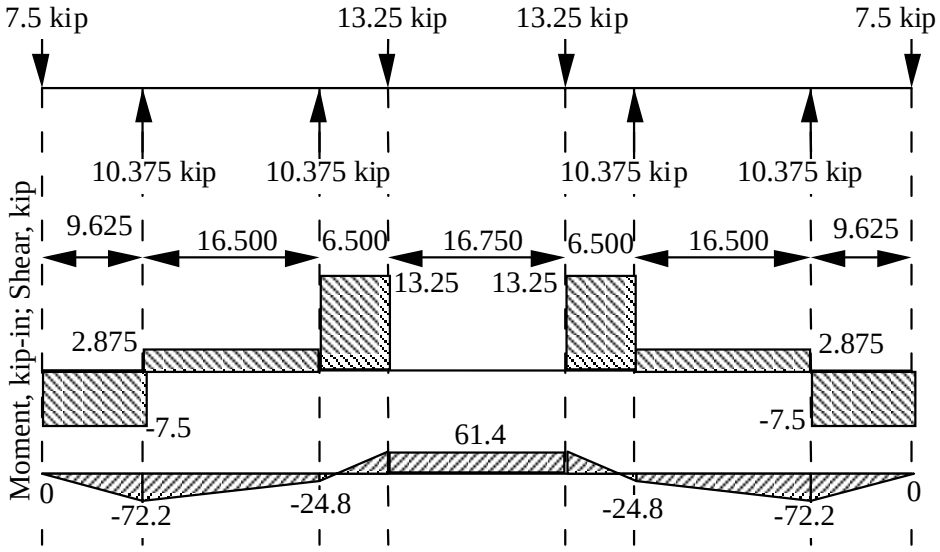

a) Maximum Static Force and Maximum Downward Dynamic Force

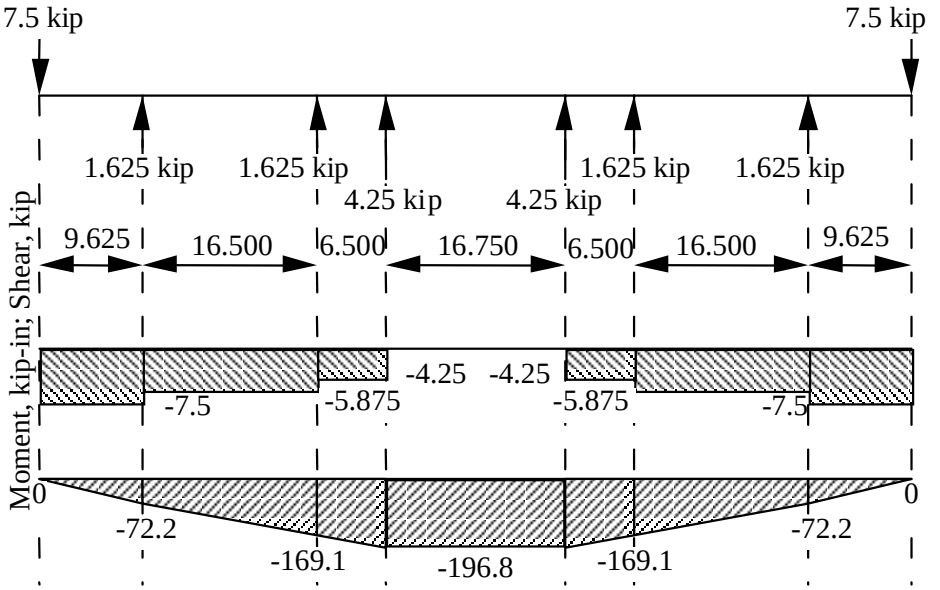

b) Maximum Static Force and Maximum Upward Dynamic Force

Note: All lengths inches; 1 inch = 2.54 cm; 1 kip = 4.45 kN
1 kip-in. = 0.113 kN-m

Figure 3.4 Load, Shear, and Moment Diagrams for Critical Loads on Longitudinal Beams of Open Loading Frame

The cross section and properties of the composite section used are shown in Figure 3.5. The properties of the elements of the composite section are presented in Table 3.1. This section is composed of two WF 5 × 16 sections and a C 10 × 15.3 channel section. This section has a section modulus of 26.7 in.^{3} (438 cm^3), which is greater than required by Equation 3.1.

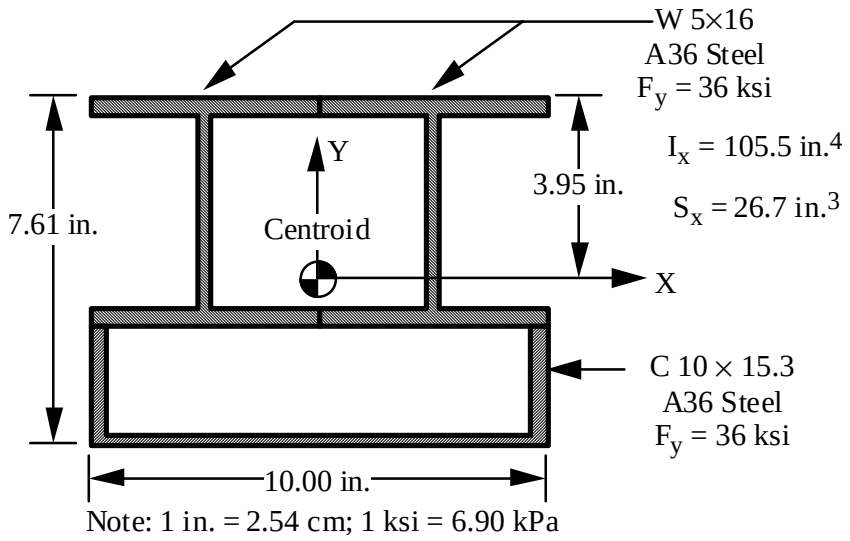

Figure 3.5 Cross Section and Properties of the Composite Section Used for the Longitudinal Beams of the Open Loading Frame

Table 3.1 Properties of Elements of the Composite Section Used for the Longitudinal Beams in the Open Loading Frame

Elements	Area (in.^{2})	Centroid* (in.)	I_X (in.^{4})
2 - W 5 × 16	9.36	5.11	42.6
1 - C 10 × 15.3	4.49	0.634	2.28

*Distance to centroid of element from bottom of composite section.

The critical loading in shear is the maximum static force and the maximum downward dynamic force, giving a maximum shearing force of 13.25 kip (58.94 kN). Assuming that the webs of the two WF sections resist all shear forces, and using the AISC criteria (AISC 1980) that the average shearing stress in the web be less than 40percent of the yield stress of the steel, we obtain the following:

$$\tau_{avg} = \frac{13.25 \text{ kip}}{2 \text{ x } 5.01 \text{ in. x } 0.25 \text{ in.}} = 5.29 \text{ ksi (36.5 kPa)} < 14.5 \text{ ksi (100 kPa)} \qquad \text{(Equation 3.2)}$$

In addition to evaluating the average shear stress, the shear stresses at the weld joint between the WF sections and the channel must be evaluated. The equation for shear stress at this joint is:

$$\tau = \frac{VQ}{I\,t} \qquad \text{(Equation 3.3)}$$

where *V* is shear force
Q is first moment of the area
I is second moment of the area
t is thickness (in this case, the effective weld thickness)

The shear stress at the weld is:

$$\tau = \frac{13.25 \text{ kip x } 3.02 \text{ in. x } 4.49 \text{ in.}^2}{105.5 \text{ in.}^4 \text{ x } 0.707 \text{in.}} = 2.41 \text{ ksi (16.6 kPa)} \qquad \text{(Equation 3.4)}$$

This is much less than the allowable shear stress of 21 ksi (145 kPa) for the E70 welding rod used.

3.4.1.2 Structural Design of Bearing Supports — The other critical structural member is the bearing support. The critical loading condition for the bearing support is the maximum static force, the dead weight of the loading system, and the maximum downward dynamic forces. The same assumptions are made for the bearing supports as were made for the longitudinal beams. In addition, any distribution of the load owing to the pillow block is neglected; all of the force is assumed to be applied at the center of the support. Figure 3.6 shows the loading diagram with shear and moment diagrams for the bearing supports. The maximum moment is 166 kip-in. (18.8 kN-m). Figure 3.7 shows the cross section and properties of composite section used for the bearing supports. This section is composed of a 2 in. × 6 in. (5.08 cm × 15.2 cm) bar of hot-rolled A36 steel with a 2 in. × 4 in. (5.08 cm × 10.2 cm) bar of cold-rolled 1018 steel. Each of these components has about the same moduli, though different yield strengths. Therefore, as long as the yield strength is not exceeded, the beams can be analyzed as if they were homogeneous, but the maximum stresses must be calculated in each component. The maximum tensile stress in the A36 steel component is:

$$\sigma_{max} = \frac{166 \text{ kip} - \text{in. x } 1.8 \text{ in.}}{25.87 \text{ in.}^4} = 11.55 \text{ ksi (79.7 kPa)} \qquad \text{(Equation 3.5)}$$

The maximum compressive stress in the 1018 steel component is:

$$\sigma_{max} = \frac{166 \text{ kip} - \text{in. x } 2.2 \text{ in.}}{25.87 \text{ in.}^4} = 14.12 \text{ ksi (97.4 kPa)} \qquad \text{(Equation 3.6)}$$

Both maximum stresses result in safety factors of more than 3. This factor of safety is somewhat less than that used for the longitudinal beam. However, the real load on the beam support is actually distributed by the pillow block, significantly decreasing the real moments

in the member. This reduction and the fact that the section is very compact should make the design very safe.

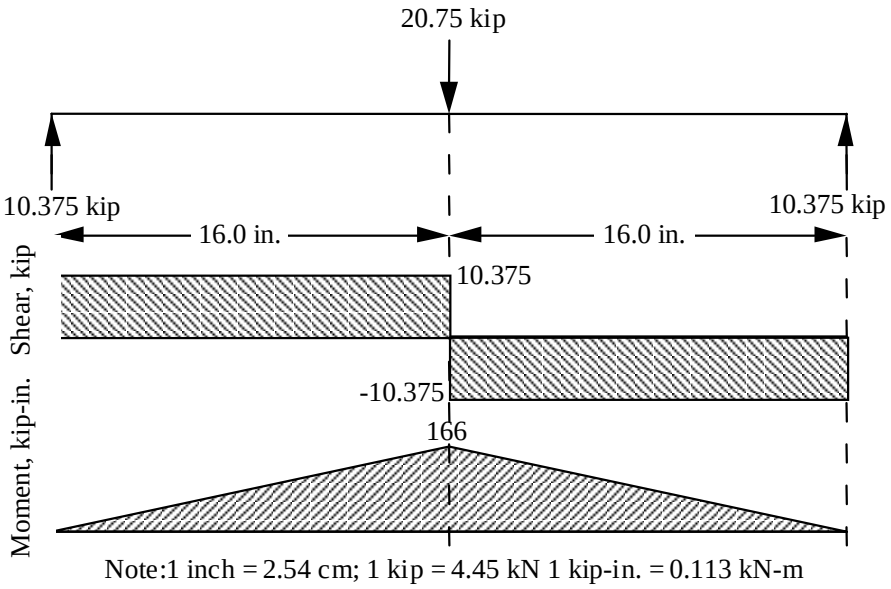

Figure 3.6 Load, Shear, and Moment Diagrams for Critical Load on Bearing Supports of the Open Loading Frame

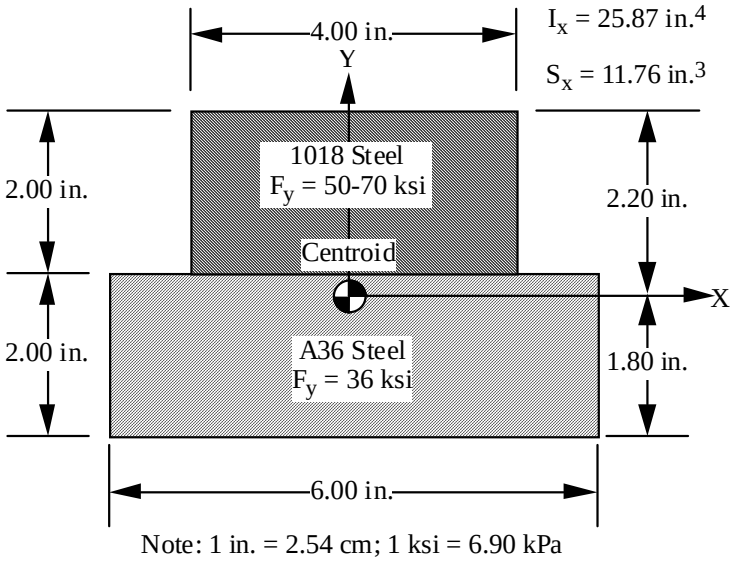

Figure 3.7 Cross Section and Properties of the Composite Section Used for Bearing Supports of Open Loading Frame

The entire cross section of 20 in.^{2} (129 cm^2) on this beam can effectively resist shear, making the average shear stress in the section very low. However, the shear stress at the weld joints could be critical. The stress at the weld joints is calculated using Equation 3.3 as:

$$\tau = \frac{10.375 \text{ kip} \times 1.20 \text{ in.} \times 8.00 \text{ in.}^2}{25.87 \text{ in.}^4 \times 0.707 \text{ in.}} = 5.45 \text{ ksi (37.6 kPa)} \qquad \text{(Equation 3.7)}$$

This shear stress is well below the allowable value of 21 ksi (145 kPa).

All critical connections between members on the loading frame consist of grade 8 bolts and welds. Each critical connection was designed such that either the bolt or the weld alone would resist the loads at the joint.

3.4.1.3 Possible Improvements to Open Loading Frame Design — The design of the open loading frame could have been improved by not using hot-rolled A36 steel for any of the solid members. This steel was difficult to machine and members were not straight and flat. The machinists were able to work around these problems, but construction would have been simpler if material such as cold-rolled 1018 steel were used for these members. Hot-rolled A36 steel worked fine for the rolled wide-flange and channel sections.

3.4.2 Design of Loading System Supports

The loading system on the Vibroseis is self-supporting. This can be seen in the side view in Figure 3.1. With the plate resting on the ground surface, the plate resists rotating and tipping in the stilt-structure and reaction mass. With the loading system resting on a roller rather than on a plate, stability becomes a concern. This can be seen in the side view of the RDD loading system in Figure 3.2. Consequently, the RDD requires a support system to resist the tipping of the loading system, as well as a lateral support to resist forces induced in the loading system by vehicle accelerations and decelerations.

3.4.2.1 System to Resist Tipping in Loading System — Tipping resistance is provided by the springs in the loading system that isolate the loading system from the vehicle. On the Vibroseis, there are four air springs, as shown in Figure 3.1. These air springs are capable of providing some tipping resistance. On a normally configured Vibroseis, the two air springs on each side are connected, so that the air pressure, and therefore the force, in each spring is equal. This allows the air springs to transfer a vertical force, but no moment. The first step taken to resist tipping of the loading system was to disconnect and reconfigure the two pairs of air springs so that the force in each spring would be independent.

The tipping problem can be analyzed using the simplified model shown in Figure 3.8. In this model, W represents the weight of the reaction mass and stilt structure, H represents the height of the center of gravity of the reaction mass and stilt structure, L represents the distance between the resisting air springs and the center of the system, k is the spring constant of the air springs, and θ is the angle of tip. The tipping moment, M_t, is:

$$M_t = W H \sin\theta \qquad \text{(Equation 3.8)}$$

For small tipping angles, the resisting moment, M_r, is:

$$M_r = 2 k L^2 \sin\theta \qquad \text{(Equation 3.9)}$$

Stability against tipping requires that the resisting moment be larger than the tipping moment:

$$2\,k\,L^2 \sin\theta > W\,H \sin\theta \qquad \text{(Equation 3.10)}$$

or,

$$2\,k\,L^2 > W\,H \qquad \text{(Equation 3.11)}$$

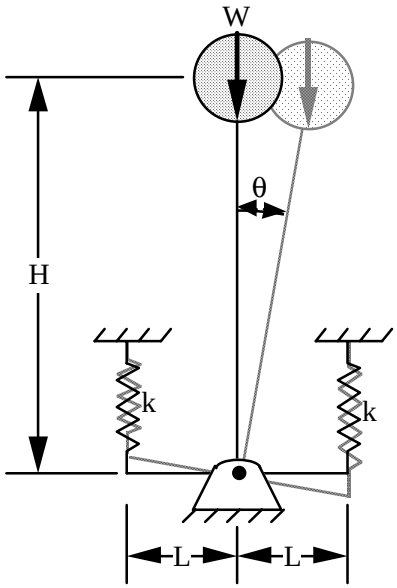

Figure 3.8 Model Used to Evaluate the Tipping Stability of the Reaction Mass and Stilt Structure with the Air Springs Providing the Tipping Resistance

The factor-of-safety against tipping, F.S., can be calculated as follows:

$$\text{F.S.} = \frac{2\,k\,L^2}{W\,H} \qquad \text{(Equation 3.12)}$$

The mass of the reaction mass and stilt structure, *W*, is approximately 53.4 kN (12 kip). The height of the center of gravity of the reaction mass and the stilt structure, *H*, is about 1.83 m (72 in.). The distance between air springs, *L*, is 0.24 m (9.5 in.).

The stiffness of the air springs is nonlinear and a function of the air pressure in the springs. An estimate of stiffness of the air springs can be made from the resonant frequency of the truck when suspended from the air springs. The truck is designed such that resonance is well below all operating frequencies to isolate the vehicle during shaking. The design resonant frequency, f_n, is 1.5 Hz (Bedenbender 1994) and the suspended weight is 30 kip. The relationship between resonant frequency, suspended weight, and stiffness is:

$$k = \frac{(2\pi\,f_n)^2\,W}{g} \qquad \text{(Equation 3.13)}$$

where k is spring constant
W is suspended weight
g is the acceleration of gravity

The stiffness for all four air springs using Equation 3.13 is 1200 kN/m (6.9 kip/in.) or 300 kN/m (1.7 kip/in.) per air spring. The factor-of-safety for the two pairs of air springs resisting tipping is:

$$\text{F.S.} = \frac{2 \text{ x } 2 \text{ x } 1.7 \text{ kip x } (9.5 \text{ in.})^2}{12 \text{ kip x } 72 \text{ in.}} = 0.71 \qquad \text{(Equation 3.14)}$$

Thus, the air springs alone do not provide sufficient resistance against tipping.

One solution to the tipping problem is to add another pair of springs to gain additional tipping resistance. A model with additional springs is shown in Figure 3.9. This model is identical to the one presented in Figure 3.8, with the addition of another pair of springs. Now, L_1 represents the distance between the inner springs (the air springs) and the center of the system, and L_2 represents the distance between the outer springs and the center of the system. Similarly, k_1 is the stiffness of the inner springs, and k_2 is the stiffness of the outer springs. The factor-of-safety against tipping, F.S., for this new system can be calculated as follows:

$$\text{F.S.} = \frac{2 \, k_1 \, L_1^2 + 2 \, k_2 \, L_2^2}{W \, H} \qquad \text{(Equation 3.15)}$$

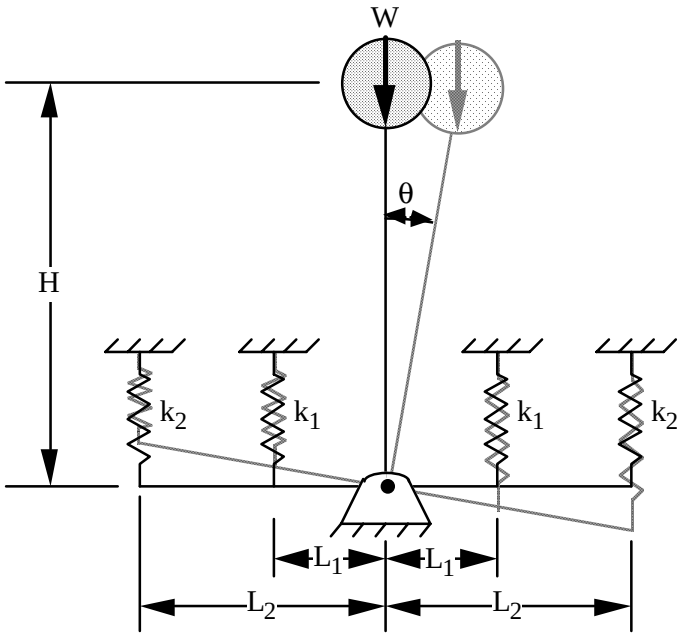

Figure 3.9 Model Used To Evaluate the Tipping Stability of the Reaction Mass and Stilt Structure System with the Air Springs and an Additional Pair of Springs Providing the Tipping Resistance

A side view of the loading frame incorporating the additional springs is shown in Figure 3.10. Hydraulic rams apply the static hold-down force to the loading feet. This force is then transferred through the air springs to the loading frame. The lift chains, between the loading feet and the loading frame, lift the loading frame to raise the loading rollers off the ground. Guide rods resist the moments and lateral forces on the loading feet. Three additional coil springs are positioned at each end of the loading foot to supply additional tipping resistance. These springs apply tension to a rod extending through the load foot and attached to the load frame. Each of the coil springs has a spring constant of (52.5 kN/m) 330 lb/in., and they are 43.2 cm (17 in.) from the center of the load frame. The factor-of-safety against tipping of this system is:

$$\text{F.S.} = \frac{(2 \text{ x } 2 \text{ x } 1.7 \text{ kip x } (9.5 \text{ in.})^2) + (2 \text{ x } 2 \text{ x } 0.99 \text{ kip x } (17 \text{ in.})^2)}{12 \text{ kip x } 72\text{in.}} = 2.03 \qquad \text{(Equation 3.16)}$$

This design provides an adequate factor-of-safety against tipping. The addition of the coil springs also has another benefit. In order to operate the RDD with a static force less than the dead weight of the loading system (80 kN [18 kip]), the loading foot must apply an upward force. Without the coil springs, this upward force would be transferred to the load frame through the lift chains. This would make a "rigid" connection between the vehicle and the loading system without any isolation, which would result in lost shaking energy and which could potentially damage the truck. With the coil springs, the pressure in the air springs can be reduced so that the load frame is lifted by the rods and supported by the coil springs, thus isolating the vehicle.

There are also two detrimental effects of the additional springs. First, the vehicle is not as well isolated as it was previously and the suspended resonant frequency of the vehicle has been increased to about 2 Hz. Second, the loading foot and guide rod now must resist moments to which they were not previously subjected. The guide rod is 15.2 cm (6 in.) diameter solid stainless steel and should be able to resist these moments, but the guide rod collar where the guide rod is attached to the loading foot could be damaged by these moments if the guide rod ever becomes loose in the guide rod collar. To prevent this from occurring, the bolts attaching the guide rod and guide rod collar are torqued daily.

3.4.2.2 System to Resist Forces Induced by Vehicle Acceleration and Deceleration — The additional coil springs stabilize the loading system against tipping. However, this system still could be subjected to large rotations owing to vehicle acceleration and deceleration or to bumps and joints in the pavement. Therefore, it was necessary to provide additional support to keep the load system vertically oriented while rolling. This support was provided by attaching two horizontal support arms between the stilt structure and the vehicle deck, one on each side of the stilt structure. These arms are attached to the vehicle and the stilt structure with tie-rod ends with spherical bearings to maintain the vehicle isolation and allow for articulation. Figure 3.11 is a side view of the loading showing one of the support arms. The support arms cannot be attached with the load system secured in its raised position, so pins are provided for quick attachment and release.

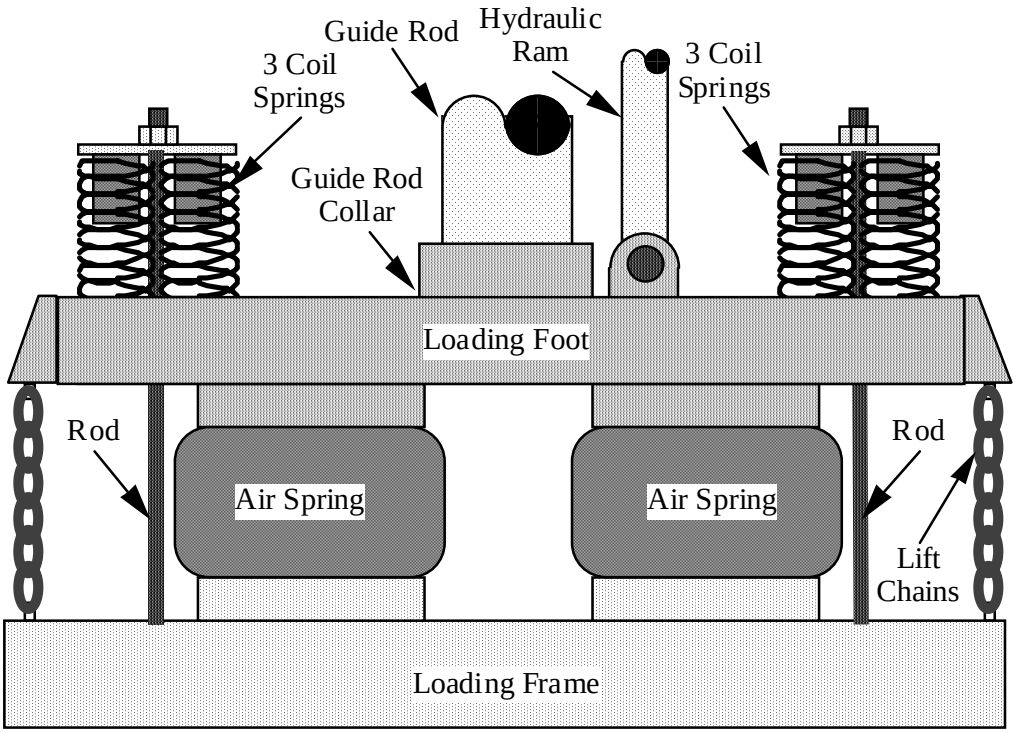

Figure 3.10 Side View of RDD Load Frame Showing Air and Coil Springs

Each of the support arms is 1.2 m (46 in.) long and is constructed of pipe with an outside diameter of 5.1 cm (2.0 in.). Each arm can resist 84 kN (18.9 kip) in compression. The tie rod ends attaching the support arms to the stilt structure and truck deck have a rated capacity of 124.5 kN (28 kip). These capacities should exceed the magnitude of the lateral forces induced on the loading system.

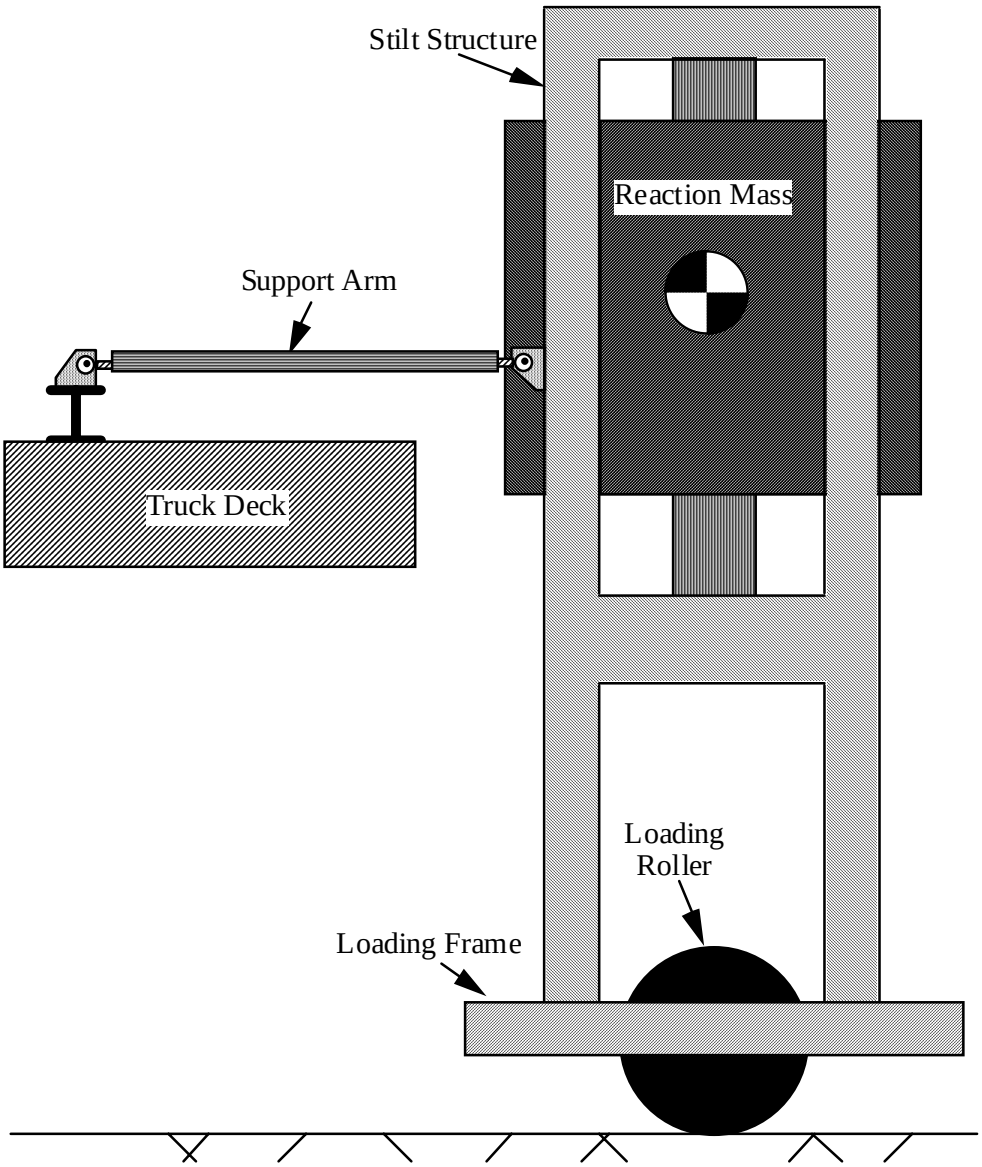

Figure 3.11 Side View of RDD Loading System Showing One of the Horizontal Support Arms To Hold the Loading System Vertical While Rolling

3.5 ROLLING DYNAMIC DEFLECTOMETER LOADING ROLLERS

The RDD loading rollers were one of the most challenging components to design. The loading rollers must be sufficiently rigid to minimize the inertial losses caused by the motion of the loading frame during shaking. The rollers must also be sufficiently compliant to minimize the contact pressure with the pavement to prevent rutting of flexible pavements.

The rollers must be able to withstand extremely adverse loading. The RDD is capable of applying a force in excess of 178 kN (40 kip) per roller. Additionally, when applying an 80-Hz dynamic force with the RDD, the loading roller is required to withstand cyclic forces equivalent to what it would experience if it were rolling at more than 320 km/hr (200 mph). In other words, the roller must be able to withstand loading rates similar to a race car's tire, but at force levels about 8 times what a typical truck tire carries.

Several alternatives were considered for the design of the RDD loading roller. Pneumatic tires were considered but eliminated because their compliance would result in excessively large inertial losses in the loading system. Solid steel or aluminum rollers were eliminated because of the excessive contact pressure and the background seismic noise that they would generate. The design for the final loading roller was an evolutionary process.

3.5.1 First-Generation Loading Roller Design

The first-generation loading roller used a wheel often used for high-capacity forklifts. These wheels, as shown in Figure 3.12, were 45.7 cm (18 in.) in diameter and 12.7 cm (5 in.) wide. They had cast aluminum hubs with a 2.5 cm (1 in.) thick, 90A durometer, polyurethane coating. Two of these wheels were used in tandem for each roller. The wheels were mounted on a 7.46 cm (2-15/16 in.) diameter unkeyed axle and fixed to a pair of pillow block bearings on the load frame. The estimated capacities of each of these components are presented in Table 3.2.

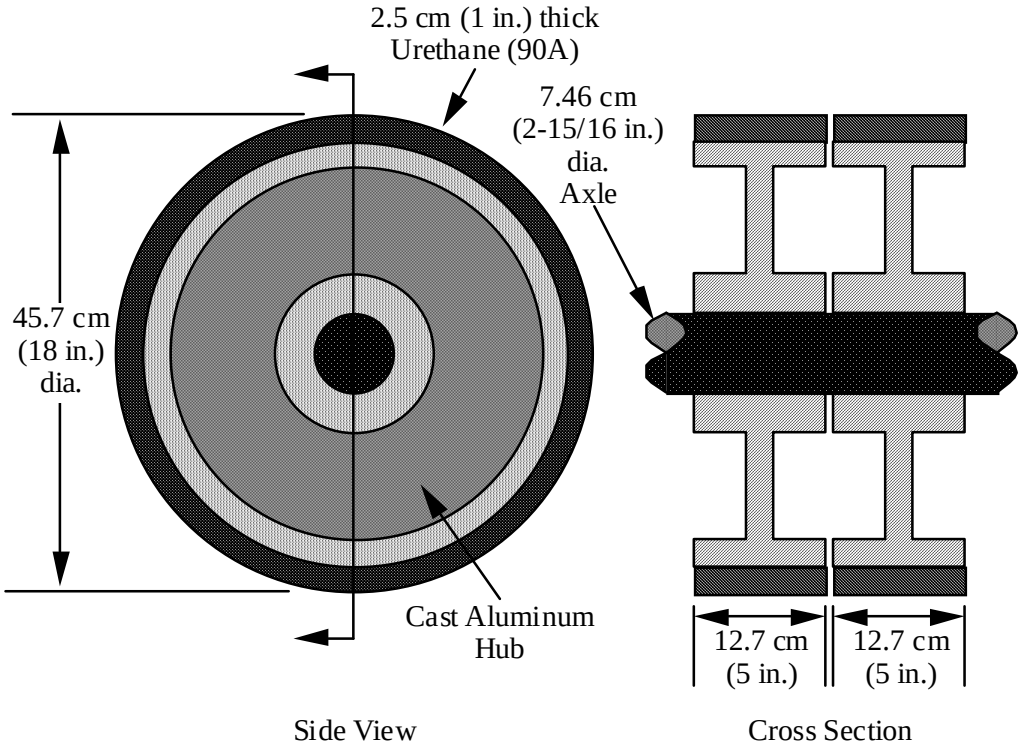

Figure 3.12 Side and Cross-Sectional Views of First-Generation RDD Loading Roller

The estimated load-carrying capacities of the various components of the first-generation loading roller are significantly lower than the loads the RDD is capable of generating. However, the capacities are large enough to perform RDD testing at load levels equivalent to the allowable axle load of most pavements. It was thought that the rollers would be safe as long as they were not overloaded.

Table 3.2 Estimated Capacities of the Components of the First-Generation RDD Loading Roller System

Component	Number Used	Individual Capacity (kN/kip)	Total Capacity (kN/kip)
Cast Aluminum Wheels	4	37.8 (8.5)	151 (34)
Axles	2	102 (22.9)*	104 (45.8)*
Pillow Block Bearings	4	59.4 (13.3)	237 (53.4)

* Assuming that load is equally distributed between the two wheels of the wheel pair.

The first-generation roller performed well for several hours of RDD testing, with a peak combined static and dynamic load of about 133 kN (30 kip). After this successful testing, the RDD was used for a stationary test, applying a large number of loading cycles to a newly constructed prototype PCC overlay at a site near El Paso, Texas. Again, the combined peak static and dynamic force was about 133 kN (30 kip). After about 40 minutes of loading at 40 Hz (about 100,000 cycles), the cast aluminum hub on three of the rollers had cracked. When the rollers were disassembled, it was found that the hubs and axles had seized, and the axles were slightly bent. The pillow block bearings appeared to have performed very well.

3.5.2 Second-Generation Loading Roller

The second-generation loading rollers were designed to be substantially stronger than the first generation loading rollers. These custom-made rollers, shown in Figure 3.13, were 38.1 cm (15 in.) in diameter and 25.4 cm (10 in.) wide. They had solid extruded aluminum hubs with a 6.4 cm (2.5 in.) thick, 85A durometer, polyurethane coating. The urethane casting for this and subsequent rollers was done by PSI Urethanes of Austin, Texas. The rollers were mounted on an 8.9 cm (3.5 in.) diameter keyed axle and fixed to a pair of proportionally larger pillow block bearings on the load frame. The estimated capacities of each of these components are presented in Table 3.3.

The estimated load-carrying capacities of the various components of the second-generation loading roller are higher than the loads the RDD is capable of generating. Thus, this system is a safer design that does not require the same level of care required in operating the RDD so as to avoid damaging the loading roller system.

Table 3.3 Estimated Capacities of the Components of the Second-Generation RDD Loading Roller System

Component	Number Used	Individual Capacity (kN/kip)	Total Capacity (kN/kip)
Cast Aluminum Wheels	2	>222 (>50)	>445 (>100)
Axles	2	299 (67.3)	600 (135)
Pillow Block Bearings	4	94.7 (21.3)	379 (85.2)

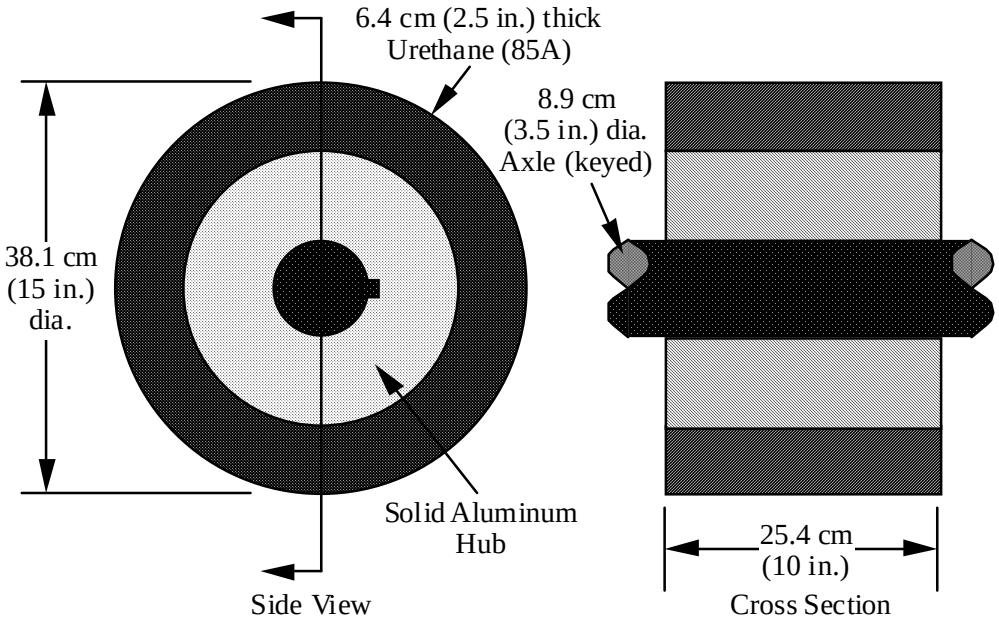

Figure 3.13 Side and Cross-Sectional Views of Second-Generation RDD Loading Roller

The second-generation loading roller was used for approximately 2 hours while testing an airport pavement. This testing was performed with a combined peak static and dynamic force of about 178 kN (40 kip). After about two hours of testing, the urethane coating on one of the rollers had debonded from the hub and slid sideways on the hub.

One possible failure mode for this roller is shown in Figure 3.14. When the urethane deformed under the heavy loading, it also deformed laterally owing to Poisson's effect. This

deformation pattern had two adverse consequences. First, it led to friction between the urethane and the hub. The heat from this friction damaged the urethane next to the hub and damaged the bond. Second, with repeated loading cycles as the wheel rotated, some of the lateral deformation became permanent. This essentially stretched the urethane coating so that it could slide off the hub. This scenario was discussed and confirmed with specialists at PSI Urethane.

All other loading roller components performed very well. The axles remained straight, the hubs and axles did not seize, and the pillow block bearings appear to have performed well.

3.5.3 Third-Generation Loading Roller

After some discussion with specialists at PSI Urethane, the third-generation loading roller was specifically designed to resist the lateral deformation shown in Figure 3.14. This roller is shown in Figure 3.15. On this roller the hub is slotted with rounded slots, much like a gear cog. These slots provide for mechanical resistance against lateral deformation. A photograph of these hubs taken before the urethane was cast is shown in Figure 3.16. Additionally, a much stiffer urethane, with a 40D durometer, was used to coat the hub. The urethane on the third-generation roller is much thicker than that on any of the earlier rollers. This serves to decrease the contact stress with the stiffer urethane. Steel retaining rings are also bolted to the hub to restrain the urethane against sideways displacement. A photograph of the third-generation loading roller with its axle and bearings is shown in Figure 3.17.

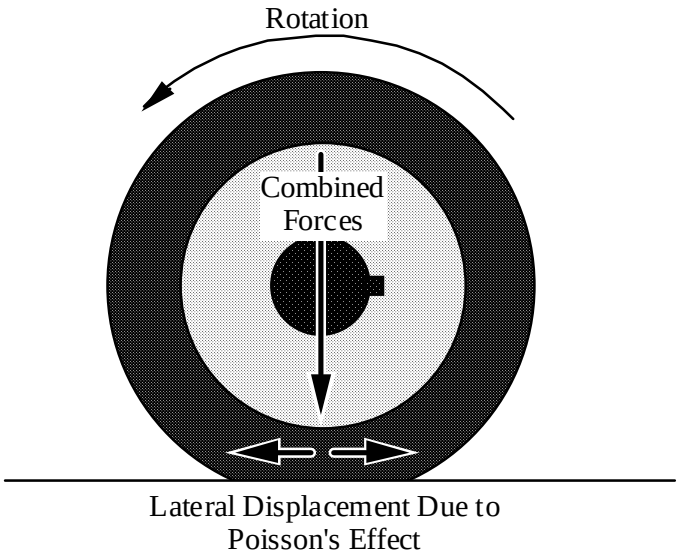

Figure 3.14 Possible Failure Mechanism Leading to Debonding in Second-Generation Roller

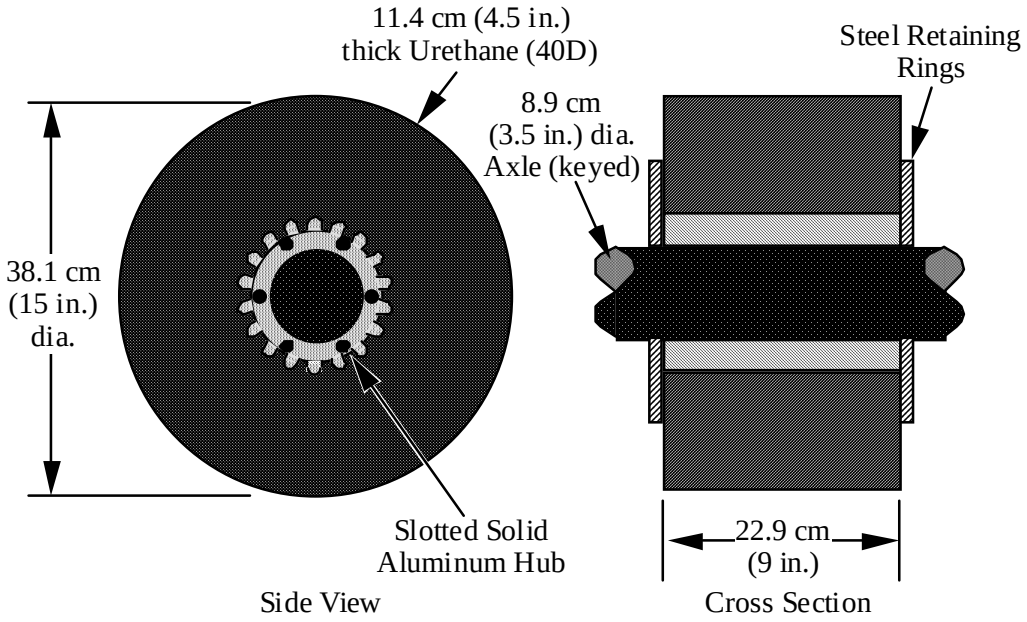

Figure 3.15 Side and Cross-Sectional Views of Third-Generation RDD Loading Roller

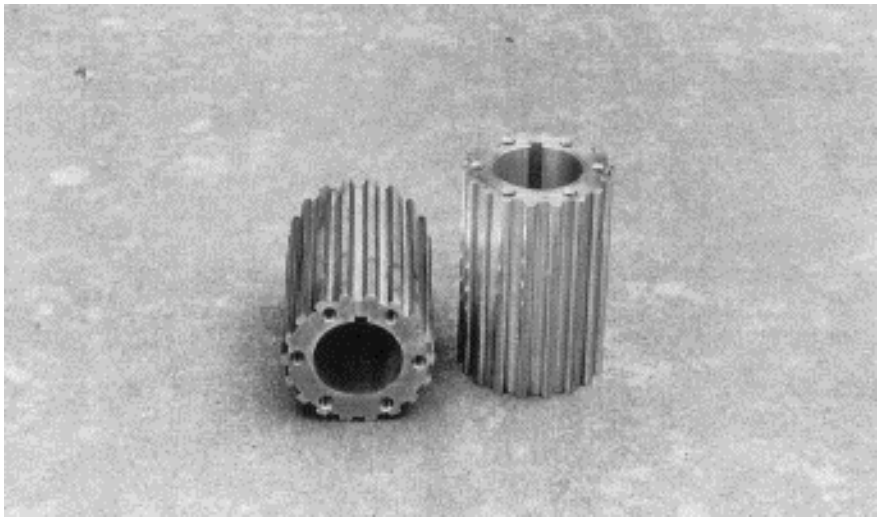

Figure 3.16 Photograph of Slotted Hubs Used on Third-Generation Loading Rollers

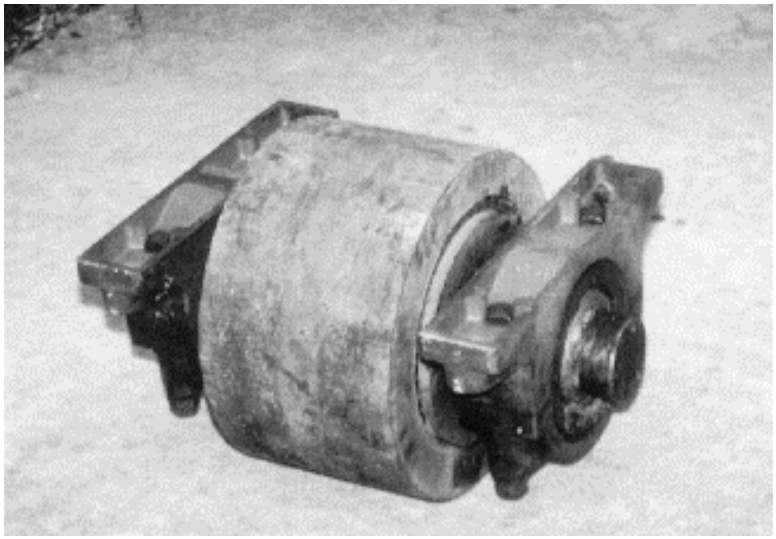

Figure 3.17 Photograph of Third-Generation Loading Roller with Axle and Bearings

The third-generation roller has performed very well. It has currently been used for more than 100 hours, much of it operating at very high force levels testing airport pavements, as well as in stationary tests applying high forces at bridge foundations. Periodically, the bolts holding the restraining rings have worked loose, but the system has still continued to perform well. This indicates that the slotted hub and stiffer, thicker urethane probably contribute more to the success of this roller than the restraining rings.

A new roller with softer urethane is currently under consideration. This would further decrease the contact stress and would make the RDD more suitable for testing flexible pavements where rutting is a danger.

3.6 ROLLING DYNAMIC DEFLECTOMETER HYDRAULIC SYSTEM

A hydraulic system is used to generate both the static and dynamic forces on a Vibroseis. The RDD has many of the same loading requirements as a Vibroseis; therefore, much of the Vibroseis hydraulic and control systems can be used on the RDD without modification. However, the RDD does require certain modifications. This section discusses the Vibroseis hydraulic system and the required modifications for RDD testing.

3.6.1 The Vibroseis Hydraulic System

The Vibroseis requires a high-energy vibration system to propagate seismic waves deep into the earth. The hydraulic systems driving the Vibroseis are capable of delivering 200 horsepower or more in vibration energy. These systems use a dedicated diesel engine to power a large hydraulic pump that drives the vibrator.

The Vibroseis that was modified for this project was a Mertz Model 9/605I built for Teledyne, Inc., in 1981. The truck was modified extensively in 1988 by the HeavyQuip Co. Thus, before it was converted to an RDD, it was already a one-of-a-kind machine.

A schematic of the hydraulic system of this truck before the RDD conversion is presented in Figure 3.18. The high-pressure hydraulic flow is provided by the main hydraulic pump, a Sunstrand model 25-7010. This is a positive displacement, piston pump. The pump is configured to be unidirectional and pressure compensated. This means that the output flow is controlled by the output pressure level. An idealized plot of the pump's performance is shown in Figure 3.19. When the output pressure is less than 20.7 MPa (3,000 psi), then the pump flow is 0.166 l/rev (10.12 in.^{3}/rev) (Sunstrand 1974). When the pressure exceeds 20.7 MPa (3,000 psi), the output flow drops to zero. When the bypass valve (shown in Figure 3.18) is open, the pump is unable to build up any output pressure. Therefore, the pump outputs full flow under no pressure, doing no work. When the bypass valve is closed, the pump pressurizes the high-pressure side of the system to 20.7 MPa (3,000 psi). After the system is pressurized, the flow decreases to zero, again doing no work. When the actuators require flow, the pressure drops slightly, causing full flow to occur until the pressure reaches 20.7 MPa (3,000 psi).

The return, or low-pressure, side of the system is at 1.04 MPa (150 psi). A charge pump is provided to maintain this pressure during operation, and a precharge pump is provided to pressurize the low-pressure side of the system before starting the diesel engine. It is necessary that the pump intake pressure be at least 0.7 MPa (100 psi) to prevent cavitation.

Additional components of the hydraulic system include filters to protect sensitive valves, pumps, and actuators; an oil cooler to maintain the hydraulic fluid temperature; and accumulators to store energy, provide for instantaneous flow levels exceeding the pump's flow capacity, and to protect the system from hydraulic transients.

There are two sets of hydraulic actuators and control valves in the schematic shown in Figure 3.18. The first raises and lowers the Vibroseis plate and regulates the static hold-down force, and the second generates and controls the dynamic forces. These systems have been modified in the RDD conversion. These systems and the modifications are discussed in the following sections.

3.6.2 Static Loading System

3.6.2.1 The Vibroseis Static Loading System — A more detailed schematic of the Vibroseis static loading system is shown in Figure 3.20. This schematic includes a simplification of the electrical control system. When the system is first pressured up, high-pressure oil is sent to the bottom of the lift cylinders, lifting the loading system off the stiff arm supports. The electrical system has a safety feature that prevents the hydraulic system from accidentally being lowered when the stiff arms are not rotated out of the way. The stiff arms support the loading system when the hydraulic system is not pressured up and could be damaged if the loading system were forced down on them. When the stiff arm limiting switches are closed and the up/down switch is moved to the down position, the direction control valve sends high-pressure oil to the top of the lift cylinders, pushing the load system down. It should be observed that the oil in the bottom of the cylinder is also under pressure, decreasing the total downward force generated. There is a pressure control valve regulating the pressure in the top of the lift cylinders. This valve is capable of regulating the pressure only from 1.4 to 20.7 MPa (200 to 3,000 psi). The downward static force generated by the system is:

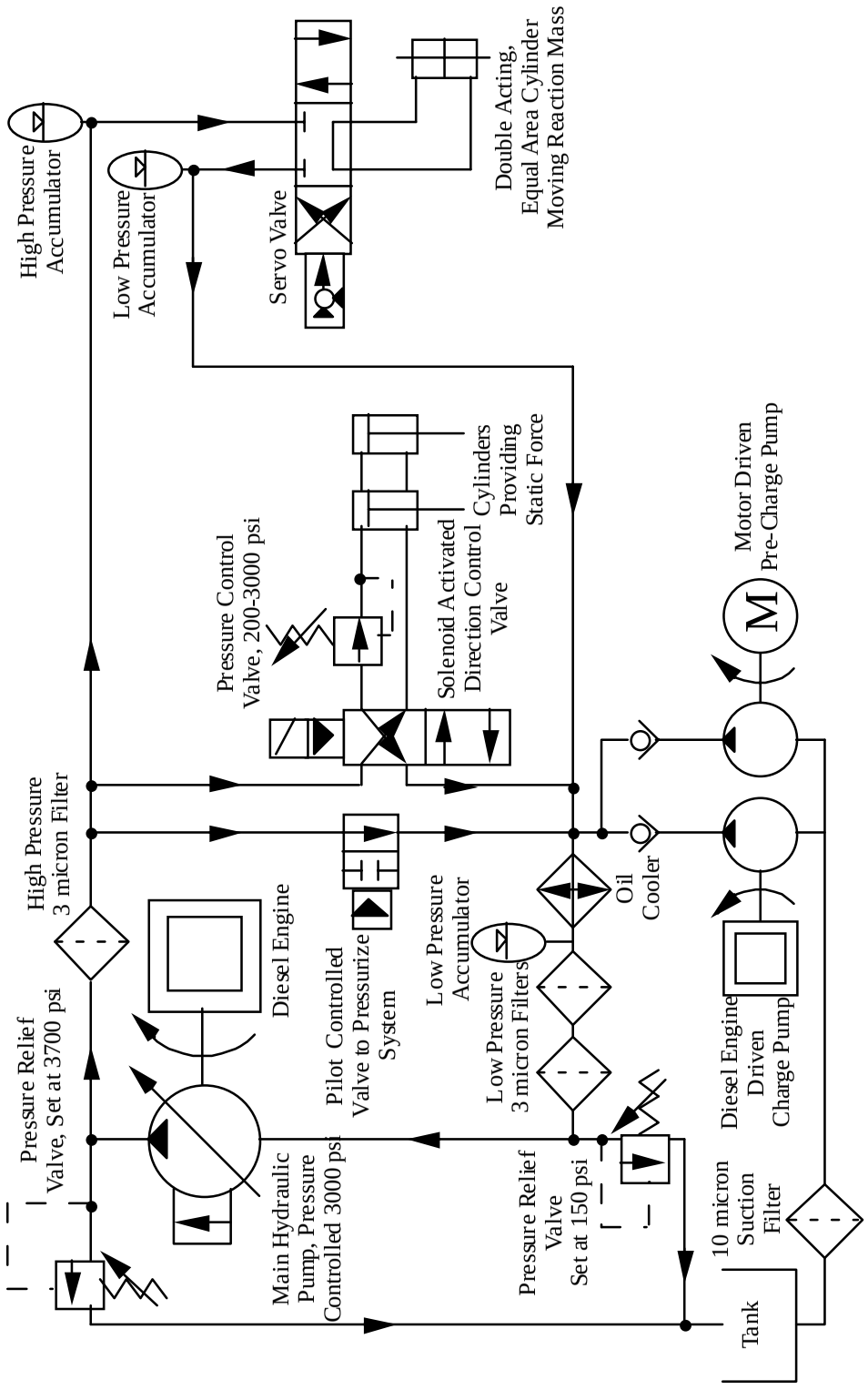

Figure 3.18 Schematic of the Vibroseis Hydraulic System

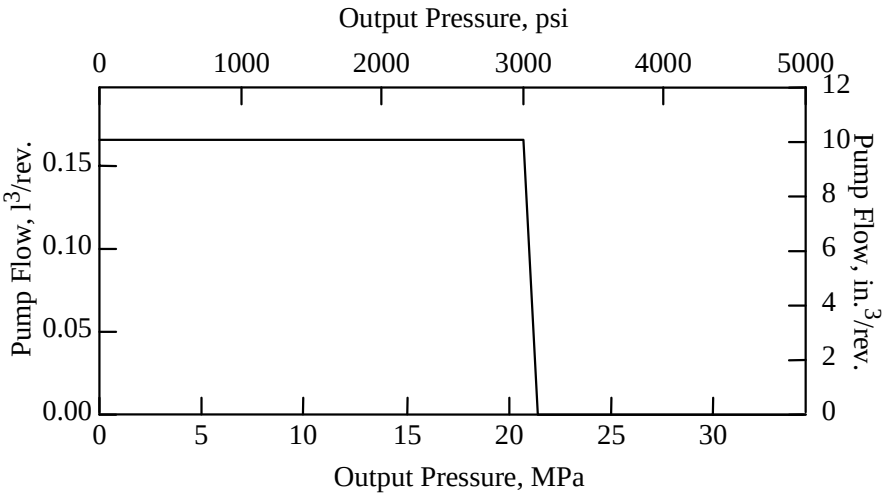

Figure 3.19 Idealized Flow-Pressure Curve, Sunstrand Model 25-7010 Hydraulic Pump, as Configured for Vibroseis Operation

$$F_s = 62.3\ \text{kN} + 2\ P\ 5.35 \times 10^{-3}\ \text{m}^2 - 1040\ \text{kPa} \times 2 \times 3.80 \times 10^{-3}\ \text{m}^2 \qquad \text{(Equation 3.17)}$$

where F_s is the downward force in kN
62.3 kN is the dead weight of the Vibroseis loading system
P is the hydraulic pressure in the top of the lift cylinder in kPa

From this equation it can be determined that the lowest static force that the Vibroseis can apply is 69.4 kN (15.6 kip). The highest force that can be generated is well in excess of the 133 kN (30 kip) weight of the vehicle minus the loading system dead weight.

In Figure 3.20 it can also be observed that there is no means provided to regulate the pressure in the bottom of the lift cylinders. This further limits the capacity of this hydraulic circuit to regulate the static force applied by the Vibroseis.

3.6.2.2 The Rolling Dynamic Deflectometer Static Loading System — The static loading system used on the Vibroseis is not suitable for the RDD for two reasons. First, it does not allow for low enough static forces. The dead weight of the RDD loading system is about 80.0 kN (18 kip), making 87.2 kN (19.6 kip) the lowest static force that could be applied with the Vibroseis system. This force is nearly a maximum axle load without combining a dynamic force. The second problem with the Vibroseis system is that adjusting the pressure control valve is difficult and dangerous when the system is pressured up.

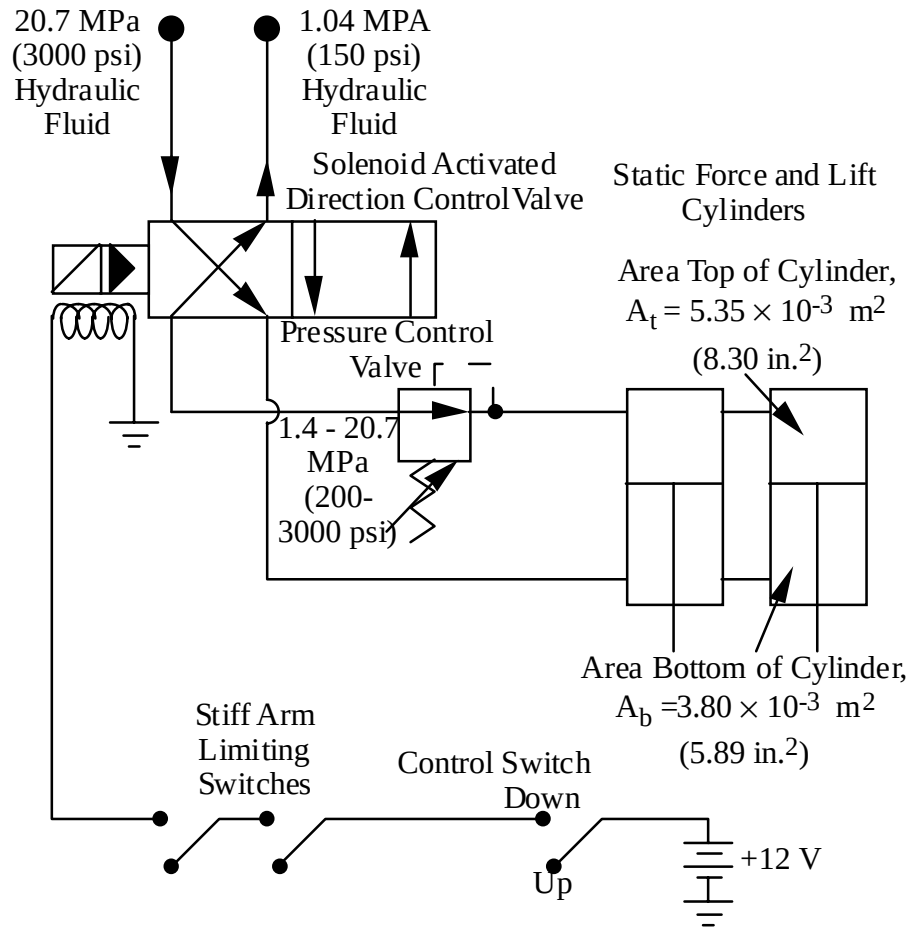

Figure 3.20 Schematic of Vibroseis Static Force and Lift System with Simplified Electrical Controls

To solve these problems, the direction control valve and the pressure control valve were replaced with a single proportional P-Q servo-valve with integrated electronics. The valve used was a Moog model D656. A schematic of the RDD static force hydraulic system is shown in Figure 3.21. This valve has an internal pressure transducer and internal feedback circuits to control both pressure and flow. Two control signals are sent to the valve: a flow control and a pressure control. The valve attempts to achieve a flow rate proportional to the flow control signal, until the limiting pressure is achieved. To reverse the direction of flow (or the direction of force in the lift cylinders) the polarity of the flow control signal is reversed. The pressure control signal must always be a positive voltage. The new servo-valve required the construction of a manifold adapter to convert the new valve ports to the port pattern of the original valve.

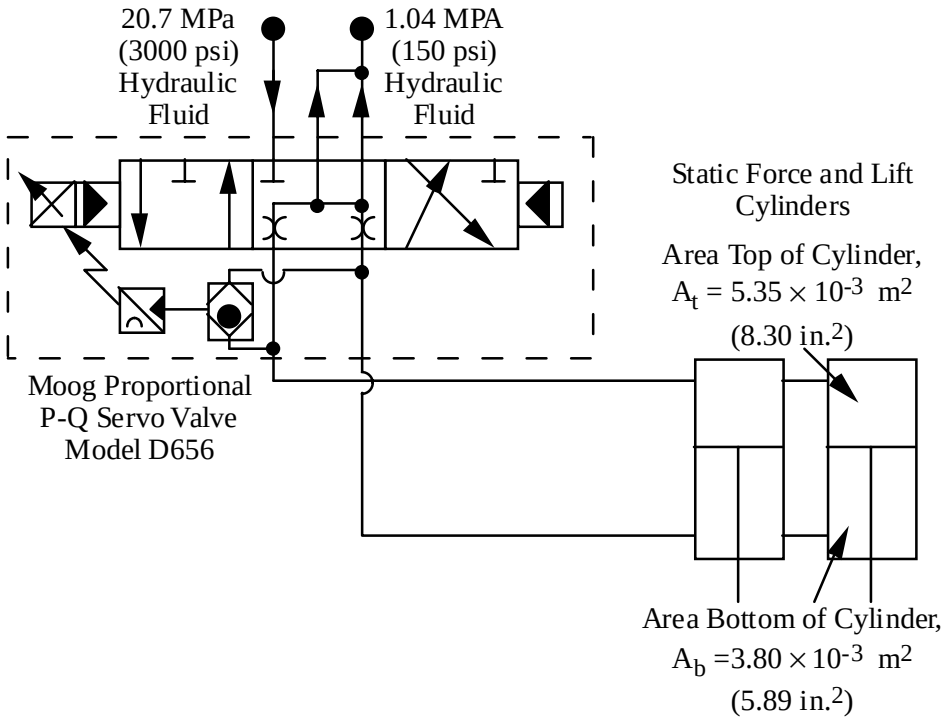

Figure 3.21 Schematic of RDD Static Force and Lift System with Proportional P-Q Valve

A control box was built to control the servo-valve. This box has several features. It outputs variable flow and pressure control signals. It is able to switch between internal and external control signals. It measures the valve's internal pressure transducer signal and displays the pressure on a digital bar graph. There is also an analog computer that uses the pressure transducer output and the direction of flow to calculate and display the applied static force. Figure 3.22 shows a schematic of this circuit. Table 3.4 gives the required relationship between the various resistors in the circuit and the resistance values used. The operational amplifiers are contained in two 728 quad-operational amplifier integrated circuits. This circuit utilizes the same stiff arms protection that the Vibroseis uses. Before any power is applied to the servo-valve, it pressurizes the bottom of the lift cylinders, lifting the loading system off the stiff arms. In order to power-up the control box and the servo-valve, the following three conditions must be met: First, the stiff arms must be rotated, closing their limiting switches; second, the up/down switch on the old control box must be in the down position; and third, the power switch on the new control box must be on.

The read-out on the valve control box neglects friction in the cylinders, guide rods, etc.; accordingly, it is slightly in error. However, the reading is still very valuable for adjusting the valve settings and accessing the system's behavior.

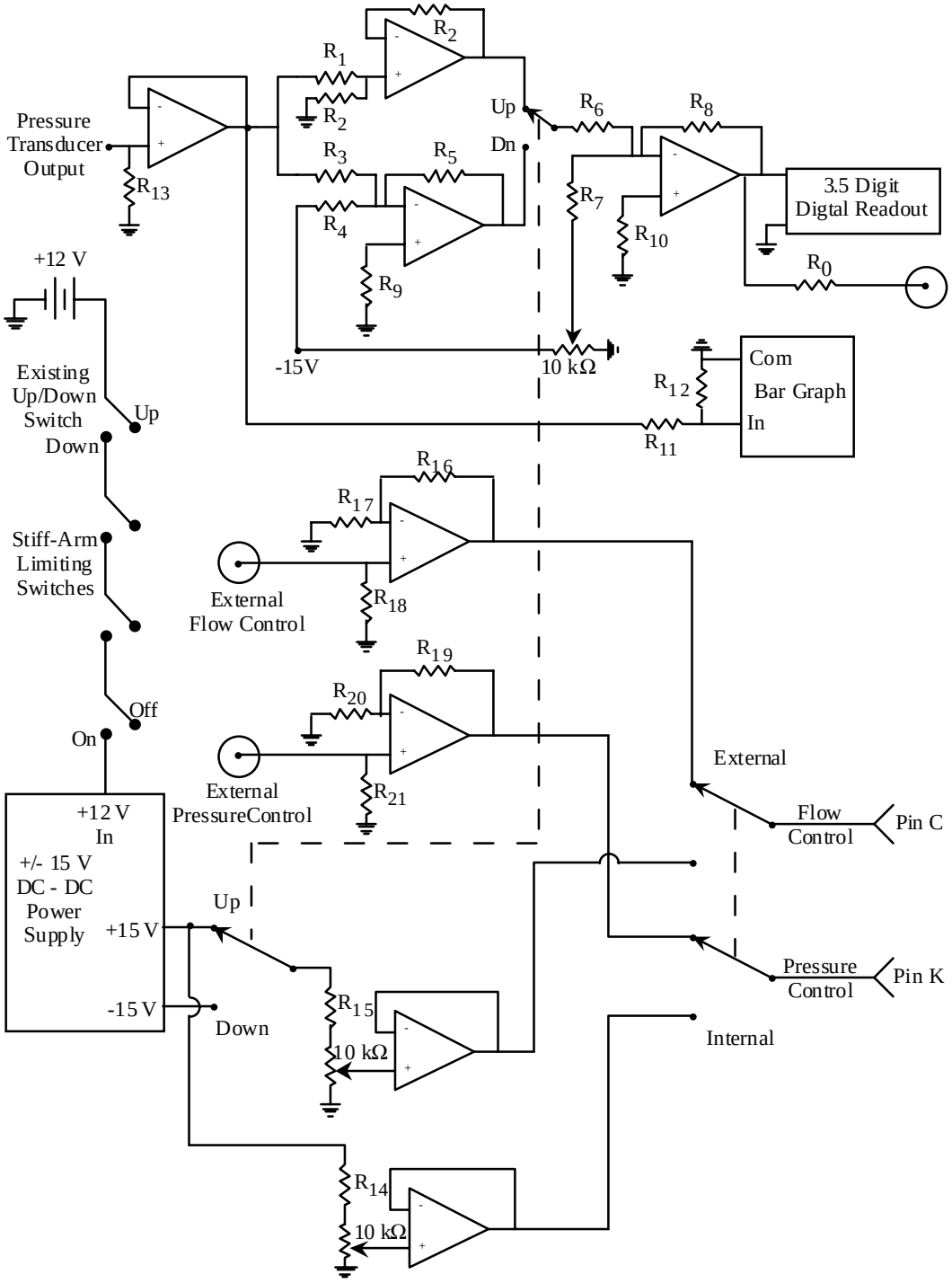

Figure 3.22 Schematic for Box Controlling Moog D656 Proportional P-Q Servo-Valve

Table 3.4 Resistor Values for Box Controlling Moog D656 Proportional P-Q Servo-Valve

Resistors	Relationship	Values
R_0	None	$R_0 = 200\ \Omega$
R_1, R_2	$\frac{R_2}{R_1 + R_2} = \frac{1}{82.50}$	$R_1 = 100.56\ k\Omega$ $R_2 = 1.23\ k\Omega$
R_3, R_5	$\frac{R_5}{R_3} = \frac{1}{58.57}$	$R_3 = 58.64\ k\Omega$ $R_5 = 1.00\ k\Omega$
R_4, R_5	$15V\,\frac{R_5}{R_4} = 0.00853V$	$R_4 = 1.76\ M\Omega$ $R_5 = 1.00\ k\Omega$
R_7, R_8	$7.5\ V\,\frac{R_8}{R_7} = 0.0350V$	$R_7 = 10.0\ M\Omega$ $R_8 = 49.9\ k\Omega$
R_6, R_8	$R_6 = R_8$	$R_6 = 49.9\ k\Omega$ $R_8 = 49.9\ k\Omega$
R_9	$R_9 \approx R_5$	$R_9 = 1.00\ k\Omega$
R_{10}	$R_9 \approx \frac{R_6}{2}$	$R_9 = 25.0\ k\Omega$
R_{11}, R_{12}	$\frac{R_{12}}{R_{11} + R_{12}} = \frac{1}{29.15}$	$R_{11} = 33.93\ k\Omega$ $R_{12} = 1.21\ k\Omega$
R_{13}	None	$R_{13} = 10\ M\Omega$
R_{14}	$10\ V = 15\ V\,\frac{10\ k\Omega}{10\ k\Omega + R_{14}}$	$R_{14} = 5\ k\Omega$
R_{15}	$10\ V = 15\ V\,\frac{10\ k\Omega}{10\ k\Omega + R_{15}}$	$R_{15} = 5\ k\Omega$
R_{16}, R_{17}	$R_{16} = R_{17}$	$R_{16} = 100\ k\Omega$ $R_{17} = 100\ k\Omega$
R_{18}	$R_{18} \approx \frac{R_{16}}{2}$	$R_{18} = 50\ k\Omega$
R_{19}, R_{20}	$R_{19} = R_{20}$	$R_{19} = 100\ k\Omega$ $R_{20} = 100\ k\Omega$
R_{21}	$R_{21} \approx \frac{R_{19}}{2}$	$R_{21} = 50\ k\Omega$

3.6.3 Dynamic Loading System

3.6.3.1 The Vibroseis Dynamic Loading System — The dynamic system uses the high-pressure oil to drive a reaction mass up and down, generating dynamic forces that are transferred to the ground surface. In this section the factors that affect the performance of this system are discussed, and the servo-hydraulic controls for the dynamic excitation are described.

A simplified drawing of the dynamic loading system listing critical specifications is shown in Figure 3.23. The primary component of the dynamic loading system is a reaction mass with an internal hydraulic cylinder. This cylinder is divided into a top and bottom chamber by a piston attached to the stilt structure. Hydraulic oil is cycled in and out of the top and bottom chambers of the hydraulic cylinder. This oil flow moves the reaction mass up and down, generating dynamic forces in the piston.

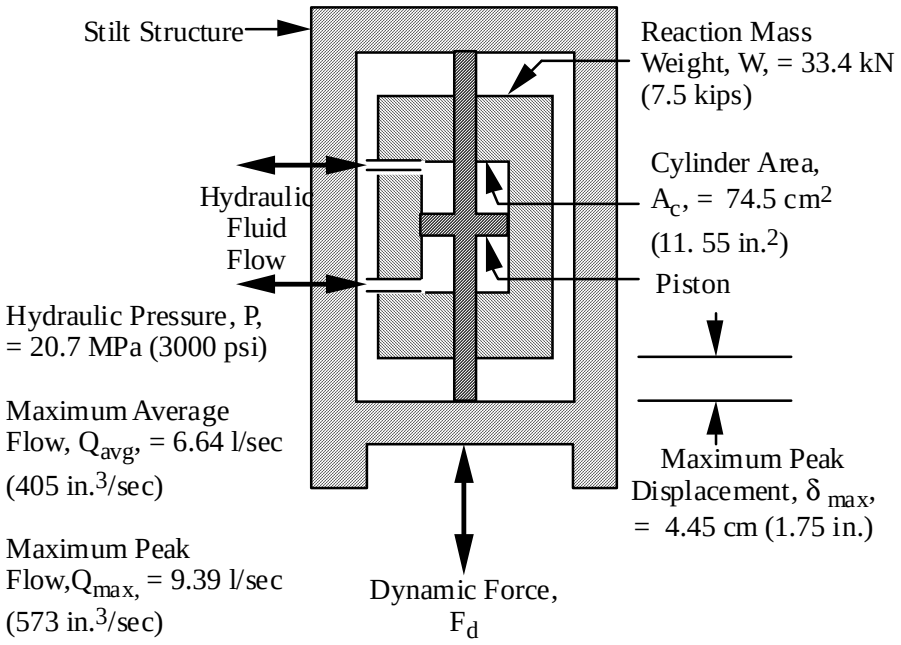

Figure 3.23 A Simplified Drawing of the Dynamic Loading System Listing Critical System Specifications

The dynamic force has three limiting functions. The first limiting function is the pressure limit. The force generated cannot exceed the oil pressure times the area of the cylinder, in this case 154.2 kN (34.65 kip). Or, using the symbols as defined in Figure 3.23:

$$F_d \leq P \times A_c = 154.2 \text{ kN } (34.65 \text{ kip}) \qquad \text{(Equation 3.18)}$$

The second limiting function is the flow limit. The flow rate and the cylinder area determine the reaction mass velocity. The frequency and velocity in turn control the mass

acceleration, and the dynamic force equals the mass times acceleration. Two different maximum flow rates are presented in Figure 3.23. The first, the maximum average flow, represents the maximum flow the pump can produce. However, the high-pressure accumulator can contribute much more flow for short periods of time, as long as the average flow does not exceed the maximum pumping rate. Thus, for a sinusoidal excitation, the maximum peak flow rate is the square root of 2 times the maximum average rate. The flow-limited maximum force is frequency dependent. The equation is:

$$F_d \le \frac{Q_{max}}{A_c} \times 2\pi f \times \frac{W}{g} \qquad \text{(Equation 3.19)}$$

where *f* is frequency
g is the acceleration of gravity

The third limiting function is the displacement limit. The displacement and frequency determine the reaction mass acceleration and, hence, the dynamic force. The equation is:

$$F_d \le \delta_{max} \times (2\pi f)^2 \times \frac{W}{g} \qquad \text{(Equation 3.20)}$$

These three limiting functions are plotted in Figure 3.24. From 0 to 4.5 Hz, the displacement limit controls the maximum dynamic force. From 4.5 to 5.7 Hz, the flow limit controls the maximum dynamic force. Above 5.7 Hz, the pressure limit controls the maximum dynamic force. Above 100 Hz, very little dynamic force can be generated because of the servo-valve response compressibility in the hydraulic fluid.

The Vibroseis used for this work utilizes Pelton Advance 1 Model 5 vibrator electronics for dynamic force control. A simplified schematic (Pelton 1980) of the dynamic force control system is shown in Figure 3.25. The control system has a function generator (designated the sweep generator in Figure 3.25) that generates an analog signal proportional to the desired force output. The servo-control system utilizes three different feedback signals. The first is the mass feedback signal that is the output of an LVDT attached to the reaction mass. This feedback prevents the reaction mass from drifting. The second is the valve feedback that is the output of an LVDT attached to the servo-valve spool. This feedback prevents the valve spool from drifting. The third is the phase compensation feedback that is the output of an accelerometer attached to the stilt structure to keep the output force in phase with the sweep generator signal.

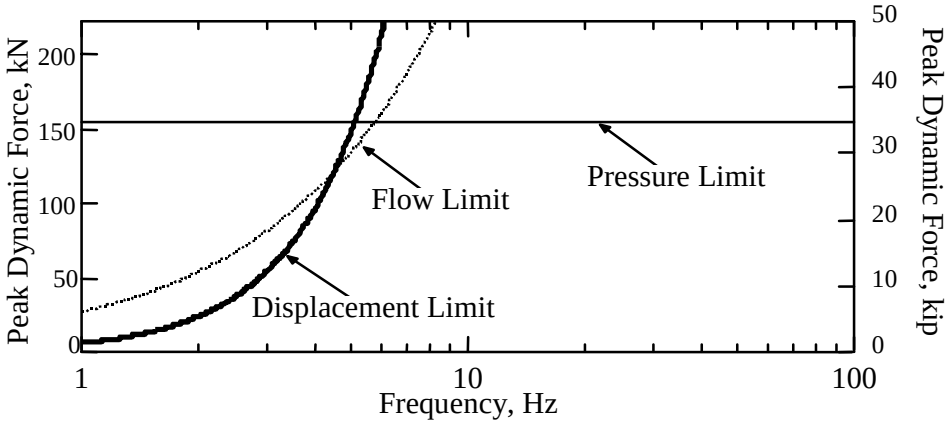

Figure 3.24 Dynamic Force Limiting Functions for the Vibroseis Loading System

Different feedback signals are more commonly used on newer Vibroseis models (Baeten and Ziolkowski 1990). Instead of the phase compensation signal shown in Figure 3.25, a better signal to use is a signal combining the output of two accelerometers, one on the stilt structure and the other on the reaction mass. The two signals are combined proportionally to the masses of the stilt structure and the reaction mass, respectively. This combined signal will be proportional to the dynamic force if all components move as rigid bodies.

The control system also has an alarm system, which is activated when the output becomes out of phase with the sweep generator signal. It is very important to maintain this phase match when several Vibroseis devices are being driven simultaneously. This alarm system is not shown in Figure 3.25.

3.6.3.2 The Rolling Dynamic Deflectometer Dynamic Loading System — The RDD dynamic loading system uses most of the same systems as the Vibroseis. The same force limiting functions presented in Equations 3.18 through 3.20 and Figure 3.22 also apply to the RDD. Some changes were made to the dynamic force control system. A simplified schematic of the RDD dynamic force control system is shown in Figure 3.26. The differences between the RDD and the Vibroseis dynamic control systems are that the capability has been added to switch between the internal and an external function generator, and the stilt structure accelerometer and phase compensation feedback have been removed. Also, the phase error alarm system has been disabled.

An external function generator is important because the internal function generator is not designed to output a continuous sinusoid, as required for RDD operation. A BNC connector and a toggle switch have been added to the control panel of the vibrator electronics to input an external forcing function and to switch between the internal and external function generators.

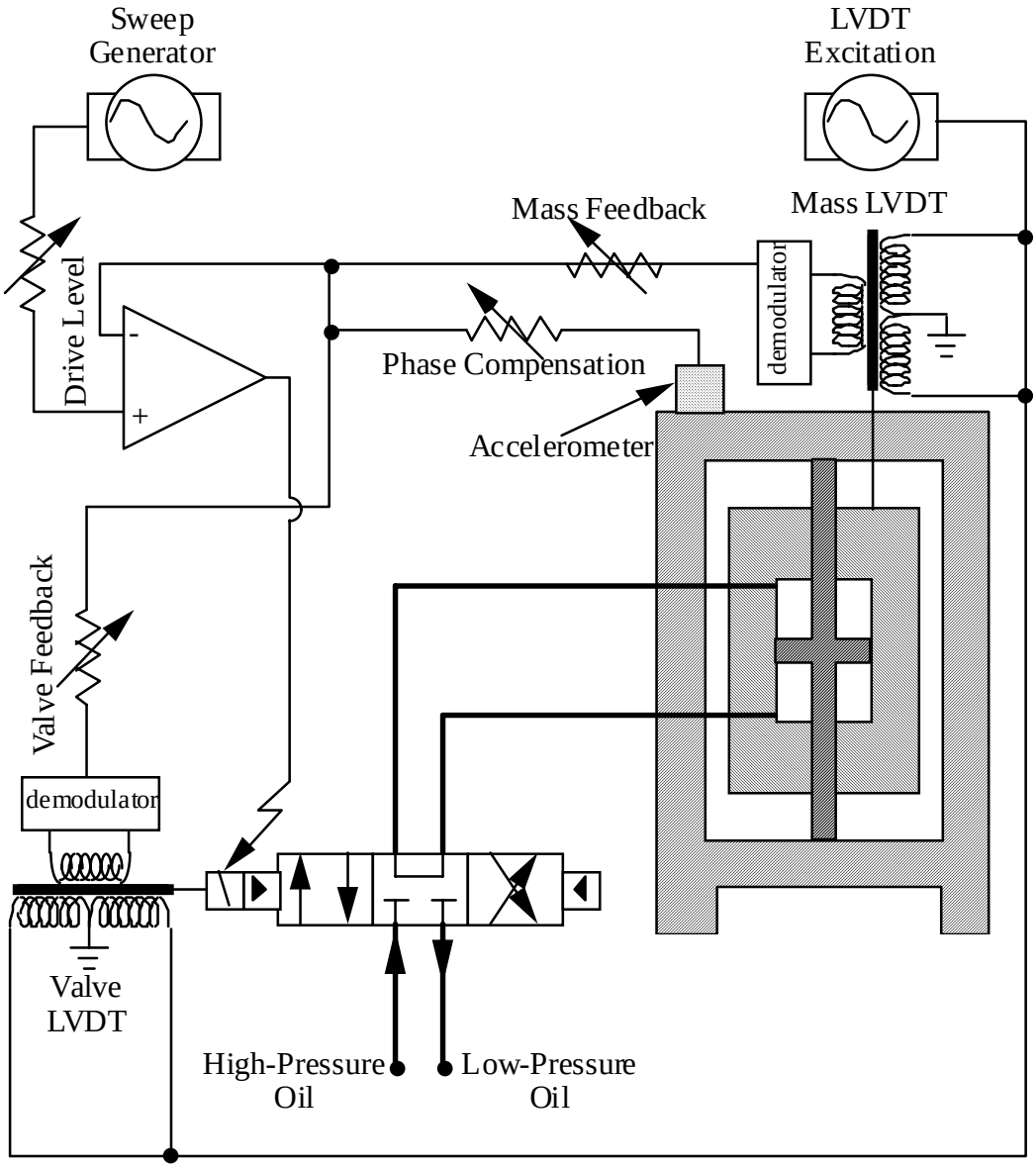

Figure 3.25 Simplified Schematic of Dynamic Force Control System for the Vibroseis

The accelerometer and phase compensation feedback were eliminated because the accelerometer performs very poorly at low frequencies, impairing the vibrator's low-frequency performance. The RDD usually operates at higher frequencies, where this is not an issue; nevertheless, low-frequency capabilities are valuable for other applications. Also, the addition of more compliant loading rollers has substantially changed the response of the stilt structure, making the stilt structure acceleration a less suitable feedback signal.

A valuable improvement to the RDD dynamic force control system would be to replace the phase compensation feedback signal with a more suitable feedback signal. For

instance, load cell output would be a suitable feedback signal. A new feedback signal would provide several benefits, including more harmonic loading, more consistent dynamic forces over rough and variable surfaces, and flatter frequency response during sweeps.

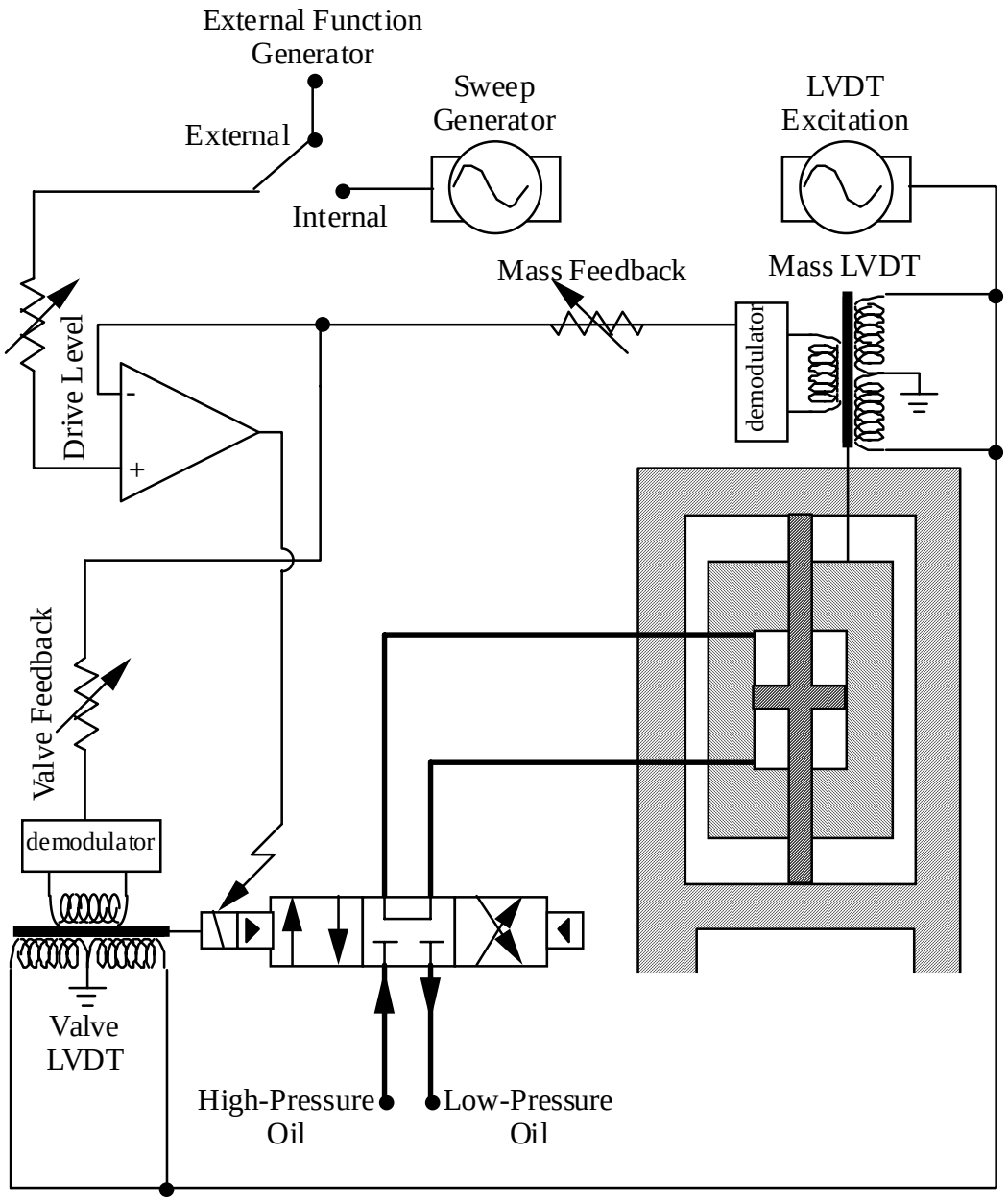

Figure 3.26 Simplified Schematic of RDD Dynamic Force Control System

3.7 SUMMARY

Vibroseis trucks used for oil exploration have a dynamic loading system that has many features needed in an RDD loading system. Accordingly, the RDD was built by modifying a Vibroseis. The Vibroseis was first modified by replacing the plate with a loading frame. The new loading frame carries forces to a pair of loading rollers, which apply the load to the pavement. After several design iterations, loading rollers capable of withstanding the RDD loading were obtained. Additional support systems to resist lateral loads imposed by the moving system and to resist tipping in the loading system were designed and built.

The RDD required modifications to the Vibroseis hydraulic system and the electronic servo-control systems. The hydraulic system is used to apply static and dynamic forces to the pavement. The Vibroseis systems controlling static loading were replaced with a servo-control system, thus providing better control and a larger range of static forces. The dynamic force control system was modified to allow for continuous operation. Further improvements can be made to the dynamic force control system by using different feedback signals as discussed in this chapter.

CHAPTER 4. DEVELOPMENT OF THE ROLLING DYNAMIC DEFLECTOMETER FORCE MEASUREMENT SYSTEM

4.1 INTRODUCTION

One of the important measurements recorded during rolling dynamic deflectometer (RDD) testing is the measure of the vertical force applied to the pavement surface. This force consists of two components: one static and one dynamic. It is important to know the static force to avoid overloading the pavement and to ensure that the static force provides a sufficient hold-down force to keep the loading rollers in contact with the pavement during dynamic loading. The dynamic force measurement, however, is the critical force measurement. The goal of RDD testing is the measurement of the dynamic displacement induced by a given dynamic force. This goal cannot be accomplished without accurate dynamic force measurements.

There are several approaches to measuring the static and dynamic forces. The first is an inertial approach. This method is, however, suitable only for measurement of the dynamic force. It is the most commonly used method in Vibroseis testing (Baeten and Ziolkowski 1990). A second approach is to make a differential pressure measurement in the actuator. This approach has also been used to measure dynamic forces in Vibroseis testing (Reust 1993, Bedenbender and Kelly 1985). A third approach is to use load cells to measure both static and dynamic forces. After initially using the inertial approach, it was decided that load cells should be used in RDD testing. This chapter discusses the inertial and load cell approaches used in RDD testing, and then describes the design of suitable load cells for RDD testing.

4.2 INERTIAL FORCE MEASUREMENTS

One approach to measuring the dynamic force generated by the RDD is to measure the accelerations of the reaction mass and the stilt structure. This is the approach commonly employed in Vibroseis testing (Baeten and Ziolkowski 1990, Reust 1993).

The configuration of the sensors used to perform this measurement is shown in Figure 4.1. One accelerometer is fastened to the stilt structure and another to the reaction mass. These two accelerometers measure the accelerations of the stilt structure and the reaction mass, respectively. If it is assumed that both the reaction mass and the stilt structure each move as rigid bodies, the dynamic force generated from the system can be determined using Newton's Second Law:

$$f_d = a_r \times m_d + a_s \times m_s, \qquad \text{(Equation 4.1)}$$

where f_d is the vector of vertical dynamic force
a_r is the vector of vertical acceleration of the reaction mass
a_s is the vector of vertical acceleration of the stilt structure
m_d is the mass of the reaction mass
m_s is the mass of the stilt structure

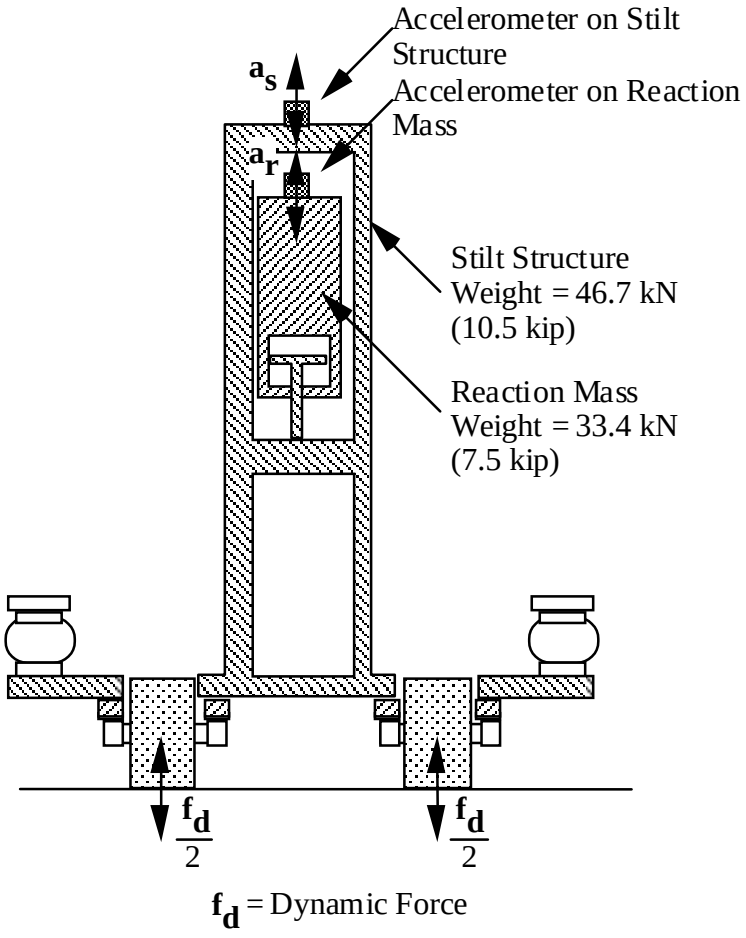

Figure 4.1 Cross Section of RDD Loading System Showing Accelerometers Used To Make Inertial Dynamic Force Measurements

The dynamic force and both accelerations, $\mathbf{f_d}$, $\mathbf{a_r}$, and $\mathbf{a_s}$, are vectors. If the stilt structure moves in phase with the reaction mass, it contributes to the total dynamic force acting on the pavement. If it moves out of phase with the reaction mass, its motion decreases the dynamic force acting on the pavement. A vector representation of these forces is shown in Figure 4.2. The magnitude of the dynamic force can be calculated using the law of cosines, as follows:

$$\left|\mathbf{f_d}\right| = \sqrt{\left|m_r\,\mathbf{a_r}\right|^2 + \left|m_s\,\mathbf{a_s}\right|^2 - 2\left|m_r\,\mathbf{a_r}\right|\left|m_s\,\mathbf{a_s}\right|\cos(180-\phi_{rs})}$$

(Equation 4.2)

where ϕ_{rs} is the phase difference between the motion of the reaction mass and the stilt structure.

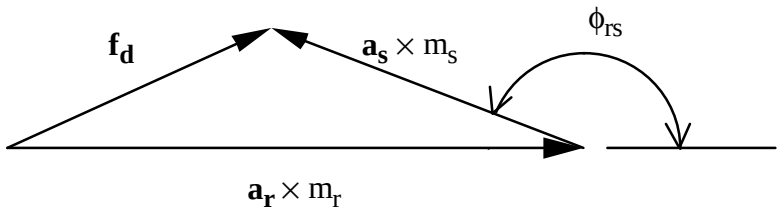

Figure 4.2 Vector Representation of Inertial Dynamic Force Measurement

Initial testing with the RDD was conducted using inertial force measurements. This work was done from July 1995 to July 1996. However, it was suspected that these force measurements were not sufficiently accurate for the design purposes of the RDD. Therefore, a test was conducted to determine the quality of the inertial force measurements. This test used the RDD loading system to apply a dynamic force to calibrated weigh-in-motion (WIM) load cells. The accelerations of the reaction mass and stilt structure were measured, following which the forces were calculated using Equation 4.2 and compared with the forces measured with the WIM load cells. This test was performed at different frequencies and at low force levels to avoid damaging the WIM load cells. The results of these tests are presented in Table 4.1.

Table 4.1 Results of Tests Comparing Dynamic Forces Measured with WIM Load Cells and Dynamic Forces Calculated Inertially

Frequency (Hz)	Dynamic Force, Measured With WIM Load Cells (kN/kip)	$\lvert m_r \mathbf{a_r} \rvert$ (kN/kip)	$\lvert m_r \mathbf{a_r} \rvert$ (kN/kip)	ϕ_{rs} (degrees)	Dynamic Force, Calculated Inertially (kN/kip)
10	8.22 (1.85)	13.5 (3.03)	2.98 (0.67)	-7	16.5 (3.70)
20	10.1 (2.26)	10.6 (2.38)	17.7 (3.99)	-14	28.1 (6.32)
60	5.38 (1.21)	18.4 (4.13)	30.7 (6.90)	-163	14.2 (3.19)

These results show very poor agreement between the dynamic forces measured with the WIM load cells and the dynamic force measured inertially. The calculated forces are consistently higher than the measured value by a factor of 2 or more. Evidently, there are more inertial losses in force than are indicated by the accelerometer on top of the stilt structure. This means that the loading system is not moving as a rigid body.

In Vibroseis studies, the inertial approach has yielded force measurements that agree quite well with load cell measurements (Baeten and Ziolkowski 1990). However, the loading

system of the RDD has been modified substantially. These modifications include an increase in the loading system mass from 62.3 kN to 80.1 kN (14 kip to 18 kip), less stiffness in the RDD open loading frame than the Vibroseis plate, and the addition of a loading roller that acts like a "soft," nonlinear spring. These modifications apparently cause the inertial approach to be less accurate for RDD testing than for the Vibroseis operations.

4.3 ROLLING DYNAMIC DEFLECTOMETER LOAD CELLS

Because of the problems encountered in using inertial force measurements on the RDD, that approach was abandoned. Instead, load cells were added to make a direct measurement of force. In this section, the design requirements for the RDD load cells are discussed. The design, construction, and calibration of these load cells are then presented.

4.3.1 Load Cell Requirements

An RDD load cell has several special requirements. First, the load cell should be located as close as possible to the point of load application to minimize the inertial losses caused by motion of components between the load cell and the point of load application. The most suitable location for the load cells is between the loading frame and the pillow block bearings, as shown in Figure 4.3. In this position, the only components that contribute inertial losses are the loading rollers and the bearings, and the mass of these components is low compared with the mass of the other loading system components.

With the load cells located in the position shown in Figure 4.3, it is essential that the height of the load cells be minimized to maintain clearance between the ground and the loading rollers when the loading system is raised. The geometry of the load cell is further complicated by the pillow block bearings. The pillow block bearings distribute the load over a footprint about 40.6 cm by 10.2 cm (16 in. by 4 in.). Most load cells are designed to measure concentrated loads, but the RDD load cell must be able to measure loads distributed by the pillow block bearings.

The RDD load cell must be an integral part of the structural system. In addition to carrying the combined vertical dynamic and static forces applied by the loading system, the load cells also must carry horizontal forces resulting from roller friction against the pavement as well as the large horizontal forces that occur when the loading rollers encounter joints, discontinuities, and other irregularities in the pavement. The magnitude and direction of these horizontal forces are practically impossible to predict, but they could possibly be as large as, or larger than, the combined dynamic and static vertical forces. Furthermore, it is necessary that the RDD load cell isolate and sense only the total vertical force in the presence of these horizontal forces.

No commercially available load cell could be located meeting the requirements stated above. Therefore, a special RDD load cell was designed and constructed.

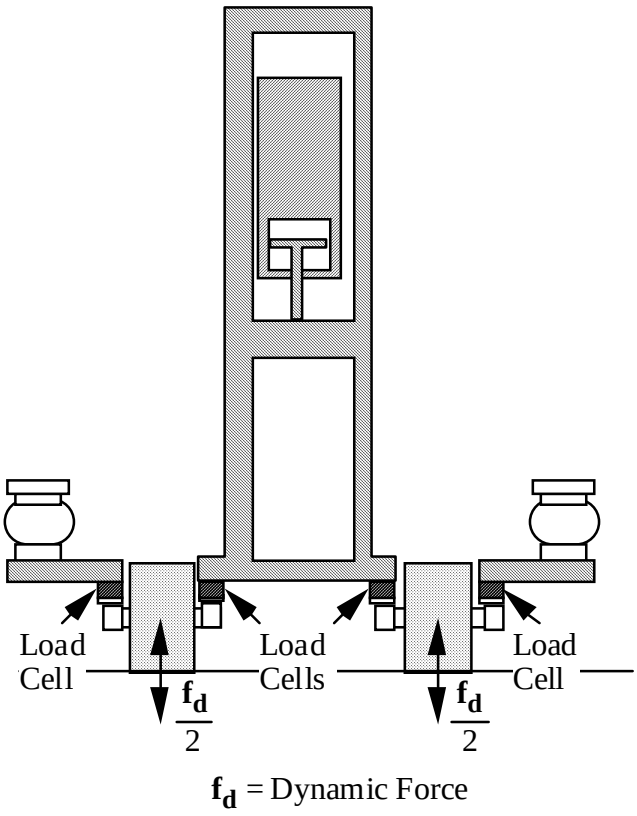

Figure 4.3 Cross Section of RDD Loading System Showing Location of Load Cells

4.3.2 Load Cell Design and Construction

A load cell was designed with multiple instrumented bending elements to measure the static and dynamic forces generated by the RDD. The multiple bending elements are conducive to measuring the distributed forces at the pillow block bearings. The bending elements are capable of withstanding the high lateral loadings imposed during RDD operation. A photograph of one of the load cells under construction is shown in Figure 4.4a. This photograph shows the strain gauges attached to the bending elements before waterproofing was applied. Figure 4.4b is a photograph showing a close-up view of the load cell strain gauges.

A side view of the load cell is shown in Figure 4.5. This view illustrates the manner in which load is transmitted from the loading frame to the bearing, causing the bending elements to bend. A simplified loading diagram, a free-body diagram, and a moment diagram of a single element is shown in Figure 4.6. The bending element acts like a 2.5 cm (1 in.) long beam that is fixed against rotation on both ends and fixed against translation on one end. When this beam is loaded at the free end, equal and opposite moments are induced at the two ends of the beam, as shown in the free-body diagram and moment diagram in

Figure 4.6. For the loading shown, the inside strain gauges experience a compressive stress owing to the bending, and the outside strain gauges experience an equal but opposite tensile stress. By placing the inside and outside strain gauges on adjacent legs of a Wheatstone bridge, both gauges contribute to the load cell sensitivity, with the gauges rendered temperature-compensating because of their proximity to each other on the bending element.

A three-dimensional view of the RDD load cell is shown in Figure 4.7. The 10.2 cm by 40.6 cm (4 in. by 16 in.) load cell has six bending elements separated by slots cut through the overall bending members. Each bending element has inside and outside strain gauges. The two center bending elements (nos. 2 and 5) each have a single inside and a single outside strain gauge, while the two right and two left bending elements each have two inside and two outside strain gauges. One set of inside and outside strain gauges on each element is incorporated into a Wheatstone bridge to measure the vertical force applied to the load cell. The extra strain gauges on the right and left elements form a separate Wheatstone bridge to measure the moment applied to the load cell. The horizontal forces acting on the loading roller can be determined from the moment.

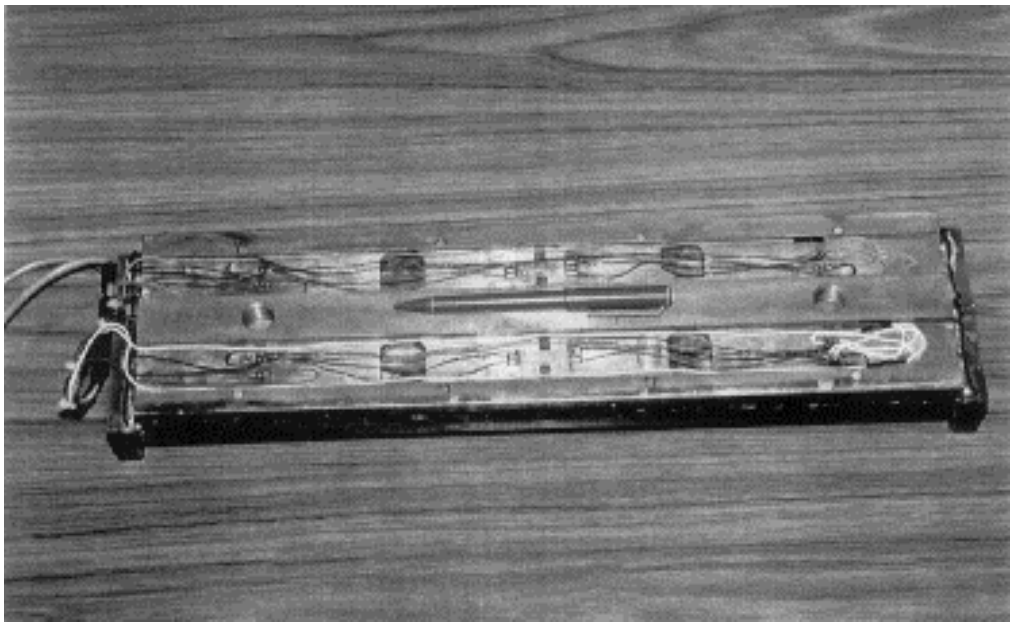

a) Photograph of RDD Load Cell under Construction

Figure 4.4 Photographs of RDD Load Cells under Construction

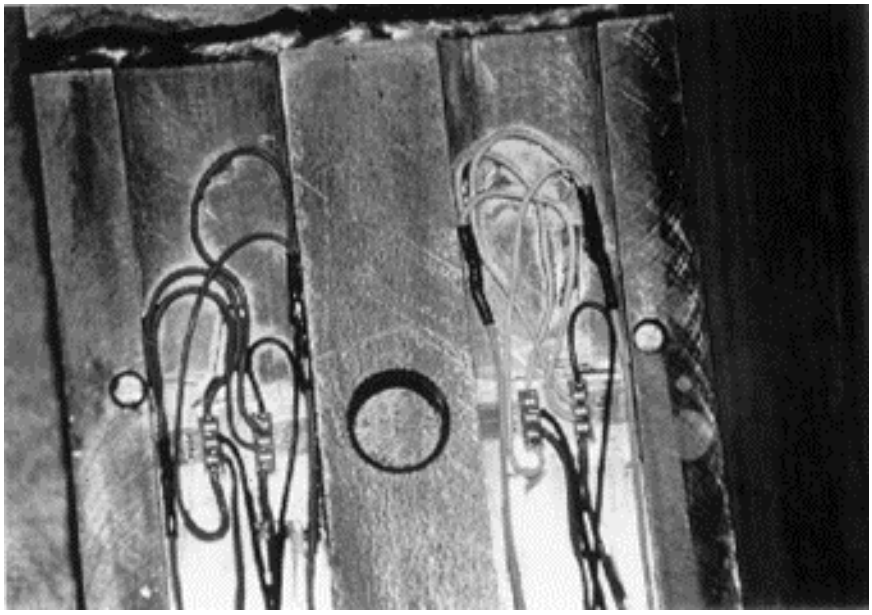

b) Close-up View of the Load Cell Strain Gauges

Figure 4.4 (Cont.) Photographs of RDD Load Cells under Construction

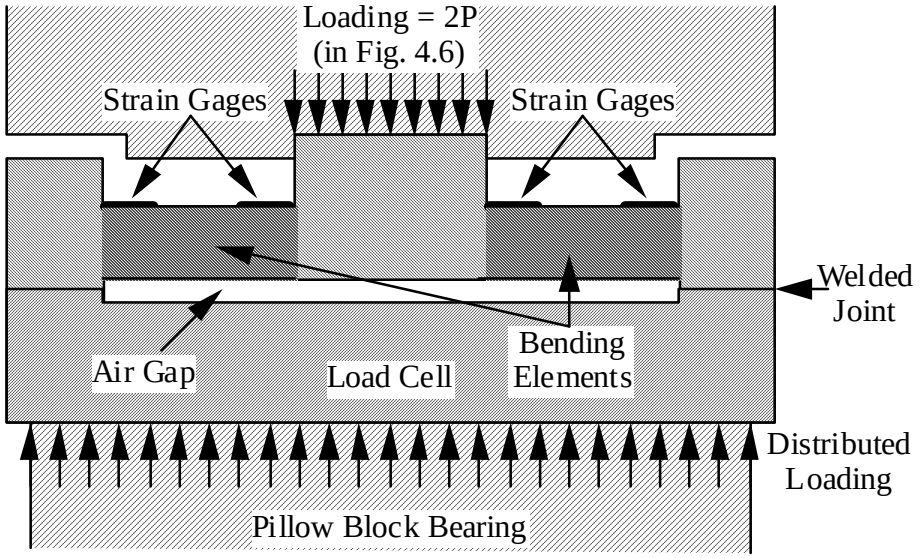

Figure 4.5 Side View of RDD Load Cell Showing Bending Elements

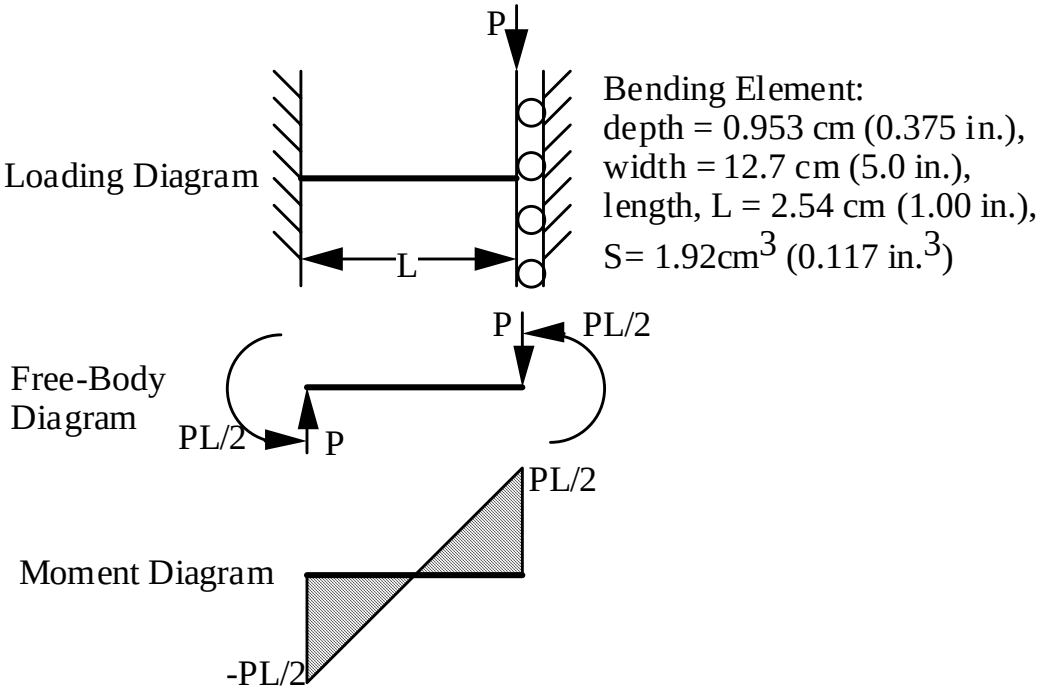

Figure 4.6 Simplified Loading Diagram, Free-Body Diagram, and Moment Diagram for a Single Bending Element on the RDD Load Cell

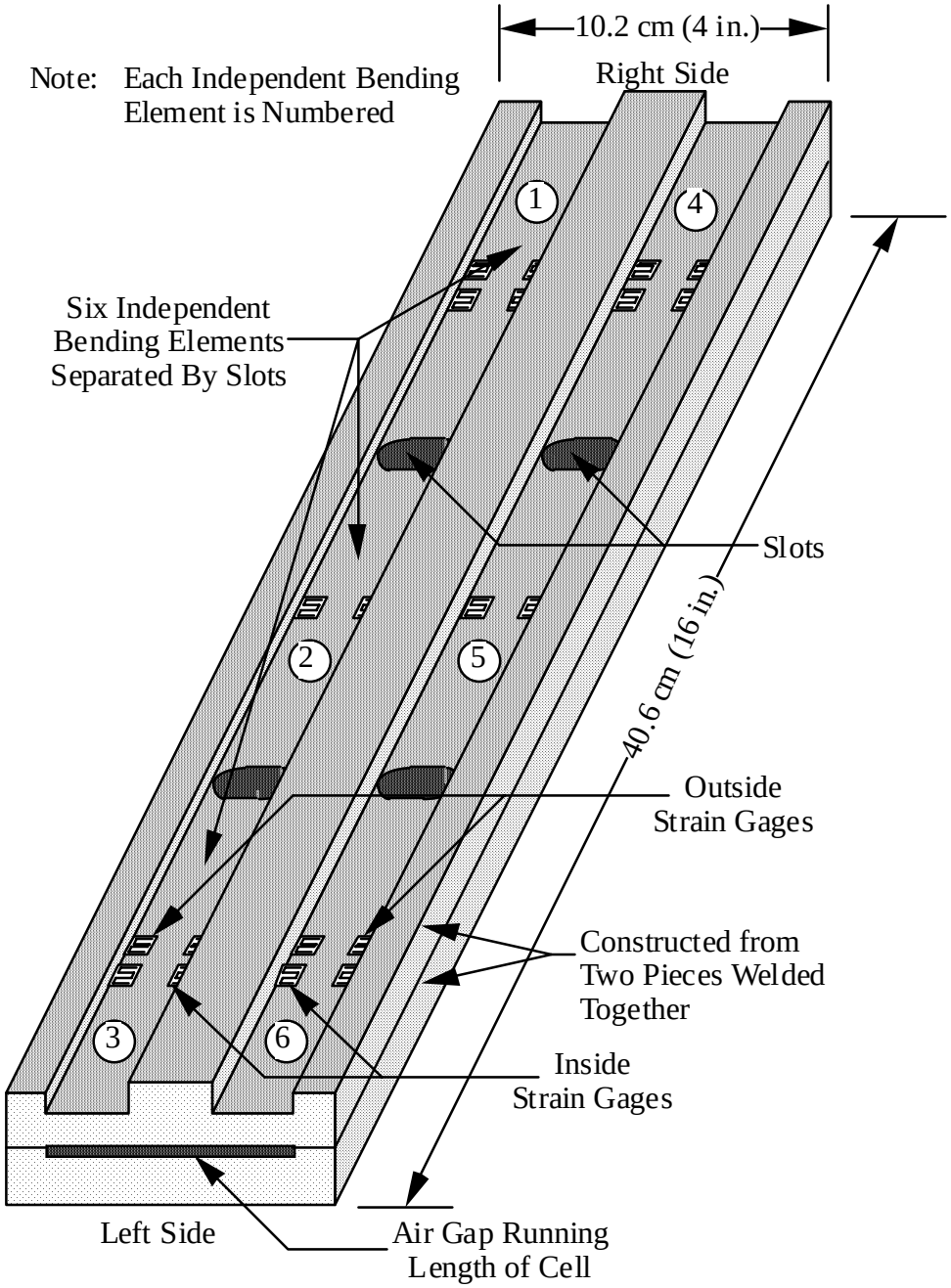

Figure 4.7 Three-Dimensional View of RDD Load Cell Showing Placement of Strain Gauges on Bending Elements

It should be noted that the bending elements have a peculiar geometry for a beam. The beam width is much greater than its depth. The elastic solution for a beam with this geometry in pure bending is the same as the solution using elementary bending theory. However, when a wide beam such as this is subjected to bending forces, the shearing stresses

are very complicated and differ from that predicted using elementary bending theory (Timoshenko and Goodier 1970). Very high shear stresses are present at the edges of the bending element. To minimize these complications in the load cells, the strain gauges were positioned at the center of the bending element, away from the high shearing stresses at the edges, and the strain gauges were oriented so as to sense the bending stresses and not the shear stresses.

Two different types of strain gauges were used on the load cells. The strain gauges on the center bending elements are Micro Measurements model WK-06-125AD-350. The strain gauges on the right and the left bending elements are Micro Measurements model EA-06-125PC-350. The different types of strain gauges were used to simplify construction. Both types of strain gauges demonstrate similar performance.

The arrangements of the various strain gauges on the two Wheatstone bridges of the load cell are shown in Figure 4.8. Moments acting on the load cell will cause bending stresses in the bending elements that are higher on one side of the load cell than on the other side. In the vertical force bridge, this unbalanced stress will cancel, making the bridge sensitive only to vertical forces. On the other hand, in the moment bridge, vertical forces will cancel, making the bridge sensitive to only moment. If the stress is not distributed linearly between the right, center, and left bending elements, part of the stress owing to a moment will be taken by the center element and will not cause strain in the outside bending elements, leading to errors in the measured moment. Thus, the moment measurements made by the load cell are not of the same quality as the vertical force measurement. This is of little concern, however, because the vertical force measurement is the critical measurement in RDD testing, while the moment measurement is used only to estimate shear stresses applied to the pavement through the loading rollers and the lateral forces applied to the load frame.

4.3.3 Load Cell Calibration

The RDD load cells were calibrated in the laboratory prior to installing them on the RDD. A hydraulic load frame was used to apply force to the RDD load cells through a calibrated load cell, and the output of the two load cells was compared. A total of five tests were performed to calibrate each bridge of each RDD load cell. The RDD load cells were first loaded concentrically, then 3.18 cm (1.25 in.) off-center in each direction, and finally 6.35 cm (2.5 in.) off-center in each direction. The purpose of eccentric loading was to calibrate the moment bridge and to study the effect of eccentric loading on the vertical force bridge. A maximum load of 145 kN (32.5 kip) was used for each test.

The vertical force calibrations for the four RDD load cells are presented in Figure 4.9. These plots represent the continuous output of the RDD load cells and the calibrated reference load cell. The slope of the calibration curve presented in each plot is the calibration factor for that load cell. The plots in Figure 4.9 show the loading and unloading curves from the concentric calibration tests. The calibration factors, however, are the average values from the concentric test and four eccentric tests. The ± error value presented with each calibration factor represents the range of calibration factors from the five vertical force calibration tests on each load cell.

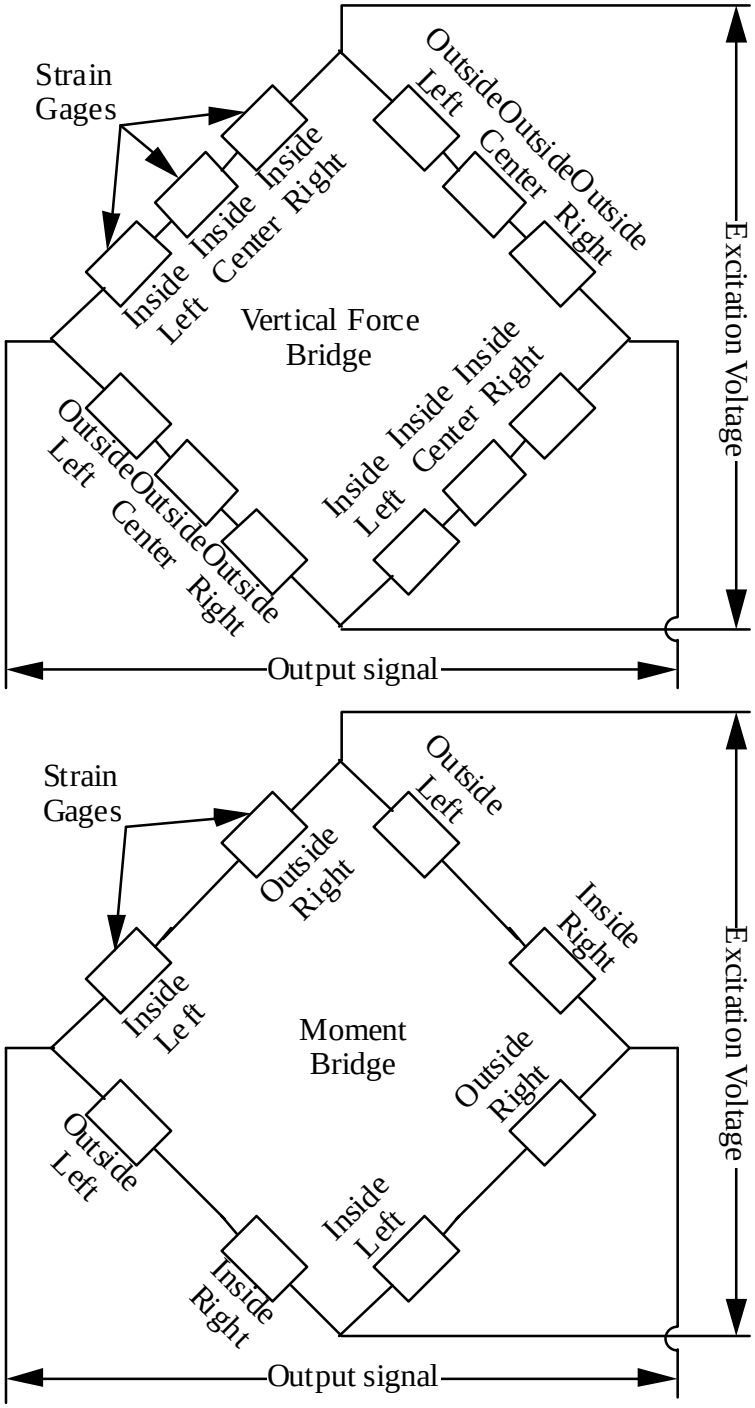

Figure 4.8 Arrangement of Strain Gauges in the Two Wheatstone Bridges Used in the RDD Load Cells

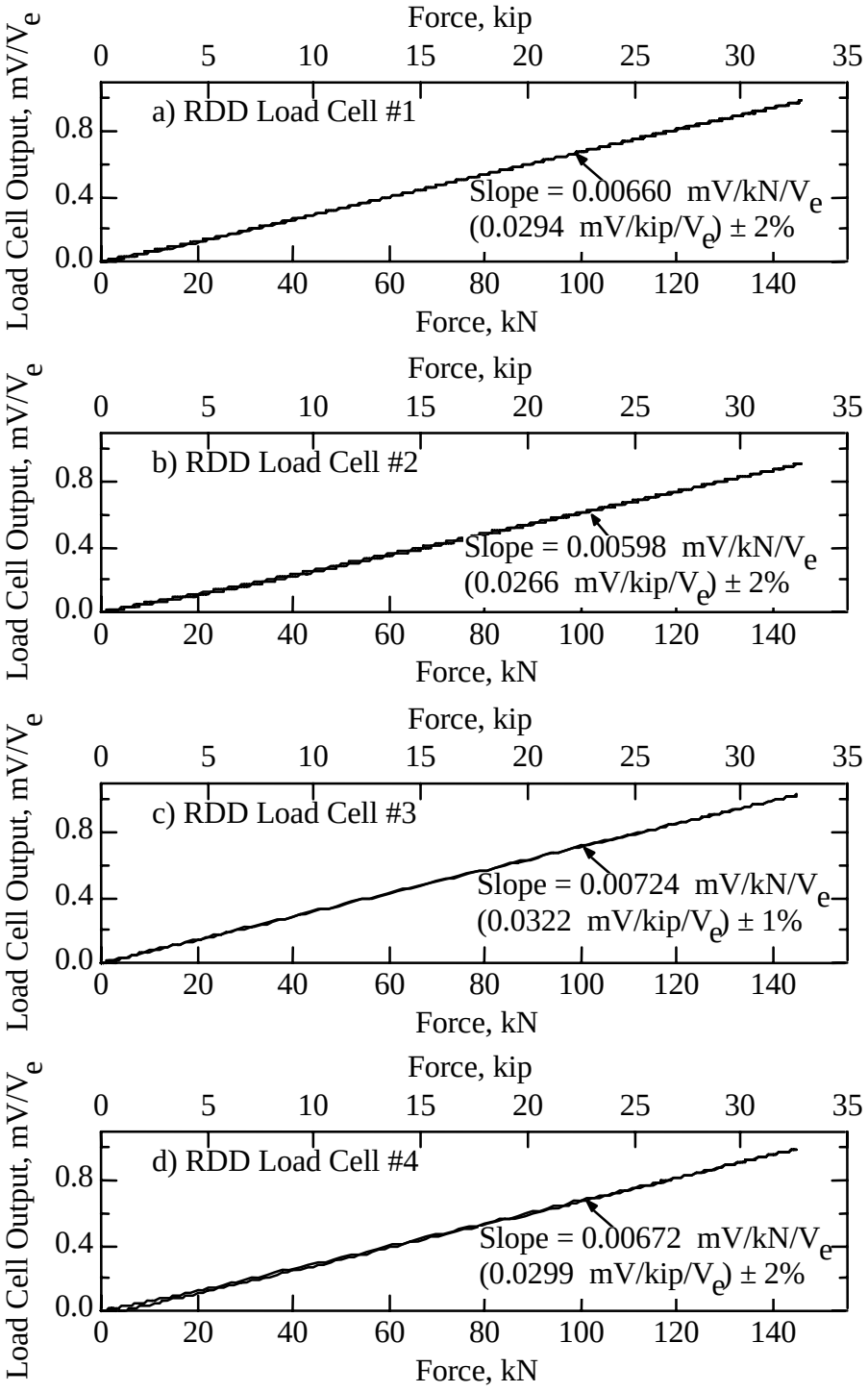

Figure 4.9 Vertical Force Calibration Curves and Calibration Factors for the RDD Load Cells

The calibration factors are quite similar for RDD load cell #1 and #4. The calibration factor for RDD load cell #3, presented in Figure 4.8c, is somewhat higher. This is because a machining error led to somewhat narrower bending elements on this load cell. The error was not serious enough to affect the structural integrity of the load cell, so the load cell was not discarded. For unknown reasons, the calibration factor for load cell #2 (Figure 4.8b) is lower than the calibration factor for the other load cells.

The moment calibrations for the four RDD load cells are presented in Figure 4.10. The slope of the calibration curve presented in each plot is the moment calibration factor for that load cell. The plots in Figure 4.10 show the loading and unloading curves from the two calibration tests with 6.35 cm (2.5 in.) load eccentricity. The ± error value presented with each calibration factor represents the total range variation from the linear calibration factor. The plots in Figure 4.9 are continuous output of the RDD load cells and the calibrated reference load cell.

The moment calibration plots shown in Figure 4.10 clearly are not linear like the vertical force calibration curves. This is due to the weaknesses in the moment measurement system discussed in the previous section. The moment calibration factors have about 7 percent to 10 percent uncertainty, compared with 2 percent uncertainty or less for the vertical force calibrations.

The lack of certainty in moment measurements is not a concern in RDD testing. Moment values are not required at any stage of the analysis of RDD measurements. The moment values are simply used to provide not only a better understanding of all loads applied to the pavement by the RDD, but also additional insight into the loads to which the RDD loading system is subjected during testing. For these purposes, these levels of uncertainty are very reasonable.

4.3.4 Load Cell Electronics

The RDD load cells require electronics to provide an excitation voltage to the strain gauge bridges and to amplify the output signals. A load cell conditioning box was designed and built to provide these functions. Some additional features were also built into the conditioning box. Summing circuits were used to obtain signals proportional to the combined loads in the load cells. Two displays were also provided in the conditioning box. The displays can be switched between the output of individual load cells and the combined output of all four load cells. The first display shows the static force exerted on any single load cell, or the combined static force on all four load cells. The second display shows the dynamic force on any single load cell, or the combined dynamic forces on all four load cells. The conditioning box also incorporated circuits to zero-out the load cells. Currently, conditioning is provided only for the vertical force bridges load cells. A flow chart showing the operations of the load cell conditioning circuit is presented in Figure 4.11.

Each leg of the vertical force strain gauge bridge uses three strain 350Ω strain gauges, as shown in Figure 4.8. This provides a high-resistance bridge with stable output at high excitation voltages. Therefore, to minimize subsequent amplification, an excitation voltage of 15 volts is applied to each bridge.

The signal from each load cell is amplified 100 times with an instrumentation-quality differential amplifier. A variable DC voltage is then summed with each signal. The level of the DC voltage is adjusted so that a zero-voltage reading is obtained from each load cell

when no forces are applied. Next, each signal is amplified by the appropriate gain to obtain an output of 222 mV/kN (50 mV/kip) from each load cell. The outputs of each individual load cell are then sent to the data acquisition system.

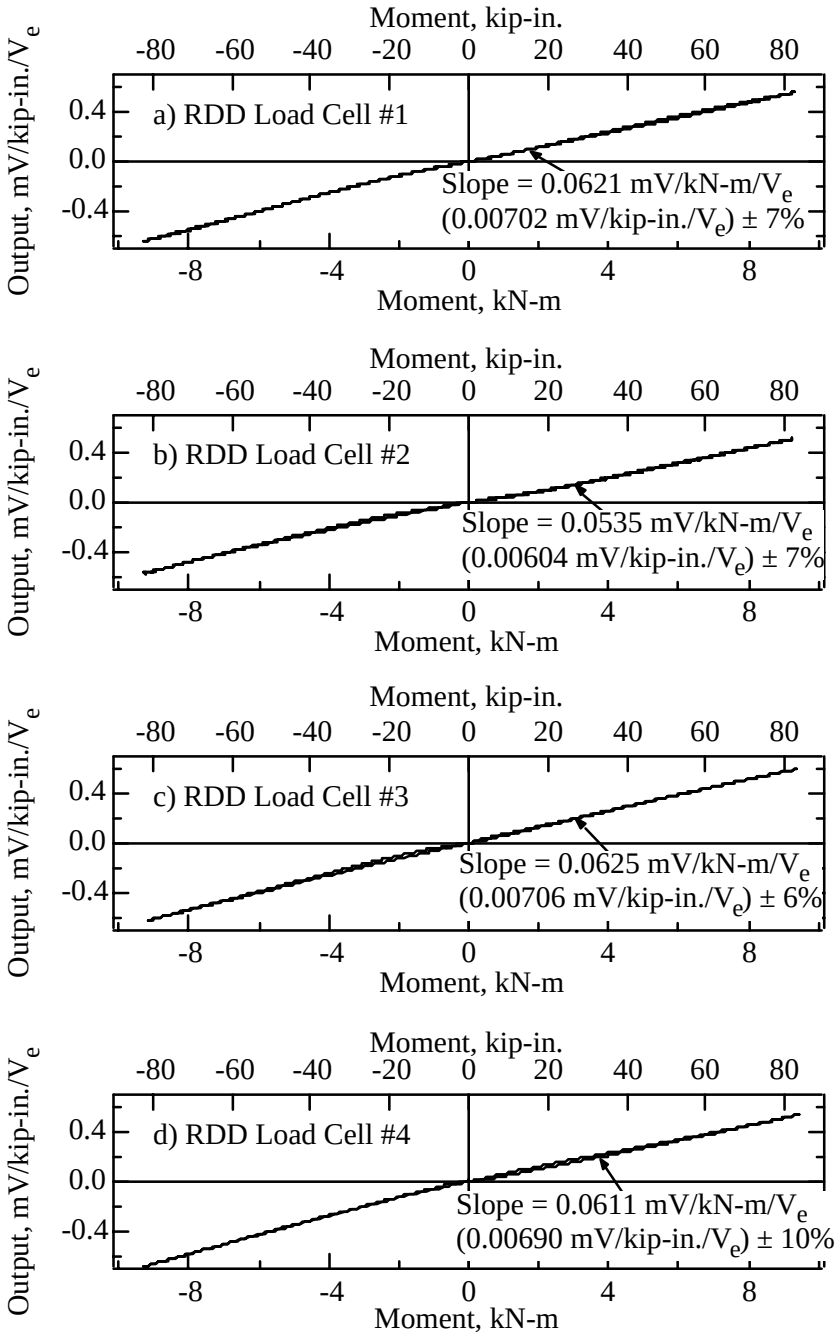

Figure 4.10 Moment Calibration Curves and Calibration Factors for the RDD Load Cells

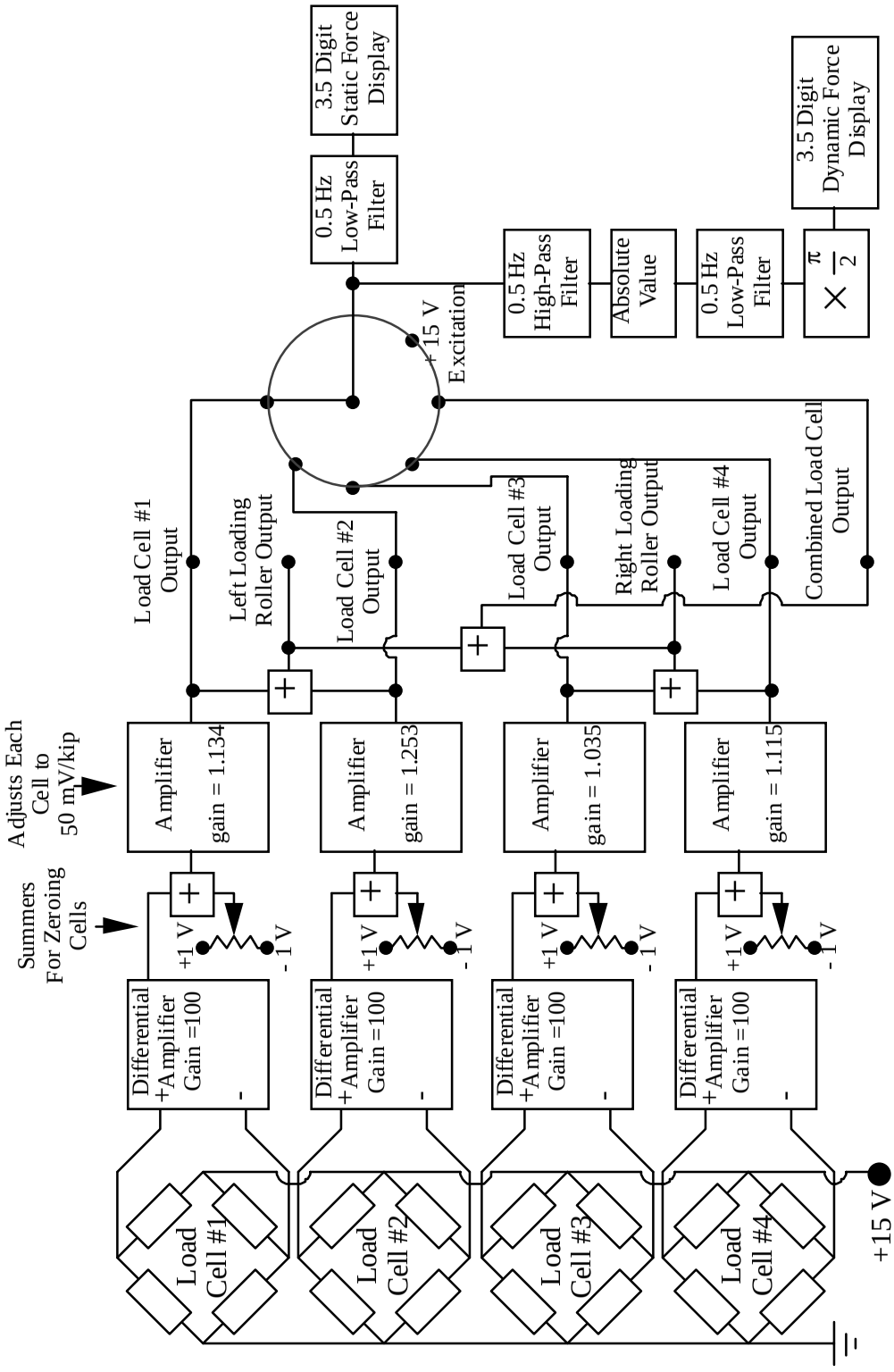

Figure 4.11 Flow Chart Showing the Operation of the Load Cell Conditioning Circuit

Next, the individual load cell outputs are summed to obtain combined loadings of interest. Load cells #1 and #2 are loaded through the left loading roller; therefore, their outputs are summed to obtain a signal proportional to the forces in the left loading roller. Similarly, load cells #3 and #4 are summed to obtain a signal proportional to the forces in the right loading roller. The combined signals from both rollers are then summed to obtain a signal proportional to the total force generated by the RDD loading system.

Each signal from the individual load cells, and the combined signal from the four load cells, goes to a rotary switch. This rotary switch is used to select a signal for the displays. The first display shows the static force. To obtain the static force, the signal is passed through a 0.5 Hz low-pass filter to remove all dynamic forces. This filtered signal is then input to a digital display with the appropriate scaling to display the force in units of kip. The second display shows the dynamic force. To obtain the dynamic force, the signal is passed through a 0.5 Hz high-pass filter to remove all static forces. The absolute value of the signal is then taken using a precision signal-processing rectifier circuit (Stanley 1984). This signal is then passed through a 0.5 Hz low-pass filter to remove its ripple and is amplified by a factor of $\frac{\pi}{2}$. This factor converts the average value of the dynamic signal, which is the output of the low-pass filter, to a peak value if the dynamic signal is sinusoidal.

4.4 POSSIBLE IMPROVEMENTS TO THE ROLLING DYNAMIC DEFLECTOMETER FORCE MEASUREMENT SYSTEM

The RDD force measurement system functions quite well and provides good results. However, there are improvements that could be made to the system. This section discusses two such improvements.

4.4.1 Inertial Compensation for Loading Roller Motions

The RDD load cells do not measure the forces applied to the pavement; rather, they measure the forces applied to the loading roller. The force actually applied to the pavement is affected by the vertical motion of the loading rollers. One method that could be used to determine the exact force applied to the pavement is to provide inertial compensation for the vertical motion of the loading rollers to the load cell output signals. This approach is very similar to the inertial force measurement approach presented in Section 4.2. One loading roller and its load cells are shown in Figure 4.12 to illustrate this approach.

The actual force applied to the pavement in this model can be calculated using the following equation:

$$f_p = (f_{lc1} + f_{lc2}) - \frac{a_{b1} + a_{b2}}{2} m_L \qquad \text{(Equation 4.3)}$$

where f_p is the vector of vertical dynamic force applied to the pavement
f_{lc1} is the vector of vertical dynamic force at load cell #1
f_{lc2} is the vector of vertical dynamic force at load cell #2
a_{b1} is the vector of vertical acceleration of bearing #1
a_{b2} is the vector of vertical acceleration of bearing #2
m_L is the combined mass of the loading roller, axles, and bearings

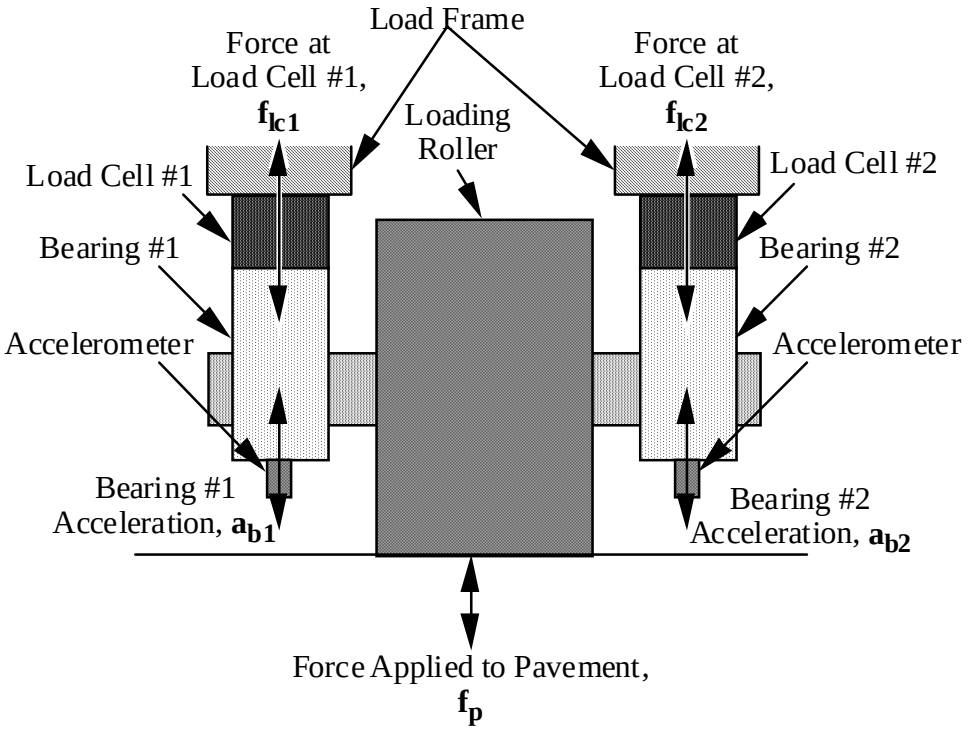

Figure 4.12 Drawing of Single Loading Roller Illustrating Inertial Compensation in the Dynamic Force Measurements

Inertial compensation for the loading roller mass could be achieved by applying an accelerometer to each bearing, as illustrated in Figure 4.12. The accelerometer output would then be scaled by a factor proportional to one-half the mass, m_L. This scaled signal would then be summed with the output of the load cell attached to that bearing. Care would need to be taken to assure that the proper polarities of load cell and accelerometer signals were summed. The scaling and summing of these signals could be performed using the operational amplifiers in the load cell conditioning box that are used to zero the load cell signals. The new force measurement system would require calibration to assure that all signals are scaled properly and to assure that the simplified model described by Equation 4.3 adequately represents the real system.

4.4.2 Shear Beam Load Cells

A somewhat simpler load cell design could be employed if an RDD loading frame were being constructed from the ground up. This approach was not taken for the existing RDD because the decision to add load cells was not made until the loading frame had already been constructed.

Simple and robust load cells could be made by incorporating instrumented shear beams into both ends of the bearing supports. Figure 4.13 shows a side view and a top view of a bearing support with four shear beams incorporated into the bearing supports.

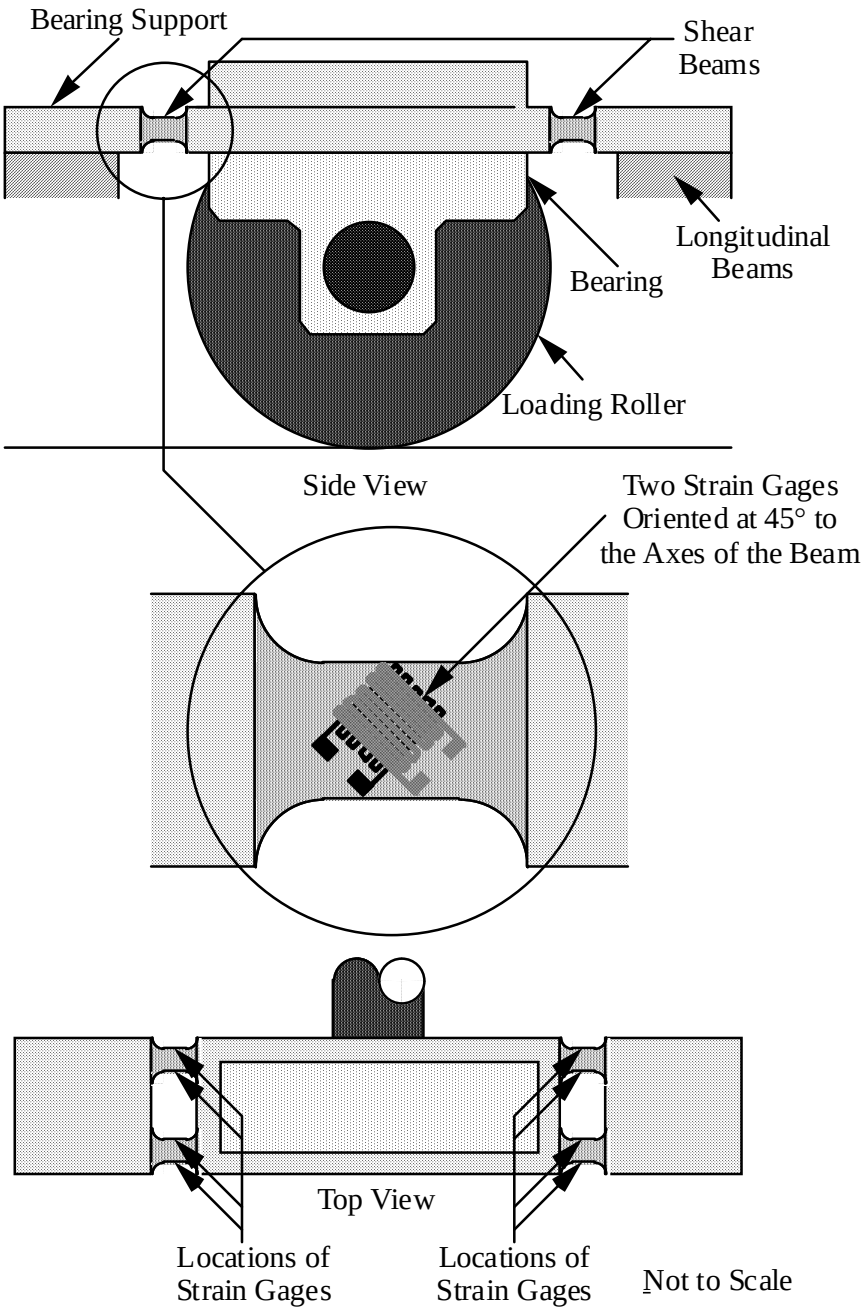

Figure 4.13 Side and Top Views of Bearing Supports Incorporating Shear-Beams Load Cells

Shear type strain gauges would be attached to both sides of each shear beam. This type of strain gauge has two grids laminated together, one on top of the other, such that their grids are perpendicular to each other. These composite strain gauges are attached to the beam so that both their grids are at a 45° angle to the axis of the beam. When the two laminated strain gauges are connected to adjacent legs of a Wheatstone bridge, they will sense only shear stress perpendicular to the axis of the beam. By incorporating the strain gauges from both ends of the bearing support into the same bridge, the bridge output will sense only the vertical force acting on the bearing support. The bridge output will be independent of axial forces, the distribution of vertical forces, and moments acting on the bearing support.

This approach to measuring forces is simpler than the load cell approach described in Section 4.3 and allows for more ground clearance for the loading rollers with the loading system raised. The disadvantage to the shear beam load cell is that it cannot be removed from the RDD for repairs.

4.5 SUMMARY

The RDD initially used an inertial approach to measure the vertical dynamic force applied to the pavement by the loading rollers. This inertial approach is the same approach used in traditional Vibroseis testing. However, after preliminary testing it was determined that the inertial approach was not producing satisfactory results for RDD testing. Load cells were added to the RDD loading system to improve the RDD force measurement. Because load cells for the RDD must have a unique geometry and robust structural properties, custom load cells were designed, constructed, and calibrated to measure the static and dynamic forces applied to the pavement by the RDD. Electronics were designed and built to provide excitation and conditioning for the load cell signals. While the load cells have the capacity to measure both vertical and horizontal forces, only the vertical measurement has currently been incorporated into the data acquisition system.

Finally, although the current RDD force measurement system is performing adequately, further improvements could be made to the system. Slight increases in accuracy could be obtained by adding an inertial compensation system to account for inertial losses in the loading rollers. On future devices, a simpler shear-beam load cell could be incorporated into the loading frame.

CHAPTER 5. DEVELOPMENT OF THE ROLLING DYNAMIC DEFLECTOR ROLLING SENSOR

5.1 INTRODUCTION

The rolling dynamic deflectometer (RDD) has three fundamental tasks. First, it must apply a moving, vertical, dynamic force to the pavement. This aspect is covered in Chapter 3. Second, it must measure the magnitude of the vertical dynamic force applied to the pavement. This aspect is covered in Chapter 4. Third, the RDD must provide a moving, vertical, dynamic displacement measurement of the pavement surface. The rolling sensors employed by the RDD to make moving displacement measurements are discussed in this chapter.

5.2 FACTORS AFFECTING PERFORMANCE OF ROLLING SENSORS

Dynamic displacement sensors that move along a pavement surface will measure undulations caused by roughness in the pavement, along with the dynamic displacements of the pavement owing to the RDD dynamic loading. This result applies to sensors that contact the pavement as well as to noncontacting sensors, such as lasers. RDD testing requires the measurement of displacements induced by the dynamic loading. The sensor output owing to pavement roughness, hereafter referred to as rolling noise, is an undesirable portion of the total signal. Typical dynamic displacements owing to the RDD dynamic load are less than 1 mm (40 mils). Even for very smooth pavements, the undulations owing to pavement roughness are greater than the induced dynamic displacements. Therefore, it is important that the RDD rolling sensors minimize the amount of rolling noise in the total signal. In this chapter, factors affecting rolling noise in the displacement signal are discussed.

Another requirement of the RDD rolling sensors is that they remain in contact with the ground so that they can sense the motion of stress waves in the pavement. Factors affecting roller contact and the constraints these factors place on the operation of the RDD are also discussed in this chapter.

Finally, the dynamic response of the RDD rolling sensor is another important consideration. The rolling sensor must be able to track the pavement motion, and displacement measurements must not be adversely affected by any resonances in the rolling sensor or any limitations on the maximum dynamic displacement measured by the sensors.

5.2.1 Rolling Noise

As a moving displacement sensor travels across a pavement surface, not only does it sense the vertical motion resulting from dynamic forces applied to the pavement, it also senses the apparent vertical motion caused by the pavement roughness. This apparent vertical motion is the rolling noise. Several strategies can be employed to minimize rolling noise, as discussed below. The strategies, of course, depend on the sensor in use. All of the rolling sensors used thus far with the RDD have been contacting sensors that consist of a wheeled carriage carrying either a velocity or acceleration transducer. Although other contacting and noncontacting sensors are possible, this discussion is limited to contacting wheeled sensors.

5.2.1.1 Effect of Wheel Diameter on Rolling Noise — As a wheel rolls over a rough surface, it contacts only the high points in the wheel path. The wheel pivots on each high point until another high point is contacted. Because of this pivoting, the path taken by the center of the wheel is a series of arcs, as shown in Figure 5.1. This figure shows a two-dimensional, synthesized cross section of a surface representing a rough pavement surface. Also shown in the figure are paths taken by the centers of two rigid wheels, one with a 2.5 cm (1 in.) diameter, and the other with a 7.6 cm (3 in.) diameter. Figure 5.1 shows that a wheel with a larger diameter moves through a smoother path than one with a smaller diameter.

To understand the effect of wheel diameter on rolling noise, the motion of a series of rigid wheels were modeled rolling over a 0.3 m (1 ft) length of the same synthesized pavement surface shown in Figure 5.1. This surface could be characterized as having a high point approximately every 0.7 cm (0.28 in.). The wheel diameters used were: 0, 2.5, 7.6, 15.2, 22.9, and 30.5 cm (0, 1, 3, 6, 9, and 12 in.). The wheel with a 0 cm diameter exactly tracks the pavement surface. The path traveled by the center of each wheel rolling over the synthesized pavement surface was calculated. The average vertical dynamic displacement of each path is defined as the average of the absolute value of the difference between the position of the center of the wheel and the mean wheel vertical position. The average vertical dynamic displacements for each of these wheels are shown in Figure 5.2. This figure shows a large reduction in vertical dynamic displacement as wheel diameter becomes just larger than the spacing between high points in the pavement. As the diameters become much larger, the reductions in vertical dynamic displacements are more moderate. For this particular pavement surface, wheels larger than 15.2 cm (6 in.) in diameter give small reductions in vertical dynamic displacement.

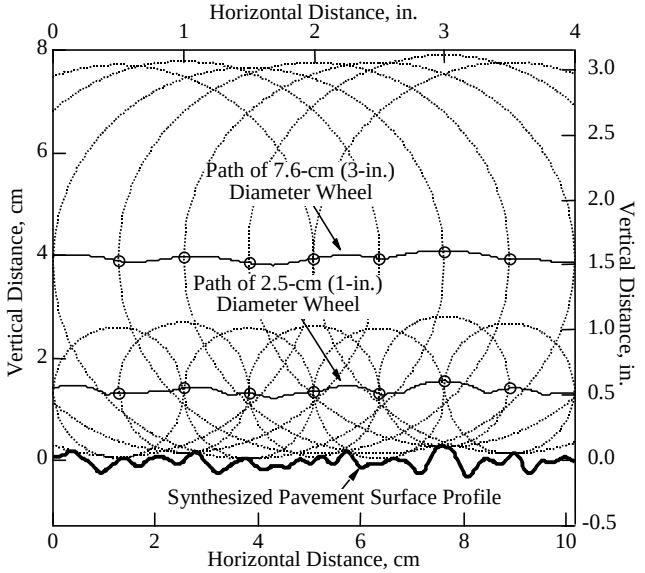

Figure 5.1 Paths of 2.5 cm (1 in.) and 7.6 cm (1 in.) Diameter Rigid Wheels over a Synthesized Surface of a Rough Pavement

For RDD testing, the frequency content of the rolling noise is more important than the total displacement resulting from the rolling noise. This is because filtering can eliminate rolling noise at frequencies distant from the RDD operating frequency. (This fact also makes the dynamic measurements with the RDD very robust.) The detrimental noise is that noise contained in a narrow band around the operating frequencies.

The effect of wheel diameter on the frequency content of the rolling noise was studied for the same wheel diameters shown in Figure 5.2, assuming a rolling velocity of 0.3 m/s (1 ft/sec). The calculated displacement spectra for the motion of the six wheels are represented in Figure 5.3. These spectra indicate that increasing wheel diameter dramatically decreases the rolling noise at high frequencies, but actually increases the noise level at low frequencies. For this synthesized pavement, the optimal benefit again accrues with a 15.2 cm (6 in.) diameter wheel. Figure 5.3 also shows that, for these operating conditions (pavement roughness and rolling velocity), using RDD operating frequencies greater than 30 Hz will also minimize the rolling noise.

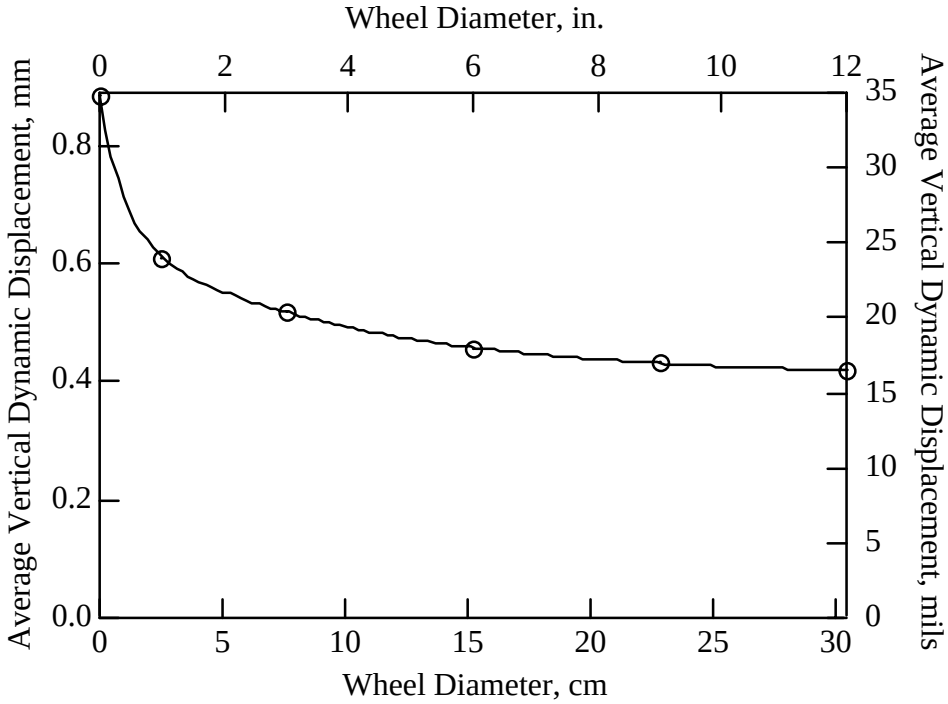

Figure 5.2 Average Vertical Displacements of Wheels with Various Diameters Rolling over the Synthesized Pavement Surface from Figure 5.1

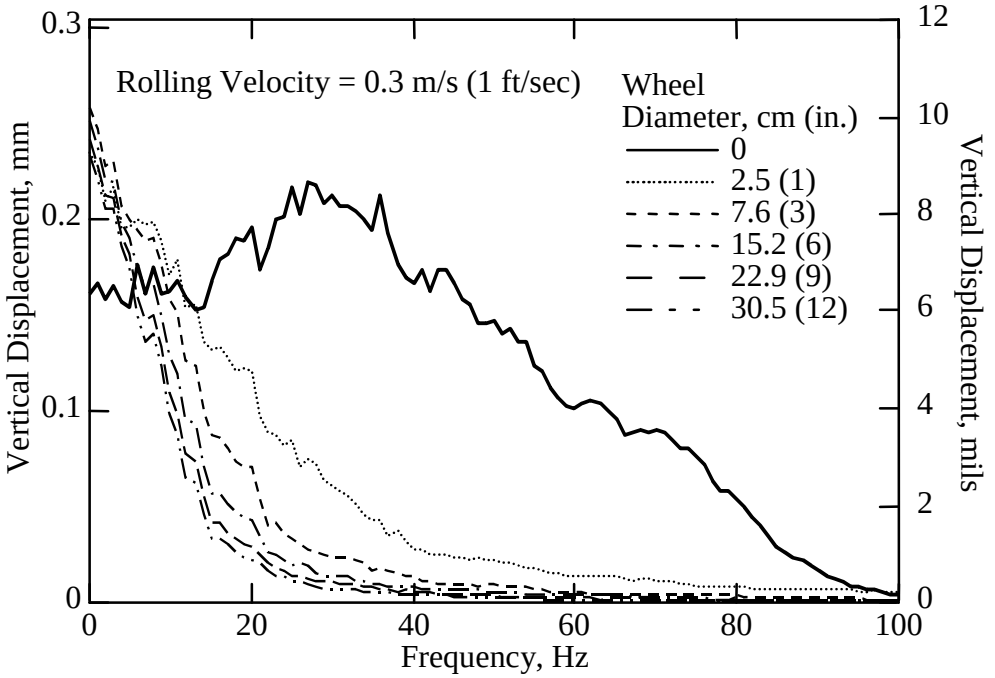

Figure 5.3 Vertical Displacement Spectra for Wheels with Various Diameters Rolling over the Synthesized Pavement Surface from Figure 5.1

5.2.1.2 Effect of Rolling Velocity on Rolling Noise — The velocity of a rolling sensor moving over a rough pavement surface also affects the rolling noise. If a rigid wheel always remains in contact with the pavement (as it should), then the actual vertical displacement of the wheel will be unaffected by the rolling velocity. However, the frequency content of the displacement will be affected. Doubling the rolling velocity will double the frequency of the rolling noise. This is exactly the same effect that is achieved by playing a phonograph record at higher speeds.

Figure 5.4 shows spectra from a rigid, 15.2 cm (6 in.) diameter wheel rolling at various speeds over the synthesized pavement surface from Figure 5.1. This figure shows that higher rolling velocities require a higher RDD operating frequency to maintain the same rolling noise level. The highest possible operating frequency for the RDD is 100 Hz. This limits the RDD rolling velocity to less than about 0.6 m/s (2 ft/sec) for relatively quiet displacement measurements.

5.2.1.3 Effect of Number of Wheels on Rolling Noise — One approach to minimizing rolling noise is to use more than one wheel to support the displacement transducer. For this approach to be effective, all wheels must remain in contact with the ground at all times, and the sensor must be arranged so that the vertical motion of the transducer is equally affected by the vertical motion of each wheel. Also, the spacings between wheels must be small relative to the wavelengths of the waves generated by the RDD, so that all the wheels move in phase with each other as a result of the RDD excitation. This approach reduces the rolling

noise because the “random” pavement roughness encountered by each wheel is independent of the roughness encountered by the other wheels, and therefore the displacement owing to the combined motion of several wheels will cancel. On the other hand, the stress waves generated by the RDD encounter each wheel at the same time, adding constructively.

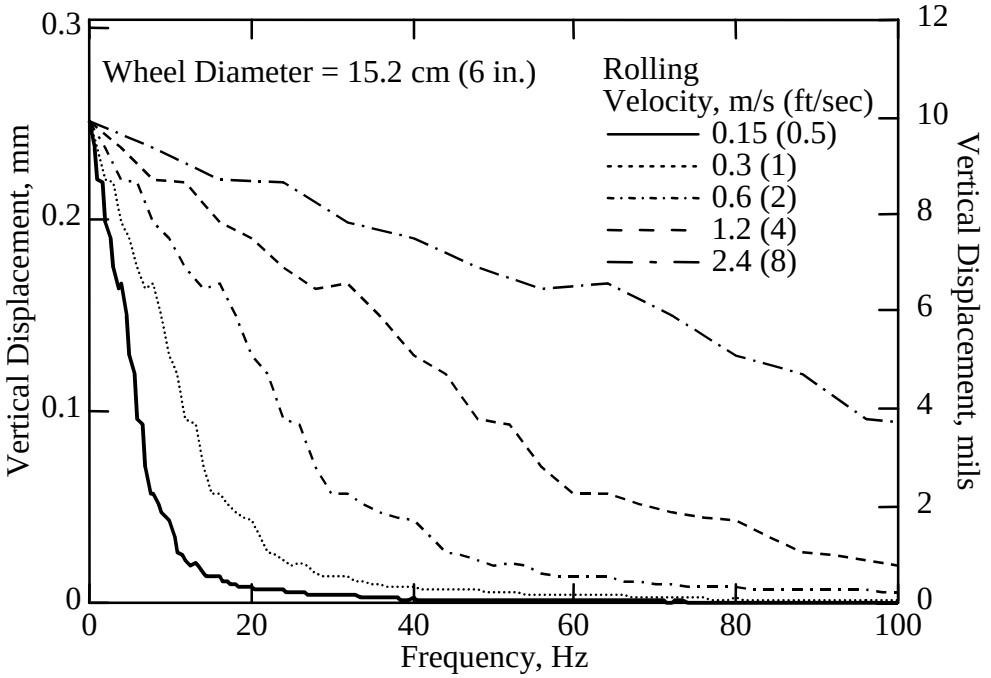

Figure 5.4 Vertical Displacement Spectra for 6-Inch Diameter Wheels Rolling over the Synthesized Pavement Surface from Figure 5.1 at Various Rolling Velocities

Five additional synthesized pavement surfaces, like the one in Figure 5.1, were generated to study the effect of multiple wheels. Each of the pavement surfaces is “random” and independent of the other pavement surfaces, but has the same average properties. The motion of a 15.2 cm (6 in.) diameter rigid wheel was modeled rolling over each of these synthesized surfaces. The combined motion for one to six wheels was then determined. The average vertical dynamic displacement from these tests is shown in Figure 5.5. There is more scatter in these results than in the previous results, because the combined motion of several wheels is a statistical rather than a mechanistic result. However, a consistent trend is evident: More wheels yield lower vertical dynamic displacements.

Again, the frequency content of the rolling noise is more important than the total displacement of the rolling noise. Spectra were calculated for the combined wheel motion assuming a rolling velocity of 0.3 m/s (1 ft/sec). These spectra are presented in Figure 5.6. The effect of increasing the number of rolling wheels on the frequency content of the rolling noise is very different from the effect of increasing the wheel diameter. The decreases in

rolling noise are more pronounced at low frequencies than at high frequencies. This means that the primary benefit of more wheels is that it might allow for slightly lower operating frequencies, or possibly somewhat higher rolling velocities.

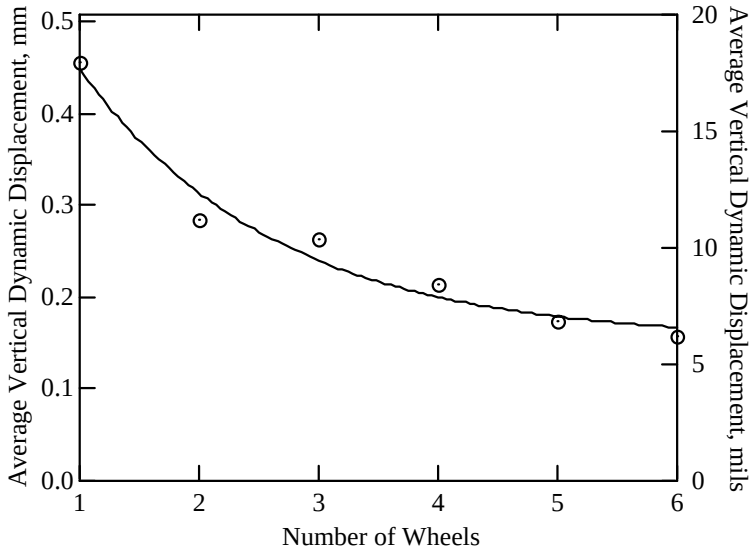

Figure 5.5 Average Combined Vertical Displacements from One to Six, 15.2 cm (6 in.) Diameter Rigid Wheels Rolling over Synthesized Pavement Surfaces Similar to That in Figure 5.1

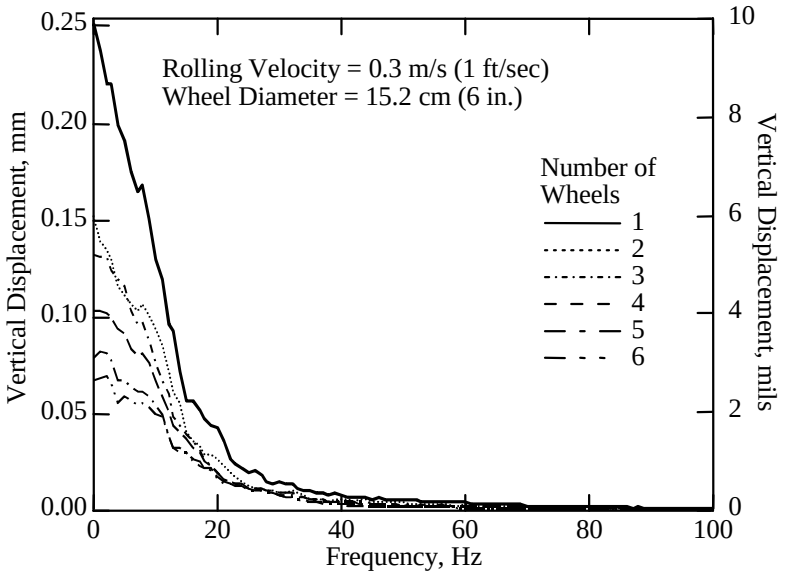

Figure 5.6 Combined Vertical Displacements Spectra from One to Six, 15.2 cm (6 in.) Diameter Rigid Wheels Rolling over Synthesized Pavement Surfaces Similar to That in Figure 5.1

The placement of the wheels is critical for obtaining the full benefit of multiple wheels on a rolling sensor. For instance, if two or more wheels encounter the same pavement feature, such as a joint, simultaneously, then there will be less reduction in noise at the transducer. Or, if a pavement feature has a regular spacing, such as tining, and the spacing between two or more wheels is a multiple of this regular spacing, again there will be less noise reduction at the transducer. Care must be taken to avoid wheel geometries where these problems would occur.

5.2.1.4 Effect of Wheel Width on Rolling Noise — The width of the wheels on a rolling transducer will also affect the rolling noise. A "wide," rigid wheel will have only a single contact point, just like the two-dimensional wheels modeled to this point. The advantage of a wider wheel is that it has a wider path. It should contact more high points across its wide path than a narrower wheel would. This means the wider wheel will experience less vertical displacement.

Different roller widths were modeled using a synthesized three-dimensional pavement. Figure 5.7 shows a 30.5 cm by 7.6 cm (12 in. by 3 in.) strip of a three-dimensional pavement model that is continuous in both horizontal directions. Rigid, 15.2 cm (6 in.) diameter wheels with widths of 0, 2.5, 5.0, and 7.6 cm (0, 1, 2, and 3 in.) were modeled rolling over this surface. The average vertical dynamic displacements from these tests are shown in Figure 5.8.

Figure 5.8 indicates some reduction in rolling noise as the wheel width becomes wider than zero, but the results for the 2.5, 5.0, and 7.6 cm (1, 2, and 3 in.) wide wheels are essentially identical. The spectra from these tests are shown in Figure 5.9. The spectra indicate a reduction in low-frequency displacement for the three rollers with nonzero widths; however, there does not appear to be any benefit at high frequencies or any benefit for wheels wider than 2.5 cm (1 in.).

This study indicates that no significant reduction in rolling noise is achieved by using wheels wider than 2.5 cm (1 in.) on a rolling sensor. Efforts would be better spent on increasing the wheel diameter or the number of wheels.

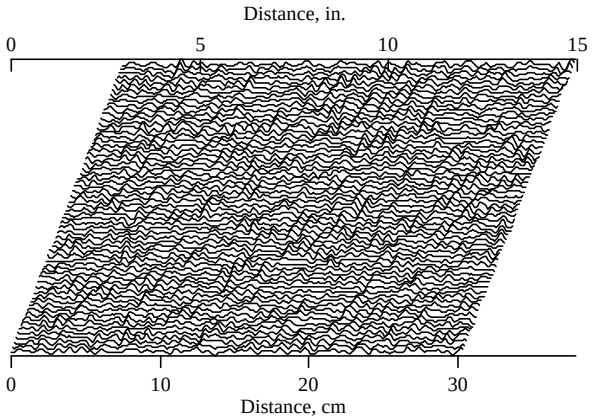

Figure 5.7 Synthesized Three-Dimensional Pavement Surface Used To Evaluate Effect of Wheel Width on Rolling Noise

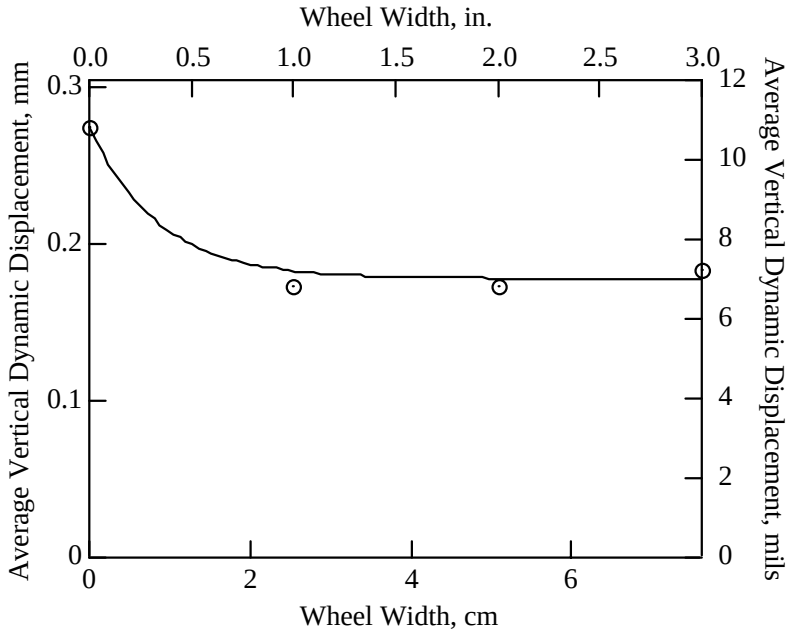

Figure 5.8 Average Vertical Displacements from a 15.2 cm (6 in.) Diameter Rigid Wheel of Various Widths Rolling over the Synthesized Pavement Surface in Figure 5.7

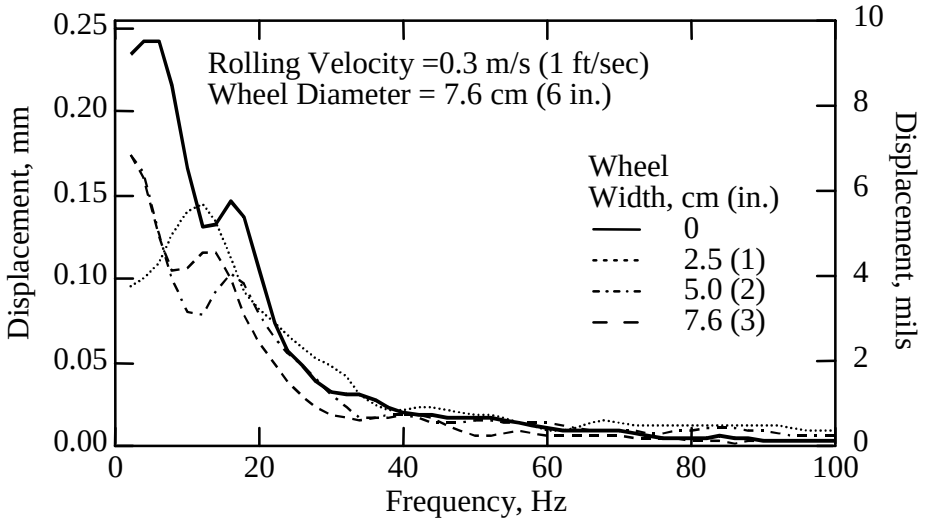

Figure 5.9 Vertical Displacement Spectra from a 15.2 cm (6 in.) Diameter Rigid Wheel of Various Widths Rolling over the Synthesized Pavement Surface in Figure 5.7

5.2.2 Sensor Contact

It is very important that the rolling sensor wheels remain in contact with the pavement surface at all times during testing. The wheels have a tendency to "bounce" off the ground while rolling at high velocities. If the only force holding the sensor to the ground is gravity, then the downward acceleration of the wheels should never exceed the acceleration of gravity if the wheel is always to remain in contact with the ground. Accelerations are shown in Figure 5.10 for a 15.2 cm (6 in.) diameter wheel rolling over the synthesized pavement surface shown in Figure 5.1 at 0.3 m/s (1 ft/sec). This figure also shows the synthesized pavement surface profile (with 4× vertical exaggeration) and the wheel displacement. A comparison of the wheel displacement and the wheel acceleration shows that the wheel experiences a constant, negative acceleration while the wheel path is traveling in an arc. However, between these arc paths the wheel experiences high positive accelerations. The arc paths represent the wheel travel while it is pivoting on a single high point, and the transitions between arcs represent the instant that the wheel encounters a new high point.

The constant negative acceleration shown in Figure 5.10 presents a possible problem for an RDD rolling sensor. In this case, the negative acceleration has a magnitude of -0.124 g. If this value were -1 g, the force between the sensor and the ground would be zero, resulting in no coupling between the sensor and the ground surface. This is especially detrimental to RDD testing because the negative acceleration persists nearly all the time, with very short instances when the wheel experiences a positive acceleration and a coupling force. This means that if -1 g is exceeded, the sensor would almost never sense the dynamic motion induced by the RDD. Therefore, it is critical that the RDD is operated in such a way that the rolling sensors never experience -1 g.

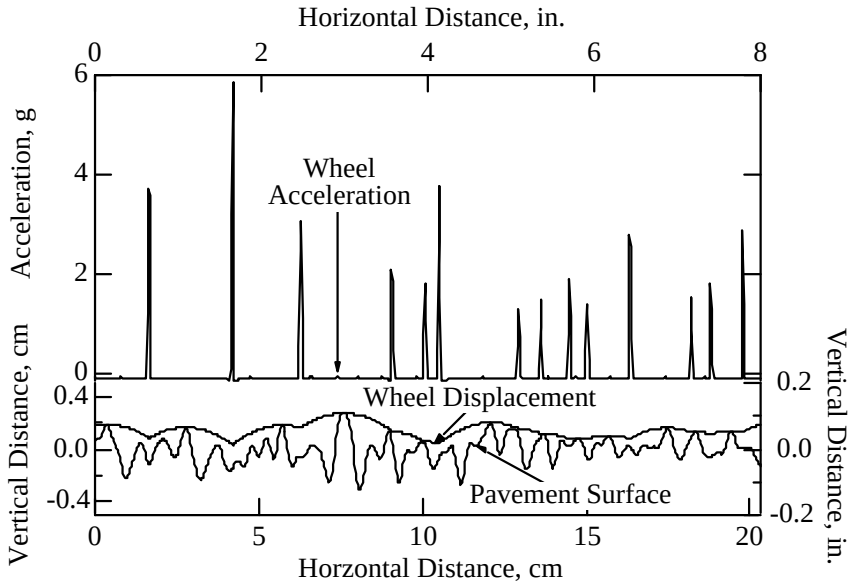

Figure 5.10 Acceleration and Displacement of 6-Inch Diameter Wheel Rolling over Synthesized Pavement Surface at 1 ft/sec

The circular arc paths in which the wheel travels approximate parabolic arcs very closely. A body travels in a parabolic arc only when subjected to a constant acceleration. Figure 5.11 shows a wheel rolling over a high point. If the height of the high point, *h*, is much smaller than the wheel radius, *r*, then the acceleration of the wheel can be calculated using the following equation:

$$\frac{d^2y}{dt^2} = \frac{-1}{r} V^2 \qquad \text{(Equation 5.1)}$$

where $\frac{d^2y}{dt^2}$ is the vertical acceleration

r is the wheel radius

V is the rolling velocity

It should be observed that the height of the high point, *h*, is not a factor in the acceleration level of the wheel. This means that contact problems are independent of the roughness of pavement. The only factors affecting the wheel acceleration are the wheel radius and the rolling velocity. Acceleration levels are plotted relative to wheel diameters and rolling velocities in Figure 5.12. The figure also shows two possible maximum negative acceleration level criteria of 0.5 g and 1.0 g. Using the conservative criteria of -0.5 g, and a rolling sensor wheel diameter of 15.2 cm (6 in.), the rolling velocity should never exceed 0.6 m/s (2 ft/sec).

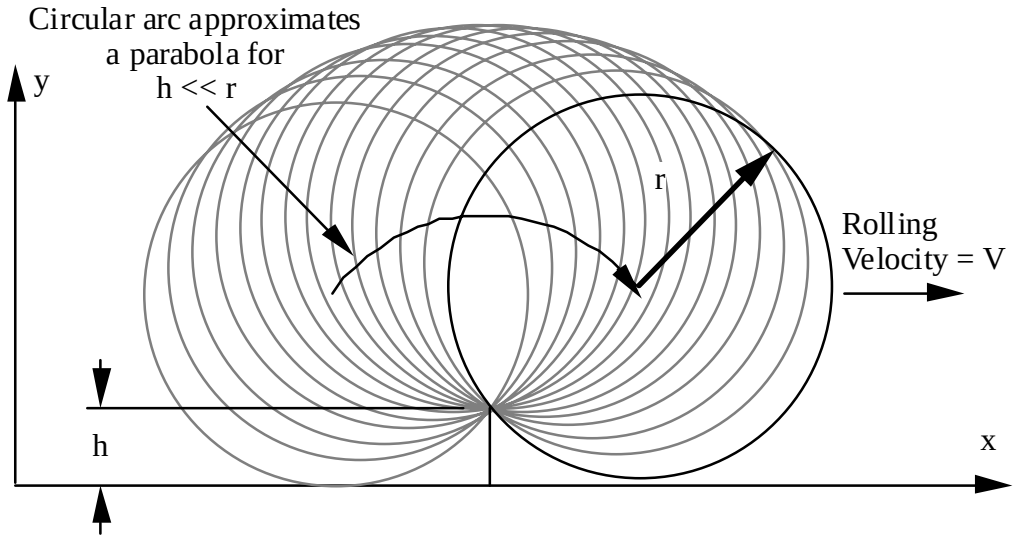

Figure 5.11 Wheel Rolling over a High Point with a Circular Arc Path

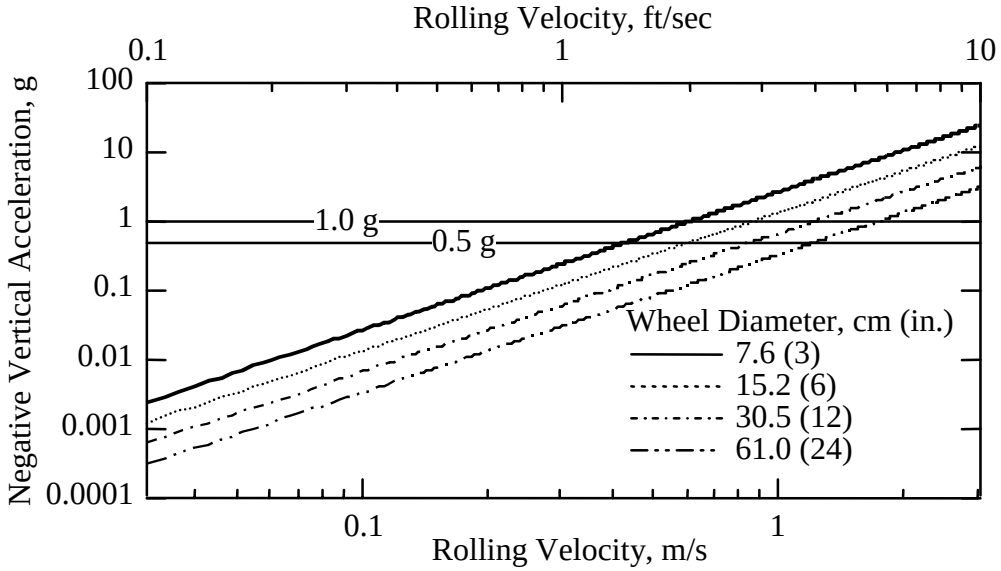

Figure 5.12 Negative Acceleration Levels Relative to Wheel Diameter and Rolling Velocity

5.2.3 Roller Stiffness

All of the analyses thus far have assumed that the wheels of the rolling sensor are rigid. A rigid wheel, like a steel wheel, would have the undesirable consequence of experiencing high levels of high-frequency noise as it rolls over the pavement. Compared with a rigid wheel, a compliant wheel would have the benefits of lower rolling noise and a decreased tendency to lose contact with the ground. Therefore, a compliant wheel should be used for the rolling sensor, but using the rigid wheel assumptions for rolling noise and wheel contact will result in a conservative design.

The disadvantage of using compliant wheels is that they introduce a resonance to the sensor. The compliant wheels act like a damped spring supporting the sensor mass, which acts as a single-degree-of-freedom resonator. This resonance causes problems if it is too lightly damped and if it occurs in the range of RDD operating frequencies.

A compliant wheel was designed using a laboratory study. Prototype wheels were constructed by laminating urethane strips to cylindrical metal hubs. These prototype wheels were vibrated on a shake table, and the wheels' resonant frequency and the amplitude of the resonant peak were measured. Figure 5.13 shows the testing configuration used. The prototype wheel shown in Figure 5.13 is balanced on the shake table. The parameters, which were varied in the different tests, were: the hub diameter, the hub mass, the hub width, the urethane thickness, and the urethane durometer.

The results of these tests were extremely complicated. Counter-intuitive results often occurred. For instance, increasing the weight of the hub often increased the resonant frequency of the prototype system. In these cases, it is felt that the increased force acting on

the urethane increased the contact area between the wheel and the shake table, resulting in a stiffer system, with the increase in stiffness proportionally greater than the increase in mass. Similarly, decreasing the urethane stiffness also often increased the resonant frequency of a prototype wheel. This too was probably due to increased wheel contact area, resulting in increased stiffness.

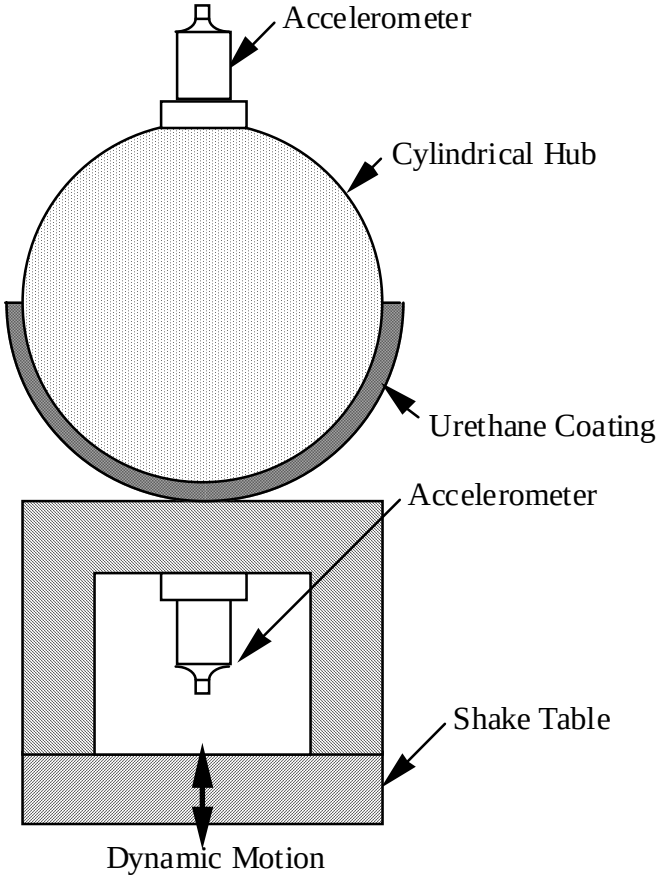

Figure 5.13 Test Configuration Used To Determine Dynamic Characteristics of Prototype Wheels

An attempt was made to establish an empirical relationship between the properties of the wheel and its resonant frequency; however, this proved to be very difficult. One important observation came from these tests. For a given hub diameter, mass, and thickness, high resonant frequencies (above 100 Hz) could be achieved by using stiff urethane, or very soft but relatively thin urethane. Furthermore, the resonances obtained with stiff urethane were lightly damped relative to those obtained with soft urethane. Using this observation,

specific combinations of hubs and soft urethanes were tested to design a wheel with a highly damped first-mode resonance above 100 Hz. This design is presented in Section 5.3.2.

5.2.4 Transducer Properties

The requirements for the transducer on the RDD rolling sensor are that the transducer accurately measure motions at frequencies from 10 to 100 Hz and that it be able to accurately track the combined sensor motion caused by rolling noise and the induced stress waves. Several types of transducers could be used to measure displacements on the RDD rolling sensor. Transducers that measure displacement, velocity, or acceleration all would work; however, velocity and acceleration transducers have the advantage of using an inertial reference, while displacement transducers require a position reference. A position reference is difficult to establish on a moving and vertically shaking truck.

The very first transducer used was a PCB model 308B02 accelerometer. This accelerometer is capable of measuring the low frequencies generated by the RDD and the required range in motion. Accelerometers, however, are extremely sensitive to high frequencies and generate high output for high-frequency motion, even if the displacements at those frequencies are very low. Some high-frequency noise is generated with a rolling sensor. When using an accelerometer, much of the signal is high-frequency noise. Because the recording equipment needs to resolve the noise and the signal, this high level of noise leaves less resolution for the signal, resulting in a lower-quality displacement measurement.

A better transducer for the RDD rolling sensor is a velocity transducer, such as a geophone or seismometer. The next transducer used was a Mark Products Model L15-B, 4.5-Hz geophone. This transducer performs well over the operating frequency range of the RDD and is not as sensitive to high-frequency noise as an accelerometer. However, the peak-to-peak coil motion of the L15-B is only 2 mm (80 mils), typical of most small, inexpensive geophones. When the geophone motion exceeds 2 mm (80 mils) peak-to-peak (p-p), it will drive the coil stop-to-stop, resulting in a distorted waveform. This distortion can be quite subtle and difficult to detect in the geophone output signal. The 2 mm (80 mil) p-p motion is more displacement than would be expected from the vertical motion induced by the RDD; however, when rolling noise is added in, this displacement could be exceeded.

The final transducer used for the RDD rolling sensor was a low-frequency velocity transducer, often called a seismometer. A Mark Products Model L22-E, 2 Hz seismometer was selected. This transducer is similar to a geophone, except that the resonant frequency is lower than that for typical geophones and the coil has a peak-to-peak coil motion of 12.7 mm (500 mils). This large coil motion assures that the transducer will measure the combined dynamic RDD motions and noise signal with no distortion in the waveform.

5.3 ROLLING SENSOR DESIGNS

Two different rolling sensors have been developed for the RDD. The first sensor was an expedient design. It utilized parts commercially available to construct a rolling sensor quickly and inexpensively. The experience gained with this sensor was used in designing the second generation (and presently used) sensor.

5.3.1 First-Generation Rolling Sensor

The first-generation rolling sensor was a two-wheeled sensor that was supported by a trailing arm attached to the truck frame. Front and side views of the first-generation rolling sensor are shown in Figure 5.14.

The wheels used for the first-generation rolling sensor were 30.5 cm (12 in.) diameter heavy-duty steel wheels. These wheels were coated with a 1.3 cm (0.5 in.) layer of 90A durometer urethane. The wheels rotated on roller bearings.

The rolling sensor was isolated from vehicle vibrations with a number of rubber vibration isolators and the pivot on the trailing arm. These measures provided very good vibration isolation.

One very convenient feature of the first-generation rolling sensor was the way it was lowered for testing and raised for transport. When raised, longitudinal beams on the loading frame would pivot the trailing arm upward, automatically raising the rolling sensor high off the ground. When the RDD loading system was lowered for testing, the trailing arm would again automatically pivot downward until the rolling sensor contacted the ground.

The geophone on the first-generation rolling sensor was calibrated by vertically driving the entire rolling sensor on a shake table to determine the frequency response of the system. This calibration curve is shown in Figure 5.15. The rolling sensor approximates a viscously damped, single-degree-of-freedom resonator. The resonant frequency of the system is 63 Hz, with the motion amplified by a factor of about 8 times at resonance. This represents a damping factor, D, of 5.5 percent of critical damping.

There were a number of weaknesses in the first-generation rolling sensor. The most glaring weakness was its dynamic response. Its resonant frequency at 63 Hz fell right in the middle of the RDD operating frequency range. The low damping aggravated this problem.

Moreover, this rolling sensor design was not conducive for use with multiple rolling sensors. Multiple sensors would require independent trailing arms, for which there is insufficient space on the RDD.

The side-by-side wheel arrangement on the first-generation rolling sensor means that both wheels will encounter tining and joints simultaneously. This negates some of the noise reduction benefits of multiple wheels, as discussed in Section 5.2.1.3.

5.3.2 Second-Generation Rolling Sensor

A new, second-generation RDD rolling sensor was designed to address the problems experienced with the first-generation sensor. This rolling sensor used custom-made wheels and involved more custom machining to optimize its performance. This rolling sensor is a freestanding, three-wheeled sensor that does not require the support of trailing arms. Plan and side views of this rolling sensor are shown in Figure 5.16. A photograph of the second-generation rolling sensor is shown in Figure 5.17.

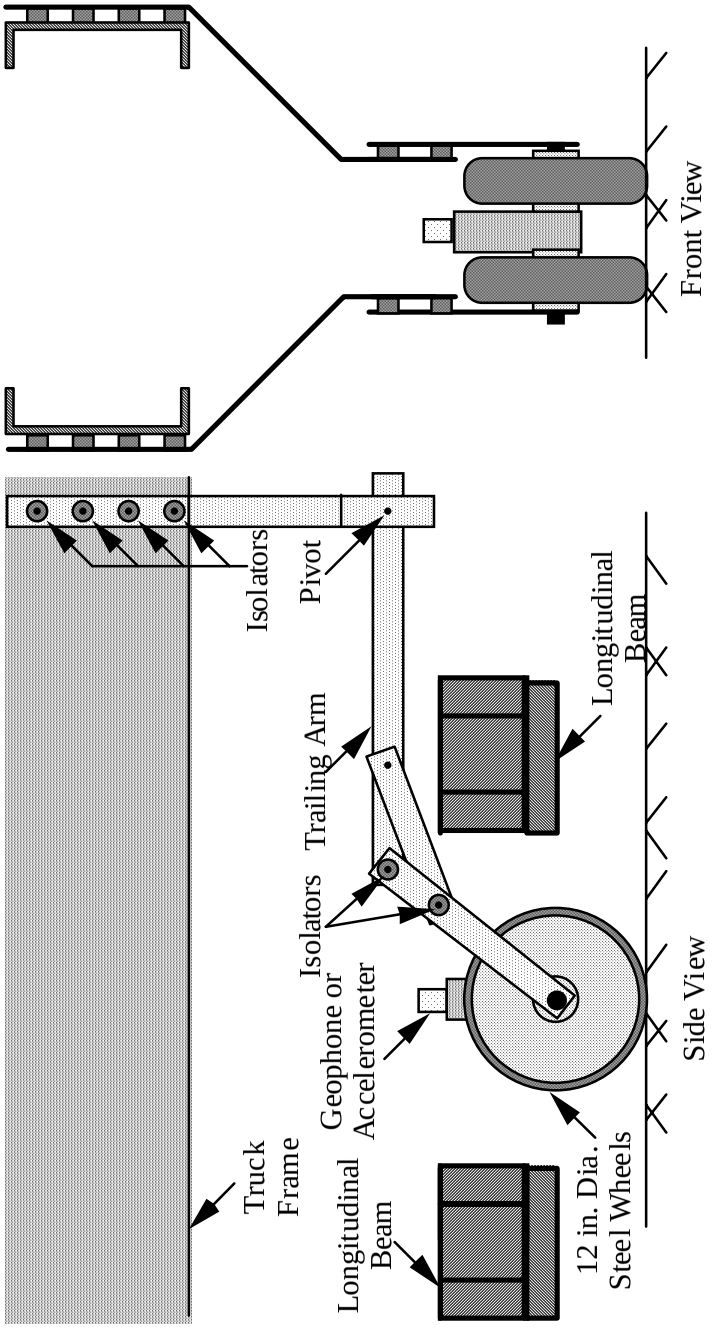

Figure 5.14 Front and Side Views of the First-Generation RDD Rolling Sensor

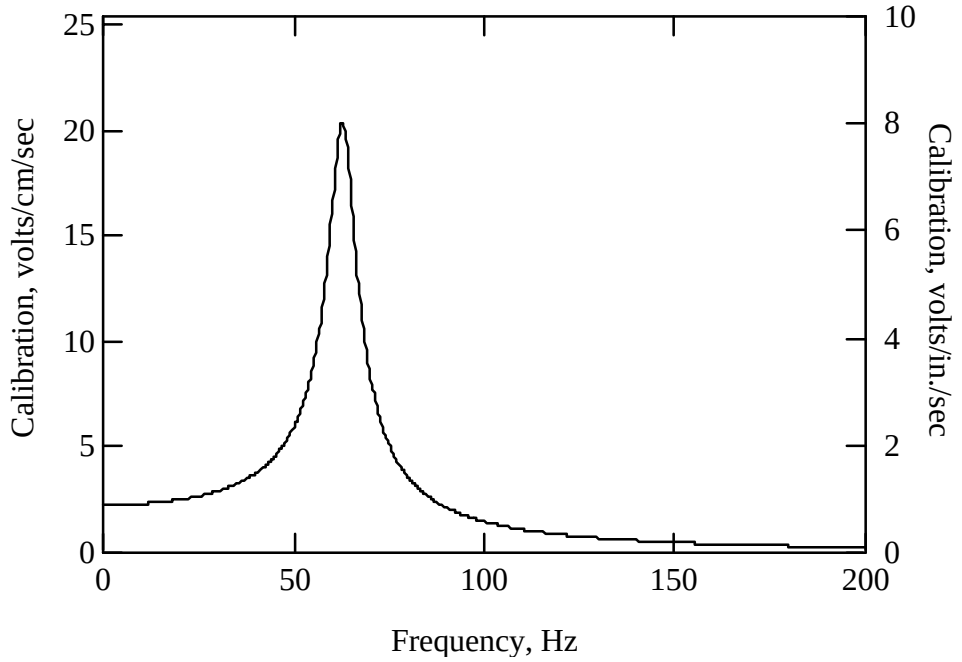

Figure 5.15 Calibration Curve for First-Generation Rolling Sensor with a Mark Products L15-B, 4.5 Hz Geophone as Its Transducer

Four second-generation RDD rolling sensors were constructed. The second-generation rolling sensor uses 15.2 cm (6 in.) diameter wheels. This diameter was selected because of the reduced levels of rolling noise associated with this wheel size, as explained in Section 5.2.1.1. A wheel width of 2.5 cm (1 in.) was selected based on the findings presented in Section 5.2.1.4. Three wheels were selected to obtain the rolling noise reduction benefits discussed in Section 5.2.1.3. The wheels are positioned so that no two wheels encounter transverse joints simultaneously. Furthermore, the wheels are positioned so that the distance between any two wheels is different and so that the spacings have few common factors. This prevents the wheels from simultaneously encountering regularly spaced pavement features, such as tining.

The transducer selected for this rolling sensor was a Mark Products L22-E seismometer, as discussed in Section 5.2.4. The transducer is positioned at a location equidistant from the three wheels so that its vertical motion will be the average of the vertical motion of the three wheels.

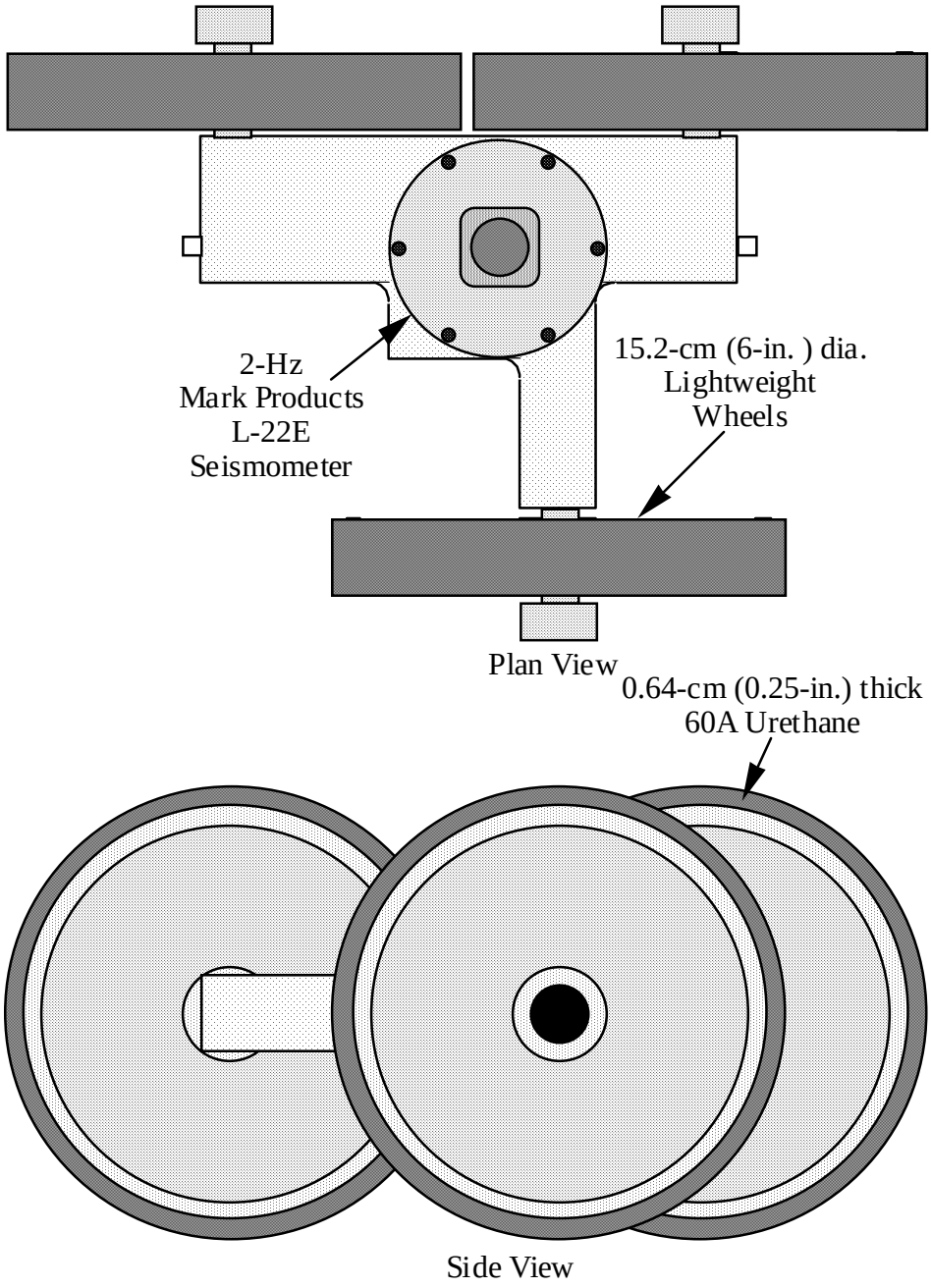

Figure 5.16 Plan and Side Views of Second-Generation RDD Rolling Sensor

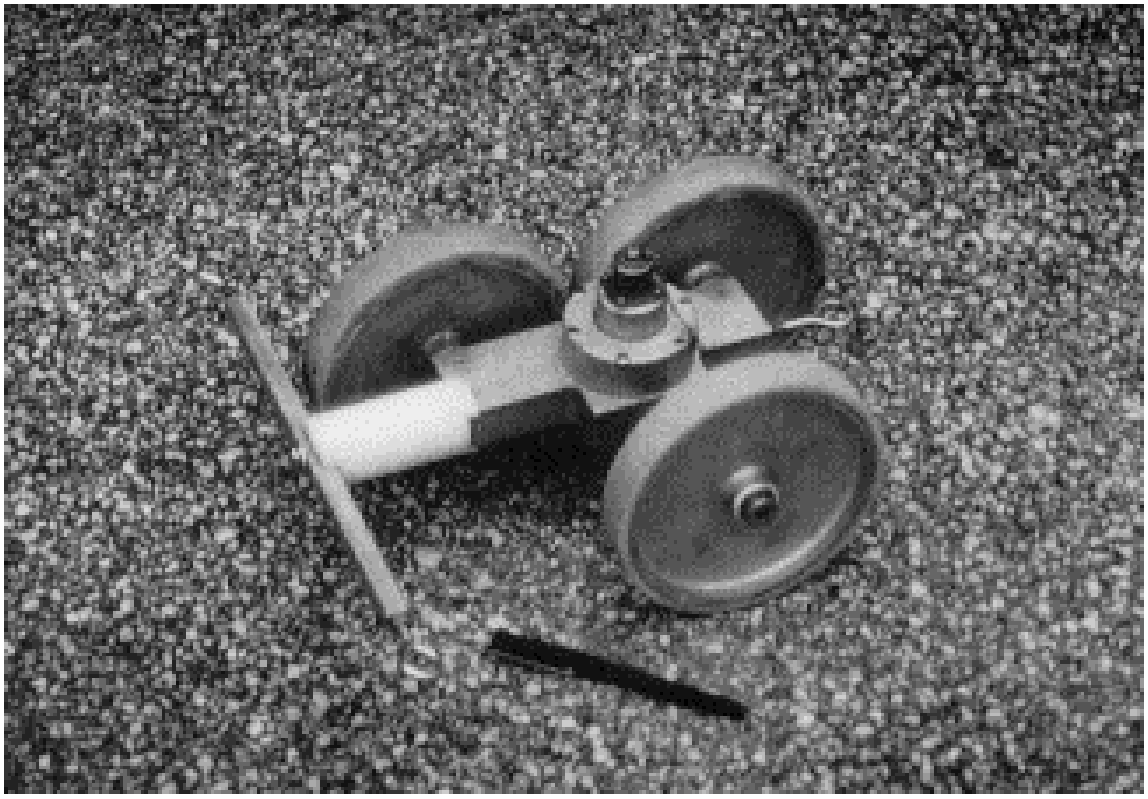

Figure 5.17 Photograph of Second-Generation RDD Rolling Sensor

The wheels were designed to be lightweight to increase the resonant frequency of the system. They are machined from 6061T aluminum with 0.64 cm (0.25 in.) thick webs and flanges. The wheels had a 0.64 cm (0.25 in.) coating of very soft, 60A durometer urethane cast on their rolling surface. This thickness and durometer of urethane was selected experimentally, as discussed in Section 5.2.3. The goal was to use a combination of sensor, mass, wheel diameter, and stiffness to achieve a highly damped first-mode resonance above 100 Hz.

The calibration curves for the four rolling sensors are shown in Figure 5.18. Two curves are presented for each rolling sensor. The first is the sensor unfiltered output. It is designated as the "Filter Out" curve. The other curve is the filtered output, and it is designated as the "Filter In" curve. The filtered signal was passed through a custom-made passive single-pole, 8 Hz high-pass filter and an attenuator. The purpose of the filter is to reduce the low-frequency rolling noise. The purpose of the attenuator is to avoid sending voltages that are too large for the data acquisition system ($-5\ V \leq voltage \leq 5\ V$).

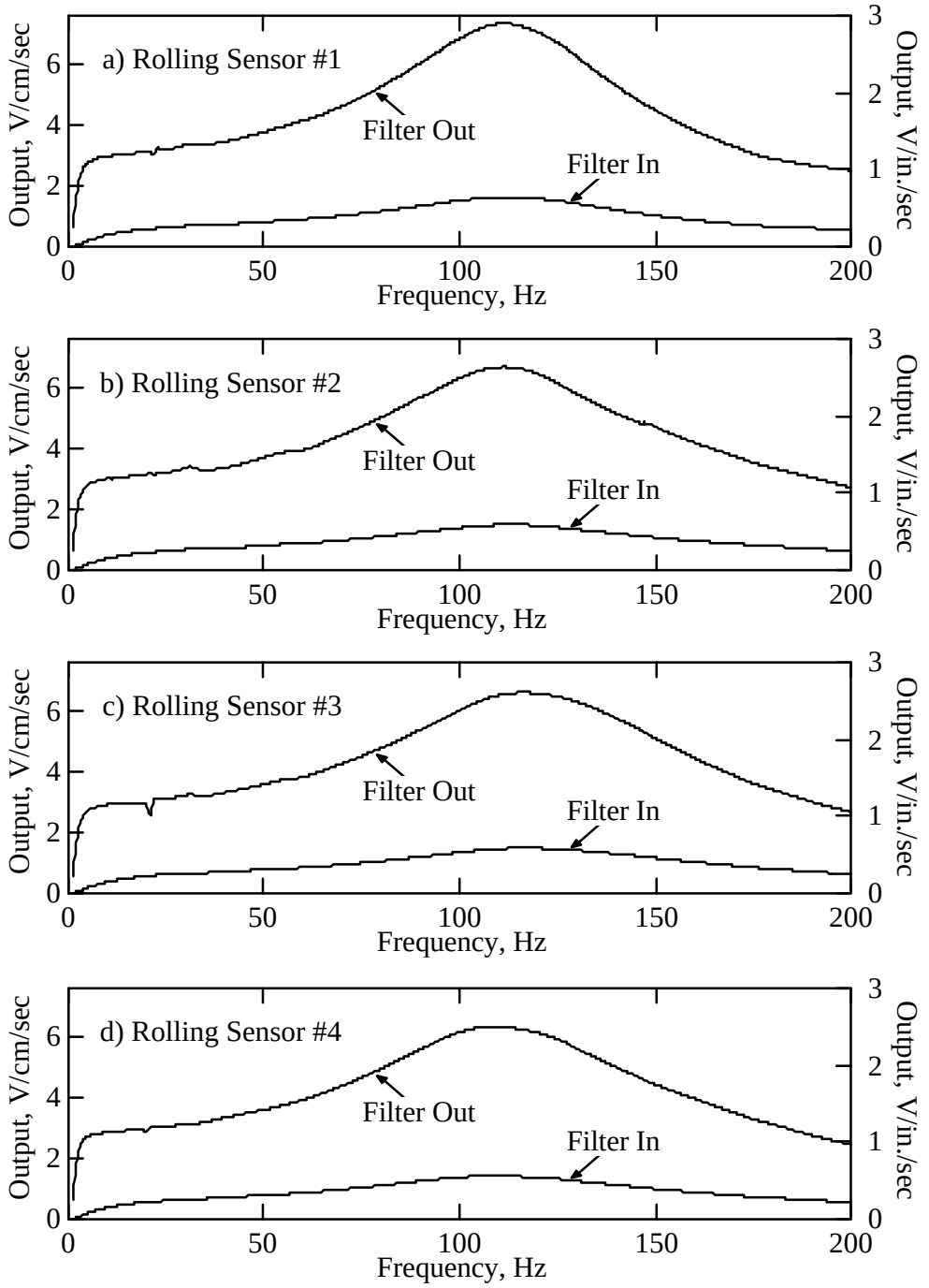

Figure 5.18 Calibration Curves for Second-Generation RDD Rolling Sensors

The first-mode resonant frequency of the second-generation rolling sensors is about 110 Hz, with an amplification factor at resonance of about 2.2. This indicates the damping ratio, D, is about 23.3 percent. This is a substantial improvement over the first-generation sensor and meets the design criteria.

The second-generation rolling sensors place one major limitation on RDD operation. To maintain contact with the pavement, rolling velocities must be limited, as discussed in Section 5.2.2. If the maximum downward acceleration caused by rolling over discontinuities is limited to 0.5 g, then according to Equation 5.1 and Figure 5.12, the maximum allowable rolling velocity is 2.0 ft/sec. This slow rolling velocity also serves to minimize the rolling noise at RDD operating frequencies, as discussed in Section 5.2.1.2.

5.3.3 Rolling Sensor Towing System

The second-generation rolling sensor is a freestanding sensor that requires no external support. However, it requires a towing system to pull the sensors along with the RDD. It is important that this towing system is isolated from the truck vibrations and that it does not contribute to coupling between the vertical movement of multiple rolling sensors. It is also important that the towing system allow flexibility in positioning the rolling sensors so that the sensor configurations can be customized according to the testing requirements.

Side and plan views of the rolling sensor towing system are shown in Figure 5.19. The towing system consists of a frame with attachment points, to which cables pulling the rolling sensors are attached. The frame is supported by four castors and attached to the truck frame with two pivot arms. Two bars pass just above the loading frame. In this configuration, the bars lift the towing system and rolling sensors off the ground when the loading system is raised. The entire system is constructed of 2.5 cm by 2.5 cm (1 in. by 1 in.) aluminum bar. A photograph of the rolling sensor towing system with sensors attached is shown in Figure 5.20.

The rolling sensors must be tied to the frame from the front, both sides, and the rear to hold them in the proper position relative to the loading rollers. Figure 5.21 shows some possible rolling sensor positions. These are just a few possibilities. Pairs of rolling sensors can be positioned to straddle longitudinal joints or any number of other configurations to obtain the required information about a given pavement.

5.4 POSSIBLE IMPROVEMENTS TO ROLLING DYNAMIC DEFLECTOMETER ROLLING SENSOR

The second-generation RDD rolling sensor works well and has been used to perform high-quality measurements. Further improvements could be made, however.

The first improvement would be to add an additional hold-down force to the sensors to eliminate the sensor contact problems discussed in Section 5.2.2. With an additional hold-down force on the rolling sensors, the rolling velocity could be increased to the point where the rolling noise becomes unbearable without losing contact with the pavement. The system supplying the additional hold-down force would need to consist of a mass suspended from, or supported above, the sensor by a soft spring. An added mass that weighs the same as the existing sensor would allow negative accelerations up to two g's without the sensor losing contact with the ground, or a 4 times increase in rolling velocity. To ensure that the sensor accurately tracks the dynamic motion, the added spring-mass system's first-mode resonance

must be well below the operating frequency range of the RDD. The added mass would also change the calibration of the sensor by increasing the wheel's contact area with the ground, probably increasing the first-mode resonance of the system (another benefit). This would necessitate recalibrating the sensors.

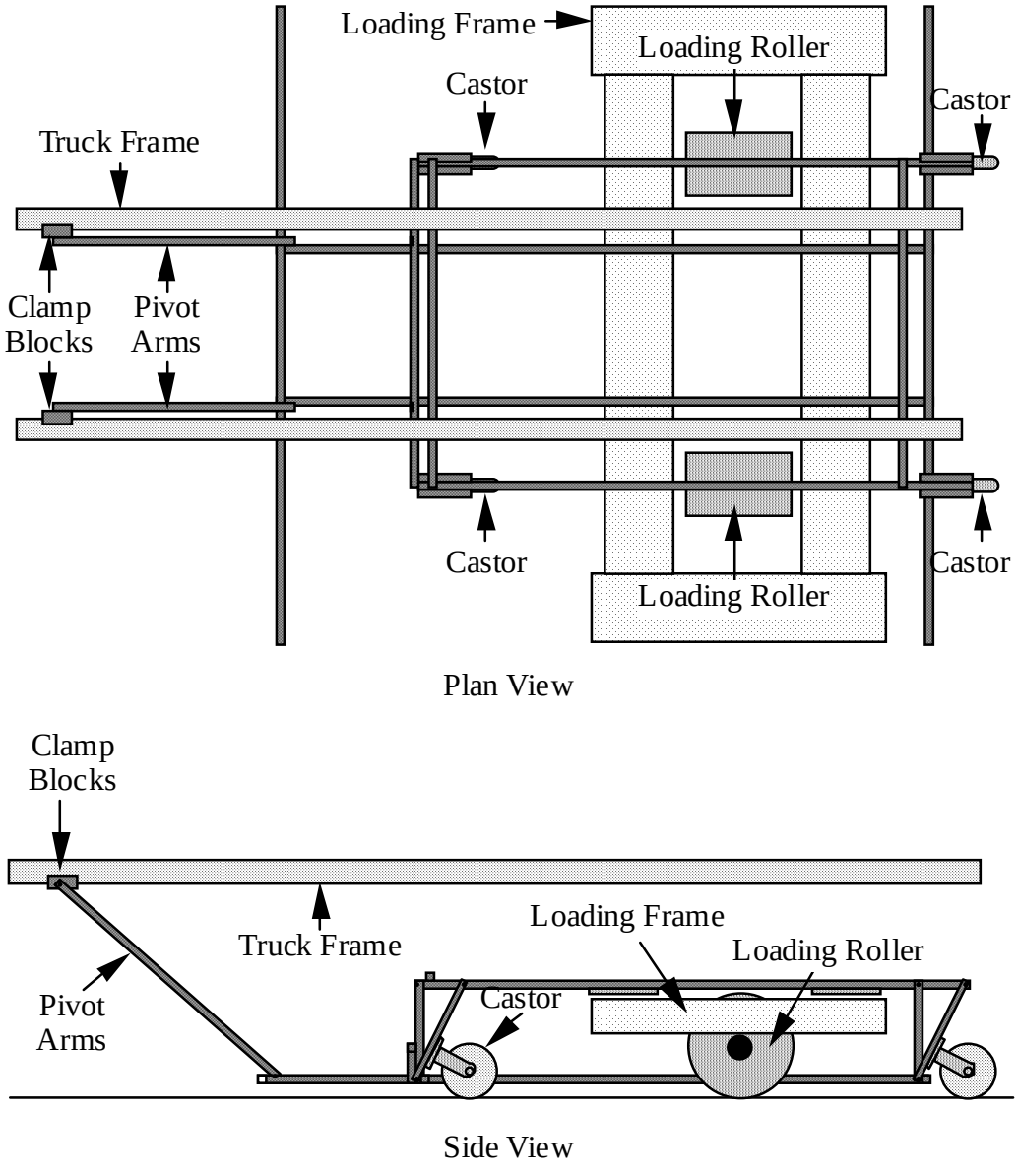

Figure 5.19 Plan and Side Views of RDD Rolling Sensor Towing System

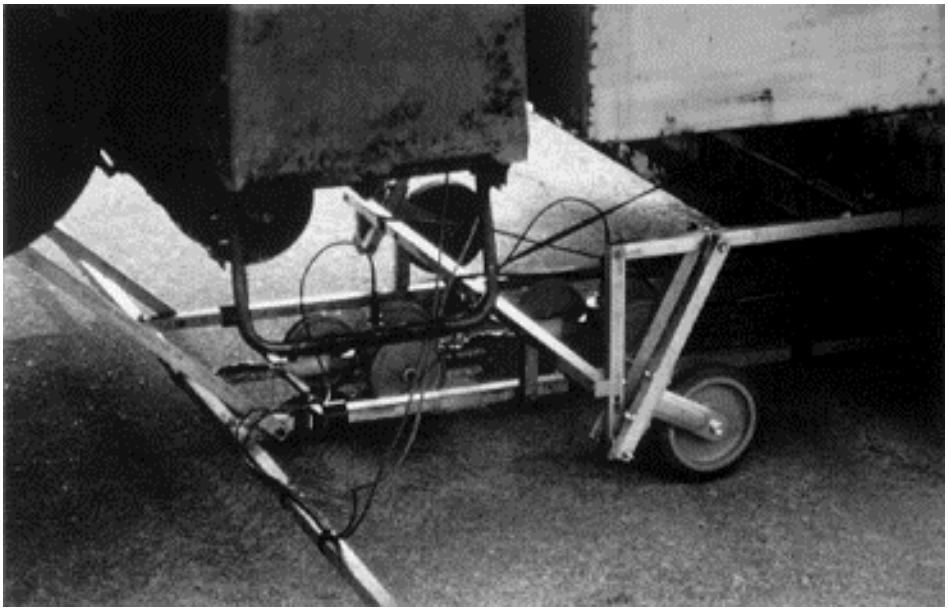

Figure 5.20 Photograph of Rolling Sensor Towing System with Sensors Attached

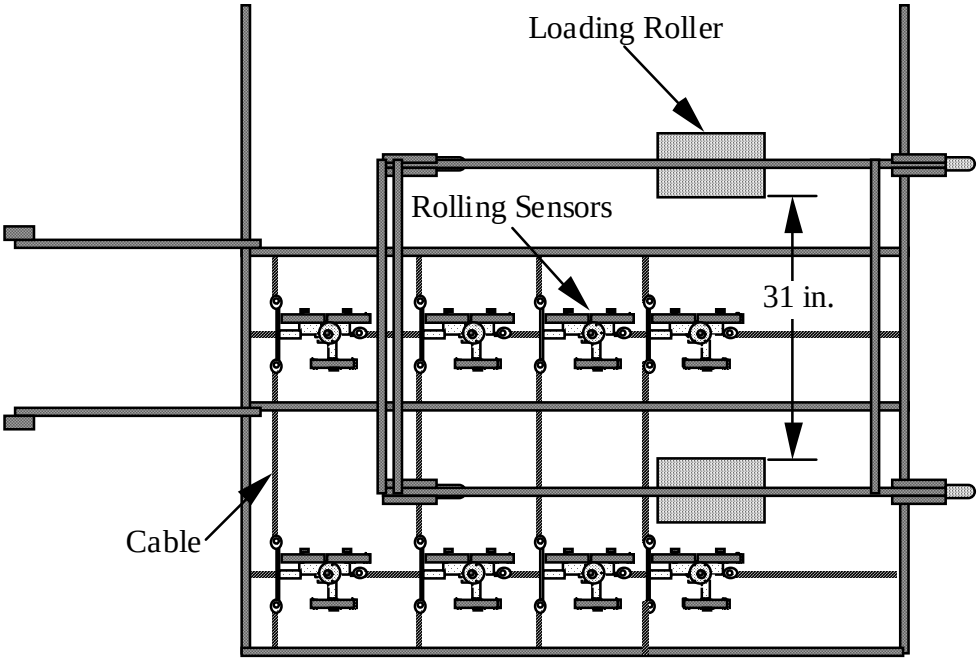

Figure 5.21 Some Possible RDD Rolling Sensor Positions with Sensor Towing System

The rolling sensors could be further improved by adding a variable, two-pole, low-pass filter that flattens the sensor calibration across the RDD frequency range. The filters would need to be adjusted to exactly flatten the response of each sensor. Before the transducer output could be effectively filtered, it would be important to convert the double-ended seismometer output to a single-ended signal with an instrumentation-grade differential amplifier. Amplification and filtering could be performed with a couple of integrated circuits per sensor.

5.5 SUMMARY

One of the most important tasks of the RDD is to measure vertical dynamic displacements induced in the pavement by the dynamic loading. The rolling noise induced by pavement roughness complicates these moving displacement measurements. The RDD uses specially designed rolling sensors to measure vertical dynamic displacements and to minimize the rolling noise in the displacement measurement.

The effects of various parameters on rolling noise were studied using rigid-body analysis of rolling wheels. The actual rolling sensor uses compliant wheels. For all the parameters studied, the rigid-body analysis results in a conservative design.

The first parameter studied was wheel diameter. Increasing the wheel diameter decreases the rolling noise. Most of the possible rolling noise reduction benefit is accrued using a 15.2 cm (6 in.) diameter wheel.

The second parameter studied was rolling velocity. Rolling velocity influences the rolling sensor in two ways. First, slower rolling velocities were found to decrease the rolling noise in any frequency band. For relatively quiet measurements with RDD operating frequencies between 40 and 100 Hz, the rolling velocity should be less than 0.6 m/s (2 ft/sec). Second, high rolling velocities cause the rolling sensor to lose contact with the pavement. For a 15.2 cm (6 in.) diameter wheel, pavement contact is maintained with rolling velocities less than 0.6 m/s (2 ft/sec).

The third parameter studied was the effect of the number of wheels used on each rolling sensor. Increasing the number of wheels decreases the rolling noise, especially at low frequencies. Therefore, more wheels on the rolling sensor allow the use of higher rolling velocities or lower operating frequencies.

The last parameter studied was the effect of wheel width. Wheel width has less impact on rolling noise than the other parameters. However, increasing wheel width decreases the rolling noise. Most of the possible rolling noise reduction benefit is accrued using a 2.5 cm (1 in.) wide wheel.

Two different rolling sensor systems have been used with the RDD. The designs and calibrations of both (the first-generation and the second-generation rolling sensors) systems are presented herein.

The first-generation rolling sensor had two 30.5 cm (12 in.) diameter wheels and was supported by an isolated trailing arm. This system had several weaknesses. It could not be used for more than a single measurement point. The geometry of the two wheels did not provide for noise attenuation as it rolled across transverse joints and tines. Additionally, the system had a lightly damped resonance in the middle of the RDD operating frequency range. Both an accelerometer and a 4.5 Hz geophone have been used as transducers on the first-generation rolling sensor. Neither transducer was totally satisfactory. The accelerometer had

poor low-frequency resolution, and the geophone distorted the displacement waveform when the combined rolling noise and induced dynamic displacements exceeded 2 mm (80 mils) p-p. This represents the stop-to-stop motion of the geophone coil.

The second-generation rolling sensor is freestanding, with three 15.2 cm (6 in.) diameter wheels. This design allows for the use of multiple sensors and an unlimited number of measurement locations. The wheel geometry minimizes rolling noise over transverse joints and tines. The sensor mass and compliance are such that the lowest sensor resonance occurs above 100 Hz. The polyurethane coating on the wheels produces high damping in the sensor resonances. A 2 Hz seismometer is used as the transducer on the second-generation rolling sensor. This transducer performs very well in the RDD frequency range, and has a p-p coil motion of 12.7 mm (500 mils), which is sufficient to prevent waveform distortion. The design of the towing system for the second-generation rolling sensors is also presented herein.

Two improvements to the second-generation rolling sensor are discussed. First, an additional hold-down force on the sensor would help maintain contact with the ground, allowing RDD testing to be performed at higher velocities. Second, a filter could be incorporated into each transducer circuit to flatten the frequency response of the sensor.

CHAPTER 6. THE ROLLING DYNAMIC DEFLECTOMETER DATA ACQUISITION AND DISTANCE MEASUREMENT SYSTEMS

6.1 INTRODUCTION

In the previous chapters, we discussed the force and displacement sensors used on the rolling dynamic deflectometer (RDD). In this chapter, we discuss the data acquisition system (DAQ) used to measure and store the outputs from these sensors. This DAQ is also used to track the distance traveled by the RDD so that the stored data can be identified with regard to position on the pavement. The DAQ is also used to monitor the operation of the RDD, and it has some capabilities to control the RDD operation.

6.2 THE ROLLING DYNAMIC DEFLECTOMETER DATA ACQUISITION SYSTEM

6.2.1 System Requirements

The first requirement of the DAQ is that it have a sufficient number of channels to measure all inputs. The RDD has four load cells. The signal conditioning box for the load cells contains an analog circuit that sums the output of the four load cells, as discussed in Section 4.3.4. Rather than measuring the single summed signal, the DAQ records the individual outputs of the four load cells, which are later summed during data processing. This allows checks on the distribution of forces between rollers and the distribution of force between the two load cells attached to each roller. A comparison of these values provides a valuable check on the operation of each load cell. Additionally, each load cell has a second strain gauge bridge that measures the moment applied to the load cell as a result of friction and horizontal forces acting on the rollers. Currently, these forces have not been studied, but it is important that the DAQ reserve four channels for doing so in the future. The RDD also has four rolling displacement sensors. Each of these requires one channel of the DAQ; additional rolling sensors might be added to the system in the future. Thus, the RDD currently requires at least twelve channels in the DAQ system.

Next, it is important to determine the required resolution of the DAQ. DAQs are available that provide 12-bit and 16-bit resolution. RDD measurements, especially the displacement measurements, are quite noisy owing to rolling noise. This rolling noise is variable with time and contains high spikes. This means that the RDD requires a large amount of “headroom” to avoid clipping the signal. In other words, the amplitude of the signal must be much smaller than the voltage range of the DAQ to prevent the signal from clipping because of large, intermittent rolling noise. In practice, the “quiet” signal should be no more than one-fourth of the DAQ voltage range. This headroom costs the DAQ two bits of total resolution. Therefore, to obtain a high-quality measurement, equivalent to 12-bit resolution, the DAQ should have 16-bit resolution.

The sampling rate is the next DAQ consideration. Nyquist sampling theory requires that the sampling frequency be slightly more than twice the highest frequency measured (Bracewell 1986). Practical filtering requirements demand that the sampling frequency be about three times the highest frequency measured. The highest possible RDD operating

frequency is 100 Hz. Therefore, the DAQ must be capable of continuously sampling twelve channels at a sampling rate of at least 300 Hz.

To obtain a high-quality measurement, signal conditioning is required upstream of the DAQ. This conditioning should include anti-aliasing filters, AC or DC coupling, differential amplification, and a sample-and-hold capability.

The system also must have transistor-to-transistor-logic (TTL) counters and digital inputs for a distance measuring system, which is discussed later in this chapter. Analog outputs capable of providing signals to control static and dynamic forces are another valuable component for the RDD DAQ.

6.2.2 Description of System

With all the considerations detailed above, National Instruments hardware and software were selected for the RDD's data acquisition and signal conditioning system. A PCI DAQ board in a PowerPC computer was selected to perform data acquisition, and an external SCXI system was selected for signal conditioning. This architecture was selected for a number of reasons. The external signal conditioning is desirable because the raw, unconditioned signals are filtered and amplified in the quiet environment of a well-shielded external chassis, rather than in the noisy environment of a computer chassis. The external chassis also allows increased functionality by cascading signals through multiple conditioning boards. Additionally, the external chassis also provides flexibility for future expansion or computer architecture changes. All of the expensive signal conditioning hardware can be reused with a different computer and DAQ board.

A flow chart showing the signal conditioning and DAQ system and the additional features of the DAQ board is shown in Figure 6.1. The signal conditioning is only shown for a single channel, but the same conditioning is provided for all sixteen channels.

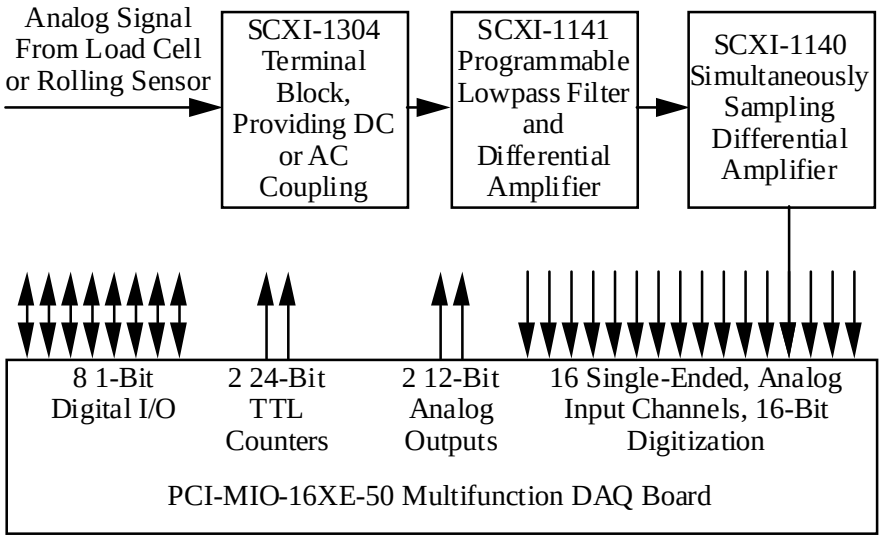

Figure 6.1 Flow Chart Showing Signal Conditioning and Data Acquisition Functions of RDD Data Acquisition and Conditioning Systems

The SCXI-1304 terminal block provides for AC or DC coupling. AC coupling is used for rolling sensor inputs because only dynamic components of this signal are of interest. DC coupling is required for the load cell signals because both the static and dynamic forces are of interest.

Anti-aliasing filtering is provided by the SCXI-1141 programmable, low-pass filter module. This is an eighth-order elliptical filter with 135 dB/octave roll-off. The filter can be programmed for a range of cut-off frequencies from 10 Hz to 25 kHz. To provide an adequate guard-band, the cut-off frequency should be set to a frequency equal to or lower than one-third the sampling frequency. The SCXI-1141 also provides programmable differential amplifiers.

The SCXI-1140 simultaneous sampling differential amplifier uses sample-and-hold circuits to allow simultaneous sampling on all channels. This is a critical factor for the measurement of the relative phase between channels. The capability to make high-quality phase measurements is not essential for normal RDD testing, but is a valuable research tool. The SCXI-1140 also has differential amplifiers with dip-switch select gains.

After passing through the simultaneous sampling differential amplifier, the signal leaves the external SCXI chassis and is passed to the DAQ board inside the computer. The DAQ board used is a National Instruments PCI-MIO-16XE-50. This board has sixteen single-ended analog inputs and performs a 16-bit analog-to-digital conversion on those channels. The board is capable of acquiring a total of 20,000 samples/sec.

The board also has two 12-bit digital-to-analog converters, providing two channels of analog output. One of these outputs may be used as a waveform generator to supply a signal to control the dynamic force supplied by the loading system. However, attempts to do this have overtaxed the throughput of the system. Efforts to resolve this problem are continuing with engineers from National Instruments, Inc. All RDD testing up to now has used an external waveform generator. The other analog output might be used in the future to regulate the static force applied by the RDD loading system.

The DAQ board also has two, 24-bit TTL counters and eight channels of TTL digital input/output. These are used to perform distance measurements, as discussed in the following section.

The computer and SCXI chassis are mounted in the cab of the truck on a vibration-isolated platform. The computer and monitor are powered by a 500W, sine-wave power inverter.

The data acquisition is controlled using National Instrument's LabView® software. The LabView® programming was performed by Dr. N. James Lee. This program controls the acquisition and storage of the results on disk, and provides displays of all of the outputs from the sensors, the testing position, and the rolling velocity.

6.3 THE ROLLING DYNAMIC DEFLECTOMETER DISTANCE MEASUREMENT SYSTEM

It is important that the DAQ monitor the distance traveled by the RDD during testing so that the measured displacement profile can be related to specific locations on the pavement. The distance measurement is achieved by attaching an optically coupled rotary encoder to one of the rear truck wheels to monitor the distance traveled by the truck. The encoder configuration is shown in Figure 6.2. A rotating shaft is attached to the center of a

wheel with a powerful magnet assembly. This shaft attaches to the rotary encoder, which is inside a weatherproof housing. The encoder housing has a Teflon bushing, which slides over a brass rod. The brass rod is attached to the truck side rail with another magnet assembly. The rod prevents the encoder from rotating with the wheel, while the bushing slides on the rod, allowing relative vertical motion between the wheel and the truck.

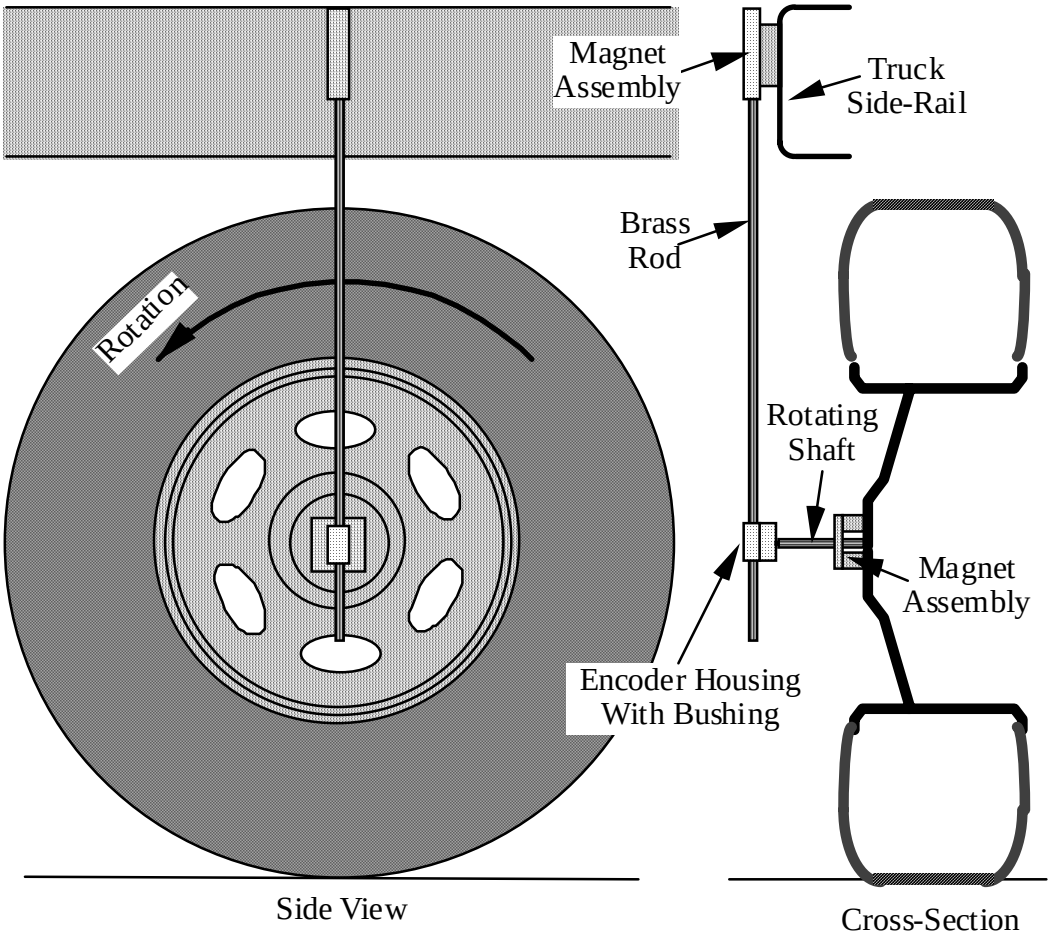

Figure 6.2 Side and Cross-Sectional Views Showing How the Rotary Encoder Mounts on a Truck Wheel

The rotary encoder outputs two TTL-compatible signals. The encoder signals consist of 128 square-wave cycles in quadrature (or 90° out of phase with each other) per rotation of the wheel. By using these two signals in an up/down counter, the encoder can track the

RDD's position when it is traveling forward and in reverse. Figure 6.3 shows what the encoder signals look like when the wheel rotates forward and backwards. Encoder channel A goes to the DAQ counter while encoder channel B goes to a digital I/O. An up/down counter checks the state of the digital I/O when the counter voltage rises. If the digital I/O is high, then the counter is incremented; if it is low, then the counter is decremented. Figure 6.3a shows the encoder signal when the wheel is rotating forward. At each rising voltage of channel A, the voltage at channel B is high. Thus, each rising voltage increments the counter. Figure 6.3b shows the encoder signal when the wheel is rotating backwards. At each rising voltage of channel A, the voltage at channel B is low. Thus, each rising voltage decrements the counter.

A small problem arose in this system. The encoder, attached to the RDD wheel, is about 6 m (20 ft) from the DAQ board in the cab of the vehicle. This requires the encoder circuit to drive about 6 m (20 ft) of cable. The capacitance of this cable caused the rise time on the square waves to be approximately 20 μsec. This long rise time led to some rising events being counted twice. This problem was solved by sending the encoder outputs through a Schmidt trigger circuit before they reached the DAQ.

The distance measurement system was calibrated by driving the RDD over a path and carefully measuring the distance of that path. The distance traveled was divided by the counter value to determine the distance-per-count. The computer constantly calculates the distance traveled by multiplying the counter value by this factor.

Subsequent testing of long airport pavements with precisely known lengths has shown that errors in distance measurements with the system are less then ± 0.7 percent. These errors have been found to be both higher and lower, so they cannot be attributed to an error in the distance-per-count factor.

6.4 POSSIBLE IMPROVEMENTS TO THE DATA ACQUISITION AND DISTANCE MEASUREMENT SYSTEM

The DAQ currently works very well, but could be improved in two regards. Several improvements could also be made to the distance measuring system.

The use of an external function generator to drive the loading system leads to small frequency discrepancies owing to small differences in the DAQ and function generator clocks. This discrepancy can be successfully accounted for during data analysis, but it unnecessarily complicates the data analysis procedure. When the data throughput problem, discussed earlier, is solved so that the DAQ can drive the loading system with one of its analog outputs, then the same clock will control both the data sampling and the function generator, solving the frequency discrepancy.

Currently, no data analysis is performed during testing; raw data are merely stored on disk for later processing. The RDD data processing procedures, discussed in Chapter 8, are very conducive to real-time analysis. Software could be written to analyze and display testing results as the RDD testing is performed.

The distance measuring system accuracy (± 0.7 percent) is currently sufficient for some applications but lacking for others. This system could probably be improved by adding a special distance measurement wheel for tracking distance, rather than using one of the vehicle wheels. Such a wheel would more accurately track the vehicle position because it would not be subject to shear forces and variable loading like the vehicle wheels. A global

positioning system (GPS) could also be incorporated into the DAQ to provide additional test position information.

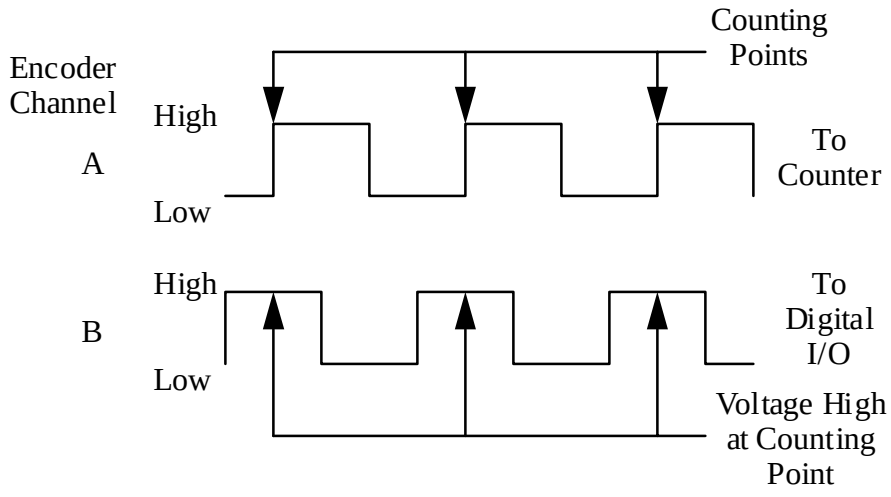

a) Encoder Outputs with Forward Wheel Rotation

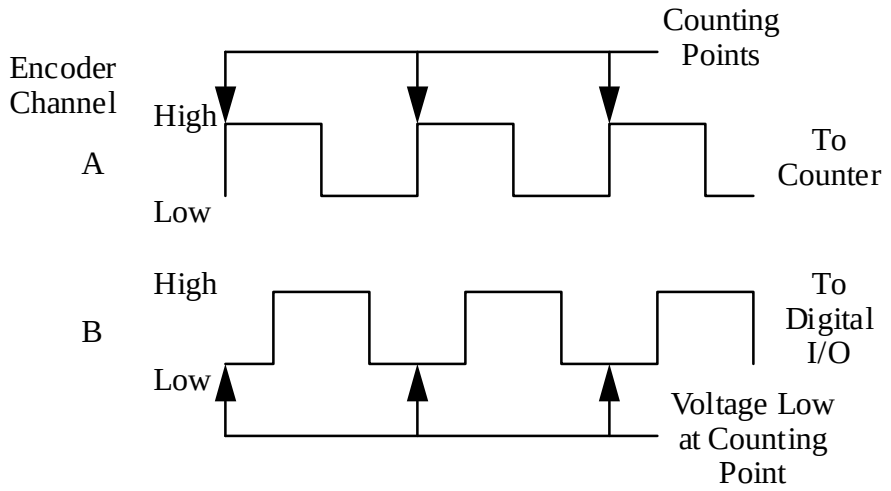

b) Encoder Outputs with Reverse Wheel Rotation

Figure 6.3 Rotary Encoder Outputs for Forward and Reverse Wheel Rotations

A video record of the pavement being tested would be another simple but valuable addition to the RDD. This would allow a visual check of the features associated with the RDD displacement profile.

6.5 SUMMARY

The RDD requires a DAQ to measure and record the forces applied by the RDD, the induced displacements, and the position of the RDD on the pavement. This DAQ must have analog inputs, digital inputs, and counters. The analog inputs are used to measure the load cell and rolling sensor outputs. There must be at least twelve analog input channels, with 16-bit analog-to-digital conversion, a sampling rate of at least 300 Hz per channel, sample-and-hold amplifiers, and anti-aliasing filters. A counter and digital input are required to monitor the position of the RDD on the pavement during testing. National Instruments hardware and software were selected for the RDD's data acquisition and signal conditioning system. A PCI DAQ board in a PowerPC computer was selected to perform data acquisition, and an external SCXI system was selected for signal conditioning. This system is controlled with LabView® software.

A distance measuring system was designed and constructed for the RDD. This system uses a rotary encoder attached to one of the truck wheels and monitors the wheel rotation with an up/down counter in the DAQ.

The current system works very well, but could be improved in a few ways. Analog outputs from the DAQ could be used as the waveform generator driving the RDD dynamic loading system. This would eliminate discrepancies between the waveform generator and the DAQ clocks. More data analysis could be performed during data collection to calculate real-time displacement profiles. The distance measurement system could be improved to increase the precision of the RDD position measurements. This could involve using a GPS. Finally, incorporating a camera to record video images of the pavement being tested would provide a valuable tool for analyzing RDD results.

CHAPTER 7. ROLLING DYNAMIC DEFLECTOMETER TESTING PROCEDURES

7.1 INTRODUCTION

This chapter describes the testing procedures used to perform rolling dynamic deflectometer (RDD) measurements on pavements. In addition, it explains the RDD operating parameters and the interaction between the parameters, which include testing velocity, operating frequency, sampling rate, force levels, and rolling sensor position (criteria used to select these parameters are also described). Finally, the chapter provides step-by-step operating instructions as well as important routine maintenance procedures.

7.2 ROLLING DYNAMIC DEFLECTOMETER OPERATING PARAMETERS

The quality and usefulness of RDD testing results depend on the operating parameters used in performing the measurements. The most important RDD operating parameters are the testing velocity along the pavement, the operating frequency, the sampling rate, the static and dynamic force levels, and the rolling sensor positions. A discussion of these parameters is complicated by their dependence on each other. Therefore, the following discussions describe the effects of each parameter on RDD testing results and its influence on the other parameters.

7.2.1 Testing Velocity along the Pavement

The testing velocity along the pavement influences the RDD results in three ways. First, it affects the noise level measured with the rolling sensors. Second, it affects the spatial resolution in the RDD measurement. Third, there is a limiting velocity beyond which the rolling sensors lose contact with the pavement. Obviously, this limiting velocity must never be exceeded.

7.2.1.1 Effect of Testing Velocity on Rolling Noise — The effects of testing velocity on the rolling noise measured with the rolling sensors were discussed in Section 5.2.1.2 and illustrated in Figure 5.4. At low testing velocities, less than 0.3 m/s (1 ft/sec), the rolling noise is concentrated at frequencies below about 20 Hz. Increasing the rolling velocity also increases the frequency of the rolling noise. Noise that occurs at frequencies besides the RDD operating frequency is filtered out during processing; therefore, the only concern is the noise level at the RDD operating frequency. The noise level at the operating frequency can be reduced by decreasing the testing velocity, increasing the operating frequency, or by isolating the operating frequency with a narrower filter. The RDD operating frequency is discussed in Section 7.2.2, and the filter design is discussed in Chapter 8.

Reasonable signal-to-noise ratios have been obtained in RDD measurements at rolling velocities of up to 0.6 m/s (2 ft/sec). However, different results may be obtained for testing at different force levels, operating frequencies, pavement stiffnesses, or pavement roughnesses.

7.2.1.2 Effect of Testing Velocity on Spatial Resolution — The testing velocity also influences the spatial resolution of the RDD measurement. As mentioned previously, frequencies other than the operating frequency are filtered out during data processing. In addition to amplifying or attenuating certain frequencies, all filters cause a "smearing" of their output, with the output representing a running average over some interval of time. This

time interval is inversely proportional to the bandwidth of the filter, as discussed in greater detail in Chapter 8. For example, if a testing velocity of 0.6 m/s (2 ft/sec) is used, and the filter averages results over 2-second time intervals, the spatial measurement resolution of the measurement is 1.2 m (4 ft). This would be insufficient for characterizing details like deflection at pavement joints. This effect is further complicated by the fact that higher testing velocities increase the rolling noise at the operating frequency. One solution for reducing rolling noise is to use a narrower bandwidth filter to reject more of the noise. However, the narrower bandwidth filter increases the averaging time interval, further decreasing the spatial resolution of the measurement.

7.2.1.3 Effect of Testing Velocity on Sensor Contact — Sensor wheels rolling on a rough surface experience negative accelerations. If these negative accelerations reach 1 g, the wheel loses contact with the pavement. The mechanism that causes the wheels to lose contact with the pavement owing to rolling velocity is discussed in detail in Section 5.2.2. Equation 5.1 controls this effect, and Figure 5.12 shows the negative accelerations generated by wheels of several diameters versus rolling velocity.

Additionally, the dynamic displacements induced by the RDD dynamic loading also subject the rolling sensors to negative accelerations. This effect is strongly influenced by the RDD operating frequency and is discussed in greater detail in Section 7.2.2.2. A criterion for maintaining pavement contact is also presented in that section.

7.2.2 Rolling Dynamic Deflectometer Operating Frequency

Rolling noise measured in RDD testing decreases with increasing frequency. Therefore, increasing the RDD operating frequency will generally improve the RDD measurement quality. However, two additional factors must be considered in selecting an RDD operating frequency. These are the site response of the test location and the contact of the rolling sensor with the pavement. These two factors are discussed below.

7.2.2.1 Site Response and Rolling Dynamic Deflectometer Operating Frequency — A very important consideration in selecting an RDD operating frequency is the site response of the testing location. Sites with shallow bedrock or a shallow stiff layer (such as a caliche layer) will have a pronounced site resonance that can interfere with the RDD results. Figure 7.1 illustrates the manner in which this resonance occurs. A soft soil layer above bedrock acts as a single-degree-of-freedom, fixed-free resonator, which traps energy at certain frequencies in the soil layer. These resonant frequencies are related to the stiffness characteristics of the pavement site (Roesset et al. 1995 and Foinquinos et al. 1995). As a first approximation, the resonant frequencies can be assumed to be related to constrained compression wave velocity and can be determined using the following equation:

$$f_n = \frac{n\, V_p}{4\, D} \qquad \text{(Equation 7.1)}$$

where f_n is the n^{th} mode resonant frequency
n = 1, 3, 5, ...
V_p is the constrained compression wave velocity
D is the depth to bedrock or stiff layer

Examples of frequency response curves for a soil layer over bedrock are shown in Figure 7.2. The amplitude ratio is the ratio of dynamic displacement at a given frequency and force level to the static displacement at the same force level. The frequency ratio is the ratio of frequency to the first-mode resonant frequency. Two response curves are shown in Figure 7.2, one for 20 percent of critical damping and the other for 3 percent of critical damping. The ratio of critical damping at a pavement site is a function of the material damping of the soil, the stiffness ratio between the soil layer and the bedrock layer, and the geometric wave spreading in the pavement and subgrade system. At frequencies much lower than the first-mode resonance, the dynamic displacement is essentially equivalent to the static displacement. Near the resonant frequency, the dynamic displacement is largely a function of the damping in the system. At frequencies substantially above the resonance, the dynamic displacement is less than the static displacement owing to inertial effects.

Ideally, the RDD should be operated at low frequencies, where the dynamic displacement closely approximates the static displacement. However, this is not always possible because the low frequencies are much noisier than high frequencies. Care must be taken not to operate the RDD at frequencies near site resonances. Measurements performed at operating frequencies near a site resonance will result in large displacements, which could be misinterpreted as indicating a pavement system that is less stiff than it actually is. When tests are performed at high frequencies, where inertial effects are significant, a dynamic model that accounts for this effect must be used, rather than a static or pseudostatic model.

The frequency response of a site can be determined with the RDD. This involves 1) testing in a stationary mode, and 2) driving the RDD with a chirp rather than sinusoidal dynamic force. The chirp rapidly sweeps the frequencies from about 5 Hz to 100 Hz. The displacements generated by the chirp are measured with the rolling sensors (which are now stationary). A response for the site is calculated by dividing the measured displacement by the measured force, in the frequency domain. This step is important because the force applied by the RDD is not uniform with frequency. The calculated response curve can be used to select an operating frequency away from site resonances.

7.2.2.2 Rolling Sensor Contact and Rolling Dynamic Deflectometer Operating Frequency — Besides site response concerns, the RDD operating frequency has other important effects on RDD test results. Generally, the rolling noise level decreases with increasing frequency; therefore, quieter measurements can be obtained by increasing the RDD operating frequency. However, increasing the RDD operating frequency increases the acceleration levels of the pavement surface, adversely affecting the sensor contact with the pavement. The vertical acceleration of the pavement surface is calculated using the following equation for steady-state harmonic motion:

$$\ddot{v}_{p_{max}} = v_{p_{max}} \omega^2 \qquad \text{(Equation 7.2)}$$

where $\ddot{v}_{p_{max}}$ is the peak vertical pavement acceleration

$v_{p_{max}}$ is the peak vertical pavement displacement

ω is the frequency in radians per second

Because of the frequency-squared term in this equation, the pavement acceleration is very sensitive to the RDD operating frequency.

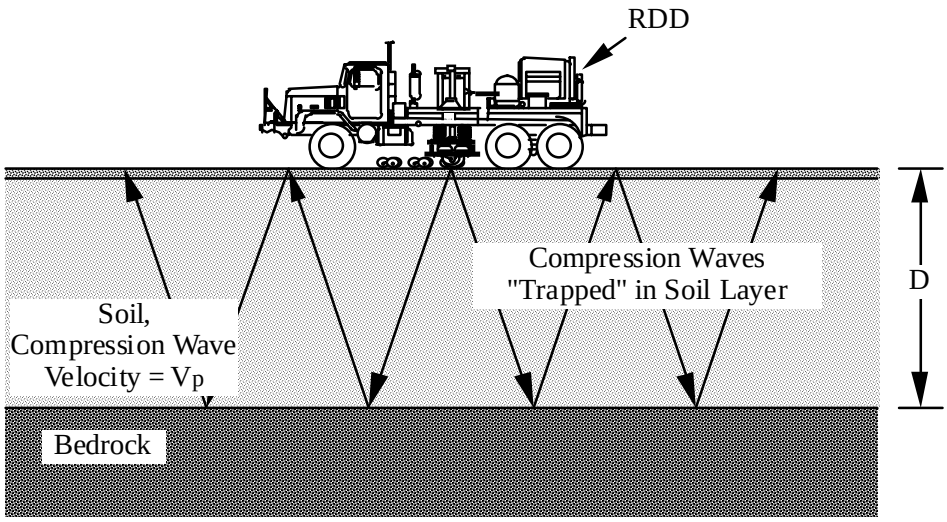

Figure 7.1 Illustration of Constrained Compression Waves Trapped in a Soil Layer Causing Site Resonance at a Pavement Site

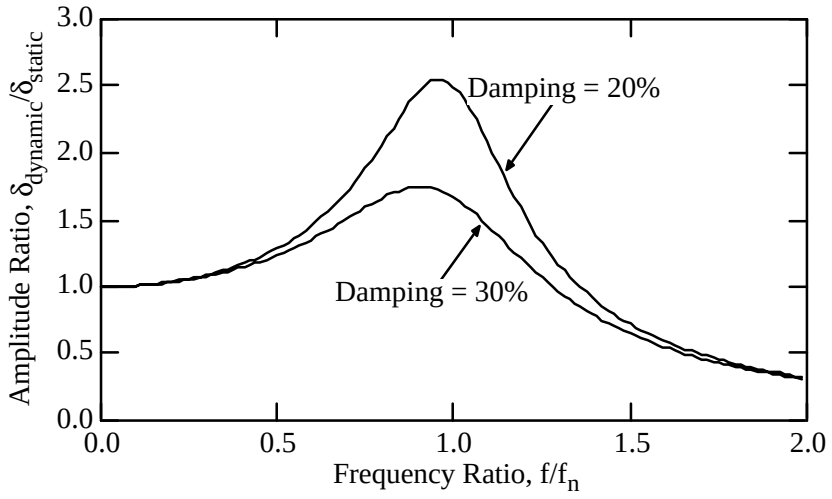

Figure 7.2 Examples of Single-Degree-of-Freedom Frequency Response Curves Illustrating Site Response for an Idealized Pavement Site with Shallow Bedrock

It is very informative to analyze the motion of an uncoupled rigid body on a vibrating surface subject to gravity. This is essentially the RDD rolling sensor. Figure 7.3 shows a model of a sensor on a vibrating surface. As long as the peak pavement acceleration is less

than the acceleration of gravity, a rigid sensor will exactly track the pavement motion. However, as soon as the pavement acceleration exceeds the acceleration of gravity, the sensor will lose contact with the pavement and its motion will not exactly track the pavement motion.

Plots of the displacement and acceleration of both the pavement and sensor are shown in Figure 7.4 for one cycle of motion with a peak pavement acceleration of 1.3 g. The time scale used in Figure 7.4 is dimensionless time, ωt. This dimensionless time will be used in the following analysis to make it independent of frequency.

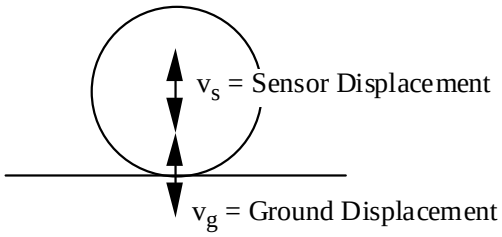

Figure 7.3 Model of an Uncoupled Sensor Resting on a Vibrating Surface

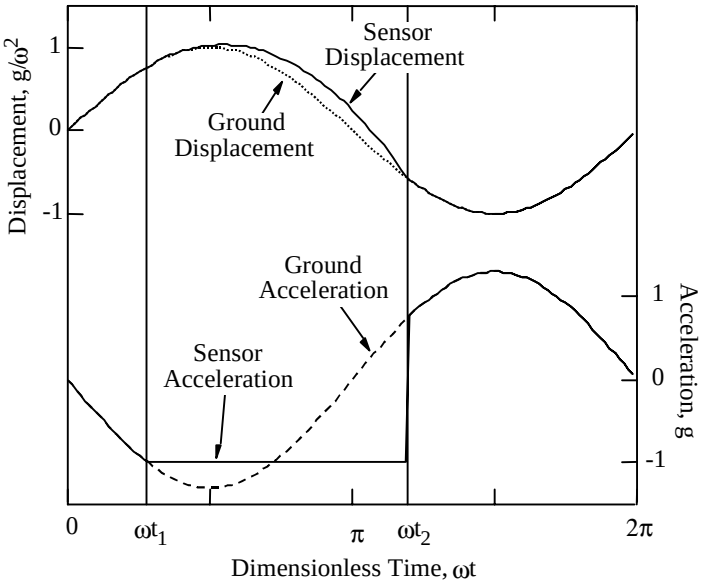

Figure 7.4 Displacement and Acceleration of Pavement and an Uncoupled Sensor with a Peak Ground Acceleration of 1.3 g

At the beginning of the cycle shown in Figure 7.4, the sensor and pavement displacements are identical. At the time designated as ωt_1, the pavement acceleration

becomes less than -1g, and the sensor loses contact with the pavement. A value for ωt_1 can be calculated using the following equation:

$$\omega t_1 = \sin^{-1}\left(\frac{g}{\ddot{v}_{p_{max}}}\right) \qquad \text{(Equation 7.3)}$$

where g is the acceleration of gravity

$\ddot{v}_{p_{max}}$ is the peak pavement acceleration

After the sensor loses contact with the pavement, its acceleration remains at a constant -1 g and it free-falls until it again encounters the pavement at time ωt_2. This analysis neglects the effects of this impact, but assumes that the sensor "sticks to" the pavement at contact. A value for ωt_2 can be determined by solving the following equation for ωt_2:

$$\sin(\omega t_1) + (\omega t_2 - \omega t_1)\cos(\omega t_1) - \frac{1}{2}\frac{g}{\ddot{v}_{p_{max}}}(\omega t_2 - \omega t_1)^2 - \sin(\omega t_2) = 0 \qquad \text{(Equation 7.4)}$$

Once values of ωt_1 and ωt_2 are determined, the displacement of the sensor, v_s, can be calculated from the following equation:

$$v_s = \begin{cases} v_{p_{max}}\left(\sin(\omega t)\right) & 0 \le \omega t \le \omega t_1 \\ v_{p_{max}}\left(\sin(\omega t_1) + (\omega t - \omega t_1)\cos(\omega t_1) - \frac{1}{2}\frac{g}{\ddot{v}_{p_{max}}}(\omega t - \omega t_1)^2\right) & \omega t_1 \le \omega t \le \omega t_2 \\ v_{p_{max}}\left(\sin(\omega t)\right) & \omega t_2 \le \omega t \le 2\pi \end{cases}$$

(Equation 7.5)

For acceleration levels where the sensor is out of contact with the pavement for an interval of time less than the period of the wave, the motion of the sensor will be a harmonically distorted sinusoid. This is the case for pavement accelerations less than about 3.3 g. Sensor displacements were calculated for a number of different acceleration levels, and this motion was analyzed in the frequency domain. Displacements at a frequency of ω were determined and the total harmonic distortion was calculated. These results are presented in Figure 7.5. At accelerations below about 1.7 g, the distorted displacement waveform has peak displacement higher than the pavement displacement, as seen in Figure 7.5a. This is the case of the distorted displacement waveform shown in Figure 7.4. The parabolic arc achieves a higher positive peak displacement than the pavement displacement, and is back in contact with the pavement before it reaches its negative peak. At higher acceleration levels, the sensor will not contact the pavement until after it reaches its negative peak. This behavior decreases the sensor displacement in the negative direction and, hence,

its peak-to-peak motion. Thus, pavement acceleration levels higher than about 1.7 g result in decreased displacement, with this effect becoming more significant above about 2 g's, as can be seen in Figure 7.5a.

The differences in the displacement amplitudes of the sensor and the pavement are less than 5 percent up to acceleration levels of 2 g. However, the total harmonic distortion is over 40 percent at 2 g, as shown in Figure 7.5b. Figure 7.5 indicates that if displacement errors of up to 5 percent with a total harmonic distortion of 20 percent are acceptable, then an uncoupled sensor will give acceptable results at acceleration levels up to 1.5 g. Thus, the rolling sensor will still track the pavement motion fairly well, even when it loses contact with the pavement for a small portion of the period of the dynamic excitation, as a result of the acceleration exceeding 1 g by moderate amounts.

The other mechanism that can cause the rolling sensor to lose contact with the pavement is the bouncing of the wheels over roughness, as discussed in Section 5.2.2. This loss of contact is more detrimental to the rolling sensor performance than that owing to pavement accelerations. The "bouncing" causes the wheel to lose contact with the pavement for time intervals much longer than the period of the dynamic excitation, resulting in no tracking of the pavement motion for that period. The results of this section and Section 5.2.2 can be combined to establish a criterion for testing velocity, operating frequency, and peak pavement displacement using Equations 5.1 and 7.2. Assuming that 5 percent accuracy in the displacement is acceptable for a given study, this criterion is:

$$\frac{1}{r} V^2 + \frac{2}{3} v_{p_{max}} (2\pi f_o)^2 \leq 1g \qquad \text{(Equation 7.6)}$$

where r is the rolling sensor wheel radius (7.6 cm [3 in.])
V is the testing velocity along the pavement
$v_{p_{max}}$ is peak vertical pavement displacement
f_o is the RDD operating frequency

If small errors in displacement are not acceptable for a study, the criterion for testing velocity, operating frequency, and peak displacement should be:

$$\frac{1}{r} V^2 + v_{p_{max}} (2\pi f_o)^2 \leq 1g \qquad \text{(Equation 7.7)}$$

The criteria from Equations 7.6 and 7.7 are plotted in Figure 7.6 for a range of peak pavement displacements. One of the factors required in the criteria presented in Equations 7.6 and 7.7 is the maximum peak displacement of the pavement to be tested. This value is not known prior to testing. However, reasonable estimates can be made of this value, and the actual value can be monitored during testing. Typically, peak pavement displacements will not exceed 0.02 mm (8 mils) on thick rigid pavements. The dynamic force level can be reduced if allowable displacements are exceeded.

One improvement that could be made to the rolling sensors is the addition of a system that provides an additional hold-down force on the sensor to help maintain contact with the

pavement. With an additional hold-down force, the criterion for testing velocity, operating frequency, and peak pavement displacement should be:

$$\frac{1}{r} V^2 + v_{p_{max}} (2\pi f_o)^2 \leq 1g + \frac{F_{hd}}{W_{sensor}} \qquad \text{(Equation 7.8)}$$

where F_{hd} is the hold-down force
W_{sensor} is the rolling sensor weight

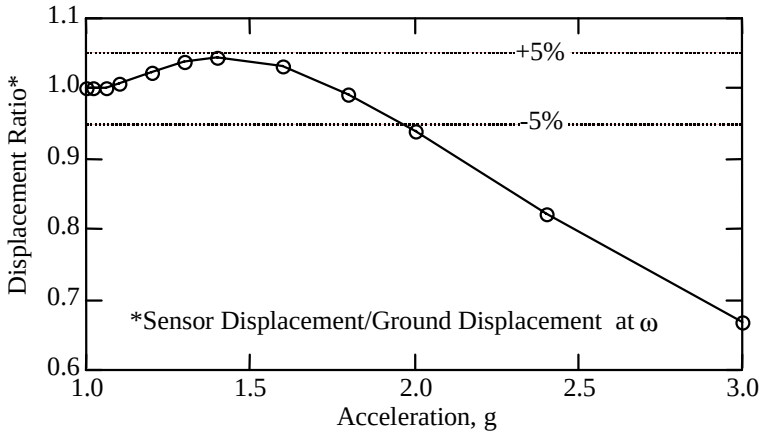

a) Displacement at a Frequency of ω

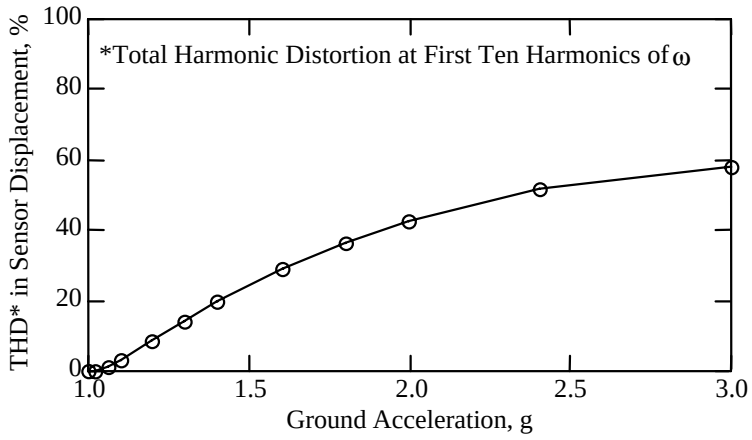

b) Total Harmonic Distortion in Displacement

Figure 7.5 Amplitude and Distortion of Uncoupled Sensor at Acceleration Levels above 1 g

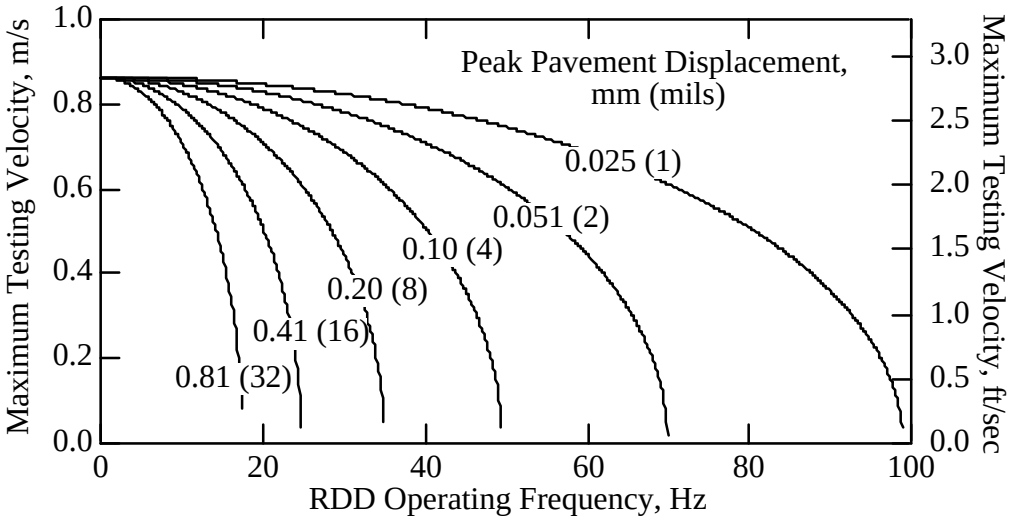

a) Testing Velocity and Operating Frequency Criteria For Precise RDD Survey

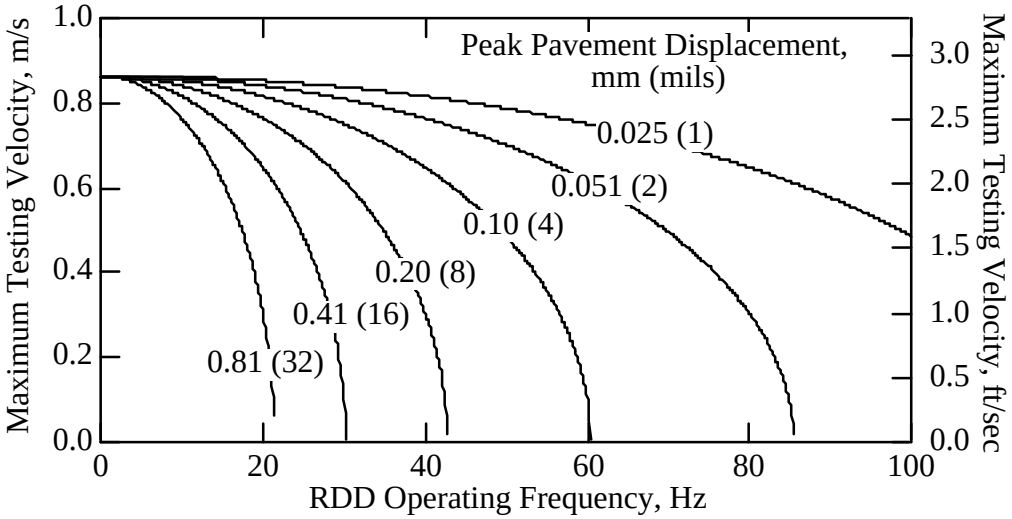

b) Testing Velocity and Operating Frequency Criteria For ±5% RDD Survey

Figure 7.6 Criteria for Testing Velocity along the Pavement and RDD Operating Frequency for a Range of Peak Pavement Displacements

7.2.3 Sampling Rate

Another important measurement parameter is the sampling rate used for data acquisition. It is essential that the sampling rate be high enough to obtain all the pertinent information, but no higher than necessary to keep the size of the data files manageable. An issue associated with the sampling rate is the cut-off frequency setting of the anti-aliasing filter. These issues are discussed in this section, and criteria for sampling rate and anti-aliasing filter cut-off frequency relative to the RDD operating frequency are presented.

The Nyquist sampling theorem states that, for a frequency band-limited function, the intervening values between equal interval sampling points can be recovered if the sampling frequency is at least two times the highest frequency in the band-limited function (Bracewell 1986). This theorem establishes that the sampling rate used for RDD testing must be at least two times the highest frequency of interest and that filters must be used to ensure that the sampled waveform is band-limited with no energy at frequencies above the highest frequency of interest. The frequency that is one-half of the sampling frequency is designated as the Nyquist frequency, f_{Nyq}, and any energy in a sampled waveform higher than the Nyquist frequency is said to "alias" to lower frequencies. Aliasing means that energy at one frequency appears to occur at a lower frequency. Frequencies that alias, "fold" back around the Nyquist frequency, as shown in Figure 7.7, to an alias frequency between 0 and the Nyquist frequency. Filters used to ensure that waveforms are band-limited prior to sampling are called anti-aliasing filters.

Ideally, an anti-aliasing filter would pass all energy up to the Nyquist frequency and reject all energy above the Nyquist frequency. Real filters cannot perform in such an abrupt manner, but have a roll-off band where energy is attenuated, though not completely. The anti-aliasing filters used on the RDD are in the SCXI-1141 modules discussed in Section 6.2.2. These are eighth-order elliptical low-pass filters. A plot of their response is shown in Figure 7.8. Each filter rolls off at 135 dB/octave, with -80 dB (a factor of 1/10,000) stop band attenuation. At frequencies higher than 1.5 times the cut-off frequency, f_c, signals are attenuated at least 80 dB.

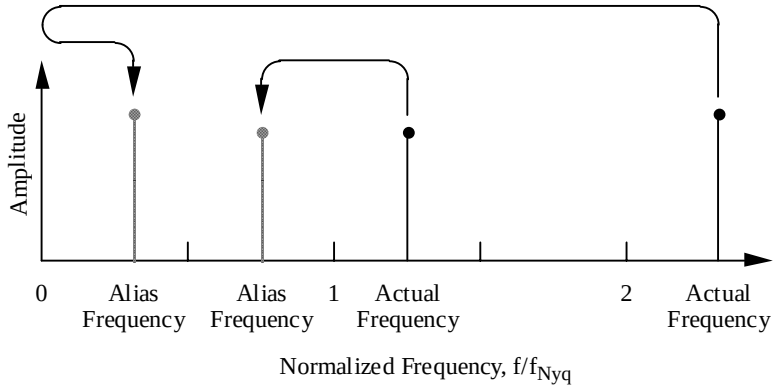

Figure 7.7 Illustration of Frequencies Higher than the Nyquist Frequency Folding around the Nyquist Frequency to an Alias Frequency

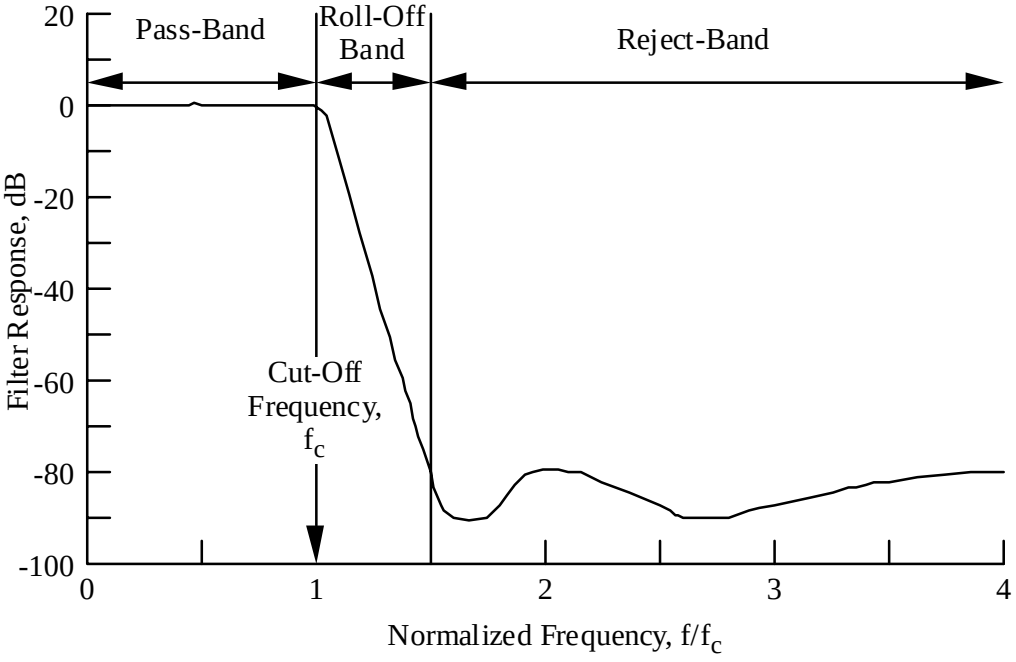

Figure 7.8 Response of Anti-Aliasing Filter Used with the RDD (after National Instruments 1996)

National Instruments (1996) recommends using a sampling frequency equal to at least three times the filter cut-off frequency. A plot showing the Nyquist frequency and aliasing products is shown for this condition in Figure 7.9. With these settings, all aliasing products are attenuated at least 80 dB, and the highest usable frequency is one-third the sampling frequency. In other words, a sampling frequency must be at least three times the highest frequency of interest.

It is possible to obtain good results using a sampling frequency lower than the National Instruments recommendation by using a "guard band." A guard band is a frequency band just below the Nyquist frequency where aliasing products are not totally attenuated. This band is potentially "tainted" by aliasing products, but it is still above the highest frequency of interest, so it can be disregarded without consequence. A plot showing a guard band for the RDD anti-aliasing filters is presented in Figure 7.9. Using this scheme, all aliasing products are still attenuated by at least 80 dB, but the sampling frequency only needs to be 2.5 times the highest frequency of interest.

The primary frequency of interest in RDD testing is the RDD operating frequency. However, it is useful to accurately characterize frequencies higher than the operating frequency. Information from higher frequencies can be used to estimate noise levels at the operating frequency. This issue is discussed in detail in Chapter 8. The highest frequency needed in RDD analysis is 1.5 times the RDD operating frequency, f_o. Therefore, using a

guard band as shown in Figure 7.10, the sampling frequency, f_s, should be set using the following criterion:

$$f_s \geq 3.75\ f_o \qquad \text{(Equation 7.9)}$$

The cut-off frequency, f_c, should be set using the following criterion:

$$1.5\ f_o \leq f_c \leq \frac{f_s}{2.5} \qquad \text{(Equation 7.10)}$$

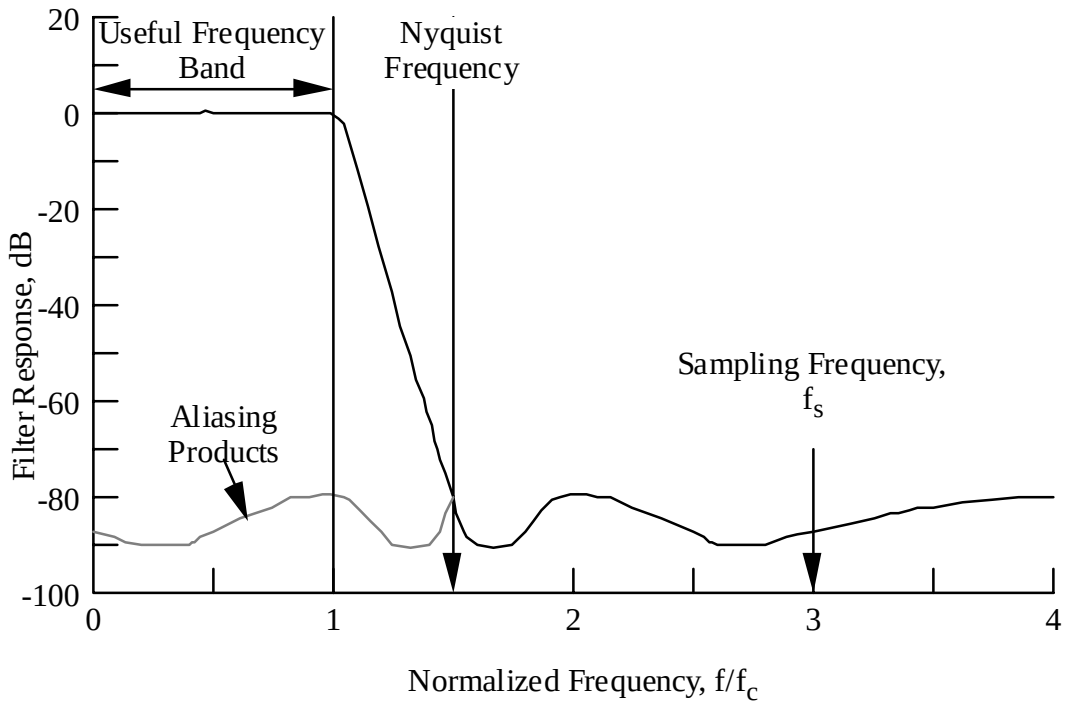

Figure 7.9 Filter Response and Aliasing Products with a Sampling Frequency Three Times the Filter Cutoff Frequency (after National Instruments 1996)

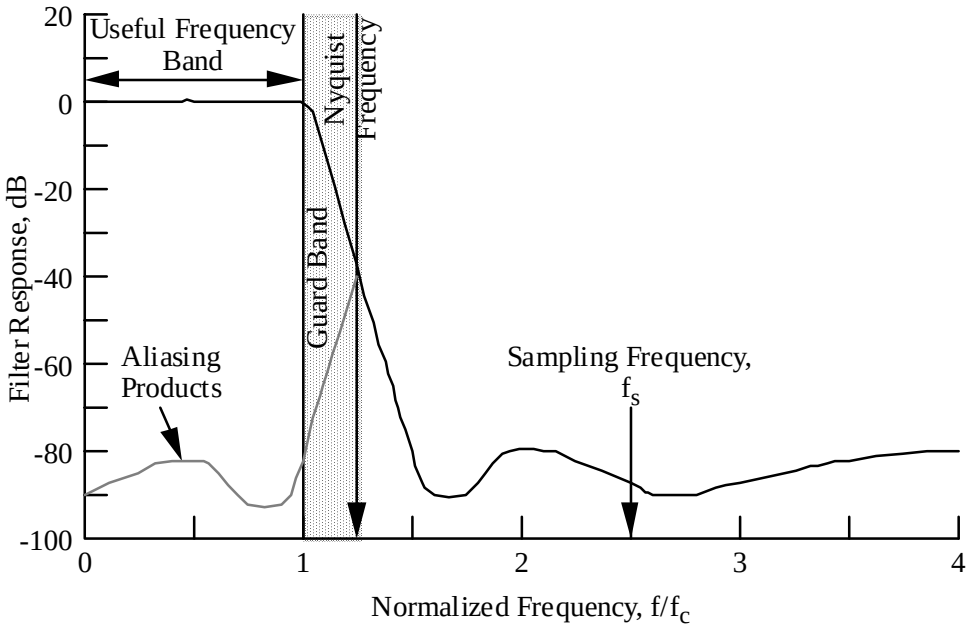

Figure 7.10 Filter Response and Aliasing Products with a Guard Band (after National Instruments 1996)

Sampling frequencies higher than the minimum values specified can be used; however, doing so does not yield data that are of better quality than those obtained at the minimum sampling frequency. The raw data look better when plotted using higher sampling frequencies. However, values intermediate between sparsely sampled data points can be recovered according to the sampling theorem. This is achieved by performing sinc function interpolation on the sparse data (Bracewell 1986). This interpolation can easily be performed on small data sets for presentation.

7.2.4 Force Levels

The static and dynamic forces applied to the pavement must also be selected. The primary concern in selecting force levels is the integrity of the pavement. The dynamic force level also has an influence on the data quality. In this section, the criteria that should be used for selecting static and dynamic force levels are discussed.

The purpose of the static force, F_s, is to provide a hold-down force on the dynamic loading system to resist the upward dynamic forces generated during testing. Thus, the static force must be greater than the peak dynamic force, F_d. The dynamic loading system performs best if the total applied force does not get too close to zero. Experience of the writer indicates the following relationship will result in good performance:

$$F_s \geq 1.25\ F_d \qquad \text{(Equation 7.11)}$$

The combined static and dynamic force, F_t, represents the maximum force applied during RDD loading. It can be calculated as follows:

$$F_t = F_s + F_d \qquad \text{(Equation 7.12)}$$

The combined static and dynamic forces should not exceed the strength of the pavement. One approach would be to limit the combined RDD loading to the allowable single axle load for the pavement to be tested. However, a vehicle applies dynamic forces to the pavement in excess of its static axle weights. This indicates that RDD loading somewhat higher than the allowable single axle load should be permissible. On the other hand, RDD loading is more damaging to pavements than normal vehicle loads in two respects. First, the RDD applies numerous load cycles to a small area of pavement in a single pass, while a vehicle applies a single cycle or only a few cycles. Second, the contact stress between the loading roller and the pavement is much higher than the contact stress beneath a pneumatic wheel. The high contact stress is of little consequence on rigid pavements but can cause rutting on flexible pavements. Currently there is little experience operating the RDD on flexible pavements, so care needs to be exercised in extending RDD testing to flexible pavements.

Decisions regarding allowable combined RDD loading should be made in consultation with those responsible for managing the pavement to be tested. The condition and properties of the pavement and the purpose and benefits of the study should be considered in making this decision.

The force and displacements should be monitored throughout testing to maintain safe levels. The pavement accelerations should also be monitored to make certain that sensor contact is maintained, as discussed in Section 7.2.1.3. If pavement accelerations become excessive, the dynamic force level can be reduced to bring accelerations down to safe levels. However, decreasing the operating frequency will do more to reduce pavement accelerations than will reducing dynamic force levels.

7.2.5 Rolling Sensor Positions

Another testing variable is the position of the rolling sensors. The rolling sensors and their towing system have been designed to afford flexibility in the positioning of the sensors. Possible arrangements for the rolling sensors are discussed in this section.

The most valuable displacement measurement would be the displacement at the loading point. Unfortunately, this is impractical for a rolling system. Further, space constraints prevent positioning of sensors adjacent to the loading rollers. As a practical matter, the best rolling sensor position is the midpoint between the loading rollers. A plan view showing this sensor position relative to the loading rollers is shown in Figure 7.11. This sensor is designated the centerline-in-line sensor. This designation indicates that the sensor is positioned at the centerline of the loading rollers and in line with the loading rollers.

It is the primary sensor position and provides a wealth of valuable information about the pavement system. All rolling sensor configurations should have a sensor in this position.

In addition to the centerline-in-line sensor, additional rolling sensors can be used to obtain further information about the pavement. The next most valuable sensors are leading-centerline sensors. An array utilizing leading-centerline sensors is shown in Figure 7.12. This array is useful for determining the deflection basin induced by the RDD loading. On jointed pavements, the displacement of leading sensors before and after they cross a joint is especially interesting. Decreases in displacement after a sensor crosses a joint indicate a poor connection or no connection between joints.

Outside sensors have also been used in RDD testing. These sensor locations, outside of the loading rollers, have not proven as valuable as the centerline sensors. However, the sensor array shown in Figure 7.13 may prove valuable in some instances. In this sensor array, two in-line-outside sensors straddle a longitudinal joint. These two sensors can be used to measure continuously the relative motion across the longitudinal joint to determine the joint efficiency.

Many other sensor array configurations are possible. With careful consideration, sensor arrays can be customized to meet the specialized needs of particular studies.

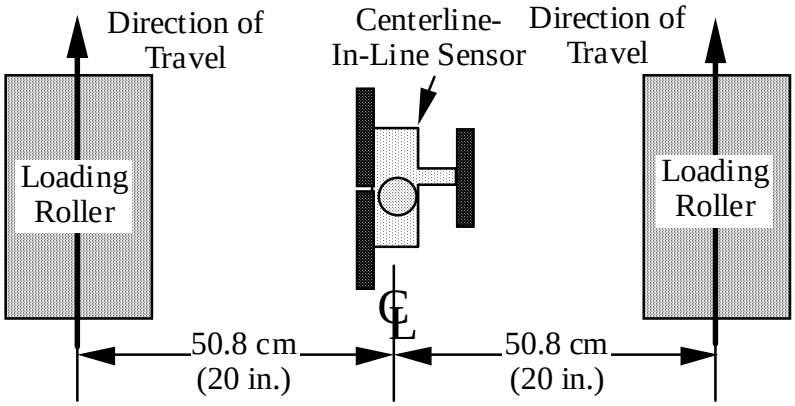

Figure 7.11 Plan View of the Centerline-in-Line Rolling Sensor Position Relative to the Loading Rollers

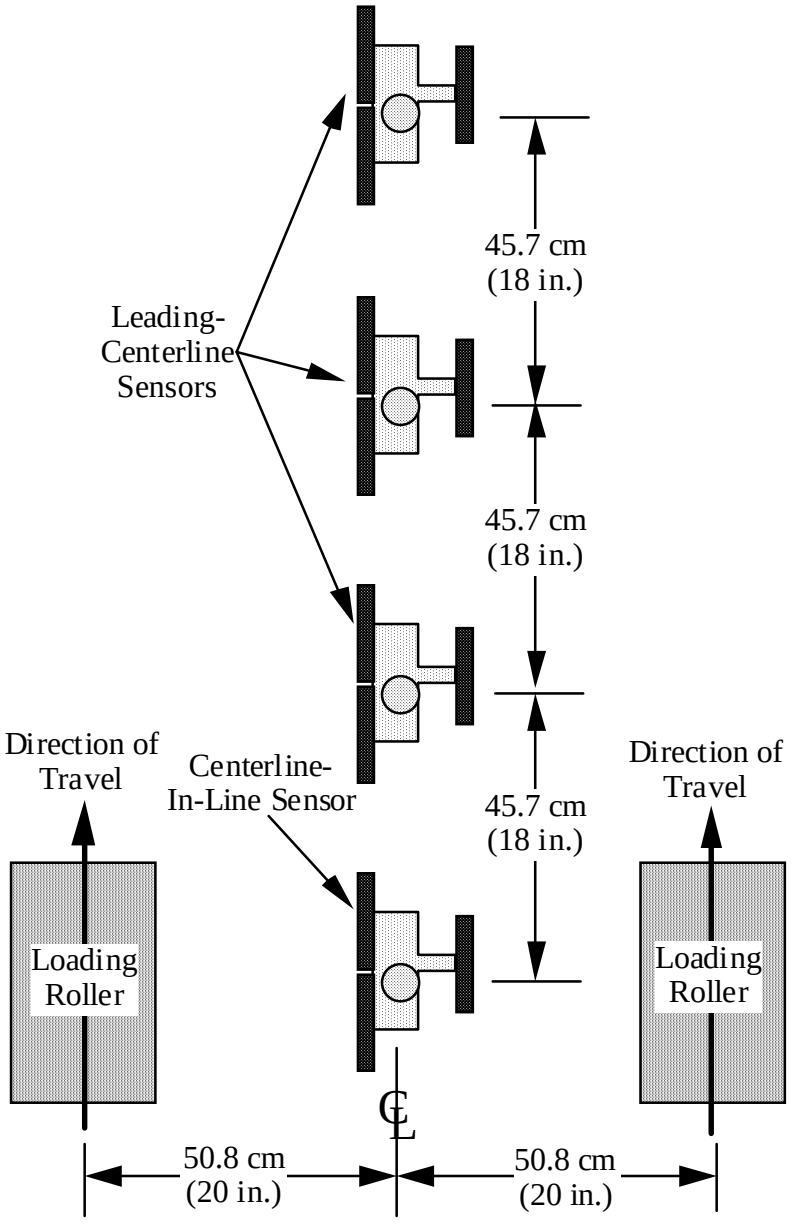

Figure 7.12 Rolling Sensor Array with Centerline-in-Line Sensor and Three Leading-Centerline Sensors

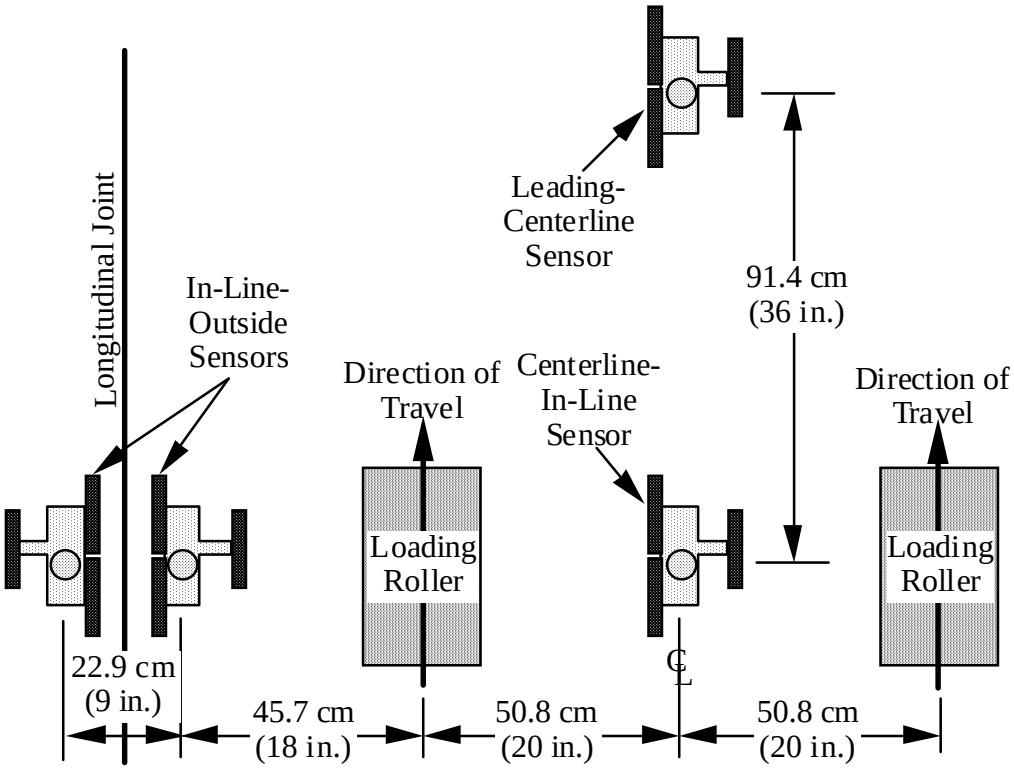

Figure 7.13 Rolling Sensor Array Utilizing Two Inline-Outside Sensors Straddling a Longitudinal Joint

7.3 STEP-BY-STEP ROLLING DYNAMIC DEFLECTOMETER TESTING PROCEDURE

This section contains step-by-step procedures for performing RDD tests. RDD operation requires two operators, one to drive the truck and the other to monitor the systems and keep a testing log. Additionally, support personnel such as traffic control are required.

Safety is of paramount concern in RDD testing. There are significant hazards in working near traffic and working on the truck near high-pressure hydraulic lines. The following steps minimize exposure to both hazards.

First, a safe staging area should be found close to the test location. The staging area should be out of traffic, flat, and on a surface conducive to crawling underneath the RDD. The following procedures should be performed at the staging area prior to testing:

1) Position sensors on towing system in the preselected pattern.
2) Power-up load cell conditioning circuits at least 20 minutes before beginning testing to obtain thermal equilibrium in load cells.
3) Set function generator to selected operating frequency.

4) Set data acquisition system (DAQ) sampling rate and anti-aliasing cut-off filter frequencies to selected values.
5) Pressure-up hydraulic system and operate lift system and shaking system at low frequencies to warm up hydraulic fluid.
6) With loading system lowered, adjust verticality by adjusting pressure in fore and aft air springs.
7) Attach distance encoder to rear wheel if high-speed travel will not be required in traveling to test location; otherwise, attach the encoder at the test site.

The traffic control crew should secure the testing location before the truck is driven to the location. After arriving, the RDD operators should remain inside the truck as much as possible to remain safe from traffic.

The following steps should be taken at the test location:

1) Lower load system at the beginning location of the test.
2) Adjust static force to selected value.
3) Pin stilt support arms in position. *Warning: this requires an operator to work near high-pressure hydraulic lines.*
4) Set distance counter to zero or appropriate starting position.
5) Note beginning position, test parameters, and data file name in testing log.
6) Begin shaking and adjust drive level to desired dynamic force level.
7) Start DAQ.
8) Start truck rolling at desired velocity along the pavement.
9) Operators should constantly monitor rolling velocity, static and dynamic force levels, displacements, hydraulic pressure, and hydraulic fluid temperature.
10) Note position of significant pavement features in the testing log, such as patches, failed sections, and bridges.
11) Where possible, test in continuous intervals of about one hour in length.
12) When stopping, shut down systems in this order: stop truck, stop shaking, and stop the DAQ.

After the testing is finished, but before leaving the test location, the following steps must be taken:

1) Unpin stilt support arms. *Warning: this requires an operator to work near high-pressure hydraulic lines.*
2) Raise and secure the loading system.
3) Remove the distance encoder from the truck wheel if high-speed travel is required to reach a secure area. *Warning: this requires an operator to work outside the truck near passing traffic.*

The RDD should then be taken to a secure area and the following procedures carried out:

1) Pressure-down the hydraulic system and idle for at least 15 to 20 minutes to cool system.
2) Power-down DAQ, load cell conditioning, and lift circuits.
3) Remove distance encoder from the truck wheel.
4) Remove rolling sensors from towing system if travel of more than a few miles is required prior to next testing location.

7.4 ADDITIONAL STATIONARY ROLLING DYNAMIC DEFLECTOMETER TESTS

Several additional stationary tests can be performed with the RDD. These tests are not conducive to performing while rolling, but can provide valuable information about site and pavement at discrete locations. These tests are: a depth-to-bedrock, or site response, test; a nonlinear pavement response test; and a pavement fatigue test. It may be desirable to couple the sensors to the pavement for these tests to avoid concerns about sensor contact.

7.4.1 Depth to Bedrock

This test involves driving the RDD with a sweep rather than sinusoidal dynamic force. The *sweep* gradually changes frequencies from about 5 Hz to 100 Hz. The displacements generated by this sweep are measured with the rolling sensors. A response for the site is calculated by dividing the measured displacement by the measured force, in the frequency domain. It is important to divide the displacement spectrum by the force spectrum so that the final response is independent of the nonuniform force spectrum applied by the RDD. The response curve can be used to select an operating frequency away from site resonances, as mentioned previously. The response curve can also be used to estimate the depth to bedrock, D, at the site (Roesset et al. 1995). The first-mode resonant frequency, f_n, of the site is selected from the response curve. An estimate must be made of the P-wave velocity, V_p, of the near-surface soil based upon the geology of the site. With these two pieces of information, an estimate of the depth to bedrock can be made using the following equation:

$$D = \frac{V_p}{4\, f_n} \qquad \text{(Equation 7.13)}$$

where f_n is the first-mode resonant frequency
V_p is the constrained compression wave velocity
D is the depth to bedrock or depth to stiff layer

7.4.2 Nonlinear Pavement Response

The RDD loading system is capable of driving most pavement systems into their nonlinear range. A simple test can be performed with the RDD to determine the force level where the pavement performance becomes significantly nonlinear. Because this test involves driving the pavement to high displacement levels, the sensors should be securely coupled to the pavement to avoid sensor contact problems.

To conduct a nonlinear response test, the pavement is driven at a selected frequency and the displacement is measured at the centerline-in-line sensor position as well as other positions. The test begins with a very low dynamic force level. As the test progresses, the drive level is slowly raised, increasing the dynamic force level. After reaching a selected maximum force level, the drive level is slowly decreased to the beginning level. These results can be presented in terms of force-displacement curves for each displacement sensor used.

7.4.3 Fatigue Testing

A fatigue test is another simple stationary test that can be performed with the RDD. In this test, a constant dynamic force is applied to a section of pavement over an extended period of time, and the displacement induced by this loading is continuously measured. Results are presented as displacement versus number of loading cycles. The number of cycles to the occurrence of fatigue damage is identified by an increase in displacement. The RDD is capable of applying many loading cycles of high loads in a very short period of time. For instance, operating at 40 Hz, 144,000 cycles of an 89 kN (20 kip) load can be applied in one hour.

7.5 ROUTINE MAINTENANCE FOR THE ROLLING DYNAMIC DEFLECTOMETER

The RDD contains many systems that require various maintenance procedures. The RDD operator should be familiar with the manufacturers' literature to properly maintain these systems. This section deals with additional procedures that should be performed on components that have been specially constructed or modified for the RDD. Very few maintenance procedures are required for these components, but they should be performed each day the RDD is operated.

The bearings on the loading rollers are in a dirty environment and are subjected to very harsh loading. A slow, constant flow of grease out of the bearing seals during operation assures that the inner bearing races remain moisture-free and clean. Accordingly, the bearings require daily lubrication. The rollers should be rotated during lubricating to distribute the grease. High quality grease should be added to the bearing housing until it flows out of the seals on both sides.

The RDD's high-frequency shaking has a tendency to loosen bolts, screws, and nuts. It is a good policy to periodically torque every fastener on the vehicle. Some especially critical fasteners should be checked daily. These include the load cell and bearing nuts, the towing system clamps, and the stilt structure support tie-rod ends.

One of the weakest and most stressed components on the RDD is the loading foot-guide rod joint shown in the photograph in Figure 7.14. If the bolts at this joint ever work loose, the socket will fail rapidly. Therefore, these bolts should be torqued daily.

The rolling sensors should also be checked daily. Their wheels should turn freely, but with no lateral movement. The shoulder bolts acting as axles must be firmly locked in place to prevent the loss of the wheels during testing.

The paths of all cables should be checked to make certain they are away from moving parts and pinch points.

7.6 SUMMARY

This chapter discussed the crucial RDD operating parameters. These parameters are: testing velocity along the pavement, operating (loading) frequency, sampling rate, static and dynamic force levels, and rolling sensor positions. Criteria were presented for selecting the best operating parameters for testing. Step-by-step operating procedures that permit safe operation of the RDD were then presented. Additionally, procedures are presented for conducting stationary RDD tests to determine depth to bedrock, the nonlinear response of the pavement, and the fatigue resistance of the pavement. Finally, a discussion of the maintenance required for the RDD was presented.

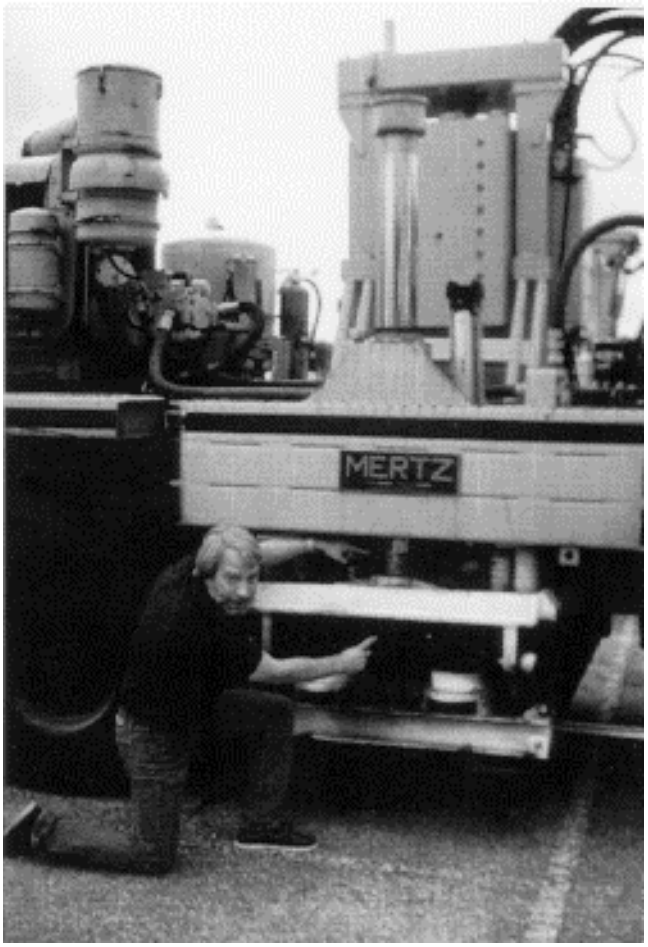

Figure 7.14 Photograph Showing Guide Rod Joint and Location of Bolts under Loading Foot

CHAPTER 8. DATA ANALYSIS PROCEDURE

8.1 INTRODUCTION

The equipment and procedures used in rolling dynamic deflectometer (RDD) testing are discussed in earlier chapters. For the RDD to be an effective tool in pavement management, data analysis procedures are also required. These procedures should include the means to determine the dynamic force applied by the RDD and the displacements induced by that load in the presence of rolling noise. The procedures should also include the means to determine the resolution and statistical confidence intervals of these results. The end result of the data analysis is a displacement profile for each rolling sensor.

Once the analysis described in this chapter is complete, the next step is to determine properties of the pavement system, based on the continuous displacement profiles. This analysis includes backcalculation to determine pavement moduli, analysis of pavement joints, and detection of cracks. Preliminary work on this additional analysis has been done by Roesset and Kim (Kim 1996) and McCullough et al. (1997). This second level of analysis is discussed in subsequent chapters in conjunction with discussions of testing results. In this chapter, the discussion is limited to the determination of displacement profiles.

8.2 AMPLITUDE DEMODULATION METHOD

The calculation of dynamic displacements and forces generated by the RDD uses the same demodulation operation performed by an AM (amplitude modulated) radio receiver. An AM radio transmitter takes an acoustic signal and multiplies the signal by (or in other words, modulates the signal with) a radio frequency carrier signal. This can be expressed mathematically as:

$$m(t) = s(t)\ sin(\omega_c t) + n(t) \qquad \text{(Equation 8.1)}$$

where $m(t)$ is the modulated signal

$s(t)$ is the acoustic signal

ω_c is the carrier frequency

$n(t)$ represents noise and radio signals at other frequencies

The AM radio receiver recovers the original acoustic signal $s(t)$ from the modulated signal $m(t)$ in the presence of noise and radio signals with other carrier frequencies.

The RDD displacement and force signals are very similar to the modulated radio signals. These signals can be described by the following equation:

$$g(t) = f(t)\ cos(\omega_o t - \phi(t)) + n(t) \qquad \text{(Equation 8.2)}$$

where $g(t)$ is an RDD force or displacement signal

f(t) is a function describing the continuous displacement or force amplitude with time

$\phi(t)$ is a function describing the continuous phase of the force or displacement signals with time

ω_o is the RDD operating frequency

n(t) represents noise, such as rolling noise

The only difference between Equation 8.1 and Equation 8.2 is an added term accounting for phase in Equation 8.2. In Equation 8.2, a continuous displacement or force function is modulated with the RDD operating frequency. The goal of RDD analysis is to recover the continuous displacement or force function, *f(t)*, from the RDD signal, *g(t)*, which includes noise. For now, the noise term, *n(t)*, is neglected in the demodulation, but it is added back into the analysis in the following section.

The RDD demodulation procedure must account for the phase term. This problem can be simplified by transforming the amplitude and phase functions, *f(t)* and $\phi(t)$, into two new functions, *a(t)* and *b(t)*, where:

$$f(t)\sin(\omega_o t - \phi(t)) = a(t)\cos\omega_o t + b(t)\sin\omega_o t \qquad \text{(Equation 8.3)}$$

where $f(t) = \sqrt{a^2(t) + b^2(t)}$

$$\phi(t) = \arctan\frac{b(t)}{a(t)}$$

The following common trigonometric relationships are used in demodulation:

$$(c\sin\omega_1 t)(d\sin\omega_2 t) = \frac{1}{2}cd\cos(\omega_1 - \omega_2)t - \frac{1}{2}cd\cos(\omega_1 + \omega_2)t \qquad \text{(Equation 8.4)}$$

$$(c\cos\omega_1 t)(d\cos\omega_2 t) = \frac{1}{2}cd\cos(\omega_1 - \omega_2)t + \frac{1}{2}cd\cos(\omega_1 + \omega_2)t \qquad \text{(Equation 8.5)}$$

$$(c\sin\omega_1 t)(d\cos\omega_2 t) = \frac{1}{2}cd\sin(\omega_1 - \omega_2)t + \frac{1}{2}cd\sin(\omega_1 + \omega_2)t \qquad \text{(Equation 8.6)}$$

$$(c\cos\omega_1 t)(d\sin\omega_2 t) = \frac{1}{2}cd\sin(\omega_1 + \omega_2)t - \frac{1}{2}cd\sin(\omega_1 - \omega_2)t \qquad \text{(Equation 8.7)}$$

These equations indicate that multiplying two sinusoids results in a combined signal consisting of a sinusoid with a frequency equal to the difference between the frequency of the two input signal frequencies, and a second sinusoid with a frequency equal to the sum of the two input signal frequencies. The amplitude of the two combined signals is equal to half the product of the two input signal amplitudes. For the RDD demodulation, all information is contained at a single frequency; thus, a homodyne demodulation procedure is used (Black

1953). In this case, $\omega_1 = \omega_2 = \omega$ in Equations 8.4 through 8.7. Substituting ω into the above equations yields:

$$(c \sin \omega t)(d \sin \omega t) = \frac{1}{2} cd - \frac{1}{2} cd \cos 2\omega t \quad \text{(Equation 8.8)}$$

$$(c \cos \omega t)(d \cos \omega t) = \frac{1}{2} cd + \frac{1}{2} cd \cos 2\omega t \quad \text{(Equation 8.9)}$$

$$(c \sin \omega t)(d \cos \omega t) = \frac{1}{2} cd \sin 2\omega t \quad \text{(Equation 8.10)}$$

$$c \cos \omega t \; d \sin \omega t = \frac{1}{2} cd \sin 2\omega t \quad \text{(Equation 8.11)}$$

The first step in demodulation is to multiply the modulated function by the complex function:

$$(\cos \omega_c t + i \sin \omega_c t)$$

where ω_c is the carrier frequency, and

$$i = \sqrt{-1}$$

Neglecting noise in RDD signals, this multiplication can be described as follows:

$$(f(t) \sin(\omega_o t - \phi(t)))(\cos \omega_o t + i \sin \omega_o t) =$$

$$(a(t) \cos \omega_o t + b(t) \sin \omega_o t)(\cos \omega_o t + i \sin \omega_o t) =$$

$$\frac{1}{2} a(t) + \frac{1}{2} a(t) \cos 2\omega_o t + \frac{1}{2} i\, a(t) \sin 2\omega_o t +$$

$$\frac{1}{2} b(t) \sin 2\omega_o t + \frac{1}{2} i\, b(t) - \frac{1}{2} i\, b(t) \cos 2\omega_o t \quad \text{(Equation 8.12)}$$

The product of this multiplication can be separated into two parts. First, the functions *a(t)* and *b(t)* times a constant, and, second, the functions *a(t)* and *b(t)* multiplied by sinusoidal functions with a frequency of $2\omega_o$. To recover the functions *a(t)* and *b(t)* from the product in Equation 8.12, the product can be filtered with a filter that rejects the frequency $2\omega_o$. The design of this filter is a critical part of demodulation. Later sections will deal with filter design. However, a low-pass filter with a cut-off frequency less than $2\omega_o$ is one that will work. This is shown below:

$$2\left[\frac{1}{2}a(t) + \frac{1}{2}a(t)\cos 2\omega_o t + \frac{1}{2}ia(t)\sin 2\omega_o t\right.$$

$$+\frac{1}{2}b(t)\sin 2\omega_o t+\frac{1}{2}ib(t)-\frac{1}{2}ib(t)\cos 2\omega_o t\Big]\underset{\rightarrow}{L-P}$$

$a(t) + i\ b(t)$ (Equation 8.13)

where $\underset{\rightarrow}{L-P}$ represents an appropriate low-pass filter.

Once the functions *a(t)* and *b(t)* are recovered, the amplitude and phase functions *f(t)* and $\phi(t)$ can be calculated using the following equations:

$$f(t) = \sqrt{a^2(t) + b^2(t)} \quad \text{(Equation 8.14)}$$

$$\phi(t) = \arctan\frac{b(t)}{a(t)} \quad \text{(Equation 8.15)}$$

To illustrate this demodulation procedure, arbitrary amplitude and phase functions, *f(t)* and $\phi(t)$, were generated. These functions are shown in Figure 8.1. These arbitrary functions were used in Equation 8.2 to synthesize the modulated waveform, *g(t)*, shown in Figure 8.2. This synthesized waveform is similar to a force or displacement RDD record. It models an RDD waveform with a sampling frequency of 150 Hz and an operating frequency of 4 Hz. This operating frequency is lower than would typically be used for RDD testing but is used here to make the waveforms easier to visualize in these figures. The real and imaginary demodulation products were calculated using Equation 8.2. These products are shown in Figure 8.3. The demodulation products were then filtered to generate the functions *a(t)* and *b(t)* as shown in Equation 8.13. These results are presented in Figure 8.4. The amplitude and phase functions were then recovered using Equations 8.14 and 8.15. These recovered functions, presented in Figure 8.5, are identical to the original functions in Figure 8.1.

The recovered force and displacement amplitude functions are of paramount importance in RDD data analysis. The phase must be properly taken into account, but it contains little useful information about the pavement system.

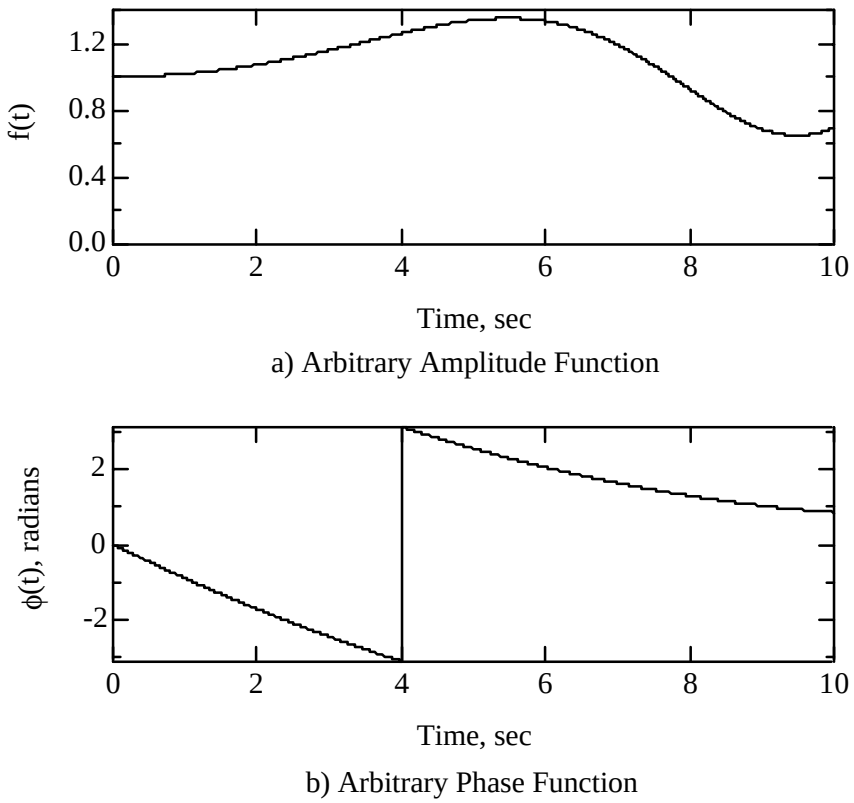

Figure 8.1 Arbitrary Amplitude and Phase Functions Used to Synthesize a Modulated RDD Waveform

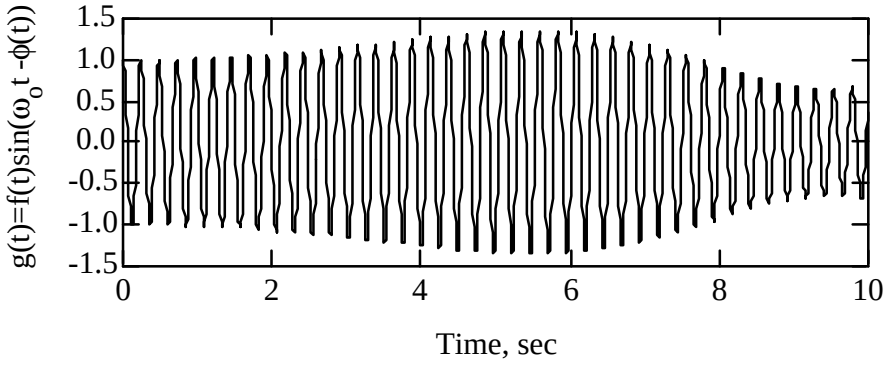

Figure 8.2 Synthesized Modulated Waveform Modeling an RDD Displacement or Force Signal with an Operating Frequency of 4 Hz

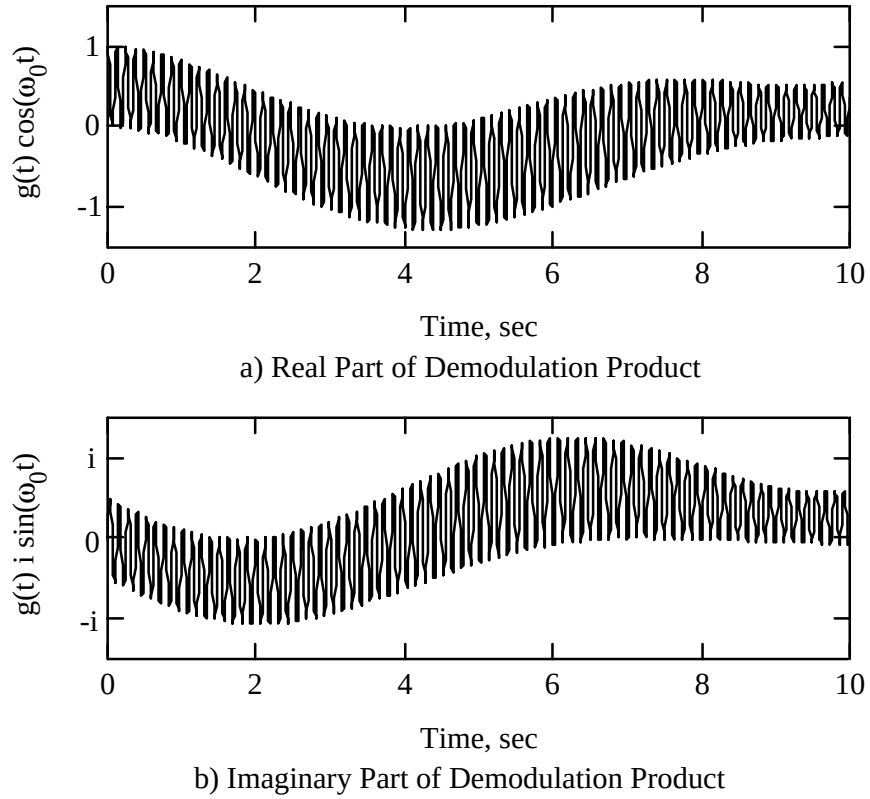

Figure 8.3 Real and Imaginary Parts of the Demodulation Product from the Synthesized Waveform in Figure 8.2

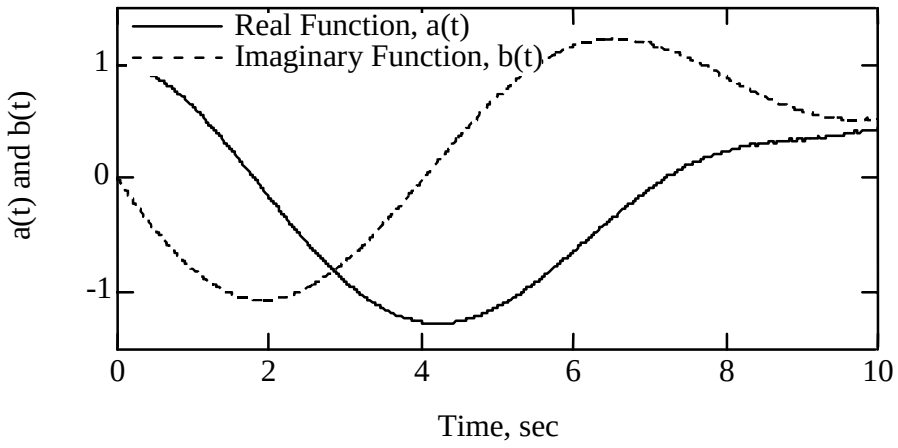

Figure 8.4 Functions a(t) *and* b(t) *Obtained by Filtering the Demodulation Products from Figure 8.3*

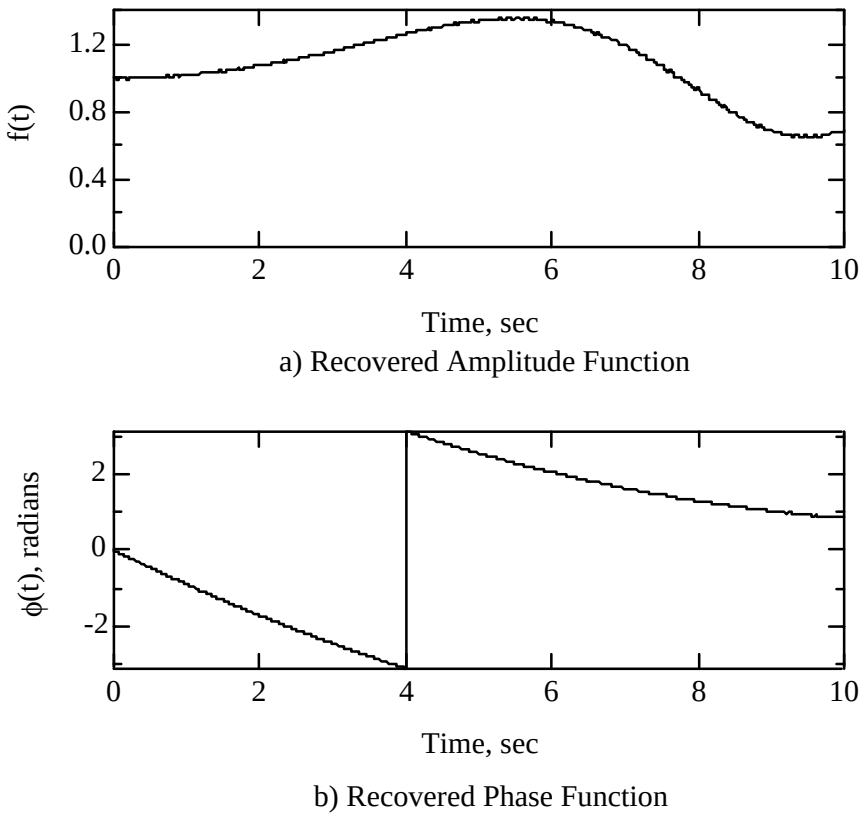

Figure 8.5 Amplitude and Phase Functions Recovered from the Demodulation Procedure Illustrated in Figures 8.1 through 8.4

8.3 NOISE IN DEMODULATION

The discussion of demodulation thus far has considered only a noiseless signal. To illustrate the effect of noise on RDD signals, a displacement signal with a 40-Hz sinusoidal component and a random noise component was synthesized. The spectrum of the noise was shaped to simulate rolling noise in an RDD rolling sensor. A 1-second interval of this synthesized waveform is shown in Figure 8.6. The spectrum of this composite signal is shown is Figure 8.7. The 40-Hz sinusoidal component represents the displacement induced by the RDD loading and is the spike in the spectrum. Energy at a single frequency, like the induced displacement, is referred to as *monochromatic.* The rolling noise is the distributed component in the spectrum.

In demodulation, the waveform containing the monochromatic and distributed energy is multiplied by the function, $cos\ \omega_o t + i\ sin\ \omega_o t$. The spectrum of the product of this multiplication is similar to the original spectrum, but all of the frequencies are shifted. Equations 8.4 through 8.7 describe these frequency shifts.

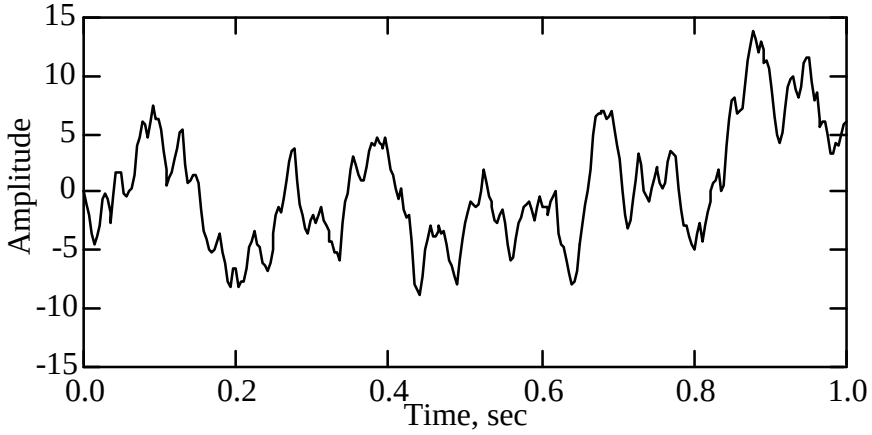

Fig. 8.6 Simulated Rolling Sensor Output Waveform Containing Rolling Noise and Displacements Induced by RDD Loading

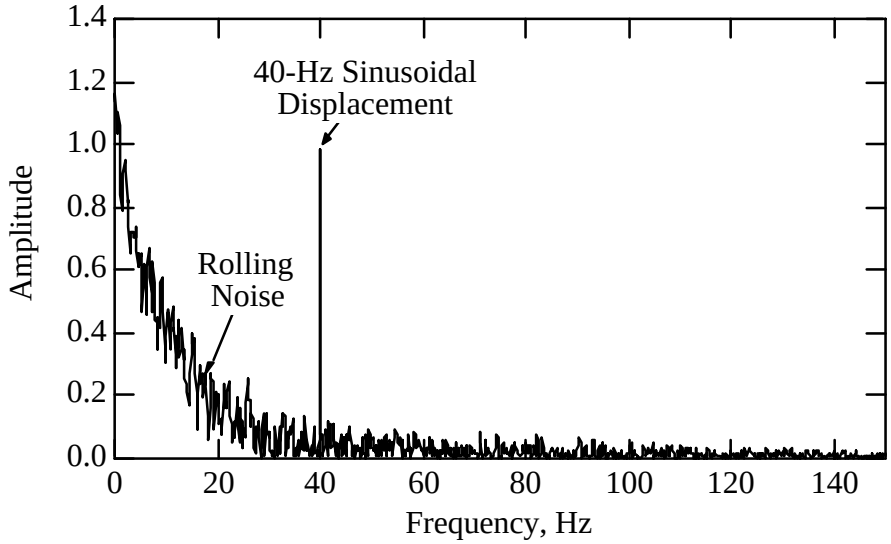

Figure 8.7 Spectrum of Waveform Shown in Figure 8.6, which consists of Rolling Noise and Displacement Induced by RDD Loading

A plot of the spectrum of the demodulation product of the waveform shown in Figure 8.6, demodulated about 40 Hz, is shown in Figure 8.8. This spectrum contains monochromatic energy at 0 Hz and 80 Hz. The amplitude of the monochromatic component is half the amplitude of the monochromatic component in the original spectrum. The distributed energy in Figure 8.8 has the same shape as the distributed energy in the spectrum shown in Figure 8.7, with the shape appearing as two mirror images. Again, the amplitude of the distributed component of the spectrum is one-half the amplitude in the original spectrum.

The spectrum in Figure 8.8 shows energy occurring at negative frequencies. The waveform that produced this spectrum is a complex-valued waveform; accordingly, negative-

valued frequencies have physical meaning. If the complex-valued waveform is viewed as rotating vectors, then the frequency represents the rate of rotation, with the sign of the frequency representing the direction of rotation. Positive-valued frequencies have rotation in the counter-clockwise direction.

The last step in the demodulation procedure is to isolate the monochromatic energy at 0 Hz. This is done with filters. An expanded plot of the region of the spectrum around 0 Hz is shown in Figure 8.9. The spike of monochromatic energy at 0 Hz and the distributed rolling noise energy can be seen in this figure. A series of filter responses from 0-Hz notch-pass filters with different bandwidths is also shown in Figure 8.9. Narrower filters will reject the energy from rolling noise, traffic noise, or other distributed energy sources to a greater extent than will wider filters. The amplitude of the portion of the filtered waveform that is a result of distributed energy will be proportional to the square root of the filter bandwidth.

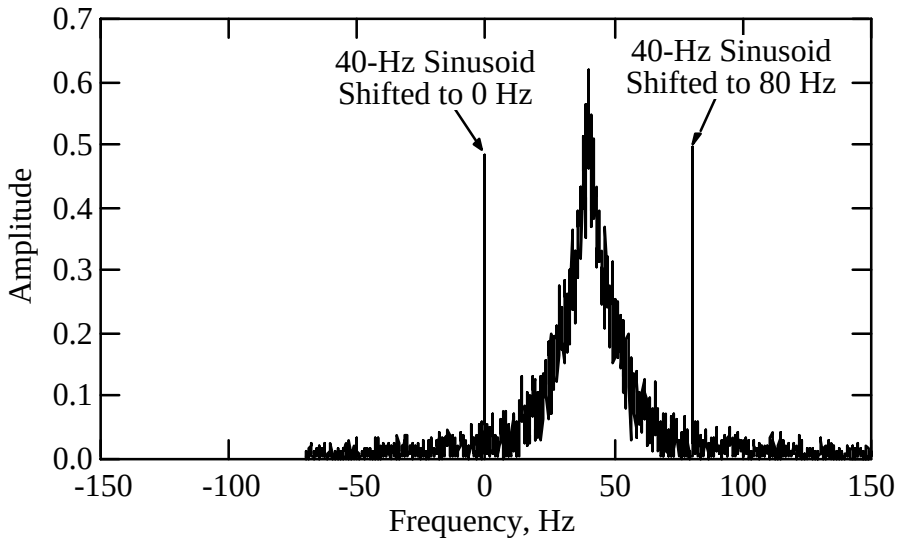

Figure 8.8 Spectrum of Demodulation Product of the Waveform Shown in Figure 8.6, Demodulated about 40 Hz

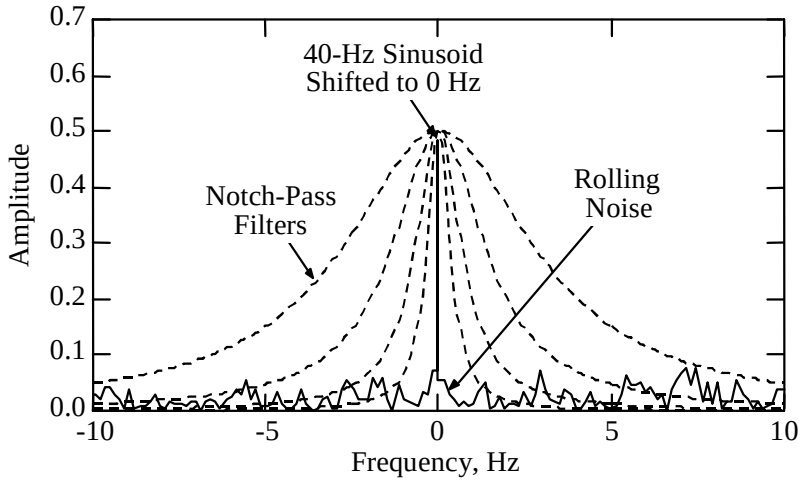

Figure 8.9 Expanded Section of Demodulation Product Spectrum Showing Several Notch-Pass Filter Responses

Monochromatic energy occurs in an infinitesimally narrow frequency band. This means that the energy at 0 Hz will not be rejected, no matter how narrow the notch pass filter centered at 0 Hz is made. This point indicates that narrower filters will result in high-quality analysis results. However, trade-offs must be made between filter width and spatial resolution. These trade-offs are discussed in the following section.

8.4 DIGITAL FILTER DESIGN

Filtering is required to isolate the demodulated signal at 0 Hz within the total demodulation product signal. There are many filters that can be used for this task. The variables that affect the performance of a filter are the filter bandwidth, the settling time, and the attenuation in the reject bands. The design of two such filters (a composite IIR and FIR filter, and a Hamming FIR filter) are discussed below.

8.4.1 Composite IIR and FIR Filter

8.4.1.1 General IIR Filter Design — A convenient filter to use in isolating the 0-Hz monochromatic energy in a demodulation product is an infinite-impulse-response digital filter (Bracewell 1986, and Ifeachor and Jervis 1993). This type of filter can be designed by positioning poles and zeros in the Z-domain. The transformation from frequency to Z-domain is:

$$z = e^{-i\ 2\pi\ f/f_s} \qquad \text{(Equation 8.16)}$$

where z is a complex-valued variable in the Z-domain

f is frequency

f_s is the sampling frequency

A plot of the Z-domain is shown in Figure 8.10. All values for *z* in Equation 8.16 plot on the unit circle, with 0 Hz corresponding to (1,0), and the Nyquist frequency corresponding to (-1,0).

Digital filters can be designed by positioning poles and zeros in the Z-domain. For stable filters, poles must be placed inside the unit circle and zeros on or inside the unit circle. Generally, to obtain a filter that will result in real output with real input, complex poles and zeros should come in complex conjugate pairs.

The response of an IIR digital filter in the Z-domain, *H(z)*, is:

$$H(z) = \frac{(z-r_1)(z-r_2)(z-r_3)...(z-r_n)}{(z-p_1)(z-p_2)(z-p_3)...(z-p_n)} \qquad \text{(Equation 8.17)}$$

where *H(z)* is the filter response

r_n is a complex value corresponding to the n^{th} zero location

p_n is a complex value corresponding to the n^{th} pole location

8.4.1.2 Design of IIR Digital Filter — A 0-Hz notch-pass filter for RDD analysis can be obtained by placing one or more poles on the real axis between 0 and 1. A two-pole filter, with both poles at (p,0), gives good results. The bandwidth of the filter can be adjusted by varying the value, *p*. The responses of several such filters are plotted in the frequency domain in Figure 8.11. Frequencies are normalized relative to the sampling frequency, f_s, to generalize the filter design procedure. A filter bandwidth, BW_{20}, is defined as the width of the filter response at -20 dB. A value of -20 dB corresponds to a filter response amplitude of 0.1 or a reduction in amplitude by a factor of 10. It can be noted that as the value of *p* approaches 1.0, the filter becomes narrower, and the filter reject-band attenuation increases. The signal will undergo further filtering, but at this stage the reject attenuation should be at least -30 dB. This indicates that poles should be greater than 0.8. If a band filter wider than this is needed, a new IIR digital filter can be designed incorporating zeros to obtain the necessary attenuation.

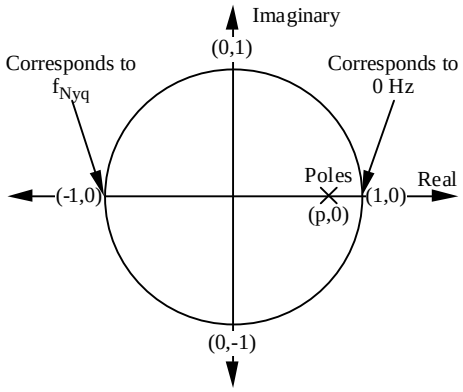

Figure 8.10 Plot of Unit Circle in the Z-Domain Showing Location of Poles for 0-Hz IIR Digital Notch-Pass Filter

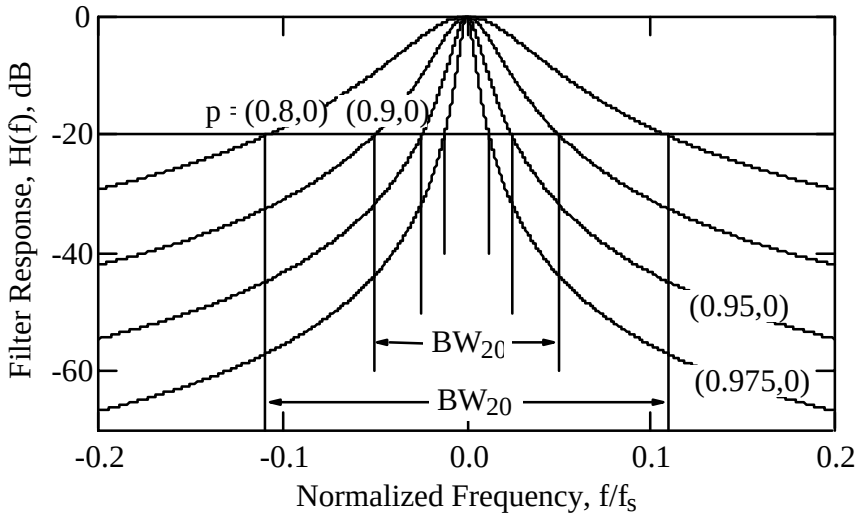

Figure 8.11 Notch-Pass Filter Responses of 0.0 Hz IIR Digital Notch-Pass Filters

The filter response of the two-pole, notch-pass filter in the Z-domain is:

$$H(z) = (1-p)^2 \frac{1}{(z-p)(z-p)} \qquad \text{(Equation 8.18)}$$

Multiplying out the denominator yields:

$$H(z) = (1-p)^2 \frac{1}{z^2 - 2pz + p^2} \qquad \text{(Equation 8.19)}$$

The term $(1-p)^2$ is a gain required to obtain a filter response of 1 at 0 Hz. It is most conveniently and efficiently applied after filtering the data. So an unscaled filter response function, *H'(z)*, is defined. The filter equation in canonical form is:

$$H'(z) = \frac{z^0}{z^0 - 2pz^{-1} + p^2 z^{-2}} \qquad \text{(Equation 8.20)}$$

The filter equation then becomes:

$$y'_n = x_n + 2p\, y'_{n-1} - p^2\, y'_{n-2} \qquad \text{(Equation 8.21)}$$

where y'_n is the n^{th} term of the unscaled filter output

x_n is the n^{th} term of the filter input

p is a pole value on the real axis, $0 < p < 1$

The scaled filter output is:

$$y_n = (1-p)^2\, y'_n \qquad \text{(Equation 8.22)}$$

where y(n) is the scaled filter output.

A plot of the BW_{20} values for several poles between 0.8 and 1 is presented in Figure 8.12. From this plot it can be seen that a good estimate of BW_{20} for this two-pole notch-pass filter can be expressed as:

$$BW_{20} \approx f_s (1\text{-}p) \qquad \text{(Equation 8.23)}$$

for $0.8 < p < 1.0$

Narrower notch-pass filters will result in increased noise attenuation and, hence, more accurate results. However, there is an important trade-off between filter bandwidth and filter settling time. The settling time of a filter represents the time required for the filter to respond to a change in input. To illustrate this effect, a sinusoidal waveform with a frequency of $4f_s$ was generated. This waveform initially has an amplitude of 1, but the amplitude abruptly decreases to 0. This waveform is shown in Figure 8.13. A normalized time scale, tf_s, is used to generalize the results for all sampling frequencies.

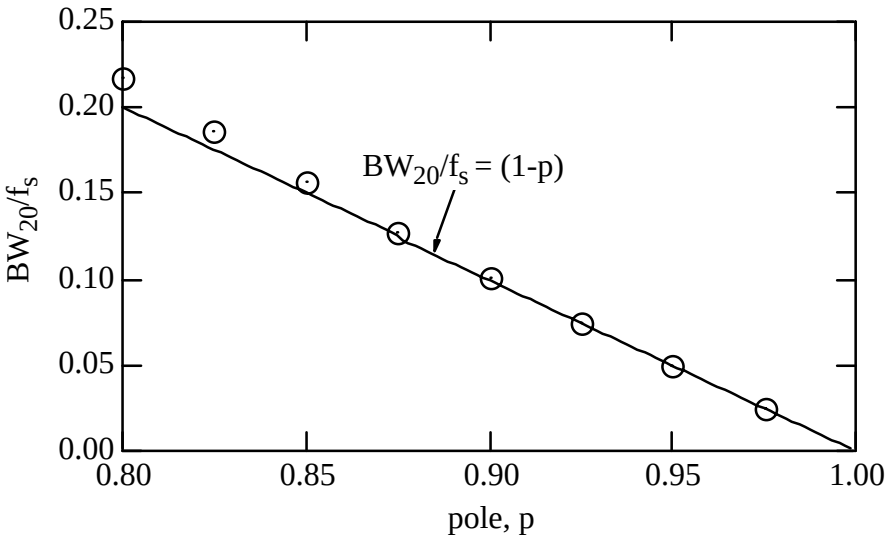

Figure 8.12 Relationship between BW_{20} and Pole Position for Two-Pole, Notch-Pass Filter

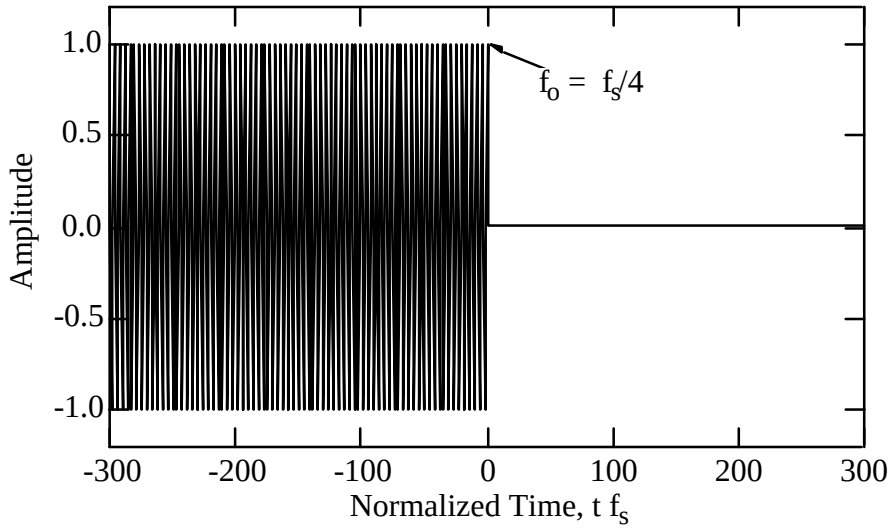

Figure 8.13 Synthesized Waveform with Abruptly Decreasing Amplitude Used to Evaluate Filter Settling Times

A demodulation product of the waveform in Figure 8.13 was calculated and filtered using several filters with a range of poles from 0.8 to 0.975. Several of these filtered waveforms are presented in Figure 8.14. Again, these results are plotted relative to normalized time, tf_s, so that the results can be generalized for all sampling frequencies. A time interval, t_{90}, is defined as the time interval required for a filter to settle 90 percent of the way to its final steady-state output. As pole values, p, approach 1.0, this settling time increases. Filter settling times, t_{90}, are plotted relative to a function of p in Figure 8.15. A value for t_{90} can be calculated using the following equation:

$$t_{90} = \frac{\frac{3.89}{(1-p)} - 2}{f_s} \qquad \text{(Equation 8.24)}$$

The filter settling time effectively "smears" the results. The results can be imagined to be a weighted average over a t_{90} interval of time. For example, if an RDD test were performed with a rolling velocity of 0.3 m/s (1ft/sec), and a spatial resolution of 0.3 m (1 ft) is required, then a pole value should be selected so that $t_{90} = 1$ *sec*. By rearranging Equation 8.24, a value of p can be calculated as follows:

$$p = 1 - \frac{3.89}{t_{90} f_s + 2} \qquad \text{(Equation 8.25)}$$

A procedure that can be used to estimate confidence intervals of the result for a given filter is presented in a subsequent section in this chapter.

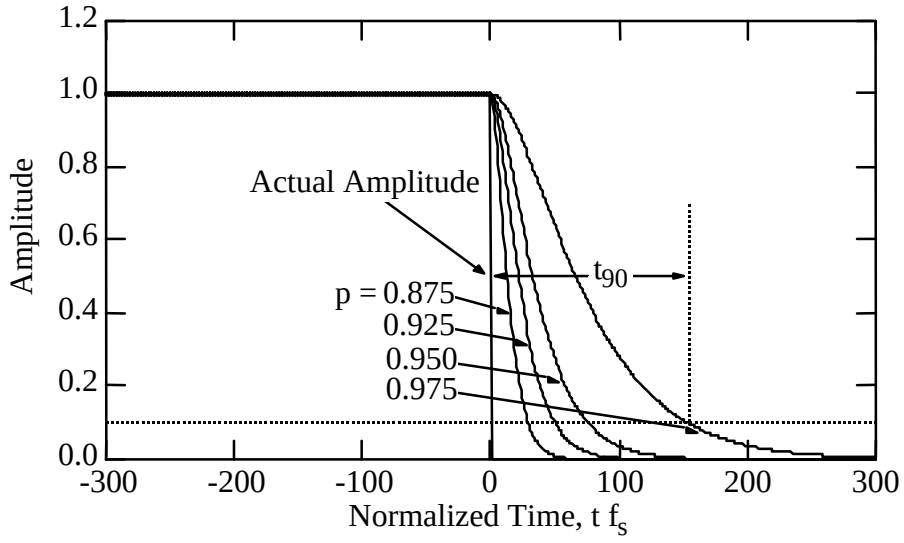

Figure 8.14 Amplitudes of Waveform Shown in Figure 8.13 Determined Using Several Digital Filters, Illustrating Filter Settling Time

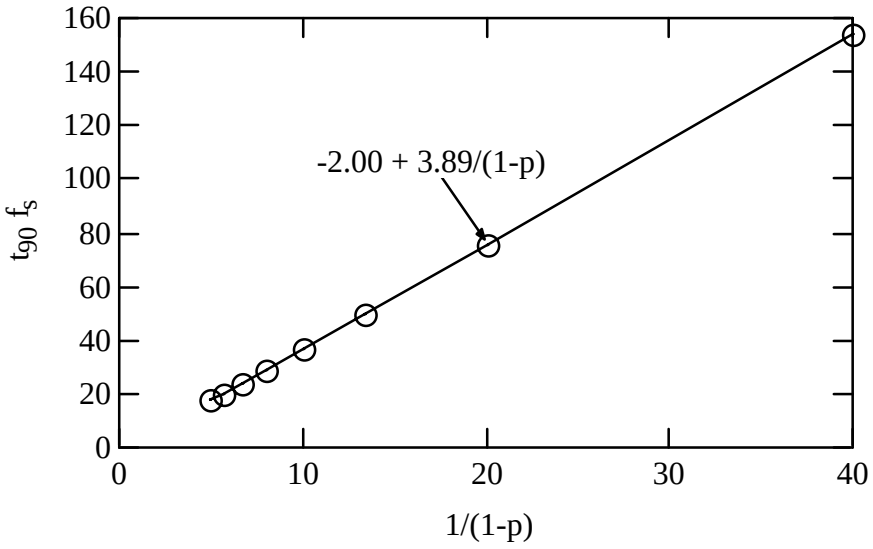

Figure 8.15 Relationship between Pole Value and Filter Settling Time for 0-Hz Two-Pole Digital IIR Notch-Pass Filter

8.4.1.3 Forward and Reverse Filtering — The "smearing" effect just described can lead to small time shifts in the data. One benefit in using digital filters is that this time shift can be canceled by filtering the data from the beginning to the end, and then from the end back to the beginning with the same filter. Any time shift will be negated because it will occur equally in both directions.

To accomplish this, a two-way filter is needed with a response equal to the square root of the one-way filter:

$$H''(z) = \sqrt{H'(z)} \qquad \text{(Equation 8.26)}$$

where *H''(z)* is an unscaled two-way filter

H'(z) is the unscaled one-way filter discussed in Section 8.4.1.2.

The poles of the two-pole filter are already designed to lie on the real axis. This means that the poles need not have a complex conjugate; therefore, a single pole filter with a pole in the same location will satisfy Equation 8.26. This filter can be described as:

$$H''(z) = \frac{1}{(z-p)} \qquad \text{(Equation 8.27)}$$

This can be expressed in canonical form as:

$$H''(z) = \frac{z^0}{(z^0-pz^{-1})} \qquad \text{(Equation 8.28)}$$

When this filter is applied in both directions, the same pole values, *p*, will result in a gain factor, bandwidth, and settling time for the two-way filter that are exactly the same as those for the one-way filter. This filter can be applied as follows:

$$y''_n = x_n + p\, y''_{n-1} \text{ , then}$$
$$y'_{N-n} = y''_{N-n} + p\, y'_{N-n-1} \text{ , then}$$
$$y_n = y'_n (1-p)^2 \qquad \text{(Equation 8.29)}$$

where y''_n is the unscaled one-way filter output

x_n is the filter input

y'_n is the unscaled two-way filter output

N is the total number of data points in the filter input

y_n is the scaled two-way filter output

To demonstrate the two-way filter, equivalent one-way and two-way filters were applied to the demodulation product of the waveform presented in Figure 8.13. A pole value, *p*, of 0.95 was used for both filters. These results are shown in Figure 8.16. This figure illustrates the time shift from a one-way filter and the manner in which a two-way filter corrects the time shift.

Two-way filtering cannot be applied in real-time data processing because the process requires a complete data set. The benefits of two-way filtering are marginal, and the errors owing to a time shift with a one-way filter will always be less than t_{90}. However, for highest-quality results, two-way filtering should be used if the data are analyzed after testing.

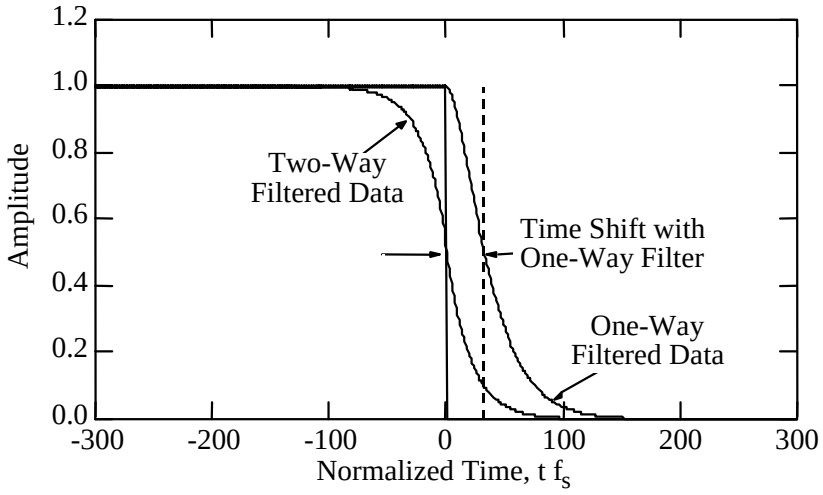

Figure 8.16 One-Way and Two-Way Filtered Data Using a Pole Value of 0.95

8.4.1.4 Addition of FIR Decimating Filter — Typical RDD sampling rates are between 150 Hz and 300 Hz. Reasonable filter settling times, t_{90}, are from 0.25 seconds to 2.0 seconds. This means that each time interval, t_{90}, will contain anywhere from 30 to 600 data points. These points are not independent, but represent a weighted average of values over a time interval of about t_{90}. This means that there is no real benefit from keeping all the data points. Furthermore, files containing data results would be too large to conveniently manipulate on common personal computers without reducing the number of data points.

One way to reduce the number of data points is to average values over some time interval. This is equivalent to a finite-impulse-response (FIR) digital averaging filter with decimation (Ifeachor and Jervis 1993). Decimation refers to a filtering procedure that has fewer points in its output than its input. The decimating FIR digital filter that averages N_{avg} data points is:

$$y_n = \frac{\sum_{j=0}^{N_{avg}-1} x_{n \times N_{avg} + j}}{N_{avg}} \qquad \text{(Equation 8.30)}$$

where y_n is n^{th} output of the decimating filter

N_{avg} is the number of points averaged per output point

x_n is the filter input

This filter will average points over a time interval of:

$$t_{avg} = \frac{N_{avg}}{f_s} \qquad \text{(Equation 8.31)}$$

where t_{avg} is the time interval the filter averages.

The frequency response for this filter is:

$$H(f) = \text{sinc}(f\, t_{avg}\, \pi) = \frac{\sin(f\, t_{avg}\, \pi)}{f\, t_{avg}\, \pi} \qquad \text{(Equation 8.32)}$$

where *H(f)* is the filter frequency response.

The magnitude of the frequency response is plotted relative to a normalized frequency, $f\ t_{avg}$, in Figure 8.17. The response of this filter consists of a primary lobe, centered about a frequency of zero, and side lobes. Between each of the lobes, the amplitude of the filter response drops to zero. These frequencies between lobes correspond to the frequencies that are periodic in the time interval t_{avg}.

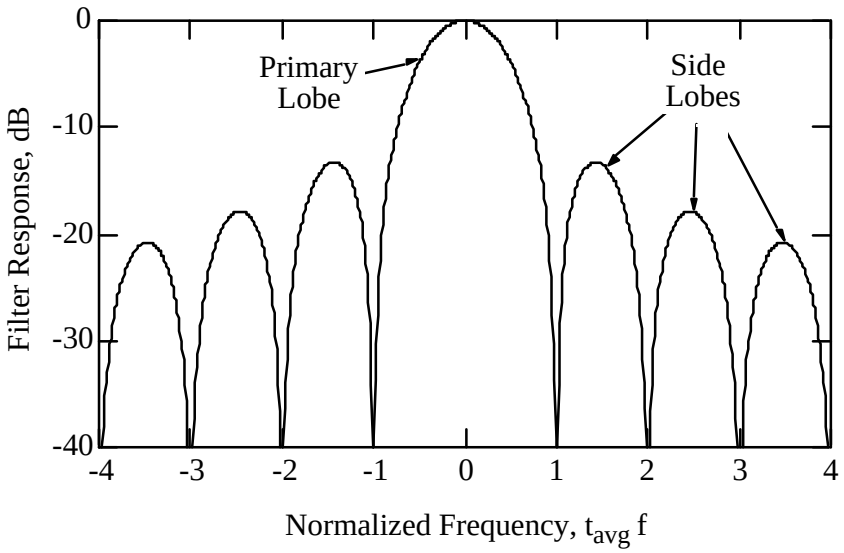

Figure 8.17 Response of FIR Digital Filter That Averages Data over a Time Interval of t_{avg}

The IIR digital filter, described in the previous section, averages the data over a time interval of t_{90}. Because t_{90} represents the approximate chronological resolution of the measurement, the FIR digital filter should average over the same interval to maintain this approximate resolution. To average over an interval of t_{90}, the number of points to average, N_{avg}, is:

$$N_{avg} \geq t_{90}\, f_s \qquad \text{(Equation 8.33)}$$

If this equation does not result in an integer value for N_{avg}, it should be rounded up to the nearest integer value. The filter response of the FIR averaging digital filter relative to N_{avg} and f_s can be expressed as:

$$H(f) = \text{sinc}\left(N_{avg}\, \pi \frac{f}{f_s}\right) \qquad \text{(Equation 8.34)}$$

The filter response of a 0-Hz two-pole notch-pass IIR digital filter with poles, p, at 0.95 is shown in Figure 8.18. Using Equation 8.24, for $p = 0.95$, it can be determined that $t_{90}\, f_s = 75.8$. This means, according to Equation 8.33, that 76 points should be averaged to maintain the chronological resolution of the IIR filter. A response for the FIR filter, with $N_{avg} = 76$, was calculated using Equation 8.34 and plotted in Figure 8.18. The effect of both filters is the product of the two filter responses. This product is also shown in Figure 8.18. The frequency axis is normalized frequency, f/f_s, to make the result independent of sampling frequency.

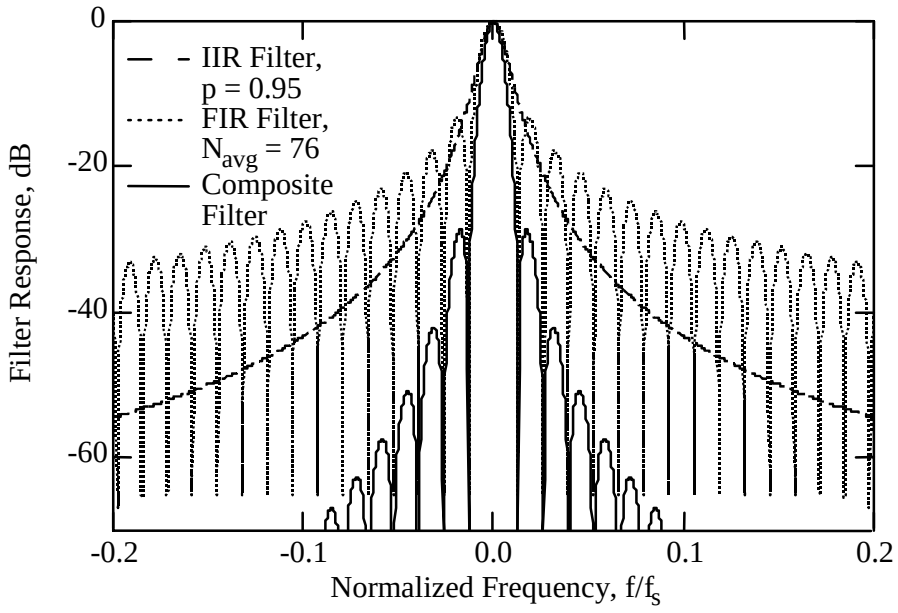

Figure 8.18 Responses of IIR Digital Filter and FIR Averaging Digital Filter and the Composite of the Two Filters

The shape and width of the primary lobe of the FIR averaging filter correspond very closely to the shape and width of the IIR filter response at frequencies near 0. However, the side lobes of the FIR filter have poor attenuation relative to the IIR filter. The composite of the two filters results in a filter response that is superior to either of the individual filters, in that it has a slightly narrower pass-band and substantially more attenuation in the reject bands.

The result of using a decimating FIR averaging digital filter after the IIR filtering is to increase the noise attenuation and reduce the number of data points, while still maintaining the same spatial or chronological resolution in the final result.

8.4.2 Design of Hamming FIR Filter

The previous sections have explained a filtering procedure that applies both an IIR digital notch-pass filter and a decimating FIR filter to the demodulation product of RDD waveforms. Similar results can be obtained by filtering the demodulation product with a more complicated decimating FIR digital filter. This procedure is similar to the approach presented by the author in 1995 (Bay et al. 1995), except that a Hamming window is used instead of the Hanning window.

An FIR digital notch-pass filter that has a frequency response and a settling time similar to that of the composite filter presented in previous sections can be designed using the window method of calculating FIR filter coefficients (Ifeachor and Jervis 1993). There are four steps in designing an FIR filter using the windowing method. First, the ideal frequency response, $H_D(f)$, of the filter is determined. Second, an impulse response, $h_D(t)$, of the ideal filter is obtained by evaluating the inverse Fourier transform of $H_D(f)$. Third, a windowing function, $w(t)$, is selected that has the desired attenuation and pass-band characteristics. Tables of possible windows and their characteristics are available in most signal processing texts. Fourth, the impulse response is multiplied by the windowing function to obtain the filter coefficients, $h(t)$, as follows:

$$h(t) = h_D(t)\, w(t). \qquad \text{(Equation 8.35)}$$

The ideal filter for this application is an impulse function at a frequency of 0. This ideal filter response is shown in Figure 8.19a. The inverse Fourier transform of an impulse at a frequency of 0 is an infinite time series with a value of 1. This time series is shown in Figure 8.19b. The window selected is a Hamming window. The equation for this window is:

$$w(n) = \begin{cases} 1 + 0.8519 \cos\left(\dfrac{2\pi n}{N_{win}}\right) & \text{for } |n| < \dfrac{N_{win}}{2} \\ 0 \quad \text{elsewhere} \end{cases} \qquad \text{(Equation 8.36)}$$

where $w(n)$ is the window function

N_{win} is the number of sampled points in a window

The product of the window function and the unity time series is the window function; therefore, the filter coefficients are the window function. These functions are plotted relative to normalized time, t/t_{win}. This represents time divided by the width of the window and can be calculated as follows:

$$t/t_{win} = \frac{t\, f_s}{N_{win}} \qquad \text{(Equation 8.37)}$$

where f_s is the sampling frequency.

The decimating version of this Hamming FIR filter is applied as follows:

$$y_j = \frac{\sum_{n=0}^{N_{win}-1} x_{(n+jN_{win}/2)} \left(1 - 0.8519 \cos\left(\frac{2\pi n}{N_{win}}\right)\right)}{N_{win}} \qquad \text{(Equation 8.38)}$$

where y_j is j^{th} output of the decimating filter

N_{win} is an even integer, representing the number of sampled points in the window

x_i is the i^{th} sample in the input waveform

This decimating Hamming FIR filter applies a weighted-average filter to segments of data N_{win} long. So that all data receive nearly the same total weight in the analysis, successive windows overlap by $N_{win}/2$ data points. A series of successive Hamming windows, as applied in Equation 8.38, is shown in Figure 8.20.

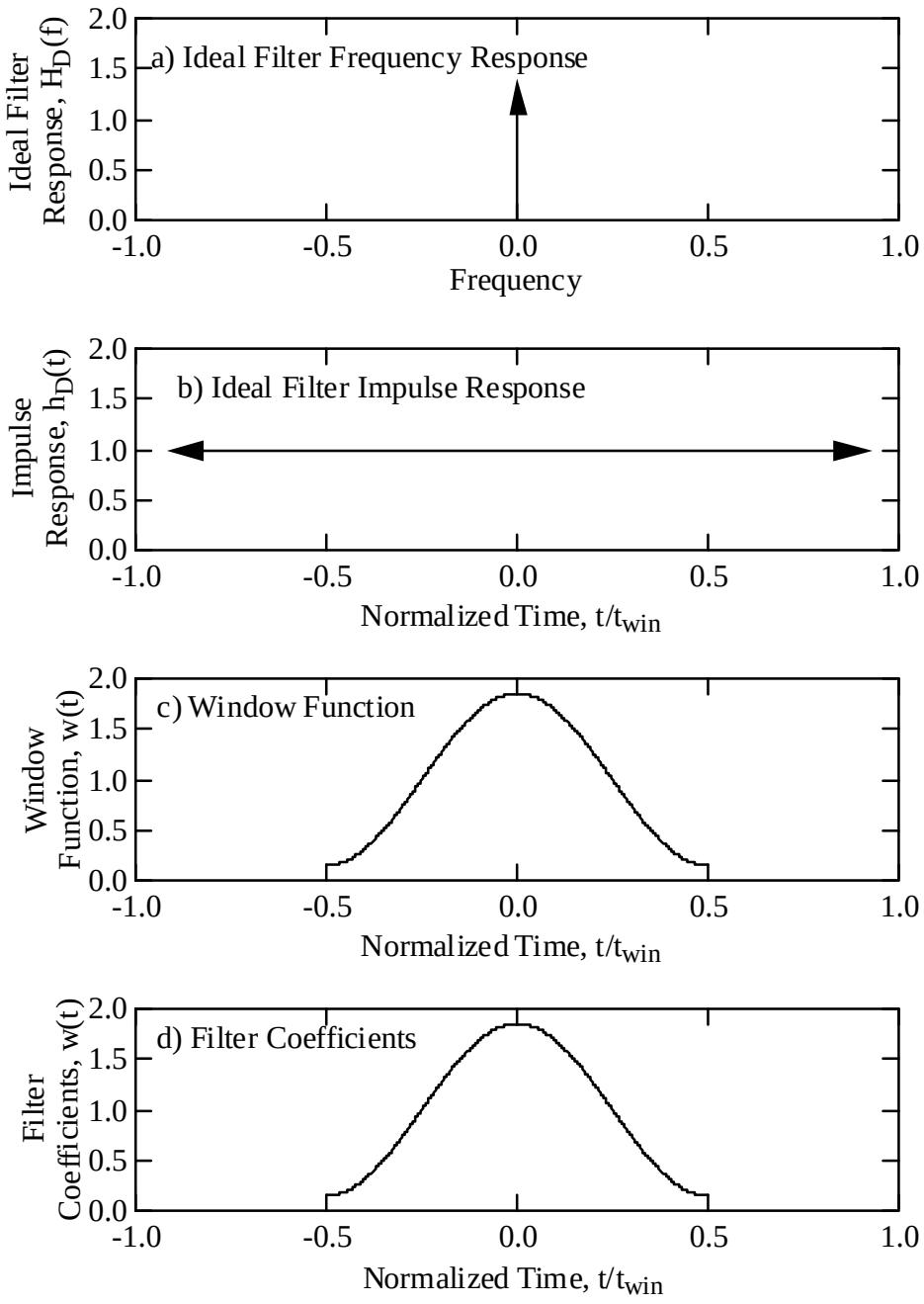

Figure 8.19 Functions Used to Design FIR Digital Filter Using the Windowing Method

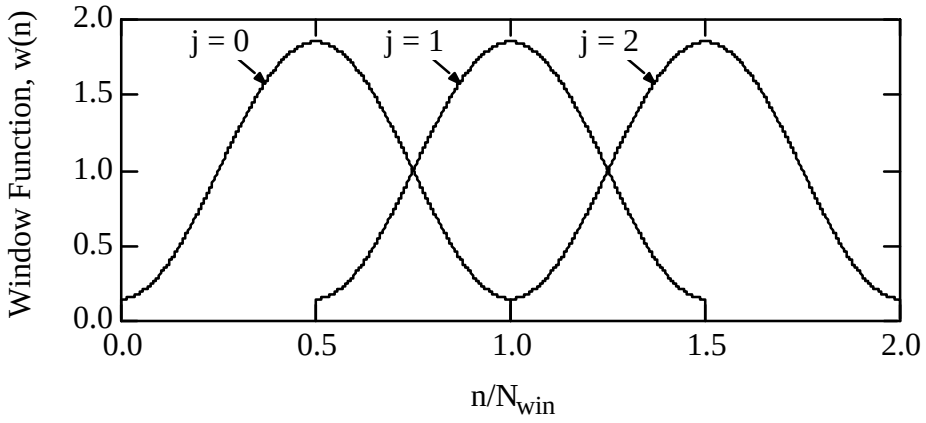

Figure 8.20 Three Successive Overlapping Hamming Windows Used as Filter Coefficients for a Decimating FIR Digital Filter

The frequency response of this Hamming FIR filter is given by the following equation:

$$H(f) = 0.4259\ \mathrm{sinc}\left(N_{win}\frac{f}{f_s}\pi - \pi\right) + \mathrm{sinc}\left(N_{win}\frac{f}{f_s}\pi\right) + 0.4259\ \mathrm{sinc}\left(N_{win}\frac{f}{f_s}\pi + \pi\right) \quad \text{(Equation 8.39)}$$

A plot of this filter's frequency response is shown in Figure 8.21 for a filter with $N_{win} = 152$. The plot is relative to normalized frequency, f/f_s. All of the side lobes in this response have attenuations greater than 41 dB, and the side lobe peaks roll off very gradually. This is the expected performance of a FIR filter designed with a Hamming window.

To apply the Hamming FIR filter, only one parameter is required, N_{win}. By knowing the required spatial resolution, d, the rolling velocity, V, and the sampling frequency, f_s, the value of N_{win} can be determined using the following equation:

$$N_{win} = \frac{2\,d}{V}\,f_s \quad \text{(Equation 8.40)}$$

N_{win} must be rounded to the nearest even integer.

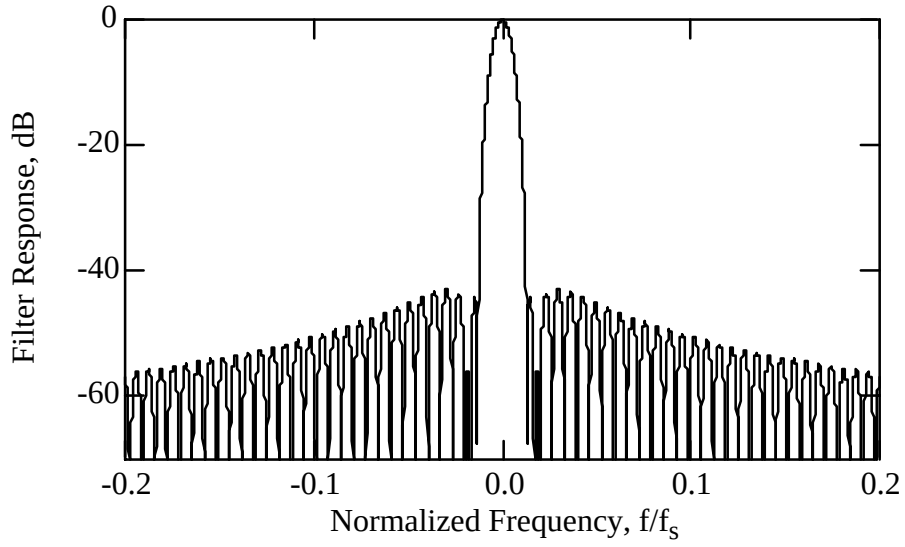

Figure 8.21 Frequency Response of Hamming FIR Digital Filter with $N_{win} = 152$

8.4.3 Comparison between Composite and Hamming FIR Filters

For comparison, a plot of the composite IIR and FIR filter presented in the previous sections is presented, along with the Hamming FIR filter, in Figure 8.22. The IIR filter uses a pole value, *p*, of 0.95, and the associated FIR filter averages 76 points, N_{avg}. This comparison applies equally to other filters, as long as they are designed using the procedures given above. The primary lobes of the two filter responses are practically identical. The composite IIR and FIR filter has an attenuation of only 29 dB at the first side lobe, while the Hamming FIR filter has at least 41 dB attenuation at all of its side lobes. The response of the composite filter rolls off much more rapidly than that of the Hamming FIR filter, resulting in much higher attenuation in most of the reject bands.

It is interesting to note, in Figure 8.22, that the two filters have nearly identical responses in their primary lobes, but the averaging FIR filter in the composite filter averages half as many points as the Hamming FIR filter. It could be concluded that the composite filter would have shorter settling times than the Hamming FIR filter. However, the situation is more complex than this because of the interaction of the two filters in the composite filter.

To compare the settling time of the two filters, an analysis must be performed in the time domain. The same analysis that was illustrated in Figures 8.13 and 8.14 was used to compare these two filters. Both filters were used to analyze a waveform with an amplitude that drops instantly to 0. The time required for the filters to respond to this instantaneous change, or the settling time, was determined. The IIR filter uses two-way filtering, and a nondecimating form of the FIR filters was used. Plots of the filtered waveforms are shown in Figure 8.23 for the IIR filter alone, the composite IIR and averaging FIR filter, and the Hamming FIR filter. The IIR filter alone shows the most rapid settling; however, it is not practical to use this filter alone. The composite filter and the Hamming FIR filter show

practically identical settling behavior. Therefore, neither filtering scheme has a comparative advantage in settling time.

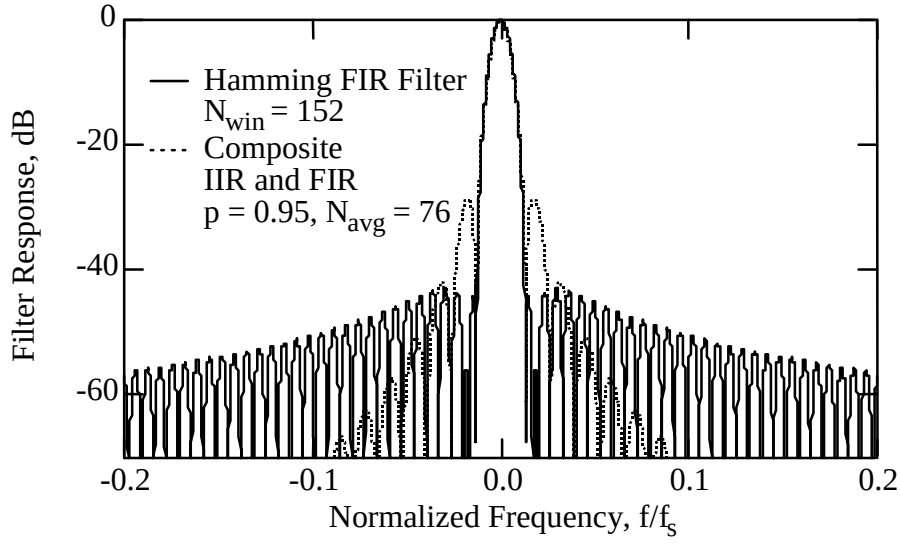

Figure 8.22 Filter Responses of Hamming FIR Digital Filter and Composite IIR and FIR Digital Filter

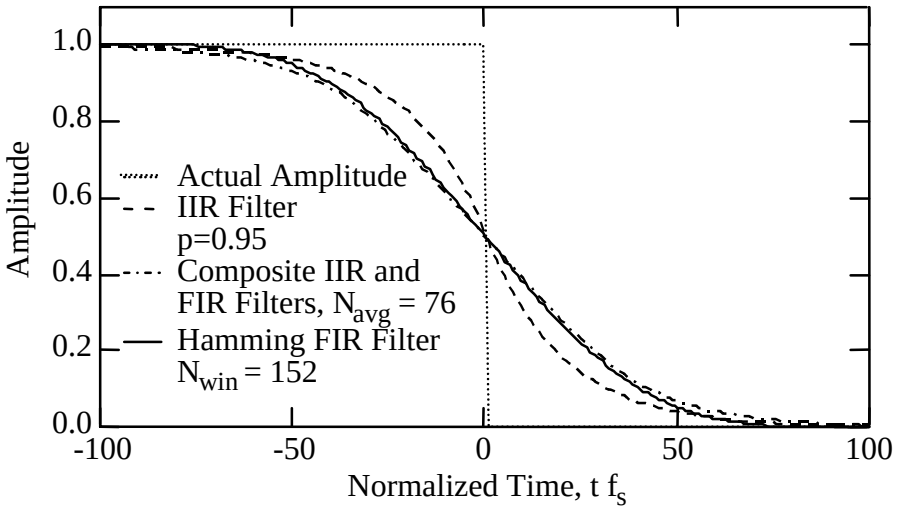

Figure 8.23 Filter Settling Performance for IIR Filter, Composite IIR and Averaging FIR Filter, and Hamming FIR Filter

Both filter schemes that have been presented, the composite filter and the Hamming FIR filter, show similar behavior in the time and frequency domains. The largest difference between the filters is the shape of the reject bands (or the side lobes). One way to compare the attenuation in the reject bands is to look at the area under the side lobes. All energy in the demodulation product will fall between plus and minus the Nyquist frequency, f_{Nyq}; therefore, frequencies above and below the Nyquist frequency are of no interest in this analysis. Figure 8.24 shows the cumulative area of the magnitude of both filter responses beginning at $-f_{Nyq}$. The areas at the points indicated as the beginning of the primary lobe represent the total area under all of the side lobes of interest. The area under the side lobes of the composite filter is about 31 percent lower than that of the Hamming FIR filter. This difference means that for noise that is uniformly distributed across the spectrum, the composite filter will attenuate more noise than the Hamming FIR filter. However, practically all of the side lobes that contribute to the total area are in the immediate vicinity of the primary lobe for the composite filter. Therefore, the composite filter could attenuate less noise than the Hamming FIR filter if the noise level is higher near the primary lobe than it is at other frequencies of the spectrum.

In most cases, both filters will work well. Under normal operating conditions, where most of the noise occurs at frequencies well below the operating frequency, the composite filter will give slightly better results. In cases in which the operating frequency is near a peak in the noise spectrum, the Hamming FIR filter will give better results.

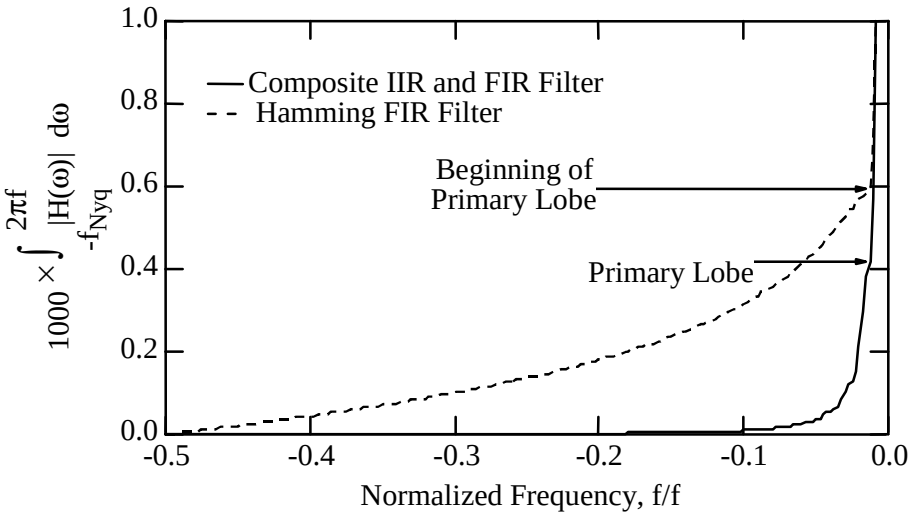

Figure 8.24 Areas under Side Lobes of Composite and Hamming FIR Filters

8.5 APPLYING THE AMPLITUDE DEMODULATION METHOD TO ROLLING DYNAMIC DEFLECTOMETER DATA

The principles of amplitude demodulation and the design of filters used in applying this method were discussed in the previous sections. In this section the particulars of how the

method is applied to calculate the magnitudes of forces and displacement measurements is discussed. The magnitude of a sinusoid of frequency f_o is shown in Figure 8.25.

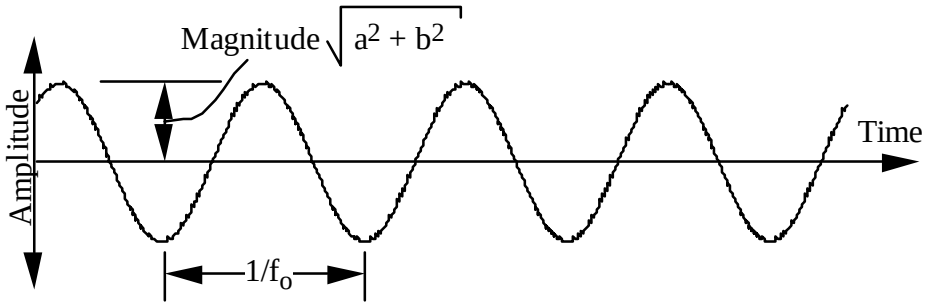

Figure 8.25 Graphical Representation of the Magnitude of a Sinusoid

8.5.1 Determining Digital Filter Parameters

Either of the digital filter designs outlined above can be used to analyze the RDD data, but in most cases the composite filter will give slightly better results. To select the filter parameters for either filter, the testing speed, *V*, and the required spatial resolution, *d*, must be known. With these values, the required time interval between measurement results, Δt_r, can be determined as follows:

$$\Delta t_r = \frac{d}{V} \qquad \text{(Equation 8.41)}$$

In order to obtain this resolution, we select t_{90} in the composite filter so that:

$$t_{90} \geq \Delta t_r \qquad \text{(Equation 8.42)}$$

A pole value, *p*, for the IIR filter can be determined from t_{90} using Equation 8.25, which is repeated here for convenience:

$$p = 1 - \frac{3.89}{t_{90}\, f_s + 2}$$

where f_s is the sampling frequency.

The only parameter that the averaging FIR decimating filter requires is the number of points to average, N_{avg}. This integer value can be determined from Equation 8.33, which is repeated here:

$$N_{avg} \geq t_{90}\, f_s$$

N_{avg} should be rounded up to the nearest integer value.

The Hamming FIR decimating filter requires only one parameter, the number of points per window, N_{win}. This can be determined from:

$$N_{win} \geq 2\ \Delta t\ f_s \qquad \text{(Equation 8.43)}$$

where N_{win} is rounded to an even integer.

8.5.2 Calculation of Dynamic Force Time Series

A flow chart showing the steps used to calculate the dynamic force time series, $F_D(t)$, is shown in Figure 8.26. These procedures can be applied either in real time during testing or after testing. The first step in data analysis is to sum the signals from the four load cells. The summed time series is then multiplied by the calibration factor to obtain a total force time series. The total force time series is then demodulated about the operating frequency, f_o, creating a complex demodulation product time series. This complex time series is then filtered using a 0-Hz notch-pass decimating digital filter. Either of the filters discussed in the previous section can be used, but the composite filter will give the best result in most cases. The magnitude of the filtered complex time series is then calculated. This magnitude (equal to $\sqrt{a^2 + b^2}$) is the dynamic force time series, $F_D(t)$.

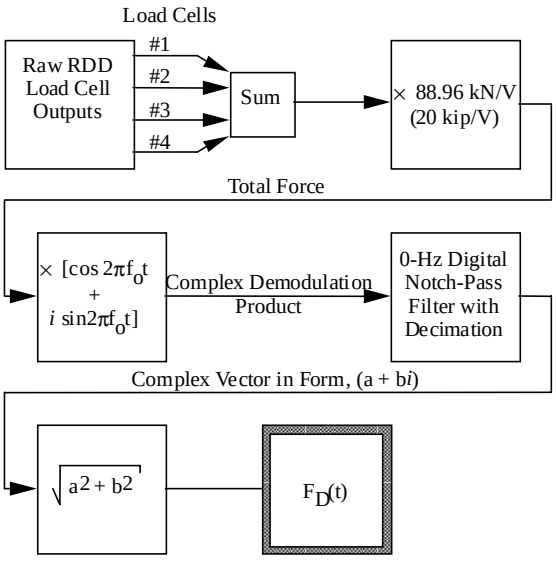

Figure 8.26 Flow Chart of the Steps Used to Calculate Dynamic Force from the RDD Load Cell Outputs

8.5.3 Calculation of Dynamic Displacement Time Series

A similar procedure is used to calculate the dynamic displacement time series, $\delta_D(t)$. This procedure is shown in the flow chart in Figure 8.27. The displacement calculation procedure must be applied to the output of each rolling sensor individually. The sensor output is first demodulated about the operating frequency, f_o. Next, the complex demodulation product is filtered with the same filter used to filter the force time series. The filtered complex time series is then multiplied by the frequency-dependent rolling sensor calibration, *RSC(f)*. This value can be obtained from Figure 5.18 for each of the rolling sensors at the operating frequency, f_o. The time series is also divided by $2\pi f_o$ to convert the velocity transducer output to a displacement output. The magnitude of the time series is then calculated to obtain the dynamic displacement time series, $\delta_D(t)$.

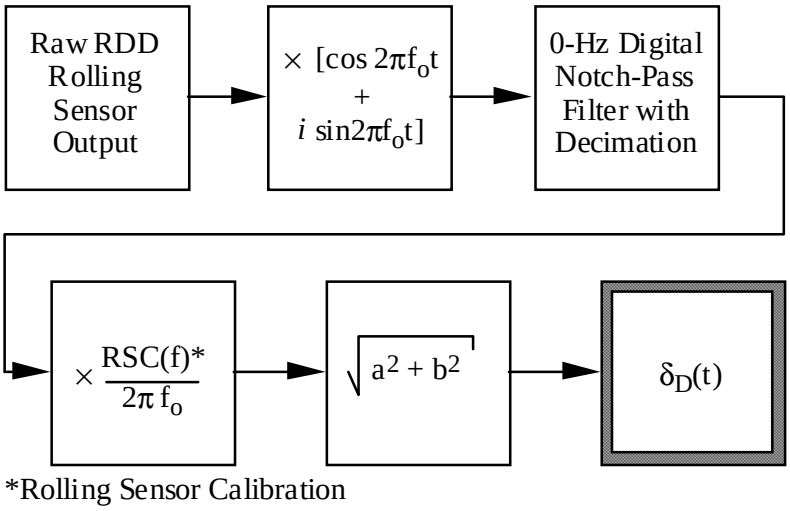

Figure 8.27 Flow Chart of Procedures Used to Calculate Dynamic Displacement from the RDD Rolling Sensor Outputs

During testing, a nominal dynamic force level, F_{nom}, is selected, and the RDD operator should closely monitor and maintain this level. However, changes in pavement stiffness and hydraulic fluid temperature will cause variations in the actual dynamic force level. The analysis must account for these changes and fluctuations. An adjusted displacement level, $\delta_A(t)$ must be calculated to obtain the displacement that would have occurred had the nominal force level, F_{nom}, been applied. This adjustment is done as follows:

$$\delta_A(t) = F_{nom} \frac{\delta_A(t)}{F_D(t)} \qquad \text{(Equation 8.44)}$$

The displacement is then reported as a displacement at the nominal force level, for example, as a 44.48-kN displacement (10-kip displacement).

8.5.4 Calculation of Measurement Distance

In addition to load cell and rolling sensor outputs, a data file that contains distance measurements is also recorded. The distance counter is polled by the data acquisition system approximately once every two seconds. The distance value and a time stamp are then recorded in the distance file. Displacement results are calculated at time intervals of Δt_r. By knowing the cumulative time of each measurement, a distance corresponding to the displacement measurement can be determined by interpolating a distance relative to the stored time stamps.

The distance intervals between measurement results will vary with testing velocity. It is often convenient to present final results at a constant distance interval. Interpolation can be performed on the analysis results to obtain evenly spaced displacements.

8.6 ESTIMATION OF CONFIDENCE INTERVALS

RDD displacement measurements will always have small errors resulting from rolling noise and traffic noise. These errors can always be decreased by decreasing the bandwidth of the digital filter used in demodulation. However, decreasing the filter bandwidth increases the filter settling time and, hence, decreases the measurement's spatial (or chronological) resolution. This means more accurate displacement results are obtained by increasing the distance between measurement points.

In order to select filter parameters that achieve the required balance between displacement accuracy and spatial resolution, tools are needed to predict a confidence interval for the displacement measurements. In this section, the effects of noise level and the phase of the noise on the measured displacements are discussed. Additionally, the statistical tools that can be used to predict confidence intervals for those measurements are presented.

8.6.1 Estimation of Magnitude of the Noise

The first step in calculating confidence intervals for displacement measurements is to determine the mean and variance of the magnitude of the noise in the measured signal. Of particular interest is the combined magnitude of all noise that is not rejected by filtering.

One approach to estimating this magnitude is to determine the noise magnitude at a number of frequencies above and below the operating frequency using identical filters. This approach is illustrated in Figure 8.28. The spectrum in this figure simulates the spectrum of a rolling sensor output with an RDD operating frequency of 40 Hz. A 40-Hz notch-pass filter response is also shown in the figure. This is the filter used to determine the induced displacement at 40 Hz. The result will include the actual induced displacement, the noise included in the filter pass-band, and a small portion of the noise in the filter reject-bands. To estimate the magnitude of the noise included in the measurement, identical analyses are

performed using notch-pass filters at a number of frequencies above and below the operating frequency. The results of these analyses will include the noise in the filter pass-band and a small portion of the noise in the reject-band. To ensure that these results do not include a small portion of induced displacement, the filters should be positioned so that the operating frequency falls at one of the filter's null points. The following equation will ensure this positioning:

$$f_n = f_o + 4\,n\,\frac{f_s}{N} \qquad \text{(Equation 8.45)}$$

where f_n are the selected frequencies above and below f_o
$n = \pm (1, 2, 3, ...)$
f_o is the RDD operating frequency
f_s is the sampling frequency
N is either N_{avg} or N_{win}, depending upon which filter is used

The analysis performed at each of these additional frequencies is identical to the analysis performed at the operating frequency, except that the signal is demodulated about f_n rather than f_o, and the rolling sensor calibration factor, RSC, is for f_n rather than for f_o. The noise level will vary with frequency. However, if it is assumed that the variation in noise is linear and an equal number of additional frequencies are selected above and below the operating frequency, then the average magnitude of the additional tests should approximate the mean noise magnitude, μ, included in the analysis at f_o. This method is very computation intensive. Three frequencies above and three frequencies below the operating frequency should be sufficient for estimating the mean noise magnitude.

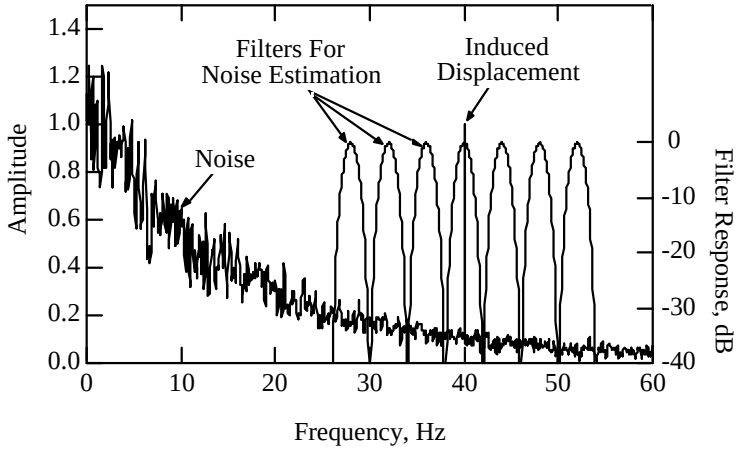

Figure 8.28 Illustration of Noise Estimation by Performing Analysis at Frequencies above and below the Operating Frequency

There are other important considerations in this analysis. None of the additional frequencies, f_n, should be greater than the maximum usable frequency as defined in Section 7.2.3. Harmonic noise will always be present at 60 Hz owing to electromagnetic interference (emi). So that this harmonic noise does not inflate noise estimates, none of the additional filters should include 60 Hz.

The noise magnitude probability distribution, $f_m(x)$, is needed to predict a confidence interval. Because magnitudes, by definition, must be greater than or equal to zero, the noise magnitude probability distribution function must only have nonzero values for $x \geq 0$. One probability distribution function that meets this criterion is the gamma distribution (Walpole and Myers 1985). The gamma distribution function is:

$$f(x) = \begin{cases} \frac{1}{\beta^{\alpha}\Gamma(\alpha)} x^{\alpha-1} e^{-x/\beta} \text{ for } x \geq 0 \\ 0 \text{ elsewhere} \end{cases} \quad \text{(Equation 8.46)}$$

The mean, μ, and variance, σ^2, of the gamma distribution are:

$$\mu = \alpha\beta, \text{ and} \quad \text{(Equation 8.47)}$$

$$\sigma^2 = \alpha\beta^2 \quad \text{(Equation 8.48)}$$

Plots of several gamma distributions with the same mean and various standard deviations, σ, are shown in Figure 8.29.

The mean and variance are needed in order to fully characterize the shape of the probability distribution function. The method outlined above can be used to estimate the mean noise magnitude. A variance estimation is more difficult. Calculating the variance of the noise magnitude at additional frequencies, as with the mean, will not give good results for two reasons. First, it is impractical to calculate noise levels at more than a few frequencies either side of the operating frequency. This small sample is a poor predictor of variance. Second, the noise level will always vary with frequency. Therefore, noise levels calculated at different frequencies will have variability that cannot be attributed to the sample variance. This will lead to overestimating the variance.

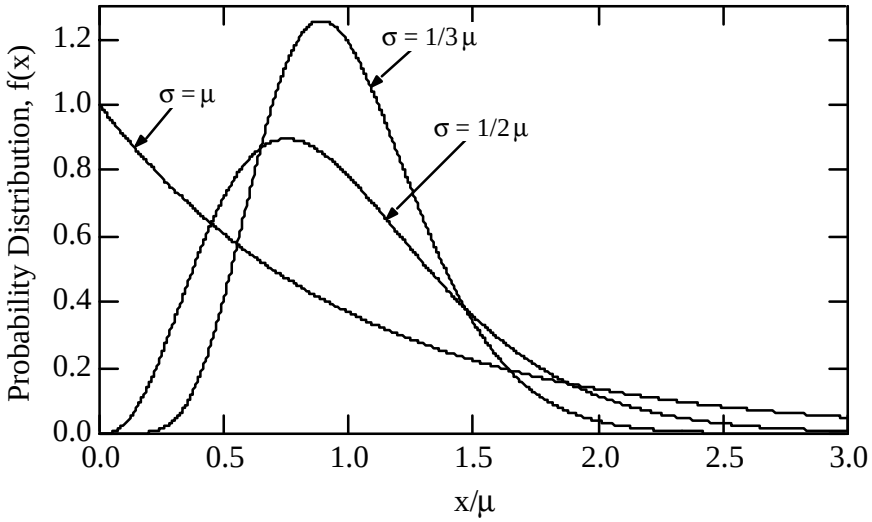

Figure 8.29 Plots of Several Gamma Probability Distribution Functions

Another approach to characterizing the variance is to make a reasonable but conservative assumption of the noise magnitude variance. One such assumption is that $\sigma = \mu$. The probability distribution function for this assumption is shown in Figure 8.29. It is a special case of the gamma distribution function called the *exponential distribution.* The exponential distribution function is:

$$f(x) = \begin{cases} \frac{1}{\beta} e^{-x/\beta} \text{ for } x \geq 0 \\ 0 \text{ elsewhere} \end{cases} \qquad \text{(Equation 8.49)}$$

The mean, μ, and variance, σ^2, of the exponential distribution are:

$$\mu = \beta, \text{ and} \qquad \text{(Equation 8.50)}$$

$$\sigma^2 = \beta^2 \qquad \text{(Equation 8.51)}$$

The probability of $x > X$ is:

$$P(x > X) = \int_0^x \frac{1}{\beta} e^{-x/\beta} dx = 1 - e^{-x/\beta} \qquad \text{(Equation 8.52)}$$

The assumed probability density function for the noise magnitude is:

$$f_m(x) = \begin{cases} \frac{1}{\mu_m} e^{-x/\mu_m} \text{ for } x \geq 0 \\ 0 \text{ elsewhere} \end{cases} \qquad \text{(Equation 8.53)}$$

where $f_m(x)$ is the probability density function of the noise magnitude

μ_m is the mean noise magnitude

8.6.2 Effect of Noise Phase on Measurement

The method outlined above for estimating the mean noise magnitude and the assumption that the noise magnitude has an exponential distribution should result in a conservative characterization of the noise magnitude. However, the noise magnitude alone does not determine the errors in displacement measurements. The phase of the noise also exerts a substantial influence on displacement errors.

To illustrate this, vector representations of the induced displacement, δ, noise, n, and total signal, s, are shown in Figure 8.30. The total signal is the vector sum of the induced displacement and the noise. Figure 8.30 shows three different vector combinations. In each case, the total signal vectors have the same magnitude and phase. The noise vectors all have the same magnitude, but different phases. In Figure 8.30a, the noise and the total signal are nearly 180° out of phase with each other, and the displacement vector magnitude is nearly equal to the sum of the total signal and the noise magnitudes. In Figure 8.30b, the total signal and the noise are nearly in phase with each other, and the displacement magnitude is about equal to the difference between the total signal and the noise magnitudes. In the last case, shown in Figure 8.30c, the total signal and the noise are about 90° out of phase with each other, and the displacement magnitude is nearly equal to the total signal magnitude.

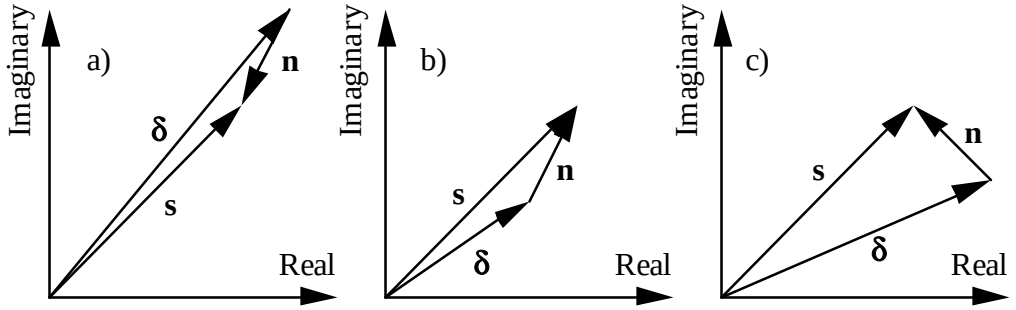

s = Calculated Displacement, **δ** = Actual Displacement, **n** = Noise

Figure 8.30 Vector Representations of Three Different Combinations of Displacement, Noise, and Total Signal Vectors

The examples given above show that knowing the magnitude of the total signal and the noise is not enough to determine the actual displacement. Therefore, phase must be accounted for in estimating the confidence intervals for the displacement measurements.

The critical phase angle in determining actual displacements is the phase angle between the total signal and the noise vectors, ϕ_{ns}. The phase of the noise is controlled by the pavement roughness and traffic noise, while the total signal phase is largely controlled by the RDD loading. The noise and the RDD loading are completely independent of each other; therefore, the phase, ϕ_{ns}, will be uniformly distributed as follows:

$$f_p(\phi) = \begin{cases} \frac{1}{2\pi} \text{ for } 0 \le \phi < 2\pi \\ 0 \text{ elsewhere} \end{cases} \qquad \text{(Equation 8.54)}$$

where $f_p(\phi)$ is the probability density function of the phase between the signal and the noise.

8.6.3 Combined Effect of Noise Phase and Magnitude

To illustrate the combined effect of noise phase and magnitude on the confidence interval of an RDD displacement measurement, a vector representation of the RDD displacement signal, *s*, is shown in Figure 8.31. Additionally, two possible actual displacement vectors, δ, are shown. The magnitude of these two displacement vectors are $|s| - b$ and $|s| + b$. The noise vectors, *n*, associated with each displacement vector are also shown. The shaded region in Figure 8.30 represents the end points of all possible displacement vectors, such that their magnitude, $|\delta|$, meets the criterion: $|s| - b \le \delta| \le |s| + b$. Estimating confidence intervals requires calculating the probability of displacement vector end points falling within the shaded region.

The arch-shaped geometry of the shaded region in Figure 8.30 greatly complicates the determination of confidence intervals. By assuming that $|n| << |s|$, the arch-shaped region can be replaced by a straight region with little loss in accuracy. This approximation is shown in Figure 8.32. Using this geometry, a range of noise magnitudes can be determined so that the magnitude of the actual displacement is within ± *b of* $|s|$. This relationship is:

$$\text{For } |\mathbf{s}| - b \le \boldsymbol{\delta} \le |\mathbf{s}| + b \text{ , then } |\mathbf{n}| \le \frac{b}{\cos\phi_{\mathbf{ns}}} \qquad \text{(Equation 8.55)}$$

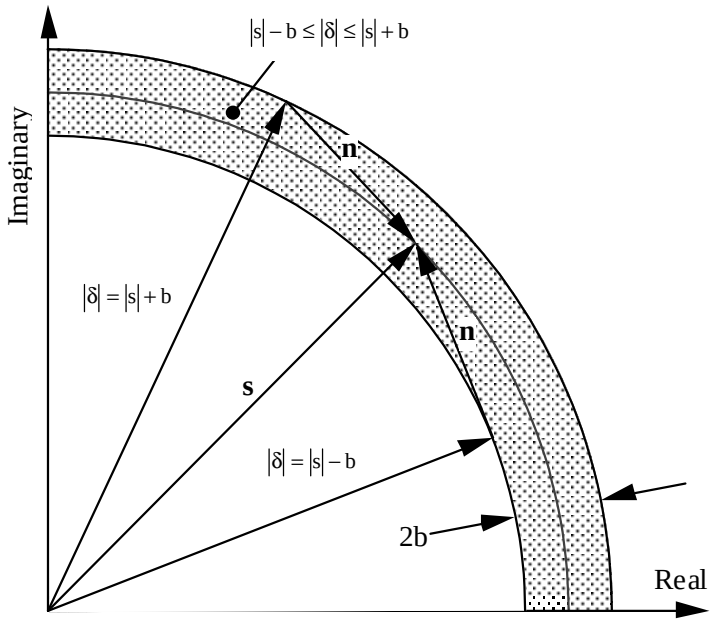

Figure 8.31 Vector Representation Showing Region Required for Calculation of Confidence Intervals for RDD Displacement Measurements

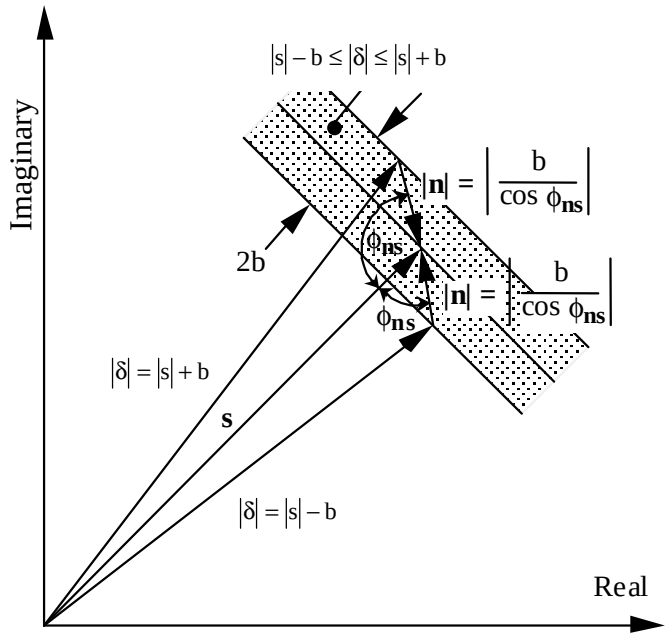

Figure 8.32 Vector Representation Showing Simplified Region Required for Calculation of Confidence Intervals for RDD Displacement Measurements, Assuming |n| << |s|

Using the relationship given in Equation 8.52, the probability of the displacement vector end point falling within the shaded region can be determined as follows:

$$P(|\mathbf{s}| - b \le \delta \le |\mathbf{s}| + b) = \int_0^{2\pi} \int_0^{\left|\frac{b}{\cos\phi_{ns}}\right|} f_m(x)\, f_p(\phi)\, dx\ d\phi \qquad \text{(Equation 8.56)}$$

where $f_m(x)$ is the noise magnitude probability distribution function given in Equation 8.51, and
$f_p(\phi)$ is the noise phase probability distribution function given in Equation 8.54.

Substituting the probability distribution functions into Equation 8.56 gives:

$$P(|\mathbf{s}| - b \le \delta \le |\mathbf{s}| + b) = \frac{1}{2\pi} \int_0^{2\pi} \int_0^{\left|\frac{b}{\cos\phi_{ns}}\right|} \frac{1}{\mu_m} e^{-x/\mu_n}\, dx\, d\phi \qquad \text{(Equation 8.57)}$$

where μ_n is the mean noise magnitude.

Performing the inside integration in Equation 8.57 gives:

$$P(|\mathbf{s}| - b \le \delta \le |\mathbf{s}| + b) = \frac{1}{2\pi} \int_0^{2\pi} \left(1 - e^{-b/\mu_n |\cos\phi_{ns}|}\right) d\phi \qquad \text{(Equation 8.58)}$$

The integration in Equation 8.58 was performed numerically for a range of values of b/μ_n. These results are plotted in Figure 8.33. From these results, the 80 percent, 90 percent, and 99 percent confidence intervals were determined. These confidence intervals are:

$$P(|\mathbf{s}| - 1.05\ \mu_n \le \delta \le |\mathbf{s}| + 1.05\ \mu_n) = 0.80 \qquad \text{(Equation 8.59)}$$

$$P(|\mathbf{s}| - 1.60\ \mu_n \le \delta \le |\mathbf{s}| + 1.60\ \mu_n) = 0.90 \qquad \text{(Equation 8.60)}$$

$$P(|\mathbf{s}| - 3.83\ \mu_n \le \delta \le |\mathbf{s}| + 3.83\ \mu_n) = 0.99 \qquad \text{(Equation 8.61)}$$

Confidence intervals thus can be determined by estimating μ_n using the method described in Section 8.6.1 and Equations 8.57, 8.58, and 8.59. This method is applied to actual data in Section 8.7.

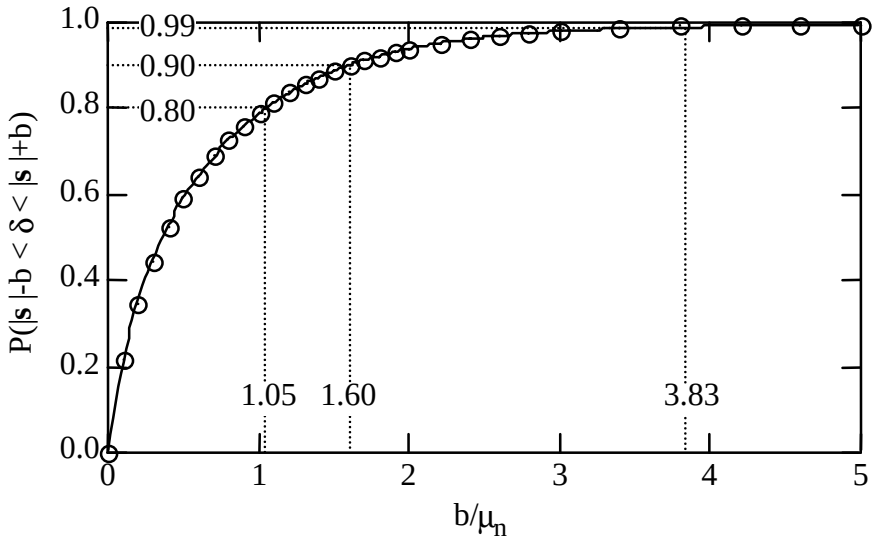

Figure 8.33 Results of Numerical Integration of Equation 8.56, Giving Confidence Intervals

8.6.4 Noise in Force Measurement

The discussion thus far has been limited to estimating confidence intervals in the displacement measurement. Some noise is also present in the force measurement, resulting in errors in the measured force. However, the noise in the load cell outputs is usually much lower than the noise in the rolling sensor outputs. Therefore, ignoring the errors in the force measurement will not significantly affect the calculated confidence intervals.

The noise in the load cell outputs should, however, be assessed to verify that it is, in fact, much lower than the rolling sensor noise. This verification can be accomplished by estimating a mean noise magnitude in the same manner used for the rolling sensor output in Section 8.6.1. If the force noise level is not sufficiently low, it indicates probable problems in the load cell circuits.

8.7 EXAMPLE ANALYSIS WITH REAL ROLLING DYNAMIC DEFLECTOMETER DATA

This section illustrates the RDD analysis procedure discussed above using a short segment of RDD testing results obtained from Interstate Highway 10 (IH-10) in Houston, Texas. (Results from this testing are presented in detail in Chapter 9.) This testing was performed with a nominal operating frequency of 40 Hz and a nominal force level of 89 kN (20 kip) peak-to-peak (p-p). The testing speed along the pavement was about 0.46 m/s (1.5 ft/sec). The data were sampled with a sampling frequency of 256 Hz, and the anti-aliasing

cut-off frequency was set to 100 Hz. Only the displacements measured with the centerline-in-line rolling sensor are presented in this section.

The combined output of the four load cells is presented in Figure 8.34. The appropriate calibration factor has been applied to the data so that the data are presented in force units. Figure 8.34a shows the measured force for a time interval of 400 seconds. The static component of the applied force is about 80 kN (18 kip). It is evident in Figure 8.34a that the dynamic force consists of a sinusoidal component and a rolling noise component. An expanded view of the force output is shown for a 0.5-sec time interval in Figure 8.34b. In order to obtain a smooth curve from the sparsely sampled data (which has only about 6 points per cycle), the data presented in Figure 8.34b is a sinc function interpolation of the measured data, with a data point frequency of 2,048 Hz (or approximately 51 points per cycle). The sinusoidal and noise components of the force measurement are more clearly seen in Figure 8.34b. The loading rollers and rolling sensor crossed a pavement joint at a time of about 185.75 sec. The dynamic force level drops somewhat at this time because the increase in pavement compliance at the joint leads to increased inertial force losses.

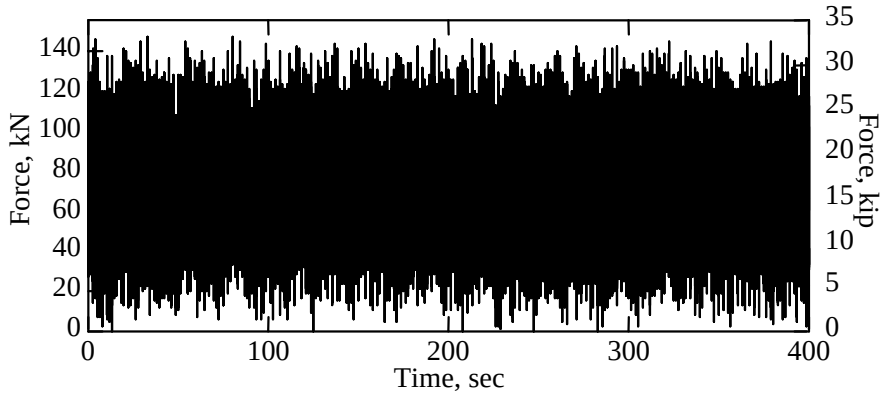

a) Combined Static and Dynamic Force

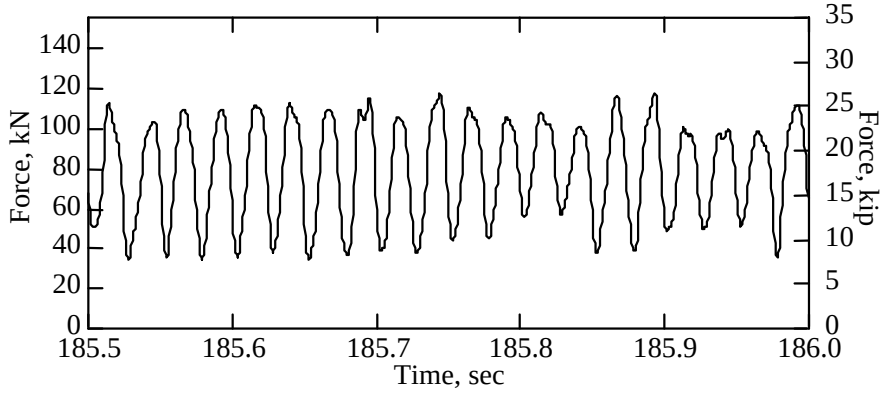

b) Expanded View of Combined Static and Dynamic Force

Figure 8.34 Force Data from RDD Testing at the IH-10 Rigid Highway Pavement in Houston, Texas

The output from the centerline-in-line rolling sensor is presented in Figure 8.35. This measurement is presented in terms of voltage because the frequency-dependent rolling sensor calibration cannot be applied to time-domain data. Figure 8.35a shows the rolling sensor output for a time interval of 400 seconds. Again, the data have sinusoidal and rolling noise components. The rolling sensor output amplitude varies with time and has spikes at regular intervals. The increases in amplitude correspond to regions of decreased stiffness at pavement joints, and the spikes are caused by the rolling sensor crossing the discontinuity at the joint. An expanded view of the rolling sensor output is shown for a 0.5-second time interval in Figure 8.35b. Again, the data presented in Figure 8.34b are a sinc function interpolation of the measured data, with a data point frequency of 2048 Hz. The expanded data show that the rolling sensor output is largely sinusoidal with superimposed rolling noise. The expanded data show a spike from the rolling sensor crossing a joint at a time of approximately 185.75 seconds.

The first step in analyzing the data presented in Figures 8.33 and 8.34 is to determine the precise RDD operating frequency. Currently, the RDD data acquisition system operates on a clock that differs from that the function generator used to drive the dynamic loading system. This leads to slight but significant discrepancies between the actual and nominal RDD operating frequency. The actual operating frequency is determined by performing a Fast Fourier Transform (FFT) on the force data and locating the spectral peak. This spectrum is presented in Figure 8.35. This spectrum comes from 256 sec of force data, which will resolve the actual frequency to about 0.0039 Hz. The actual RDD operating frequency for the data is 40.086 Hz. This value is used in this section for all subsequent analyses.

The only additional data required for RDD analysis are the relationships between time and testing position measured with the distance encoder. This relationship is presented in Figure 8.37. This plot verifies that the actual testing velocity was very close to 0.46 m/s (1.5 ft/sec). The time-position relationship in Figure 8.36 is used to present all subsequent results in terms of position on the pavement rather than time.

The demodulation method discussed in this chapter was used to calculate dynamic forces and dynamic displacements for the data presented in Figures 8.34 and 8.35. These calculations were carried out using both the composite IIR-FIR and the Hamming FIR digital filters for a range of resolution times (also referred to as the interval between measurement results, Δt_r) from 16 to 0.25 seconds. These resolution times correspond to spatial resolutions from 7.3 to 0.1 m (24 to 0.38 ft). Example dynamic force and dynamic displacement results are shown in Figure 8.38. These results were calculated using a composite IIR-FIR digital filter with a resolution time of 1 second (which results in 0.46 m [1.5 ft] spatial resolution). The dynamic force applied to the pavement is presented in Figure 8.38a. The peak dynamic force level was about 40 kN (9 kip) with some fluctuations. The dynamic displacements are presented in Figure 8.38b. The shape of the dynamic displacement plot is influenced by the mechanical properties of the pavement and the applied force levels. The influence of fluctuations in the applied dynamic force level are removed by using Equation 8.44 to calculate adjusted displacements.

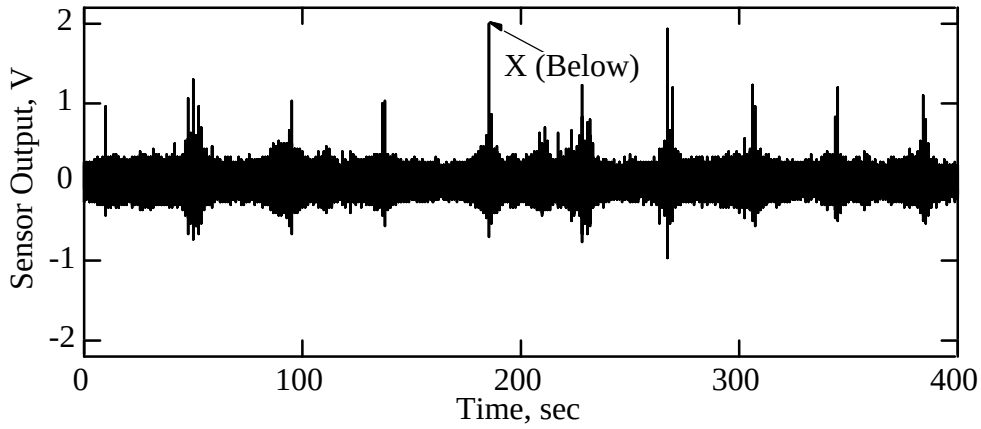

a) Rolling Sensor Output

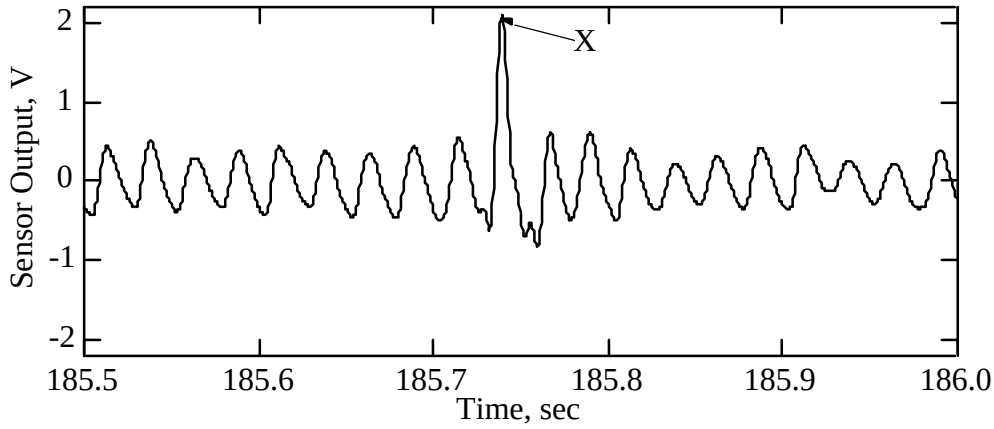

b) Expanded View of Rolling Sensor Output

Figure 8.35 Output of Centerline-in-Line Rolling Sensor from RDD Testing at the IH-10 Rigid Highway Pavement in Houston, Texas

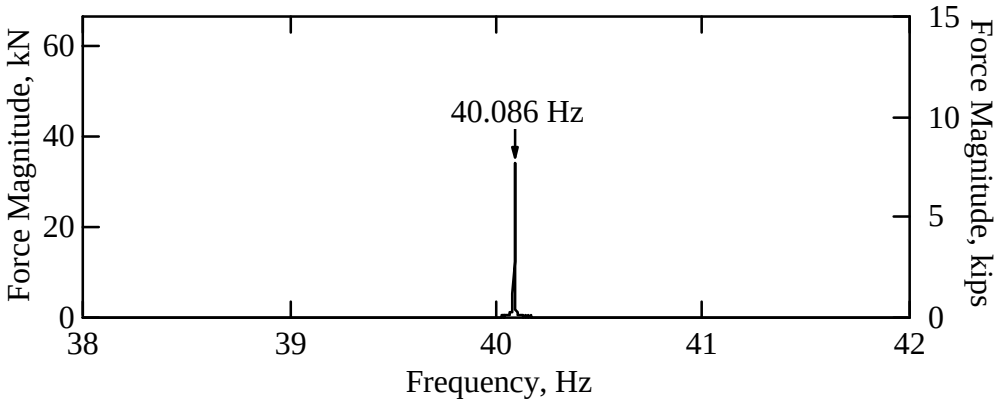

Figure 8.36 Force Spectrum Used to Determine the Actual RDD Operating Frequency for Testing, IH-10 in Houston, Texas

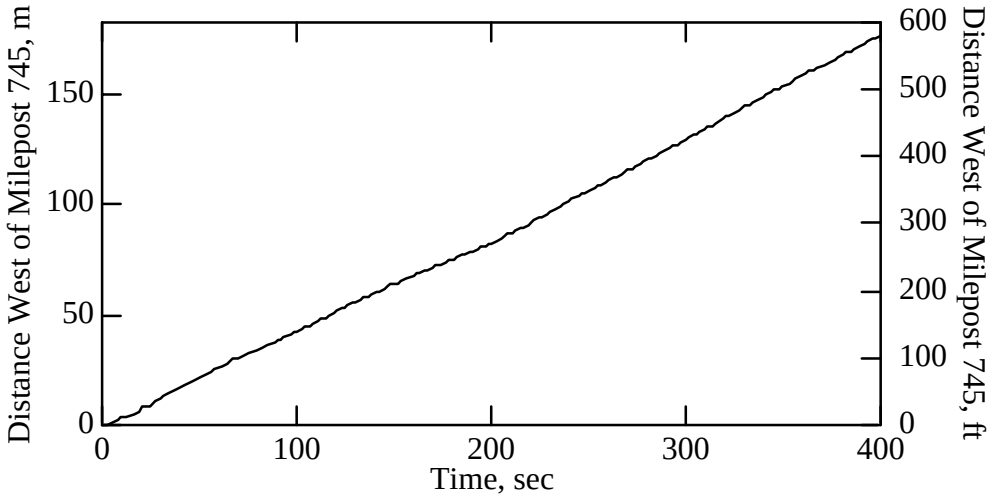

Figure 8.37 Time-Position Relationship for Testing, IH-10 in Houston, Texas

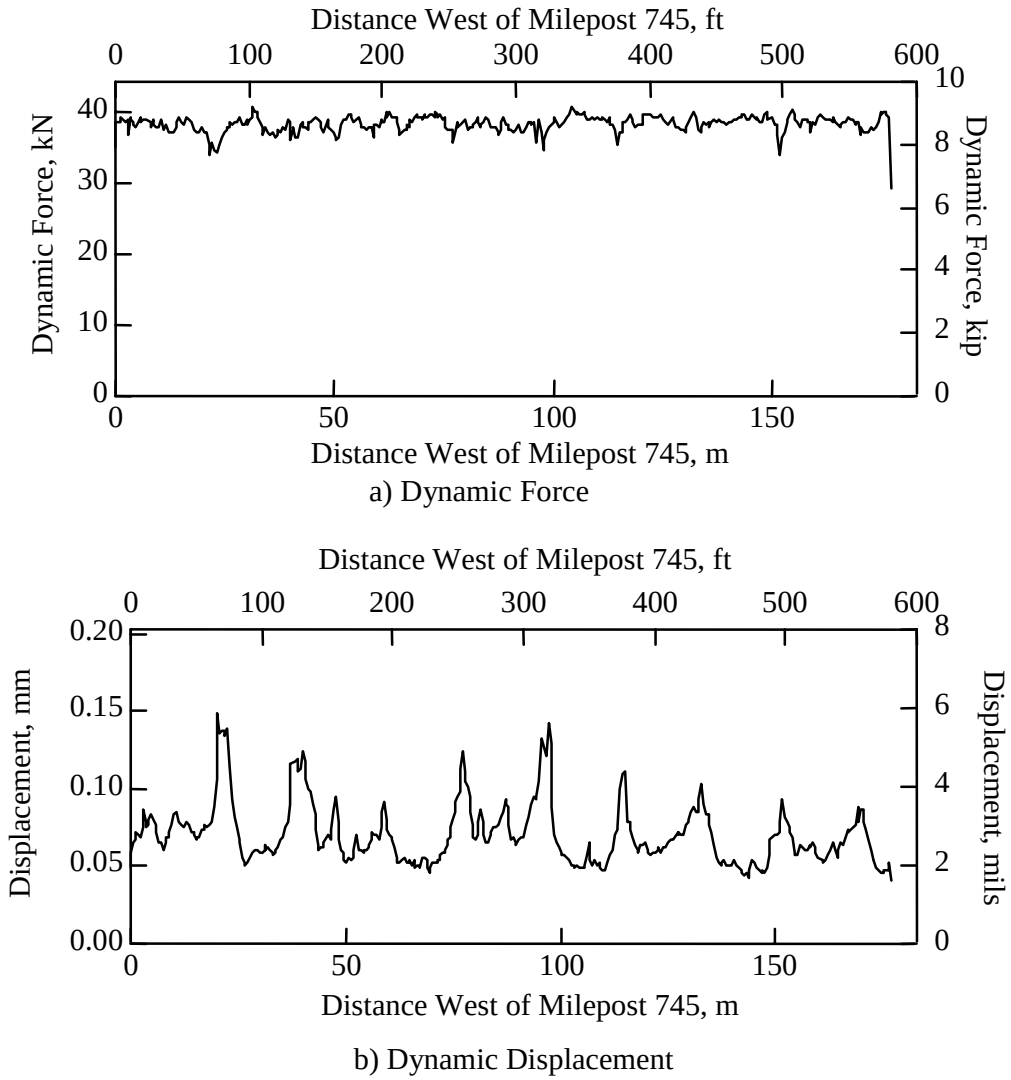

Figure 8.38 Dynamic Forces and Dynamic Displacements Calculated Using a Composite IIR-FIR Digital Filter with a Resolution Time of 1 second; Testing along IH-10 in Houston, Texas

It is very important to understand the relationship between the accuracy and the spatial (or time) resolution of RDD measurements. Very accurate measurements can be obtained at the expense of spatial resolution by using long resolution times. Alternatively, high spatial resolution can be obtained at the expense of measurement accuracy by using short resolution times. This relationship is illustrated by the following series of plots of adjusted displacements with 90 percent confidence intervals for various resolution times.

Figure 8.38 shows the displacement profile (using adjusted displacements) calculated from the data presented in Figures 8.34 and 8.35 with a resolution time of 16 seconds. This corresponds to a spatial resolution of 7.3 m (24 ft). The results from the entire section are

presented in Figure 8.39a, and an expanded view showing the displacement profile near a joint is presented in Figure 8.39b. These results represent the average displacements over 7.3 m (24 ft) intervals; thus, they do not show small details like joints very well. However, the 90 percent confidence intervals are quite narrow, indicating very accurate measurements.

Displacement profiles calculated using resolution times of 4 seconds, 1 second, and 0.25 seconds are presented in Figures 8.40, 8.41, and 8.42, respectively. Again, profiles from the entire section are presented in Figures 8.40a, 8.41a, and 8.42a. Expanded profiles near a joint are presented in Figures 8.40b, 8.41b, and 8.42b.

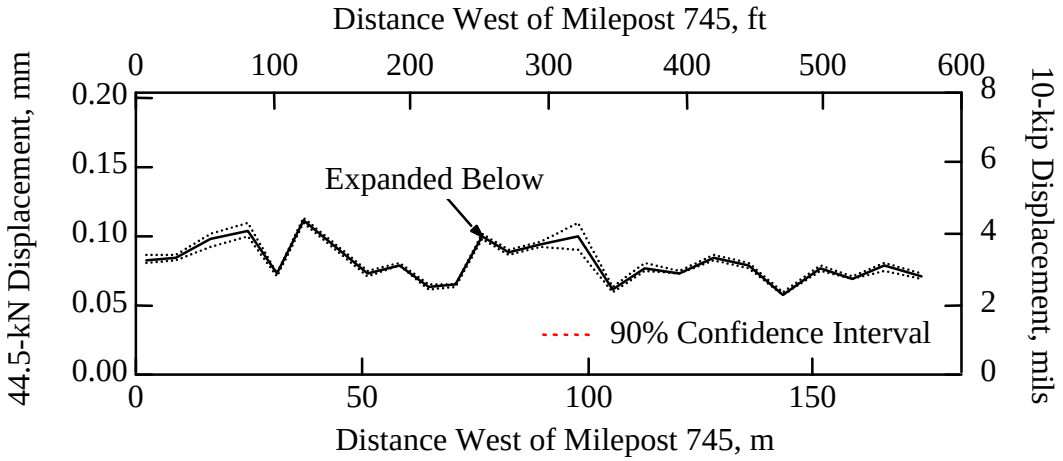

a) Displacement Profile

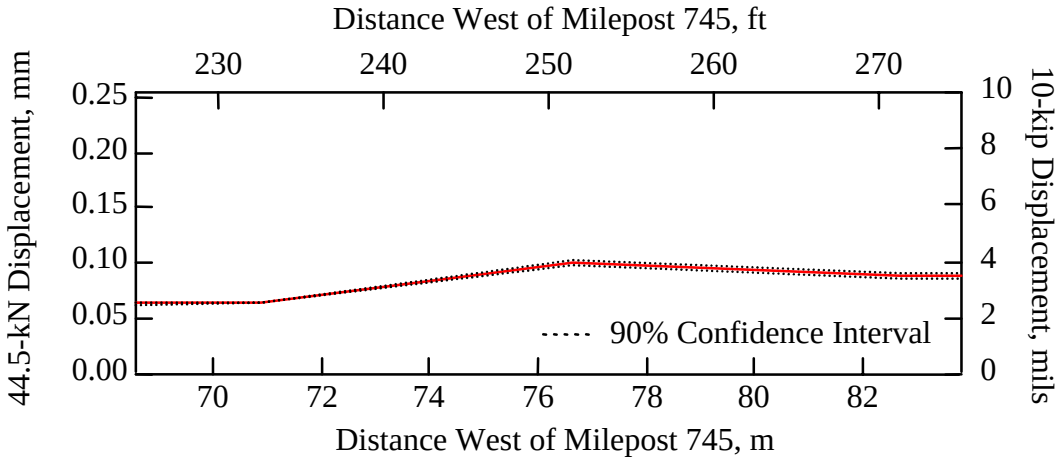

b) Expanded View of Displacement Profile Near Joint

Figure 8.39 Adjusted Displacements Calculated Using Composite IIR-FIR Digital Filter with a Resolution Time of 16 seconds; Testing along IH-10 in Houston, Texas

This series of figures shows how small pavement details, such as joints, become more apparent in the displacement profile as shorter resolution times are used in the analysis. Also, the 90 percent confidence intervals become wider with shorter resolution times, indicating less accurate measurements. However, the confidence intervals really only become very wide at each joint because of the increase in rolling noise associated with the rolling sensor crossing the joint. The confidence interval remains reasonably narrow away from the joints for all of the resolution times used, even 0.25 seconds. A resolution time of 1 second appears to have adequate spatial resolution to accurately characterize joint behavior with reasonably narrow 90 percent confidence intervals.

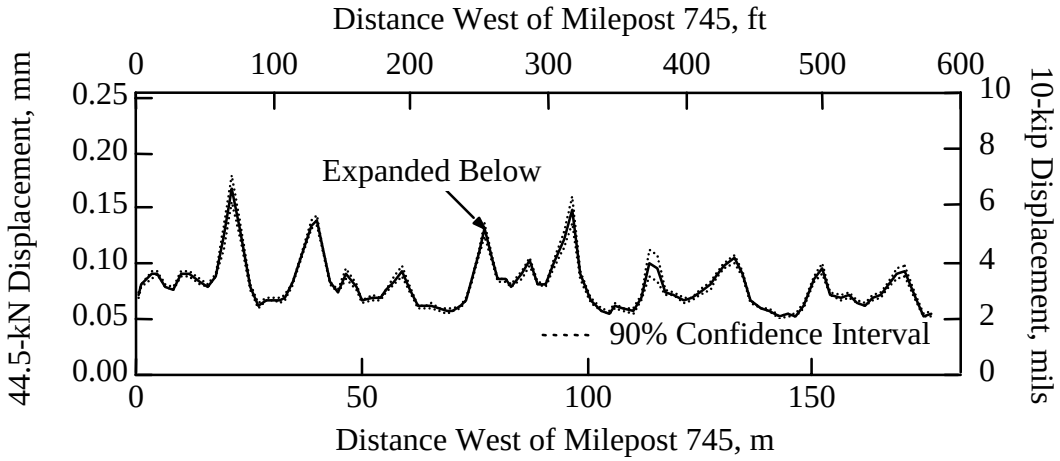

a) Displacement Profile

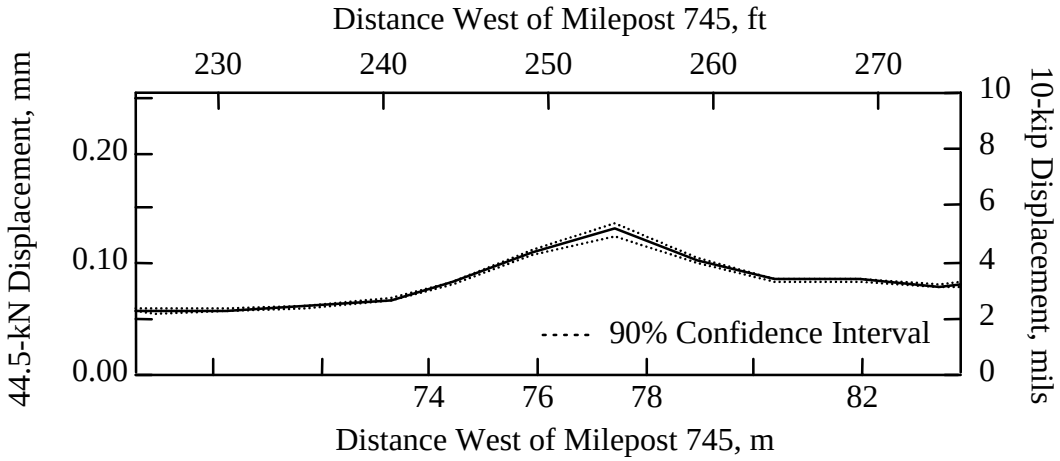

b) Expanded View of Displacement Profile Near Joint

Figure 8.40 Adjusted Displacements Calculated Using Composite IIR-FIR Digital Filter with a Resolution Time of 4 seconds; Testing along IH-10 in Houston, Texas

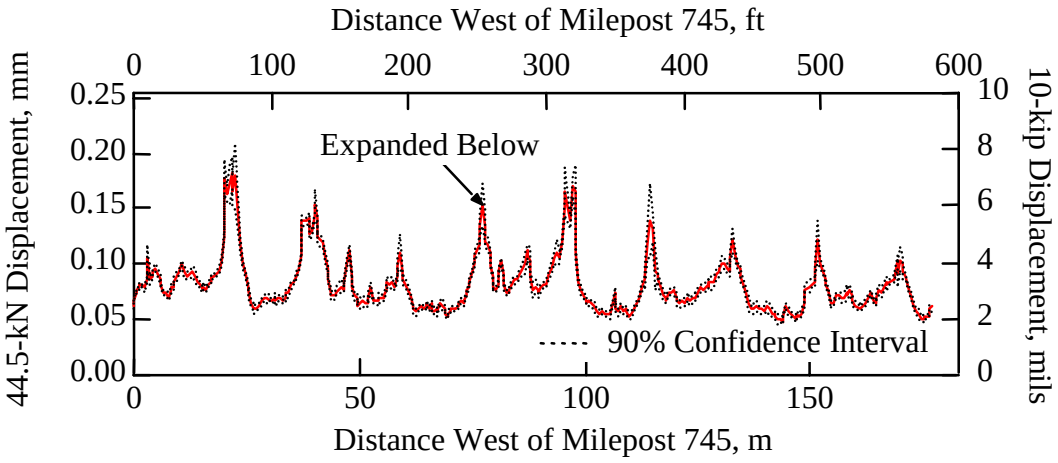

a) Displacement Profile

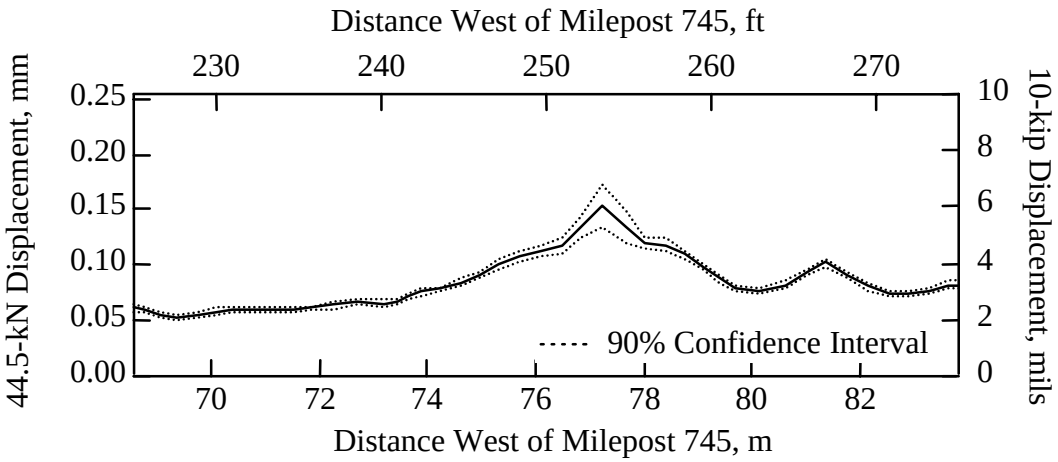

b) Expanded View of Displacement Profile Near Joint

Figure 8.41 Adjusted Displacements Calculated Using Composite IIR-FIR Digital Filter with a Resolution Time of 1 second; Testing along IH-10 in Houston, Texas

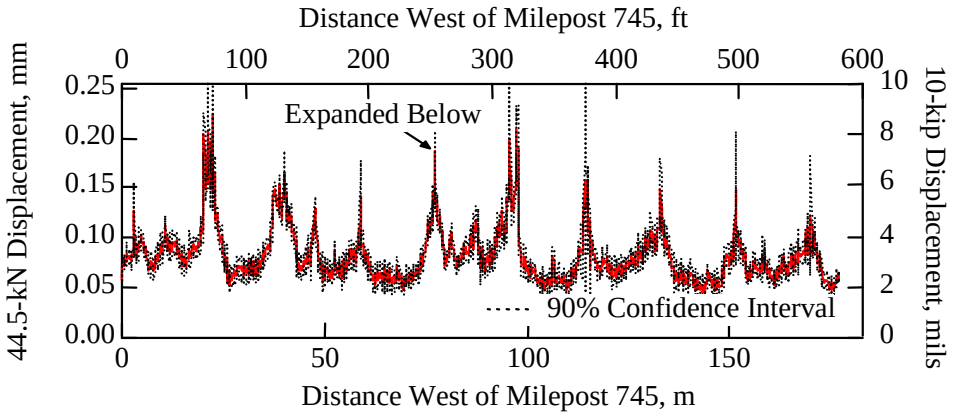

a) Displacement Profile

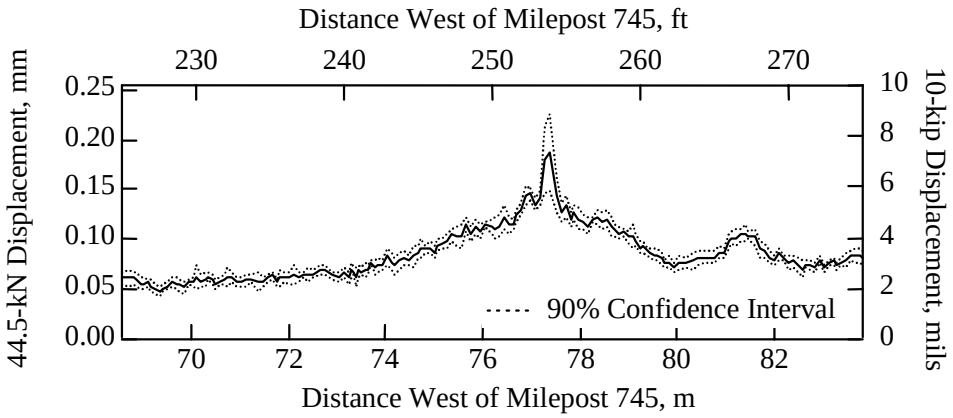

b) Expanded View of Displacement Profile Near Joint

Figure 8.42 Adjusted Displacements Calculated Using Composite IIR-FIR Digital Filter with a Resolution Time of 0.25 seconds; Testing along IH-10 in Houston, Texas

The analyses illustrated in Figures 8.39 through 8.42 were repeated using Hamming FIR digital filters. The results of both sets of analyses are summarized for both the force and the displacement results in Figure 8.43. The average 90 percent confidence interval represents the average over the entire section as a percent of the displacement or force. Figure 8.43 illustrates three important points. First, increasing the measurement resolution time decreases the 90 percent confidence interval for both force and displacement measurements. Second, the 90 percent confidence interval for displacement measurements is about 2.5 to 3 times higher than that for force measurements. This comparison indicates that neglecting the noise in the measurements when calculating confidence intervals for displacement profiles is justified. Third, results obtained using a composite IIR-FIR digital filter are very similar to the results obtained using a Hamming FIR digital filter. For these data, the composite IIR-FIR digital filter rejected slightly more noise than the Hamming FIR filter, resulting in somewhat narrower 90 percent confidence intervals.

8.8 SUMMARY

This chapter has discussed the procedures used to analyze RDD data in detail. The product of this analysis is a continuous displacement profile of the pavement tested. The amplitude demodulation method is used to calculate the dynamic force applied to the pavement and the displacement induced by that force. Digital filters play an important role in the amplitude demodulation method. Two different digital filter designs were given, and the comparative advantages of each were presented. With either filtering method, the filter settling time influences the time and spatial resolution and accuracy of the measurement. Long filter settling times result in less spatial and time resolution, but high accuracy. Short filter settling times result in high time and spatial resolution, but decrease the accuracy owing to an increase in the impact of rolling noise. The digital filter parameters can be adjusted to obtain a desired combination of accuracy and spatial resolution in the displacement profile. The accuracy of the analysis results can be determined using statistical tools to calculate confidence intervals.

The analysis procedure was illustrated using a section of RDD data measured on a rigid highway pavement on IH-10 in Houston, Texas. These data were analyzed using various filter parameters to illustrate their impact on confidence intervals and spatial resolution of the measurement. These results show that very accurate displacements are obtained for regions of pavement away from joints for all of the filtering parameters used in these analyses. The compromise between accuracy and spatial resolution becomes more important near joints. For these data, an interval between measurement results, Δt_r, of 1 second, with the digital filter parameters associated with this interval, was found to give a reasonable compromise between accuracy and spatial resolution near joints.

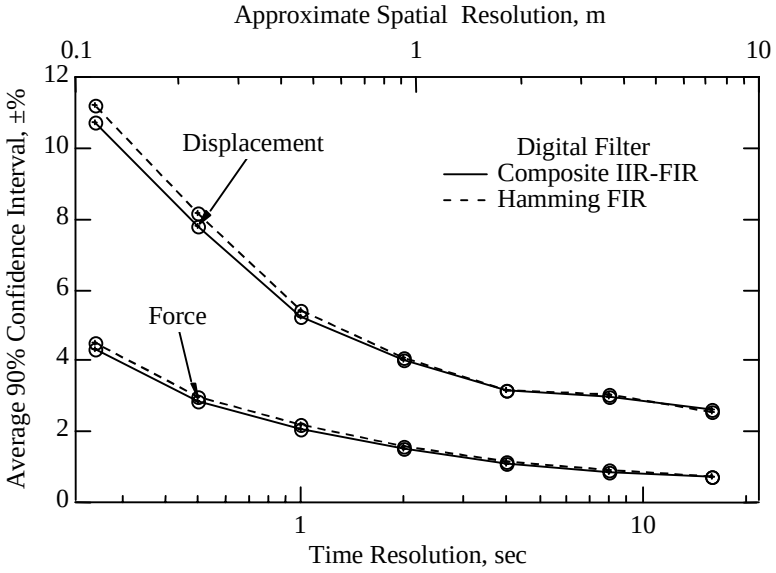

Figure 8.43 Average 90 percent Confidence Intervals for Force and Displacement Measurements versus Measurement Resolution for Composite IIR-FIR and Hamming FIR Digital Filters; Testing along IH-10 in Houston, Texas

CHAPTER 9. RESULTS OF ROLLING DYNAMIC DEFLECTOMETER TESTING AT TWO HIGHWAY SITES

9.1 INTRODUCTION

The rolling dynamic deflectometer (RDD) is a valuable tool for characterizing highway pavements. The speed of testing allows the RDD measurements to be performed with a limited amount of interference to existing traffic. Further RDD testing can be performed successfully in the presence of vibrations resulting from traffic in lanes adjacent to the testing lane. The effectiveness of the RDD at characterizing highway pavements has been demonstrated with testing at two different sites on Interstate Highway 10 (IH-10) over a total length of 33.5 km (21 mi). The first site is near Orange, Texas, and the second site is in Houston, Texas. The results of these tests are presented in this chapter.

9.2 ANALYSIS METHOD

A slightly different method was used to analyze the data presented herein than was presented in Chapter 8 because these data were analyzed before the methods presented in Chapter 8 were fully developed. The method used to analyze the highway tests is equivalent to the analysis method proposed in Chapter 8 using a composite IIR-FIR filter, except that the order in which the various steps in the analysis were applied were rearranged. An IIR digital notch-pass filter was first used to reject all frequencies except the operating frequency. The filtered data were then demodulated and a decimating FIR filter used to obtain the final results. The only difference between this method and the method presented in Chapter 8 is that the IIR digital filter is applied to the raw data rather than the demodulation product. This means that a different IIR digital notch-pass filter must be designed for each RDD operating frequency used. This method yields results identical to those obtained using the method proposed in Chapter 8, but lacks the flexibility of the proposed method.

Digital filter parameters were selected to obtain a measurement resolution time, Δt_r, of 1 second. This resolution time was shown to give adequate spatial resolution to characterize the joint behavior, and good measurement accuracy at midslab regions and joints.

9.3 TESTING ON IH-10 NEAR ORANGE, TEXAS

9.3.1 Background

On August 14 and 15, 1996, RDD testing was performed on approximately 11 km (7 mi) of Interstate Highway 10 (IH-10) near Orange, Texas. This testing was conducted by the writer, Dr. Kenneth H. Stokoe, II, and Dr. N. James Lee. Traffic control was provided by the Texas Department of Transportation (TxDOT). Additionally, falling weight deflectometer (FWD) testing was performed simultaneously at this site by Mr. Mark McDaniel of TxDOT.

9.3.1.1 Testing Location — A map of the testing location is shown in Figure 9.1. The test section is located between mileposts 874 and 878. Testing was performed in the outside (right) lane along both eastbound and westbound sections of IH-10.

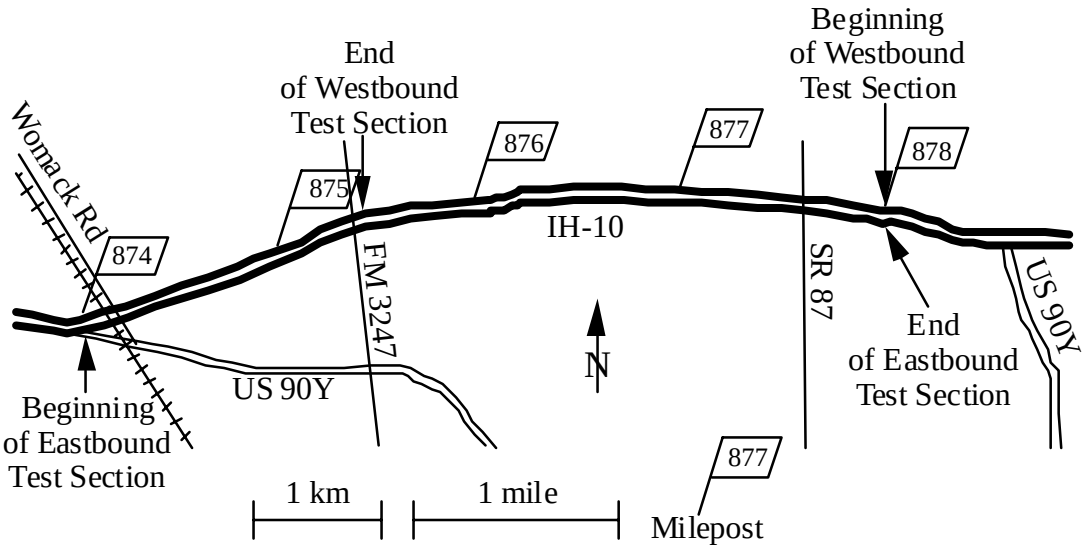

Figure 9.1 Map of RDD Test Sections on IH-10 near Orange, Texas

9.3.1.2 Pavement Properties — The pavement on IH-10 near Orange, Texas, is unreinforced, jointed PCC pavement, with joints spaced every 4.6 m (15 ft). The pavement consists of 25 cm (10 in.) thick PCC, 10 cm (4 in.) sand shell base, and 20 cm (8 in.) select fill (silty-sand) subbase. The subgrade is soft, clayey soil. The pavement was constructed in 1959.

9.3.1.3 Traffic Control — Traffic control was provided by the TxDOT Beaumont District. For this testing, the outside (right) lane was closed to traffic for RDD and FWD testing. Sections of highway 1.6 km (1 mi) long were closed to traffic with signs and cones. RDD testing for each 1.6-km (1-mi) section took approximately 1.5 hours. When RDD testing reached the end of a closed section, the RDD was removed from the highway, the traffic control crew removed the cones and signs, and the next mile of highway was closed. The change procedure took approximately 1.5 hours. No problems were encountered from adjacent traffic during this testing, even though a significant amount of heavy truck traffic was present.

9.3.1.4 Testing Procedures — All RDD testing was performed using an operating frequency of 40 Hz. Testing was conducted using a speed along the pavement of 0.46 m/s (1.5 ft/sec). A static force of about 80 kN (18 kip) and a p-p dynamic force of about 44.5 kN (10 kip) were applied to the pavement. The testing was divided into segments of pavement approximately 305 m (1,000 ft) long. New data files were initiated at the beginning of each segment, and the RDD was stopped at the completion of each segment to minimize the size of the data files. Subsequently, it has been found that there is no advantage to small data files and that testing is much more efficient when performed in longer segments on the order of 1.6 km (1 mi.).

The configuration used for the rolling sensors in this series of tests is shown in Figure 9.2. This configuration uses two sensors positioned along the centerline between the two loading rollers (designated as centerline sensors) and two sensors positioned along a line outside the loading rollers (designated as outside sensors). Each pair of sensors has one sensor in-line with the loading rollers (designated as in-line sensors) and one sensor leading the loading rollers by 0.914 m (3 ft) (designated as leading sensors). The centerline sensors are positioned on the outside wheel path of the highway traffic, and the outside sensors are positioned 0.305 m (1 ft) from the lane-shoulder joint. The centerline sensors are placed in a position more heavily loaded than the position of the outside sensors and, based on analysis of this work, provided more valuable data than the outside sensors. A photograph of the RDD testing in progress near Orange, Texas, is shown in Figure 9.3.

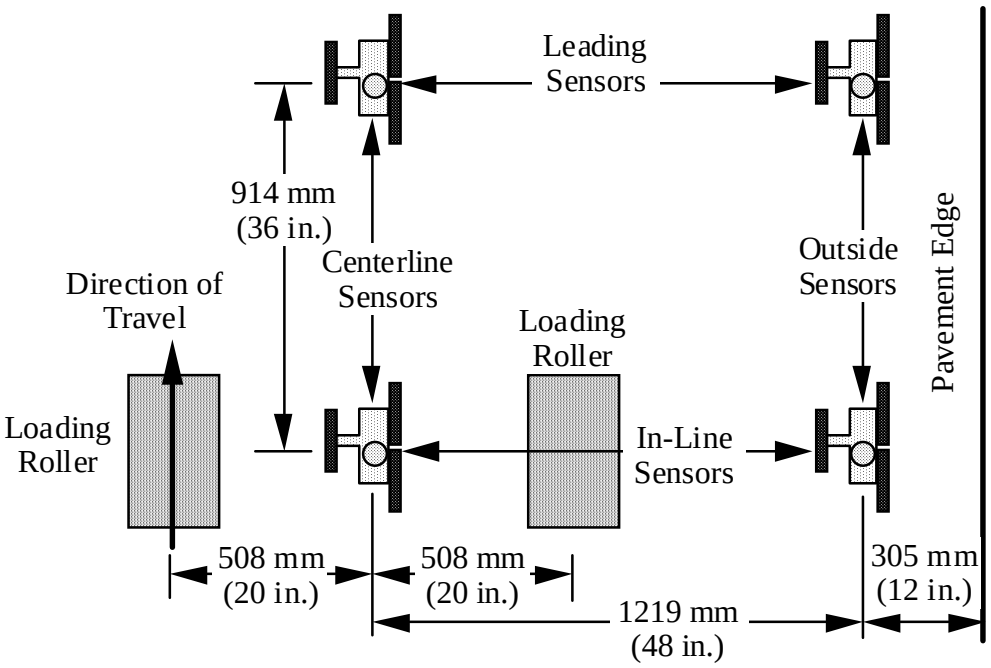

Figure 9.2 Rolling Sensor Configuration Used for RDD Testing on IH-10 near Orange, Texas

Figure 9.3 Photograph of RDD Testing on IH-10 near Orange, Texas

9.3.2 Results

9.3.2.1 Typical Displacement Profiles — Displacement profiles measured with all four rolling sensors on a typical section of pavement are presented in Figure 9.4. Figure 9.4a shows the displacement profiles measured with the two centerline sensors. The peaks in the displacement profile measured with the centerline-in-line sensor correspond to the location of joints (or cracks) in the pavement. The displacement profile measured with the leading-centerline sensor, also shown in Figure 9.4a, exhibits a response very different than the centerline-in-line sensor. Generally, the leading sensor measured smaller displacements than the in-line sensor. This is to be expected because the measurement point is farther from the loading rollers where the forces are applied.

Interestingly, as soon as the leading-centerline sensor crosses a joint, the displacement measured with that sensor decreases abruptly. This phenomenon is illustrated in Figure 9.5 for clarity. This figure shows the displacement profile measured with the leading-centerline sensor across a single joint, with drawings of the loading rollers and leading sensor at three different positions relative to the joint, designated Positions A, B, and C. Arrows from each drawing show the displacement that was measured when the loading rollers and leading sensor were in that position. In Position A, the leading sensor is on the approaching side of the joint and a displacement, D_A, of 0.128 mm (5.02 mils) was measured. In Position B, the leading sensor has crossed over to the departing side of the joint on the next slab while the loading roller is still on first slab, and a displacement, D_B, of 0.0479 mm (1.89 mils) was measured. The displacement has decreased abruptly because the two slabs are not connected with dowels or keys, allowing the slabs to move somewhat independently of each other. In Position C, the loading roller crosses the joint so that the loading roller and the leading sensor are again on the same slab, and the displacement increases to 0.174 mm (6.84 mils).

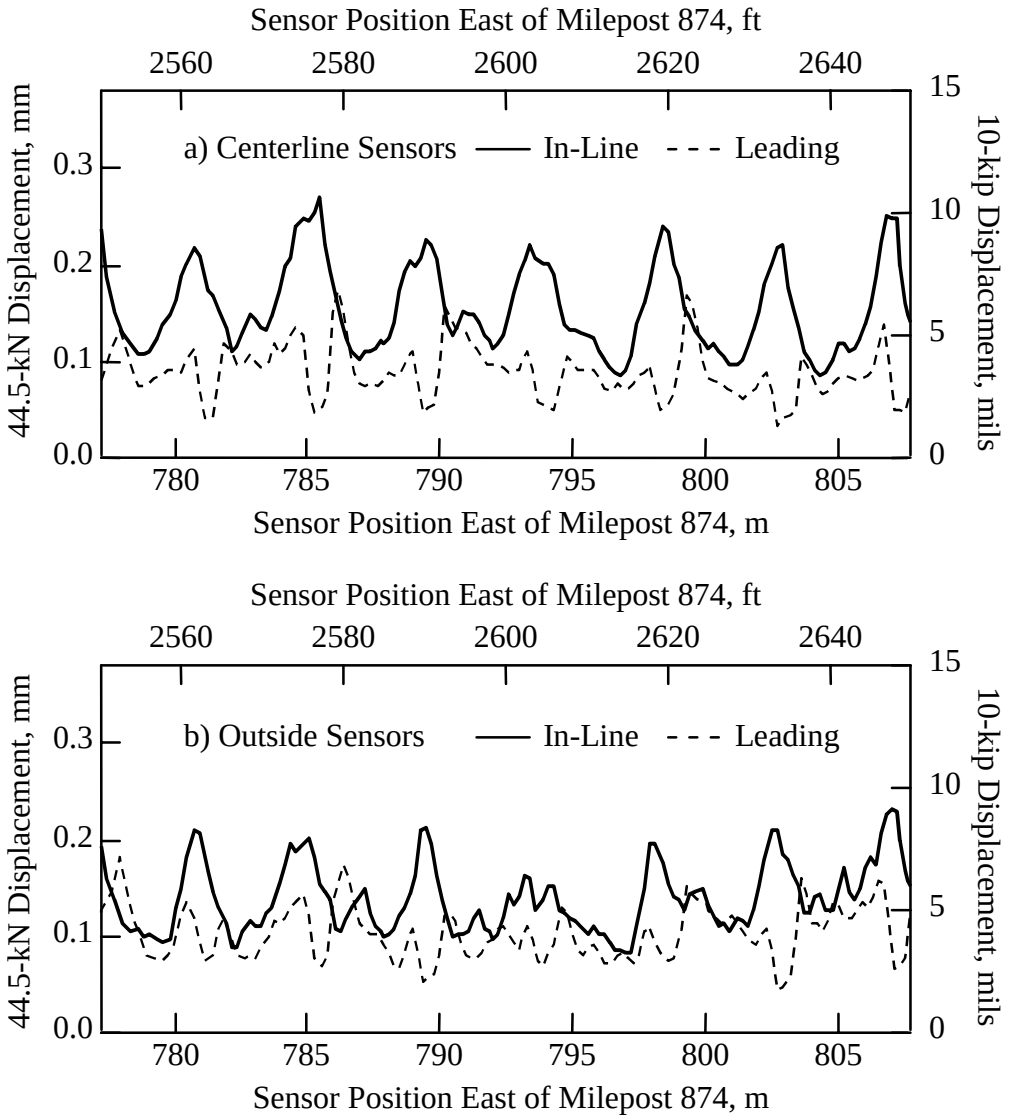

Figure 9.4 Displacement Profiles Measured with Four Rolling Sensors on a Typical Section of IH-10 near Orange, Texas

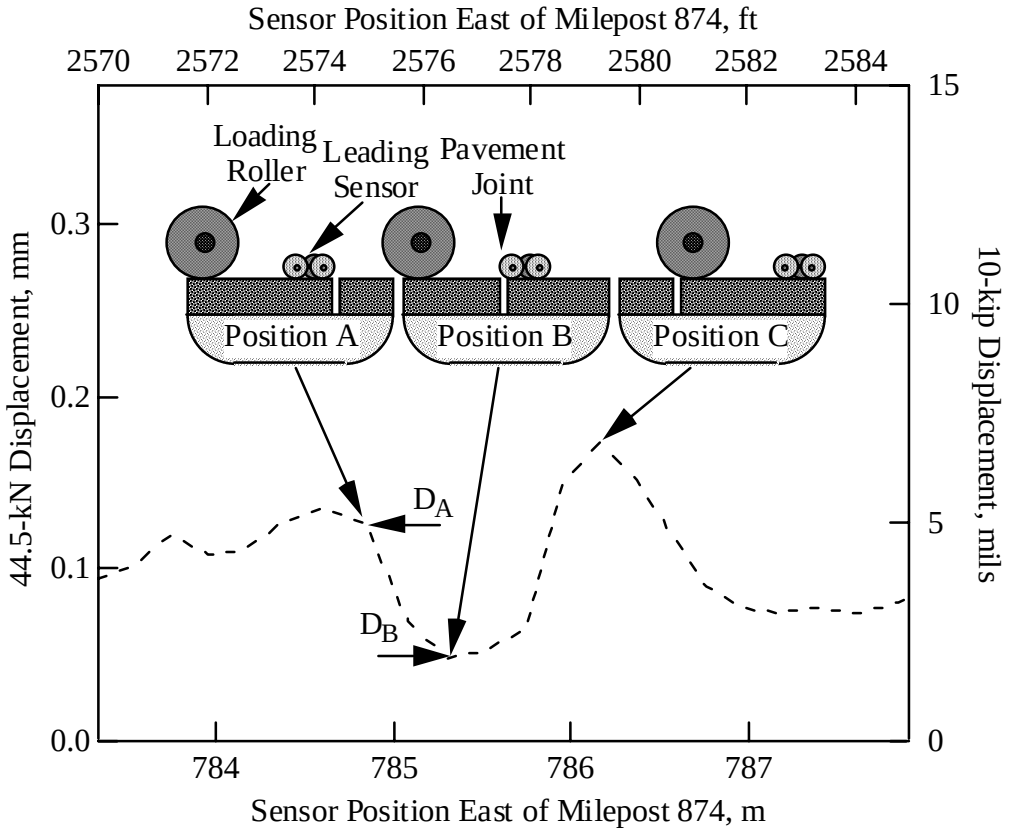

Figure 9.5 Displacement Profile Measured with Leading-Centerline Sensor across a Single Joint

The leading sensor displacement profile can be used to estimate the load transfer efficiency of each joint. This calculation is performed using the displacements measured in Positions A and B in Figure 9.5 as follows:

$$\text{Load Transfer Efficiency} = \frac{D_B}{D_A} \times 100\%. \qquad \text{(Equation 9.1)}$$

For the joint shown in Figure 9.5, the load transfer efficiency is 38 percent.

The displacement profiles measured with the outside sensors are presented in Figure 9.4b. These profiles exhibit similar behavior to those from the centerline sensor. However, the displacements measured with the outside sensors are lower than those measured with centerline sensors. This is consistent with the fact that the outside sensors are positioned farther from the two loading points. Also, the displacement profiles measured with the

outside sensors are complicated by their proximity to the edge of the slab and the efficiency of load transfer across this longitudinal joint.

The displacement profiles measured with the outside sensors contain valuable information about the pavement system. Currently, however, tools to analyze two-dimensional deflection bowls have not been developed. Therefore, only displacement profiles from the centerline sensors will be presented in the remainder of this discussion.

9.3.2.2 Displacement Profiles of Intact and Cracked Slabs — The displacement profile measured with the centerline-in-line sensor for a 549 m (1880 ft) length of pavement is shown in Figure 9.6. This interval of testing is especially interesting because the displacement increases beginning at about 800 m (2,600 ft). Regions with the lower and higher displacements are shown in expanded forms in Figure 9.7. For the "intact slab" results shown by the solid line in Figure 9.7a, peaks in the displacement profile are spaced about every 4.6 m (15 ft) in this region. These peaks correspond to the joint locations, and the pavement tested is intact, with no midslab cracking. In the plot with a higher displacement designated as "cracked slab" in Figure 9.7a and shown by the dashed line, the peaks are spaced approximately 2.3 m (7.5 ft) apart. This indicates that the slabs have experienced midslab cracking. It is interesting to see that the displacements measured at joints and at cracks are similar for the intact and cracked slabs. However, the displacements measured at the midpoints between joints and the displacements measured at the midpoints between joints and cracks are quite different, with higher midslab displacements in the cracked slabs.

Another interesting conclusion from this testing is shown in the expanded displacement profile in Figure 9.7b. In this figure, the regions of the slab where the displacement is influenced by the joint are delineated. The region of influence extends more than 1 m (3 ft) on either side of the joint or crack. This means that the deflections along the entire length of the slab are influenced by joints and cracks for regions of this pavement where midslab cracking has occurred. This is significant if elastic properties of the pavement are to be backcalculated from deflection measurements. Most models used for such backcalculations assume that layers have an infinite lateral extent. In pavement regions where the displacement is influenced by a nearby joint or crack, backcalculation will result in erroneous elastic properties estimates. The RDD can be used to determine the extent of such regions, representing an improvement over methods like FWD and Dynaflect testing, where it is not apparent if cracks and joints influence displacements. Also, the location on the "intact" slab where FWD testing should be performed is only about 2 m (6 ft) long. Therefore, equipment should be carefully positioned on the slab for the laterally "uniform" condition to be approximated.

A phenomenon observed in these tests is shown in Figure 9.8. In this figure, the displacement profiles measured with the two centerline sensors on a section of pavement with cracked slabs are presented. In this case, the displacement profile measured with the leading sensor does not exhibit the same behavior shown in Figures 9.4 and 9.5. In those data, the displacement measured with the leading sensor decreases abruptly when the sensor crosses a joint. With cracked slabs, as shown in Figure 9.8, this abrupt decrease is not present. Instead, the displacement measured with the leading sensor roughly parallels the displacement measured with the in-line sensor at a lower level. This difference in the behavior of cracked and intact slabs is the prevalent pattern in the measurements near

Orange, Texas. The reasons for this behavior are poorly understood and more investigations need to be conducted to understand these results.

9.3.2.3 Falling Weight Deflectometer Testing — Falling weight deflectometer (FWD) testing was conducted simultaneously with the RDD testing described above. During the time that the RDD tested 11 km (7 mi) of continuous pavement, FWD tests were performed at the center of each slab and at the joint between slabs over a total pavement length of 213 m (700 ft). In this instance, besides giving more comprehensive coverage on each slab, the RDD was more than one order of magnitude faster than the FWD. Production levels 50 percent higher than this level have been obtained in RDD testing when the RDD test intervals have been longer than the 305 m (1,000 ft) intervals used at this site.

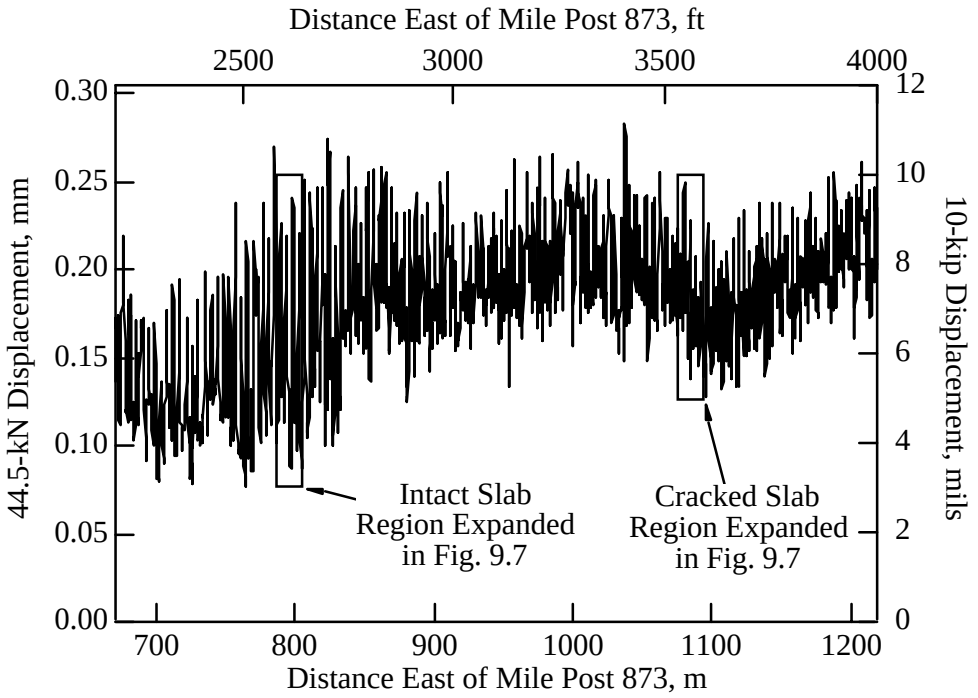

Figure 9.6 Displacement Profile Measured with Centerline-in-Line Sensor at Section of IH-10 near Orange, Texas

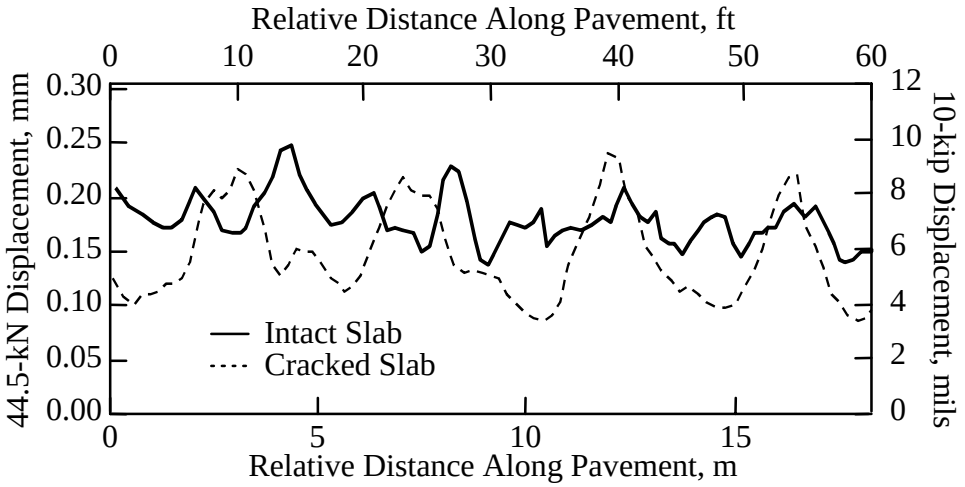

a) Expanded Displacement Profiles From Fig. 9.6

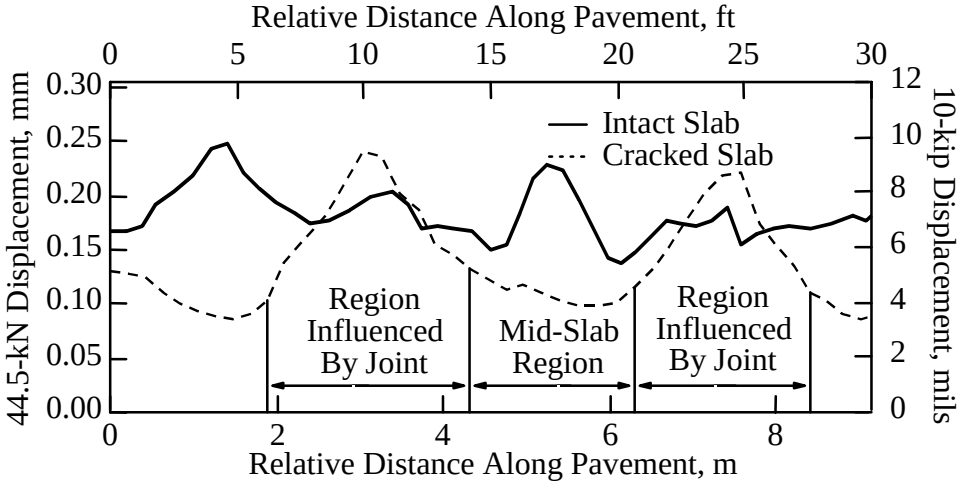

b) Expanded Displacement Profile Showing Region Influenced by Joints

Figure 9.7 Expanded Displacement Profiles from Figure 9.6 Showing Intact and Cracked Sections and the Region Influenced by Joints

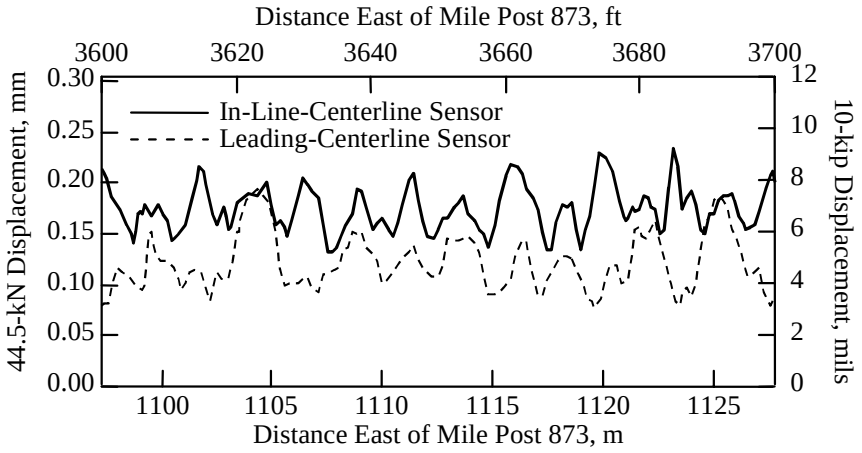

Figure 9.8 Displacement Profiles Measured with Both Centerline Sensors on a Section of Pavement with Midslab Cracking on IH-10 near Orange, Texas

9.4 TESTING ON IH-10 IN HOUSTON, TEXAS

9.4.1 Background

On November 12 through 15 and December 2 and 3, 1996, RDD testing was performed on approximately 27.2 km (17 mi) of IH-10 on the west side of Houston, Texas, by the writer and Dr. N. James Lee. This testing was part of the Center for Transportation Research (CTR) Research Project LOA 96-05, "Analysis of IH-10 and IH-610 for Cost Effective Rehabilitation." The primary purpose of the testing was to determine if a concrete overlay would be suitable for rehabilitation of that section of IH-10. A TxDOT crew from the Houston TxDOT warehouse provided traffic control for the project.

9.4.1.1 Testing Location — A map of the testing location is shown in Figure 9.9. The test section is located between mileposts 742 and 751. Testing was performed in the inside (left) lane of both eastbound and westbound sections of IH-10. Testing was performed in the inside lane rather than in the more heavily trafficked outside lane to prevent conflicts with exiting and entering traffic.

9.4.1.2 Pavement Properties — This pavement is a reinforced, jointed PCC pavement with doweled joints spaced every 18.3 m (60 ft). This pavement consists of 25 cm (10 in.) PCC, 15 cm (6 in.) of cement-stabilized base, and 20 cm (8 in.) of lime-treated subbase over the natural clayey subgrade. This pavement was constructed in the mid-1960's and was designed for a 20-year life (McCullough et al. 1997). The pavement is currently in poor condition with numerous damaged and patched regions.

9.4.1.3 Traffic Control — On the first day of testing, traffic control consisted of two illuminated-sign trucks plus a truck with a crash cushion following closely behind the RDD. This scheme allowed for extremely efficient testing, with no need to stop testing while cones were placed and removed from the highway. Unfortunately, early on the second day of testing, a minor traffic accident involving three automobiles occurred when one vehicle

struck the crash cushion. After this event, TxDOT personnel decided that the testing lane should be entirely closed to traffic. This was done with sign trucks and cones to move and keep traffic out of the testing lane. Sections of the highway that were 1.6 km (1 mi) long were closed, with extensive downtime experienced between testing on each section.

9.4.1.4 Testing Procedures — The RDD testing was performed using an operating frequency of 40 Hz. Testing was conducted using a vehicular speed along the pavement of 0.46 m/s (1.5 ft/sec). A static force of about 80 kN (18 kip) and a p-p dynamic force of about 44.5 kN (10 kip) were applied to the pavement. The testing was divided into segments of pavement approximately 1.6 km (1 mi) long. New data files were begun at the beginning of each segment, and the RDD was stopped at the completion of each segment.

The configuration used for the rolling sensors in this test series is shown in Figure 9.10. This configuration employed three sensors positioned on the centerline between the two loading rollers (designated as centerline sensors). One sensor is in-line with the loading rollers (designated as the in-line sensor) and two sensors are leading the loading rollers (designated as leading sensors), one by 0.914 m (3 ft) and the other by 1.37 m (4.5 ft). A photograph of the RDD testing in Houston is shown in Figure 9.11

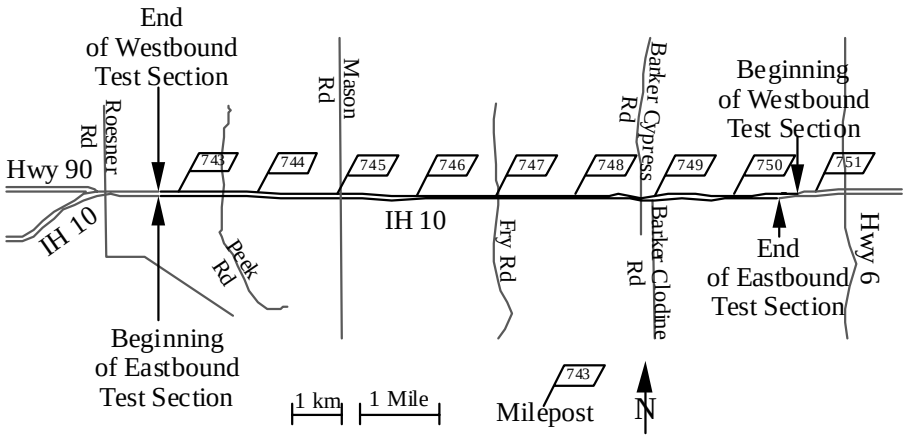

Figure 9.9 Map of RDD Test Sections on Eastbound and Westbound IH-10 in Houston, Texas

9.4.2 Results

The displacement profiles measured with the centerline-in-line sensors for the entire test section are presented in Figures 9.12 though 9.20. Each figure shows the profiles measured between two adjacent mileposts for eastbound and westbound testing. The eastbound data beginning at milepost 744 were accidentally lost and are therefore not presented. The gaps in the profiles between mileposts 745 and 746 in Figure 9.15 represent the location of a bridge where testing was not performed.

The peaks in the displacement profiles represent the displacements at joints in the pavement, and troughs in the displacement profiles represent the midslab displacements. These displacement profiles show that there is much variability in the pavement stiffness, both at the joints and at the midslab regions. Generally, higher displacements were measured

in the eastbound tests than the westbound tests (between mileposts 742 and 744 is an exception to this generalization). This finding is consistent with heavier loading in the eastbound lanes (loading generated by trucks hauling sand and gravel into Houston from gravel pits along the Colorado River west of Houston). Presumably, this trend would have been even more pronounced if testing could have been performed on the outside lanes that carry more heavy truck traffic.

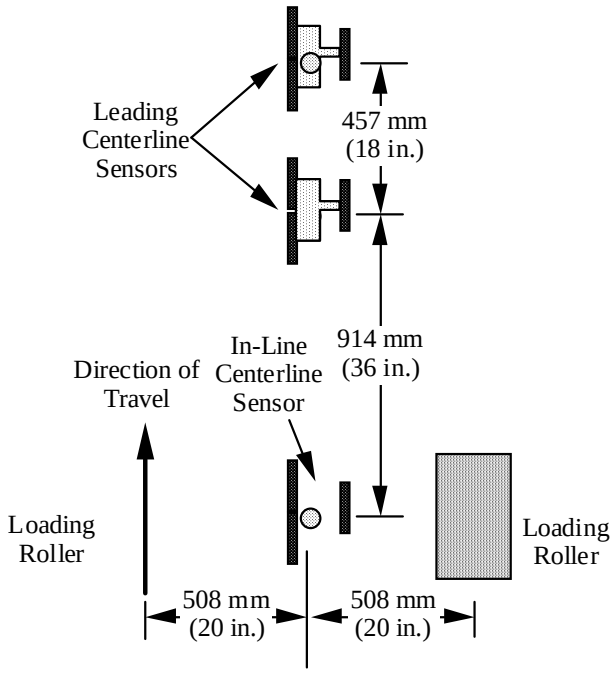

Figure 9.10 Configuration of Rolling Sensors used for RDD Testing along IH-10 in Houston, Texas

Figure 9.11 Photograph of RDD Testing on IH-10 in Houston, Texas

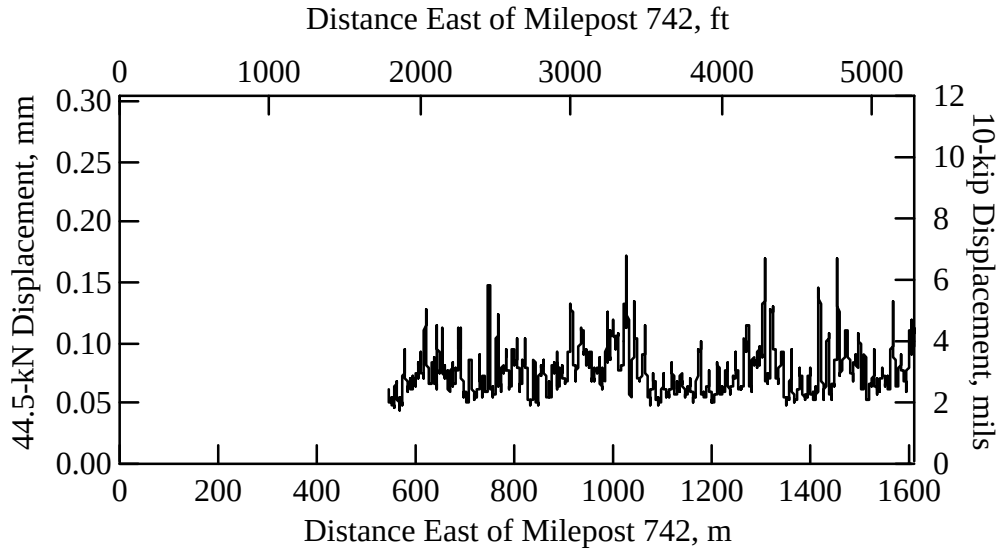

a) Eastbound Testing

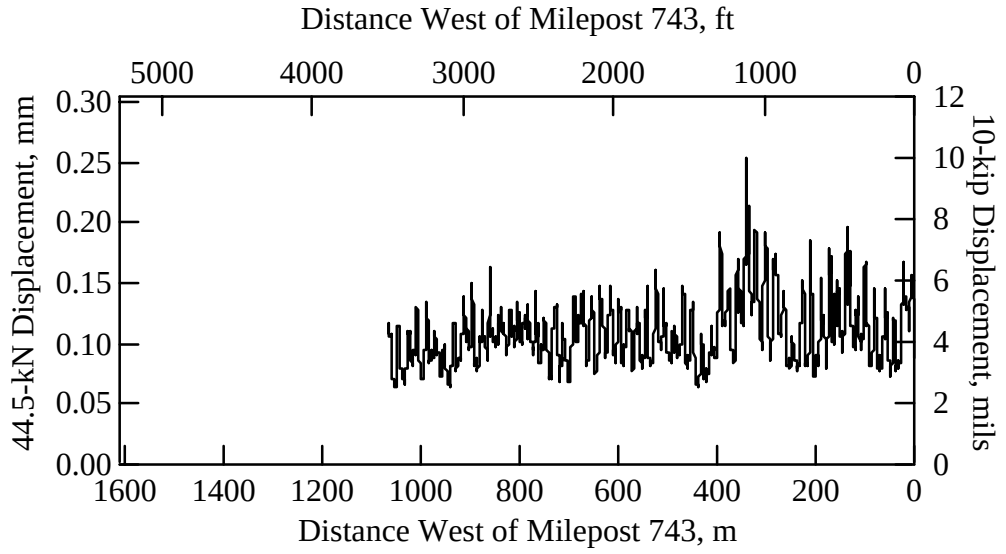

b) Westbound Testing

Figure 9.12 Displacement Profiles Measured with Centerline-in-Line Sensor between Mileposts 742 and 743 on IH-10 in Houston, Texas

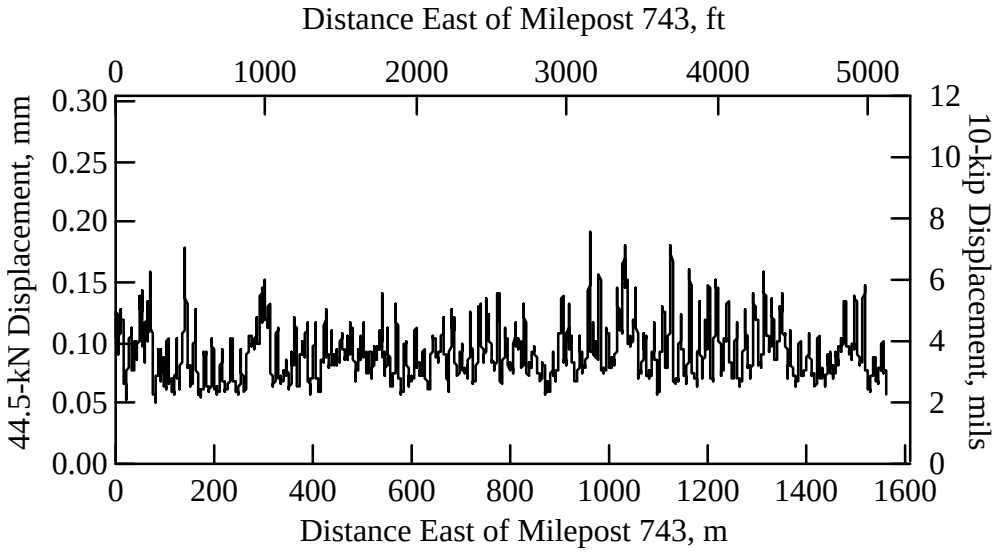

a) Eastbound Testing

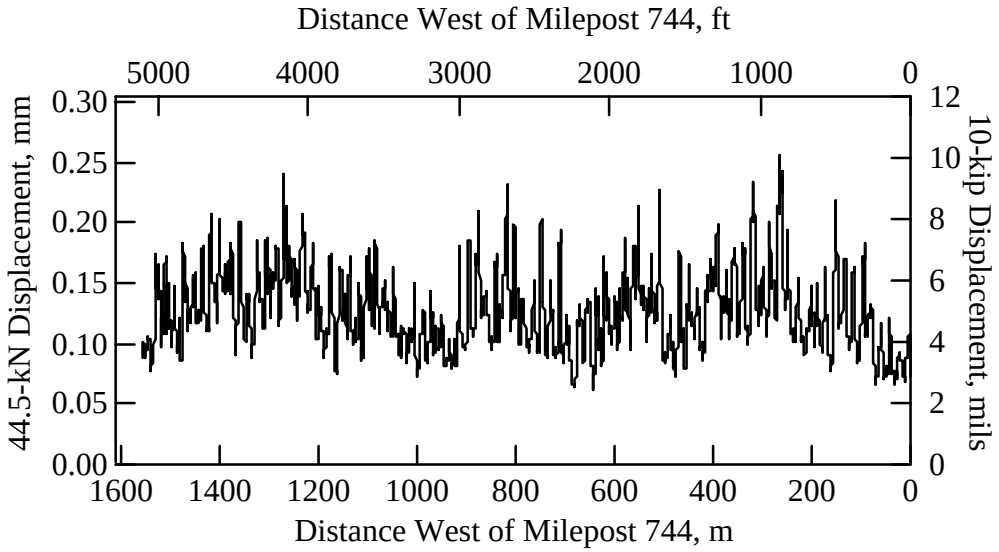

b) Westbound Testing

Figure 9.13 Displacement Profiles Measured with Centerline-in-Line Sensor between Mileposts 743 and 744 on IH-10 in Houston, Texas

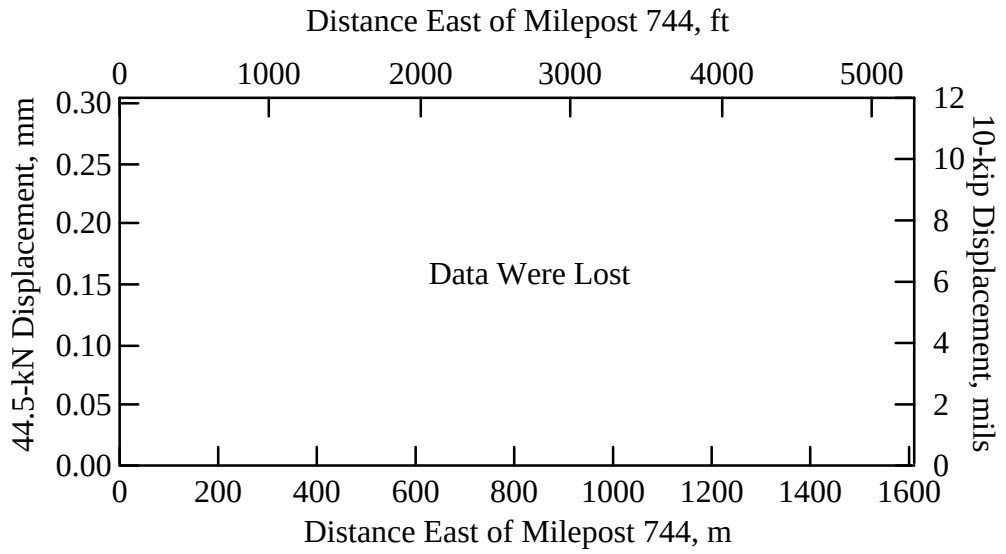

a) Eastbound Testing

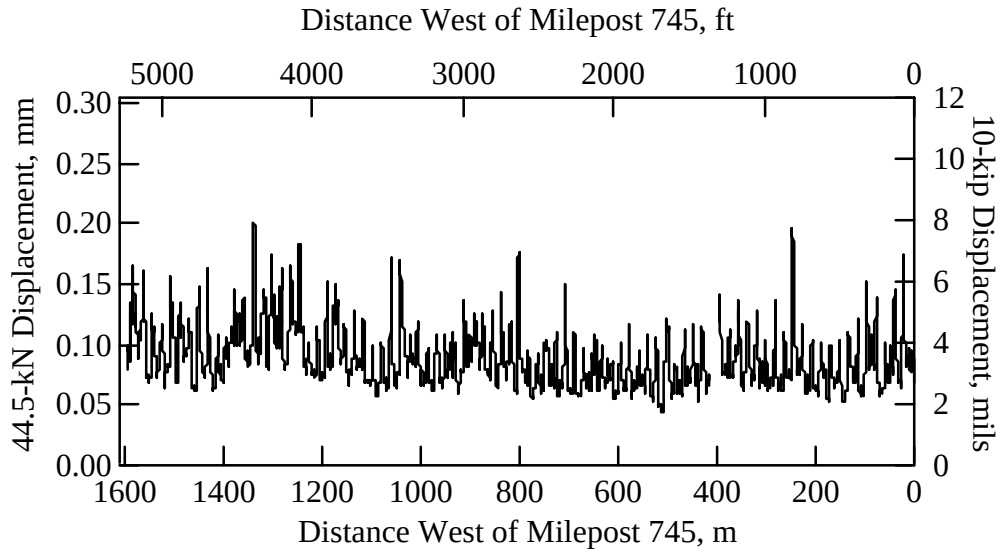

b) Westbound Testing

Figure 9.14 Displacement Profiles Measured with Centerline-in-Line Sensor between Mileposts 744 and 745 on IH-10 in Houston, Texas

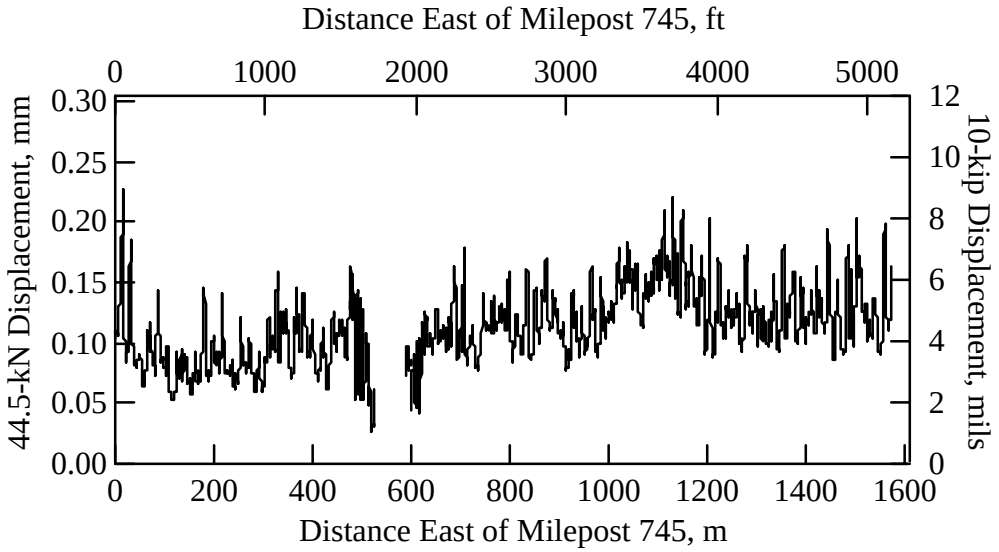

a) Eastbound Testing

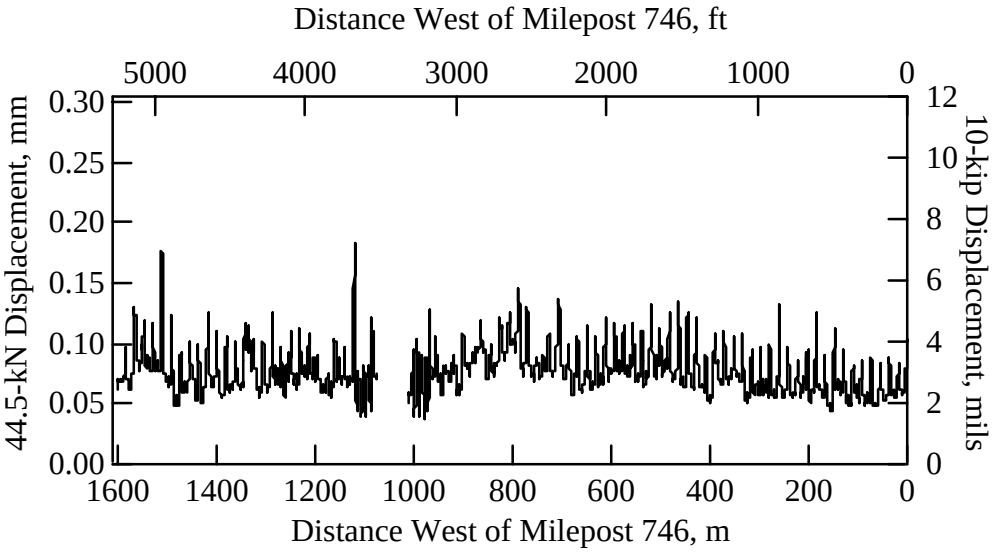

b) Westbound Testing

Figure 9.15 Displacement Profiles Measured with Centerline-in-Line Sensor between Mileposts 745 and 746 on IH-10 in Houston, Texas

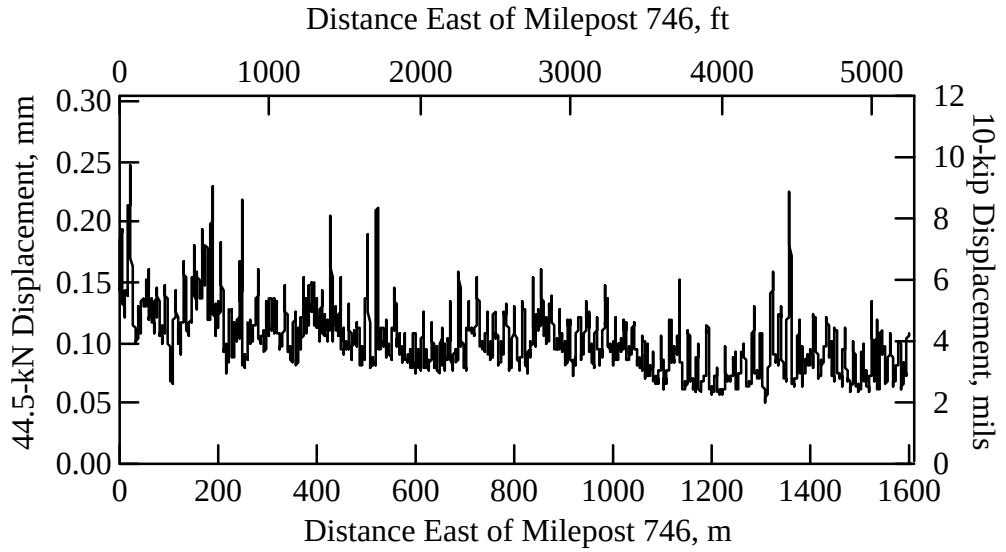

a) Eastbound Testing

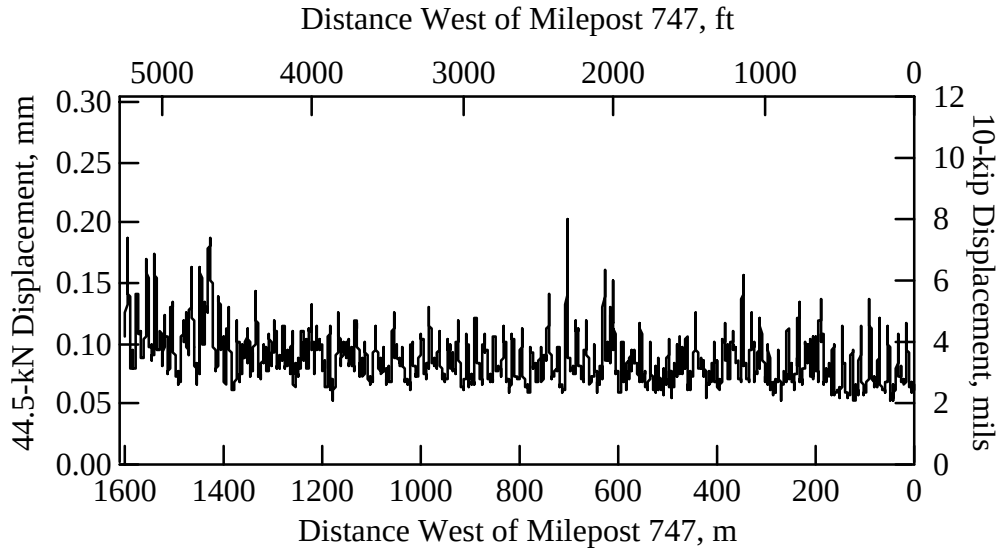

b) Westbound Testing

Figure 9.16 Displacement Profiles Measured with Centerline-in-Line Sensor between Mileposts 746 and 747 on IH-10 in Houston, Texas

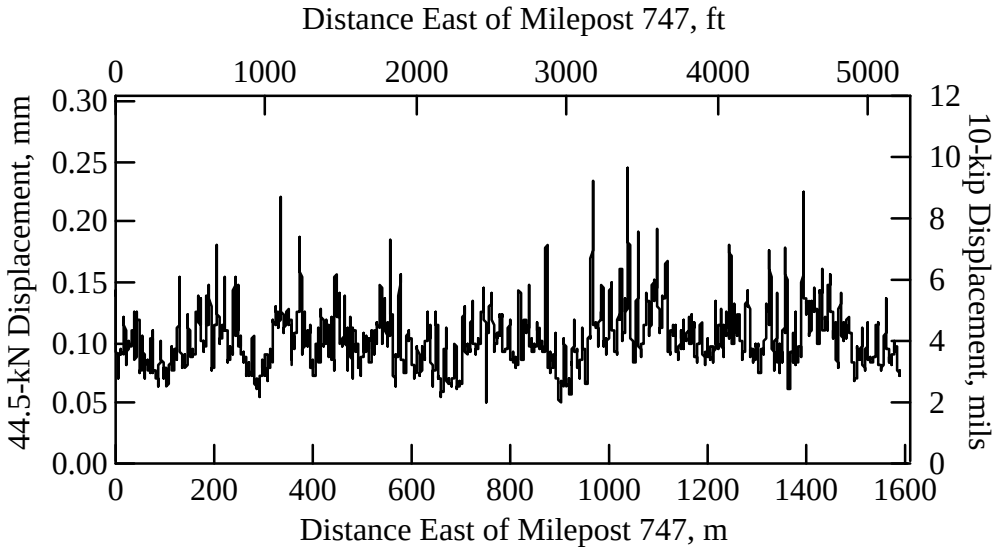

a) Eastbound Testing

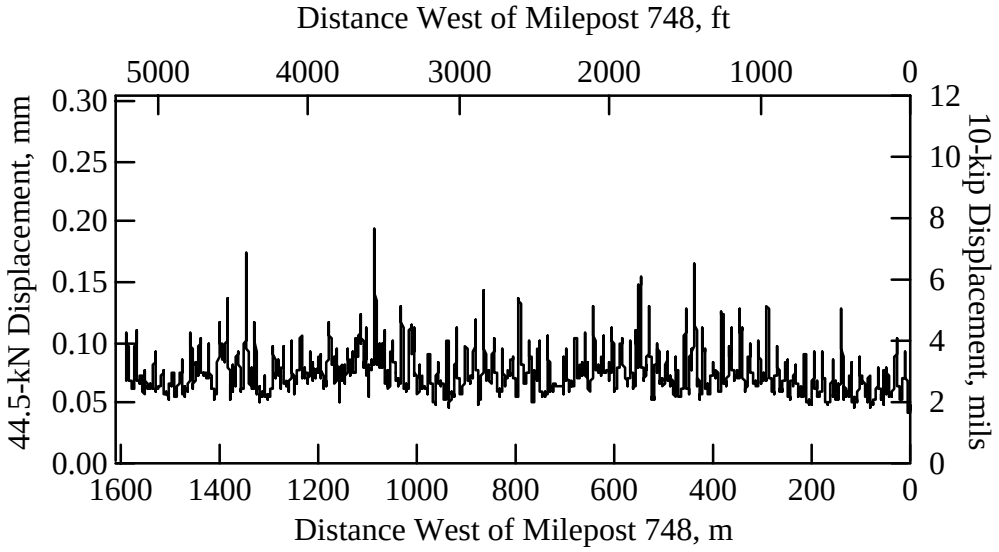

b) Westbound Testing

Figure 9.17 Displacement Profiles Measured with Centerline-in-Line Sensor between Mileposts 747 and 748 on IH-10 in Houston, Texas

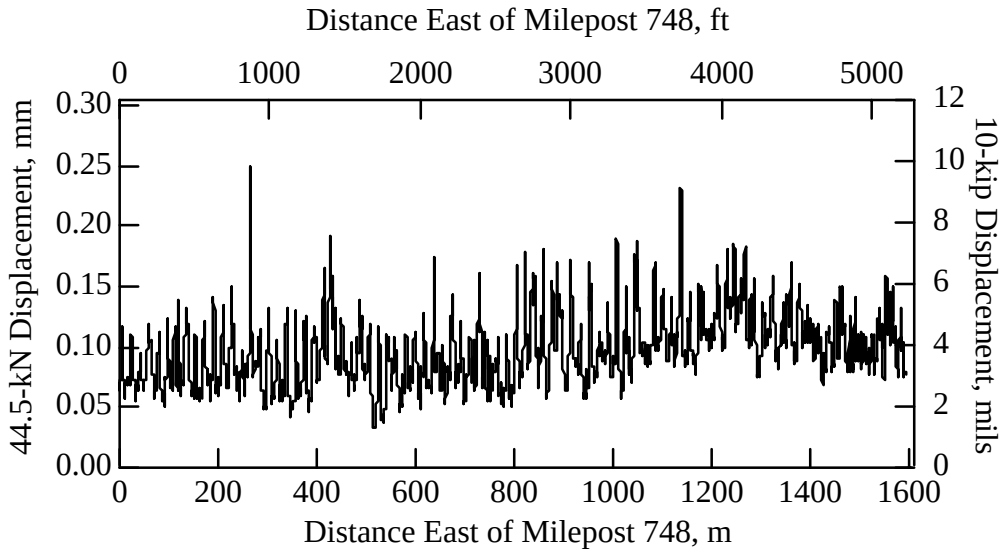

a) Eastbound Testing

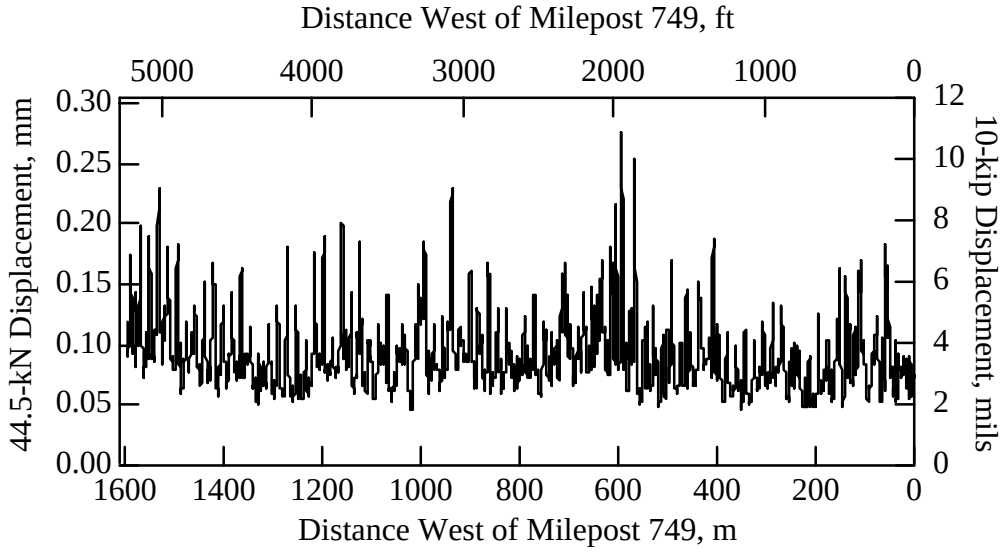

b) Westbound Testing

Figure 9.18 Displacement Profiles Measured with Centerline-in-Line Sensor between Mileposts 748 and 749 on IH-10 in Houston, Texas

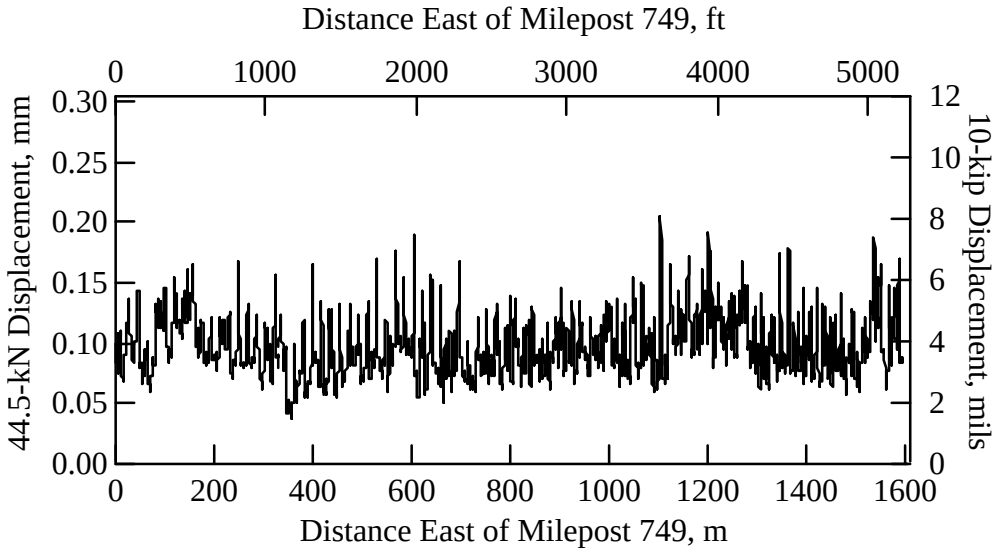

a) Eastbound Testing

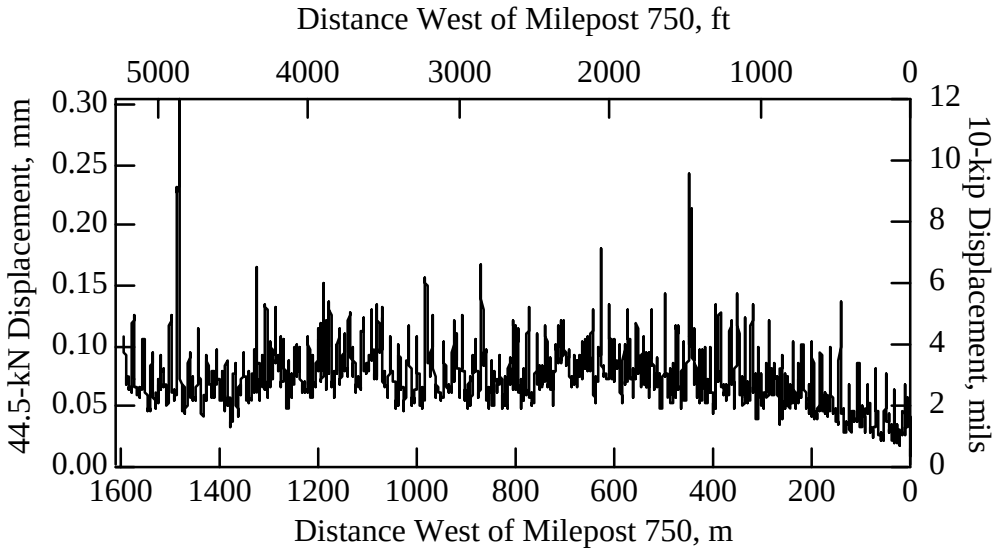

b) Westbound Testing

Figure 9.19 Displacement Profiles Measured with Centerline-in-Line Sensor between Mileposts 749 and 750 on IH-10 in Houston, Texas

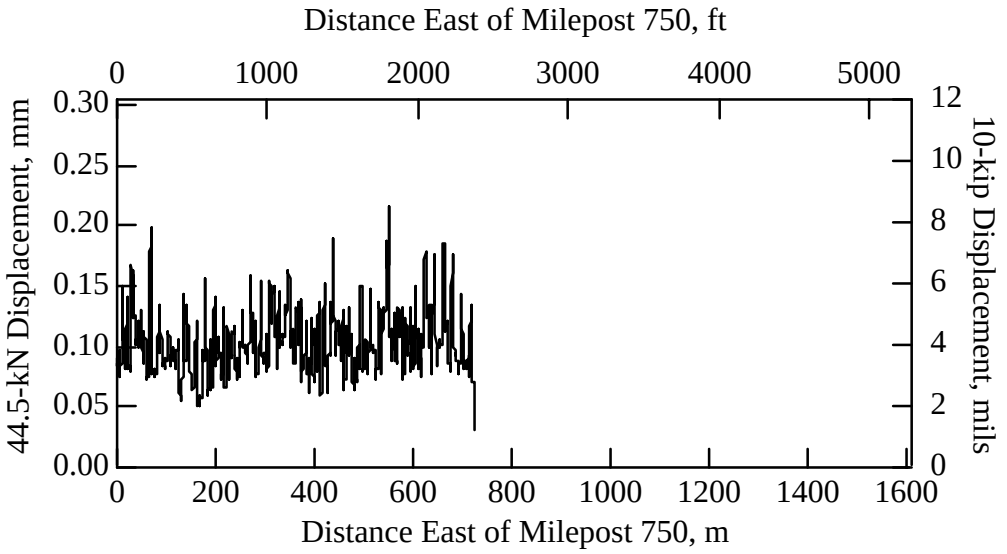

a) Eastbound Testing

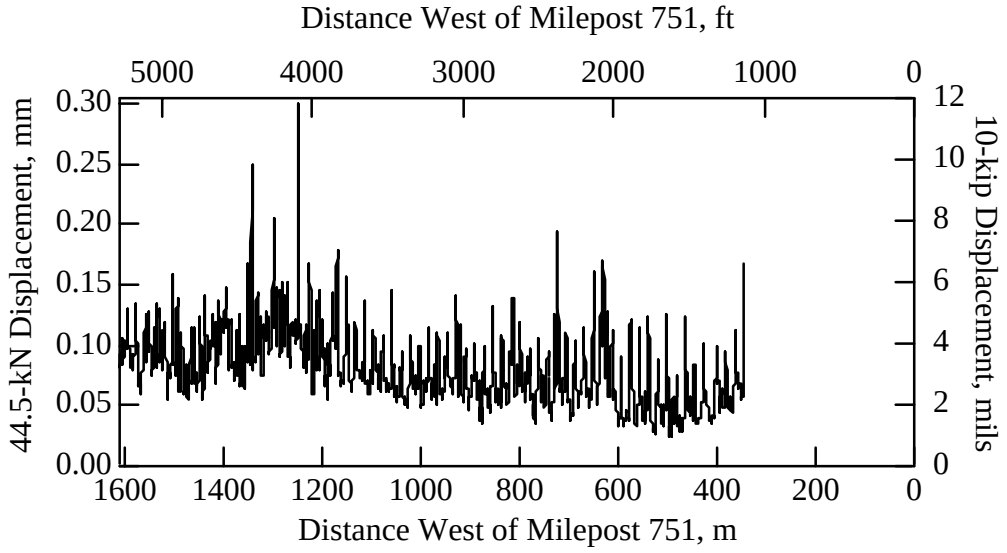

b) Westbound Testing

Figure 9.20 Displacement Profiles Measured with Centerline-in-Line Sensor between Mileposts 750 and 751 on IH-10 in Houston, Texas

9.4.2.1 Typical Results on Unpatched Pavement — Interesting results can be obtained by looking at expanded displacement profiles. A 91 m (300 ft) interval showing an expanded displacement profile from a typical section of highway is shown in Figure 9.21. The peaks in this displacement profile are spaced at intervals of 18.3 m (60 ft), corresponding to the locations of the pavement joints. Unlike results from IH-10 near Orange, there is a significant midslab region that is not influenced by the joints. One joint is included in this section that exhibited especially high displacements. A photograph of this joint is shown in Figure 9.22. This joint has opened up and is experiencing spalling. Based on a simple relative comparison, this joint is probably in need of repair.

The displacement profiles measured with the leading sensors are plotted along with that of the in-line sensor in Figure 9.21. The leading sensors show that the amplitude of the displacement decreases with distance from the loading point. These data can be used to determine the shape of the induced deflection basin. The leading sensors exhibit no abrupt decrease in displacement as the sensors cross joints, indicating that the dowels connecting the joints are still functioning well.

9.4.2.2 Typical Results on Patched Pavement — Another typical 91 m (300 ft) interval showing an expanded displacement profile is presented in Figure 9.23. This interval includes a patched joint. A photograph of a typical patched joint is presented in Figure 9.24. The patching process involved removing the pavement in the vicinity of the patch and replacing that section with two slabs, such that a new joint is located at the same position as the original joint. Thus, three joints are present in the area where only one joint existed in the original pavement. The three joints explain the three closely spaced peaks in the displacement profile at the location of the patch. The patch shown in Figure 9.23 exhibits high displacements. This behavior is typical of nearly every patch in the test section.

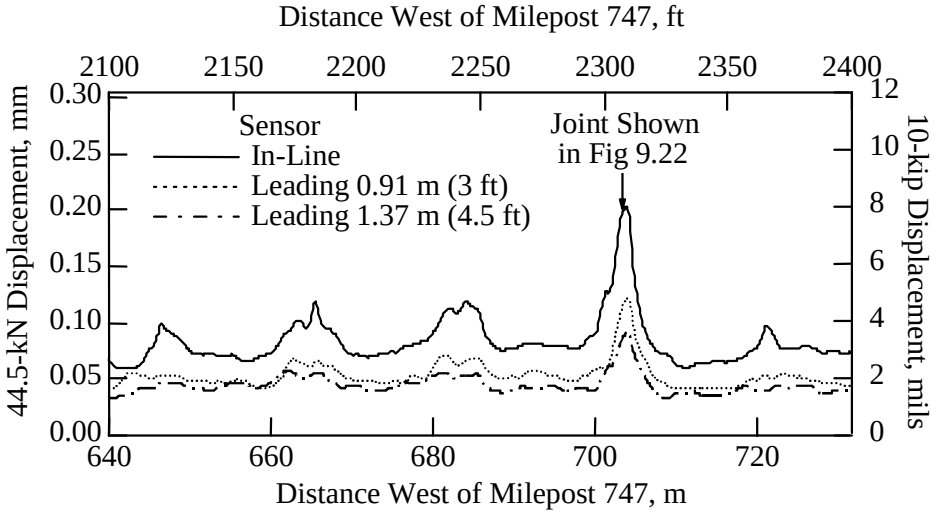

Figure 9.21 Typical Displacement Profiles with One Poorly Performing Joint from IH-10 in Houston, Texas

Figure 9.22 Photograph of Poorly Performing Joint Shown in Displacement Profiles in Figure 9.21

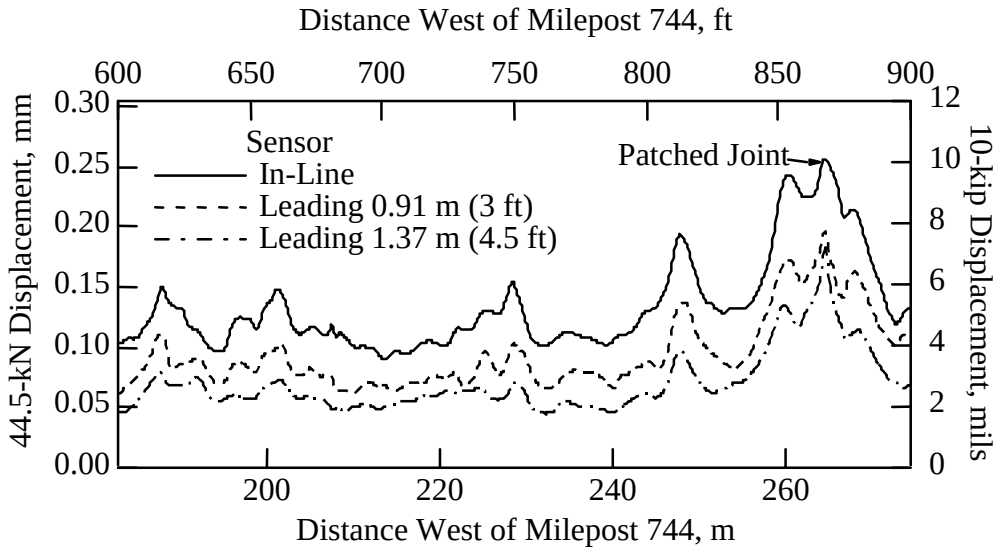

Figure 9.23 Typical Displacement Profiles with One Patched Joint from IH-10 in Houston, Texas

9.4.3 Pavement Rehabilitation Design

The proposed design for the rehabilitation of this section of IH-10 is based largely on the results of the RDD testing (McCullough et al. 1997). The high displacements at many joints eliminated the possibility of using a thin, unbonded concrete overlay to retrofit the pavement, because cracks would probably reflect through the overlay from the poorly performing joints.

As a result of the RDD testing, an alternative retrofit plan has been proposed. All poorly performing joints will be identified from the RDD results. These joints are to be repaired with a full-depth patch. The repaired pavement will be covered with a 5 cm (2 in.) thick asphalt layer. The asphalt will then be topped with a 25 cm (10 in.) thick unbonded concrete overlay.

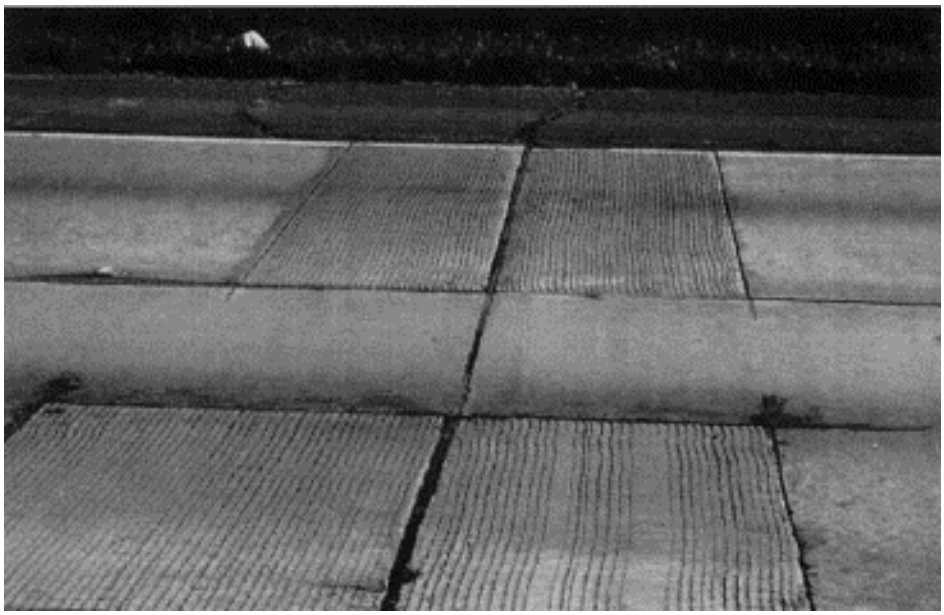

Figure 9.24 Photograph of Typical Patched Joint from IH-10 in Houston, Texas

9.5 SUMMARY

The rolling dynamic deflectometer (RDD) is an effective tool for evaluating continuous displacement profiles along pavements. Continuous displacement profiles can be used to: 1) quantify the lateral variation in pavement flexibility (stiffness); 2) locate features such as soft or weak zones, joints, and cracks; and 3) evaluate the efficiency of load transfer across joints or cracks. With other commonly used nondestructive techniques, which test only at discrete points, there is the danger that important or critical features of the pavement could be missed. This limitation is overcome by the continuous nature of the RDD test.

The effectiveness of the RDD at characterizing highway pavements was demonstrated through testing at two different locations on IH-10, one near Orange, Texas, and the other in Houston, Texas. Testing at the Orange site demonstrated the effectiveness of the RDD in

evaluating joint and midslab behavior on unreinforced concrete pavements. FWD testing was also performed at this site, and the RDD showed testing efficiencies more than an order of magnitude higher than what the FWD showed. Additionally, the RDD characterized regions influenced by joints and cracks in the pavement, which could not be determined from FWD testing. Failing to account for these regions of influence will result in erroneous interpretations of the FWD measurements.

The testing in Houston demonstrated the effectiveness of the RDD in characterizing reinforced, jointed concrete pavements. These results proved useful in designing a rehabilitation scheme for this section of pavement. A thick unbonded concrete overlay was selected based on the joint behavior shown in the RDD results. Additionally, poorly performing joints requiring repair prior to overlaying pavement were identified from the RDD results.

RDD testing has been conducted on these pavements while entire lanes have been closed to traffic and using a moving crash truck to divert traffic in the vicinity of the RDD. Testing using a moving crash truck rather than closing a lane is about twice as efficient; however, for highways having heavy traffic, a crash truck is probably not as safe as closing the lane would be.

CHAPTER 10. ROLLING DYNAMIC DEFLECTOMETER TESTING AT THE DALLAS-FORT WORTH INTERNATIONAL AIRPORT

10.1 INTRODUCTION

The RDD was used to test airport pavements at the Dallas-Fort Worth (DFW) International Airport as part of a project to predict the remaining life of the DFW pavements (McNerney et al. 1997[1] and [2]). Tests were performed on an operating runway, a newly constructed but not yet operational runway, and on an operating taxiway. A great deal of valuable information about the airport pavements was obtained from the displacement profiles measured with the RDD. This information included measurements of the overall pavement stiffness, longitudinal variability, lateral variability at selected locations, the performance of joints, and the effect of traffic on pavement performance.

10.2 BACKGROUND

RDD testing was conducted at the DFW airport over three nights and one day from August 29 through September 2, 1996. The testing on operating airport pavements was performed at night to avoid interfering with airport traffic. Testing on the newly constructed but not yet opened runway was performed during the day. An average of about 3.7 km (2.3 mi) of pavement was tested in 6 hours of testing each night. This included testing of short transverse sections and short longitudinal sections of pavement that required extensive set-up time. Photographs of the testing at DFW are shown in Figure 10.1.

10.2.1 Testing Locations

An image of the pavements on the east side of the DFW airport with the testing locations identified is shown in Figure 10.2. This image was generated from an aerial photograph. Testing was performed along the entire length of Runway 17R-35L and Taxiway L. Tests were also performed on a 1,500 m (5,000 ft) long section of a newly constructed runway; the remainder of the new runway was not available for testing because of construction activities. At the time the photograph (Figure 10.2) was taken, this runway was only partially constructed. All testing was performed near the longitudinal centerline of the runway or taxiway. Additional tests were performed in the transverse direction across the runways and taxiway.

10.2.2 Pavement Properties

All pavements tested at DFW have the same general layer profile shown in Figure 10.3. The pavement consists of 43 cm (17 in.) of PCC over 23 cm (9 in.) of cement-stabilized base, which in turn is over 23 cm (9 in.) of lime-treated subbase (lime-treated natural subgrade). The natural subgrade is 0.6 to 12.2 m (2 to 40 ft) of clayey soil. The concrete is reinforced with dowelled and sawn joints, as discussed below.

a) Setting up RDD for Night Testing

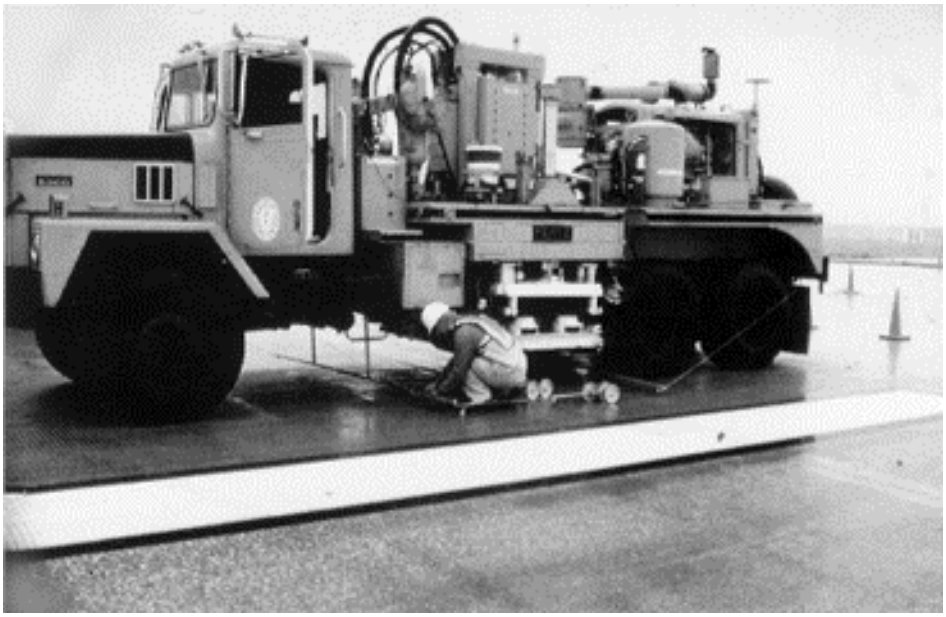

b) Setting up RDD for Testing on New Runway

Figure 10.1 Photographs of RDD Testing at the DFW Airport

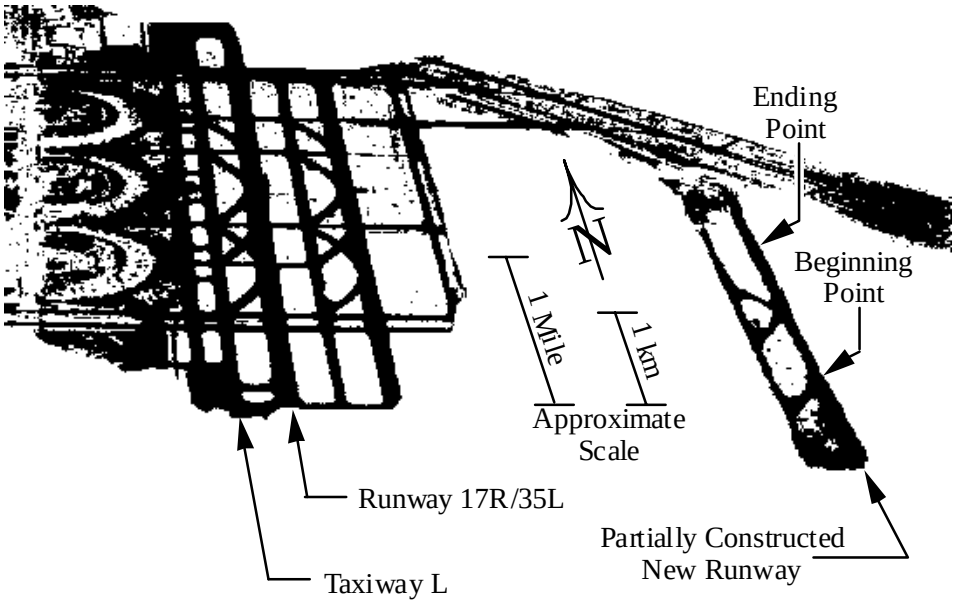

Figure 10.2 Aerial Image of Pavements on East Side of DFW Airport Showing the RDD Testing Locations

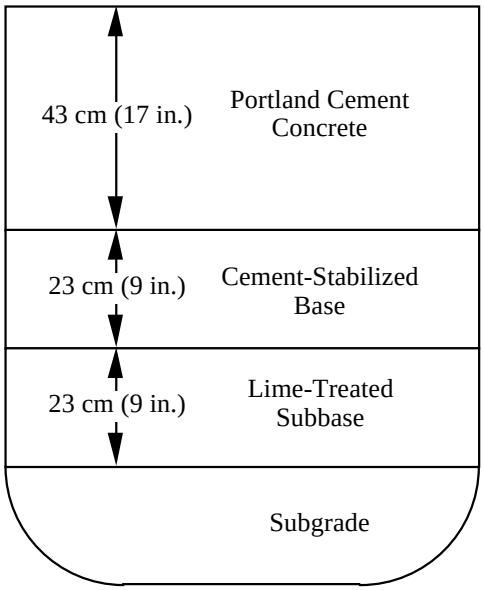

Figure 10.3 Pavement Profile of the Runways and Taxiway Tested at the DFW Airport

A plan view of a typical section of Runway 17R-35L is shown in Figure 10.4. Runway 17R-35L consists of slabs 15.2 m by 15.2 m (50 ft by 50 ft). There are four slabs across the width of the runway, with asphalt or concrete shoulders at the edges. The slabs are tied together with dowelled joints, as shown in Figure 10.4. Sawn joints or naturally occurring cracks are between all dowelled joints. Where cracking has occurred, the cracks have been routed and sealed. Most aircraft traffic occurs on the two center slabs.

The construction of Taxiway L is similar to that of Runway 17R-35L, except it is only two slabs wide. A plan view of a typical section of Taxiway L is shown in Figure 10.5. This taxiway consists of slabs 15.2 m by 15.2 m (50 ft by 50 ft), with asphalt or concrete shoulders at the edges. The slabs are tied together with dowelled joints. Sawn joints or naturally occurring cracks are between all construction joints. Where cracking has occurred, the cracks have been routed and sealed.

A plan view of the new runway is shown in Figure 10.6. This runway has slab lengths of 15.2 m (50 ft) and widths of 11.4 m (37.5 ft). Like Runway 17R-35L, the new runway is four slabs wide with asphalt and concrete shoulders. All the joints between the slabs are dowelled. Additionally, sawn joints were constructed at the midpoints between the construction joints.

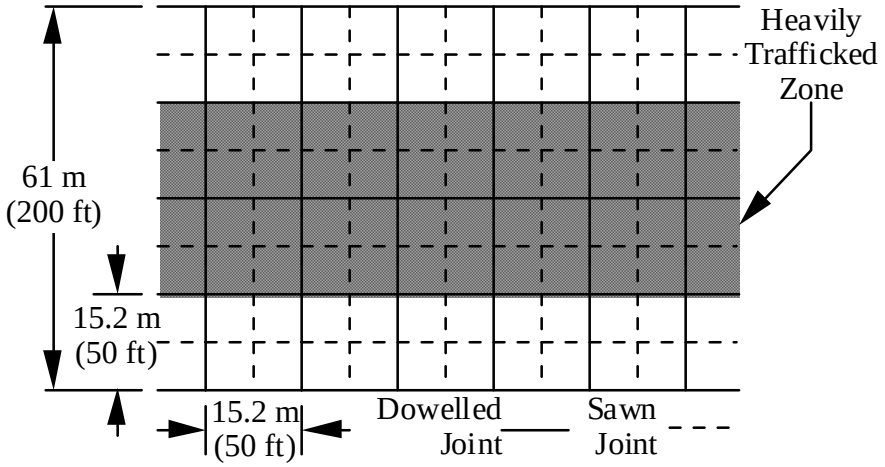

Figure 10.4 Plan View of Typical Section of Runway 17R-35L, DFW International Airport

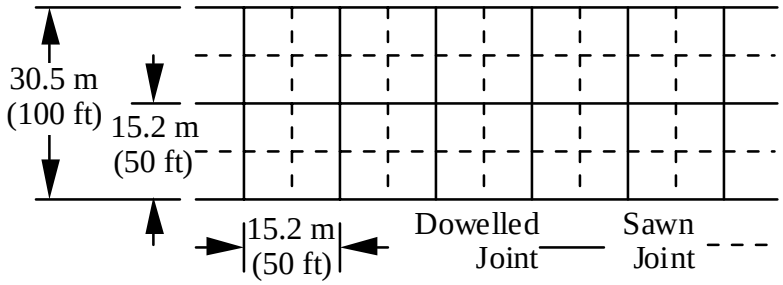

Figure 10.5 Plan View of Typical Section of Taxiway L, DFW International Airport

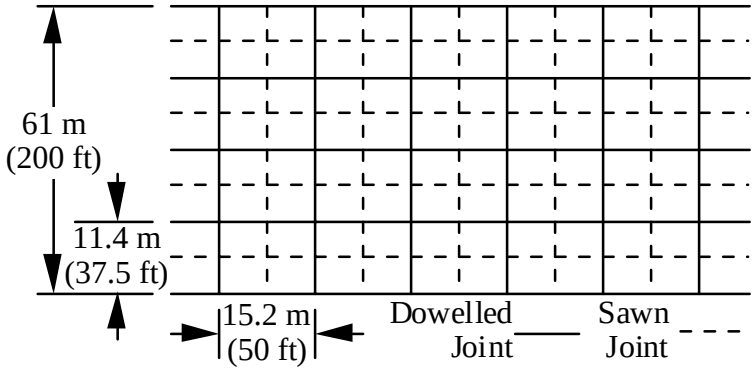

Figure 10.6 Plan View of Typical Section of New Runway at DFW International Airport

10.2.3 Testing Procedures

The RDD testing at DFW was performed using an operating frequency of 40 Hz. Testing was conducted using a vehicular speed along the pavement of about 0.3 m/sec (1 ft/sec). A static force of about 160 kN (36 kip) and a p-p dynamic force of about 89 kN (20 kip) were applied to the pavement. The testing was divided into pavement segments ranging from 305 to 915 m (1,000 to 3,000 ft) long. New data files were begun at the beginning of each segment.

A plan view of the rolling sensor configuration used for these tests is shown in Figure 10.7. Four rolling sensors were used. Two sensors positioned at locations equidistant from the two loading rollers are designated the centerline sensors. The sensor between the loading rollers is designated the centerline-in-line sensor, and the other is designated the centerline-leading sensor. Two other sensors were positioned outside the loading rollers straddling a longitudinal joint (for the longitudinal tests). The purpose of these two sensors was to assess the joint performance by measuring the relative movement on both sides of the longitudinal joint.

All sensors provide valuable information about the pavement system. However, the largest displacements occurred at the centerline-in-line sensor. Therefore, the centerline-in-line sensor provided the most useful information. Information obtained by the other sensors

was used to evaluate the shape of the deflection basins; however, the analytical tools required to analyze these data have yet to be developed. Therefore, data obtained from the centerline-in-line sensor only are presented herein.

10.3 TESTING RESULTS

10.3.1 Runway 17R-35L

The displacement profile measured with the centerline-in-line sensor along the entire length of the runway is shown in Figure 10.8. This testing was performed within about 1.5 m (5 ft) of the joint at the longitudinal centerline of the runway. Only general characteristics and trends in the pavement stiffness can be discerned from Figure 10.8 because of the compressed horizontal scale. One feature that is readily discernible from Figure 10.8 is a region with high displacement at the north end of the runway. About 610 m (2,000 ft) from the north end of the runway, the pavement abruptly becomes stiffer. The 610 m (200 ft) long section exhibiting generally higher displacements is a runway extension that was constructed about 5 years ago. The remainder of the runway was constructed 22 years ago. It is interesting to see that the new construction is not behaving as well as the old runway (from a load-displacement point of view).

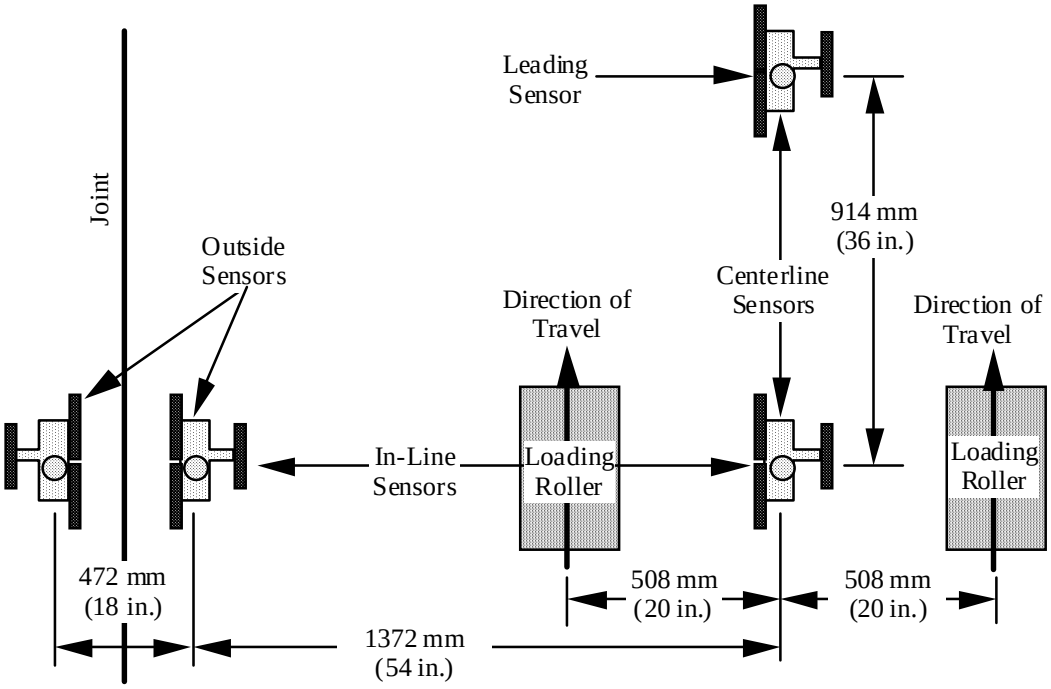

Figure 10.7 Plan View of Rolling Sensor Configuration Used for RDD Testing at the DFW International Airport

Four sections of the displacement profile in Figure 10.8 are marked in the figure so that further discussion can be presented in conjunction with expanded profiles. Two of these sections, A and B, are on the 22-year-old runway and the other two, C and D, are on the 5-year-old runway extension. These four sections are expanded to show more detail in the pavement system.

The two expanded sections from the 22-year-old section of runway are shown in Figure 10.9. The expanded displacement profile for Section A, shown in Figure 10.9a, is from the section of the 22-year-old runway exhibiting the highest displacement. (It was easy to identify this section once the complete runway had been tested.) The peaks in the displacement profile correspond to the location of joints and cracks. The locations of the dowelled joints are identified in Figure 10.9a. The lower peaks that occur between dowelled joints correspond to sawn joints and cracks. This pattern of high displacements at dowelled joints and lower displacements at sawn joints and cracks was prevalent in all testing at DFW. It is interesting to note that the cracks and sawn joints are transferring load more efficiently than the dowelled joints. This improved efficiency probably occurs because of the continuous steel across the crack combined with the rough nature of the "plane" along which the crack has developed. The cracks and sawn joints influence the displacements over a region of pavement that extends 2.1 m (7 ft) each side of the crack on average. The dowelled joints influence the displacements over a region that extends 2.6 m (8.5 ft) each side of the joint on average.

The expanded displacement profile for Section B, shown in Figure 10.9b, has displacement levels typical for the 22-year-old pavement. Again, the pattern of alternating high displacement dowelled joints and lower displacement sawn joints and cracks is clearly seen. A slightly different pattern is present in one slab shown in Figure 10.9b; in the slab centered at about 2,350 m (7,720 ft), two cracks occurred rather than just one. The displacements measured in Section B are lower than the displacements measured in Section A at cracks, at the joints, and at the intact interiors of the slabs. This performance indicates an overall stiffer pavement system at Section B. Further studies are required to determine the reason or reasons for this difference. For this section of pavement, the cracks and sawn joints influence the displacements over a region of pavement that extends 2.0 m (6.5 ft) each side of the crack on average. The dowelled joints influence the displacements over a region that extends 2.1 m (7 ft) each side of the joint on average.

Expansion of the displacement profiles of Sections C and D in the 5-year-old runway extension are shown in Figure 10.10. Section C, shown in Figure 10.10a, has displacements typical of the runway extension while Section D, shown in Figure 10.10b, has the highest displacements measured in the runway extension. In the runway extension, the sawn joints exhibit displacements as large as the dowelled joints and are not readily discernible by the displacement amplitude like they are on the other pavements. The displacements measured at the intact midslab regions of Sections C and D are quite similar. The large displacements measured at Section D are limited to the regions around joints and cracks. On Section C, the joints and cracks influence the displacements over a region that extends 2.1 m (7 ft) each side of the crack or joint on average. This region extends 2.3 m (7.5 ft) each side of the crack or joint on average for Section D.

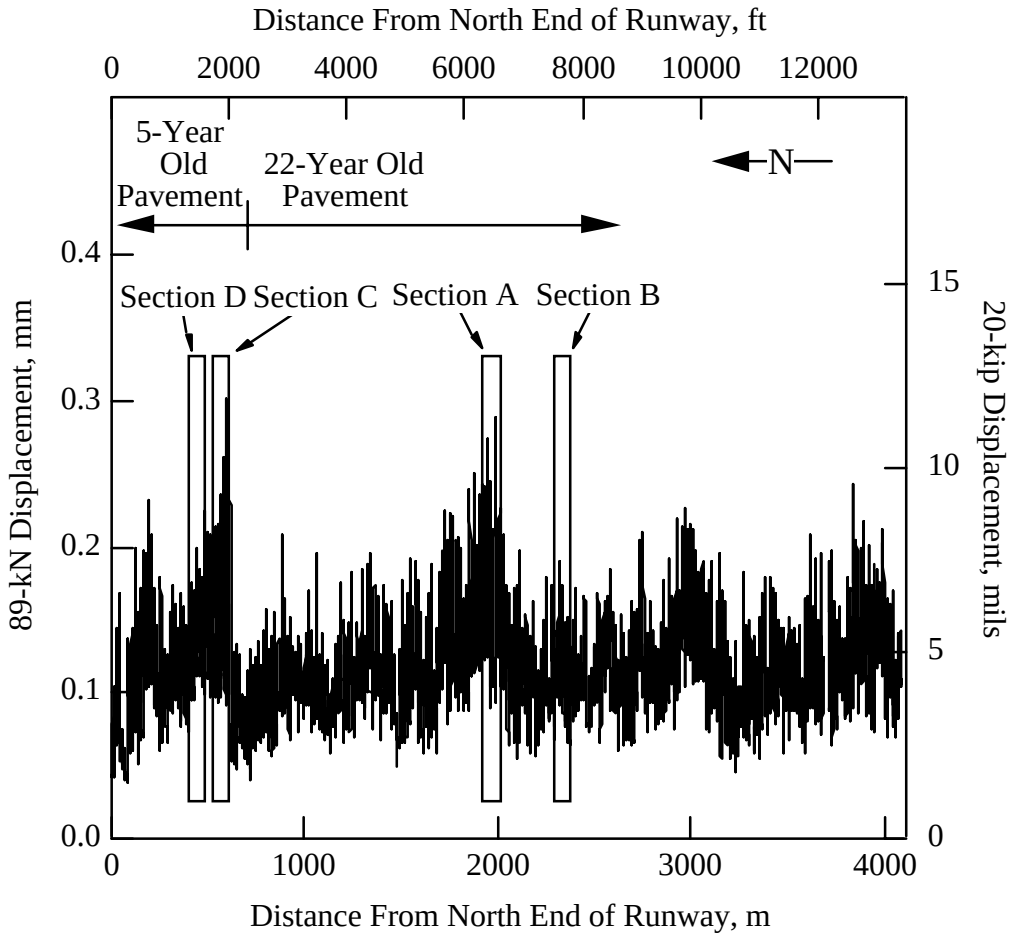

Figure 10.8 Continuous Displacement Profile Measured with the Centerline-in-Line Sensor on Runway 17R-35L at the DFW International Airport

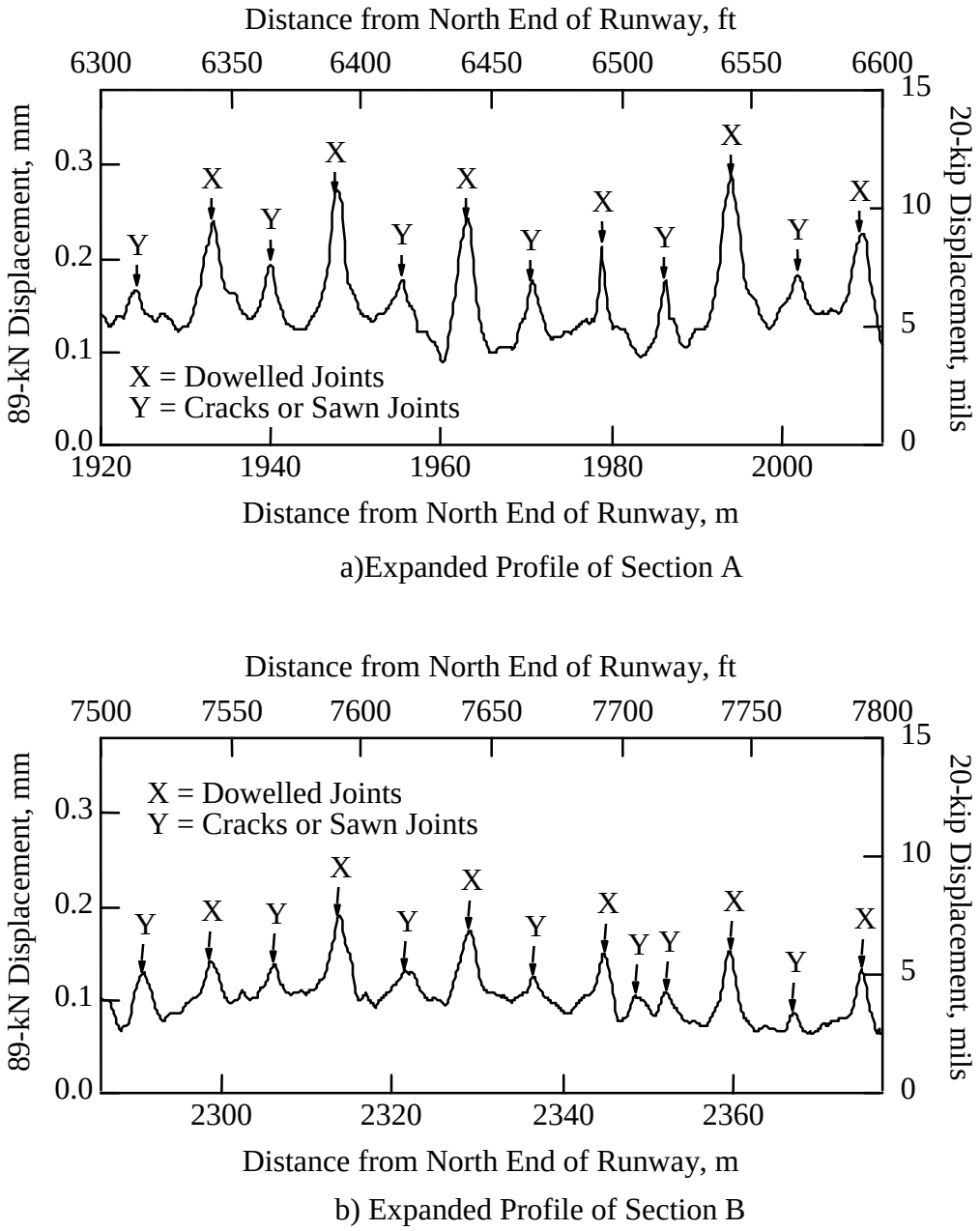

Figure 10.9 Expanded Displacement Profiles from 22-Year-Old Pavement on Runway 17R-35L, DFW International Airport

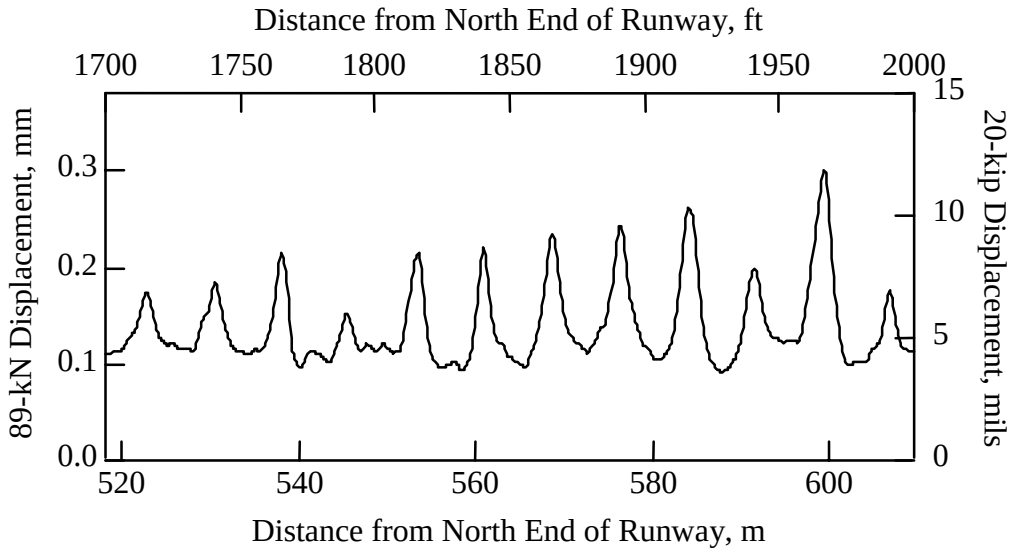

a) Expanded Profile of Section C

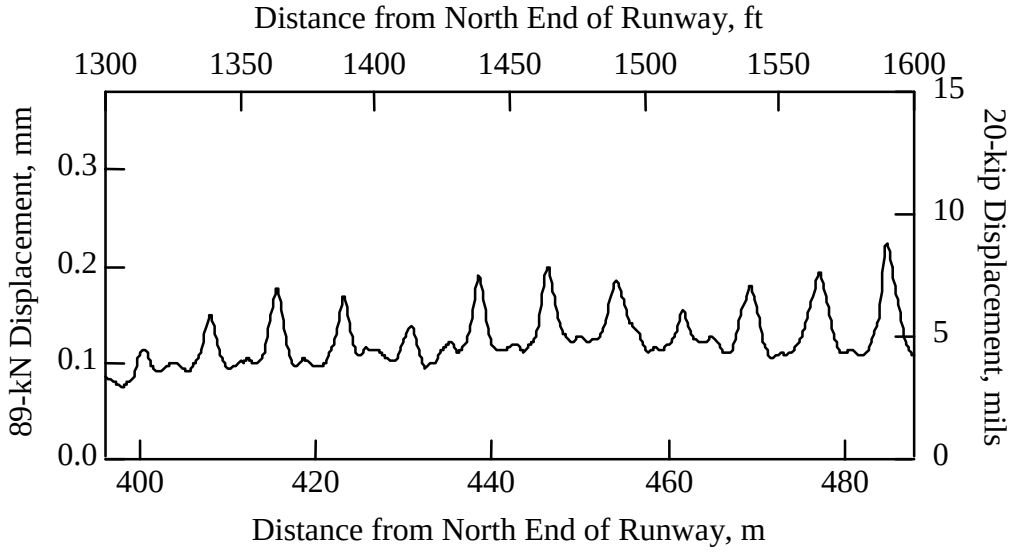

b) Expanded Profile of Section D

Figure 10.10 Expanded Displacement Profiles from 5-Year-Old Pavement on Runway 17R-35L, DFW International Airport

RDD tests were also performed in the transverse direction across the runway at four locations on the 22-year-old runway pavement and at four locations on the 5-year-old runway extension pavement. These displacement profiles are plotted in Figure 10.11. The transverse displacement profiles from the 22-year-old runway pavement are plotted in Figure 10.11a. Unfortunately, the section of the original runway selected for transverse profiling was one of

the stiffest sections; a less stiff section may have had more interesting results, but the selection of sites was made before the RDD results were available. Displacement profiles from the transverse tests on the 5-year-old runway extension pavement are shown in Figure 10.11b. These transverse displacement profiles, like the longitudinal profiles, have large displacement peaks at the construction joints and smaller displacement peaks at the sawn joints at the centers of the slabs. The large displacements at the edges of the runway are caused by free pavement edges.

It is especially interesting to compare the midslab displacements measured near the center of the runway with the midslab displacements measured near the edges of the runway. Regions near the center of the runway have been subjected to heavy aircraft traffic loading, while the edges of the runway experience very little traffic. To compare the pavement performance at the center of the runway with the performance near the edge, average midslab displacements were calculated for each slab and each measured profile. Dividing by the average midslab displacement near the edges then normalized these displacements.

Normalized midslab displacements are plotted in Figure 10.12a for the 22-year-old runway pavement and in Figure 10.12b for the 5-year-old runway extension pavement. The 22-year-old pavement exhibits displacements about 26 percent higher near the center of the pavement than at the pavement edge. The 5-year-old runway extension exhibits displacements about 50 percent higher near the center of the pavement than at the pavement edge. The joints near the center of the runway (shown in Figure 10.11) also exhibit higher displacements than the joints near the edge of the runway. In both Figure 10.12 and 10.11b it can be seen that the maximum displacements in the 5-year-old runway extension profiles occur somewhat to the east of the center of the runway. This is likely due to a high-speed exit that diverts much of the aircraft traffic to the east side of the runway in that region.

10.3.2 Taxiway L

The displacement profile measured with the centerline-in-line sensor along the entire length of Taxiway L is shown in Figure 10.13. This testing was performed within about 1.5 m (5 ft) of the joint at the longitudinal centerline of the runway. Only general characteristics and trends in the pavement stiffness can be discerned from Figure 10.13 because of the compressed horizontal scale of the plot. Three sections of the taxiway, designated E, F, and G, are identified and are expanded in subsequent figures for discussion purposes.

Expansions of the three displacement profiles identified in Figure 10.13 are presented in Figure 10.14. Section E, shown in Figure 10.14a, exhibits extremely high displacements. This section does not show the pattern of construction joints every 15.2 m (50 ft) as expected because it has been sawn at short intervals to prepare it for deep repairs. Section F, shown in Figure 10.14b, exhibits the highest displacements for intact sections of the taxiway. It is interesting to note, however, that these displacement levels are substantially lower than the highest displacements on Runway 17R-35L. The cracks and joints influence the displacements over a region that extends 2.2 m (7.3 ft) either side of the crack or joint on average on Section F. Section G, shown in Figure 10.14b, exhibited the lowest displacements on the taxiway. These displacements are lower than the lowest displacements measured on Runway 17R-35L. Many cracks and joints had no significant influence on the magnitude of the displacements measured at Section G. Those cracks and joints that do

influence displacements influence only a small region. Based on these displacement comparisons, Taxiway L appears to be performing better than Runway 17R-35L.

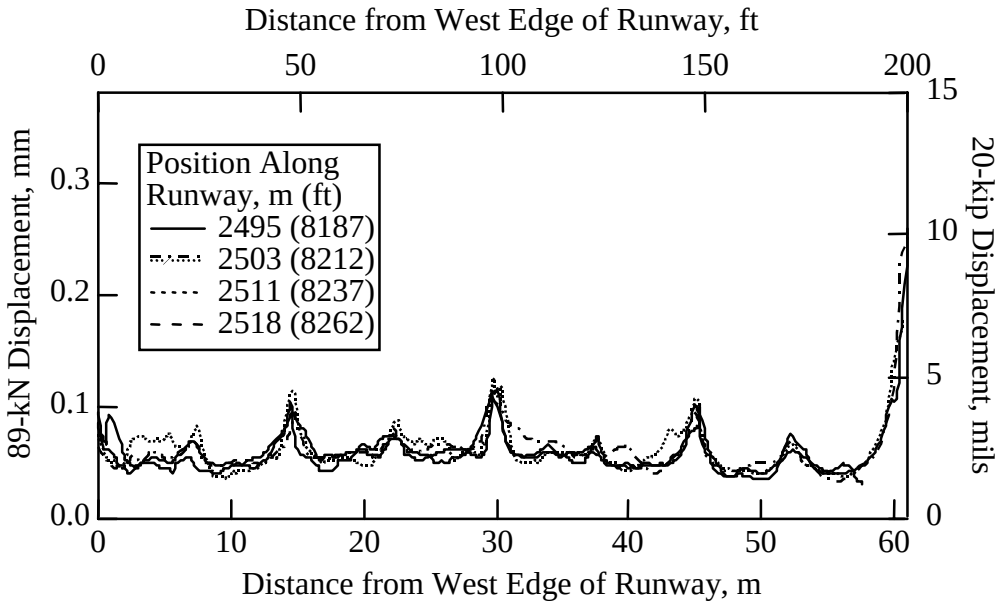

a) 22-Year Old Runway Pavement

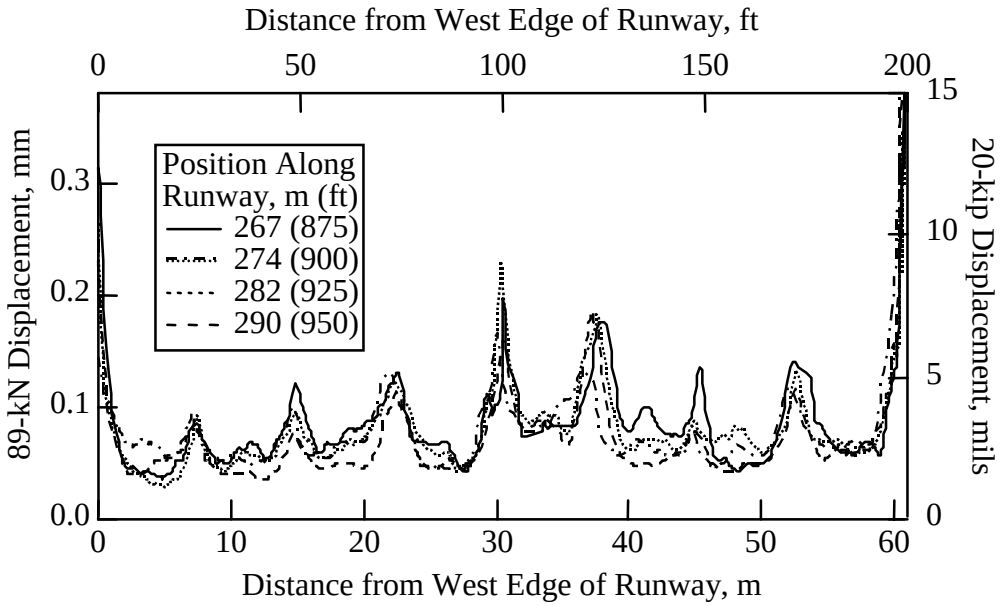

b) 5-Year Old Runway Extension Pavement

Figure 10.11 Displacement Profiles along Transverse Alignments of Runway 17R-35L at the DFW International Airport

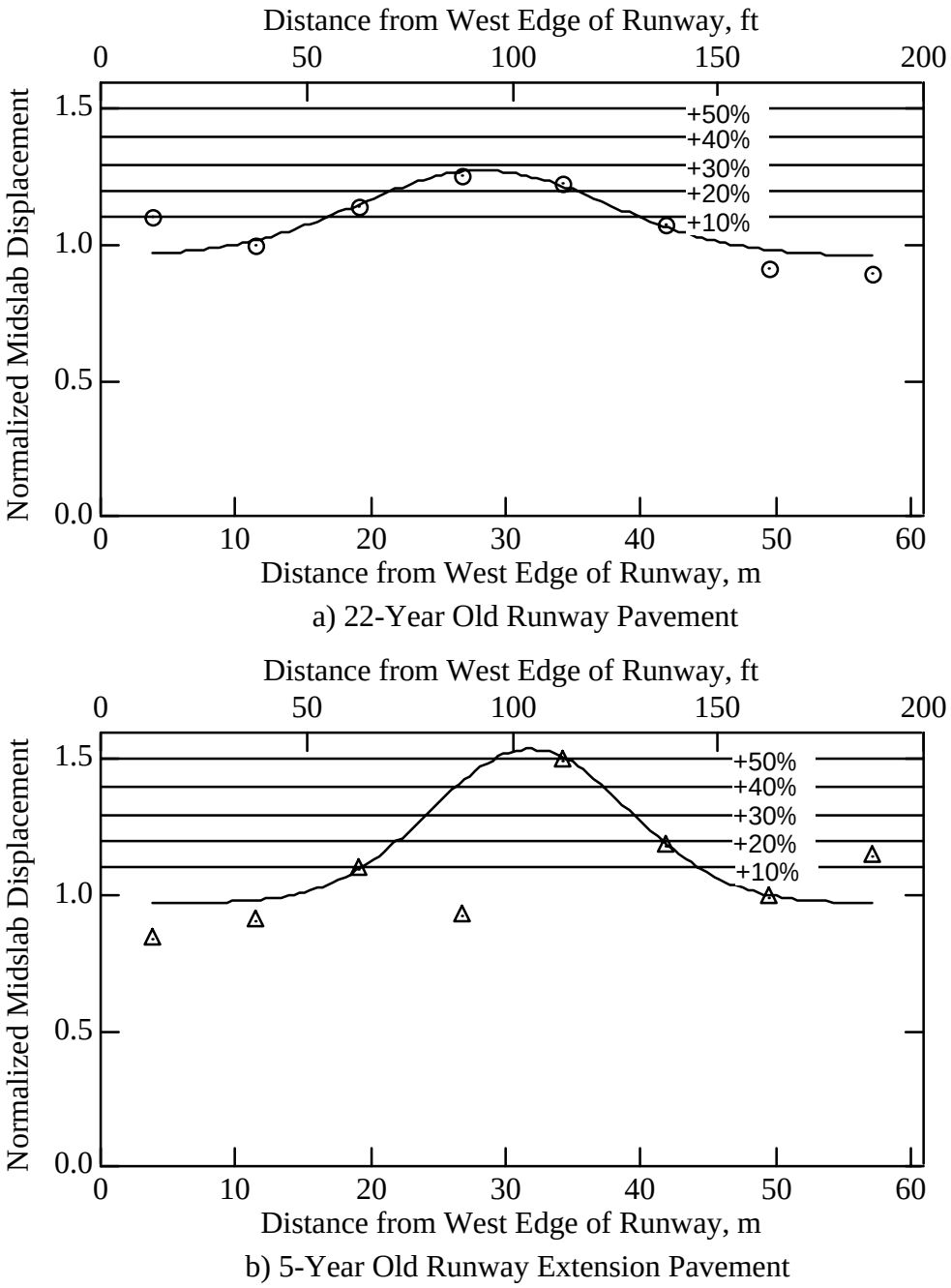

Figure 10.12 Normalized Midslab Displacement Measured on 22-Year-Old and 5-Year-Old Pavements of Runway 17L-35-R, DFW International Airport

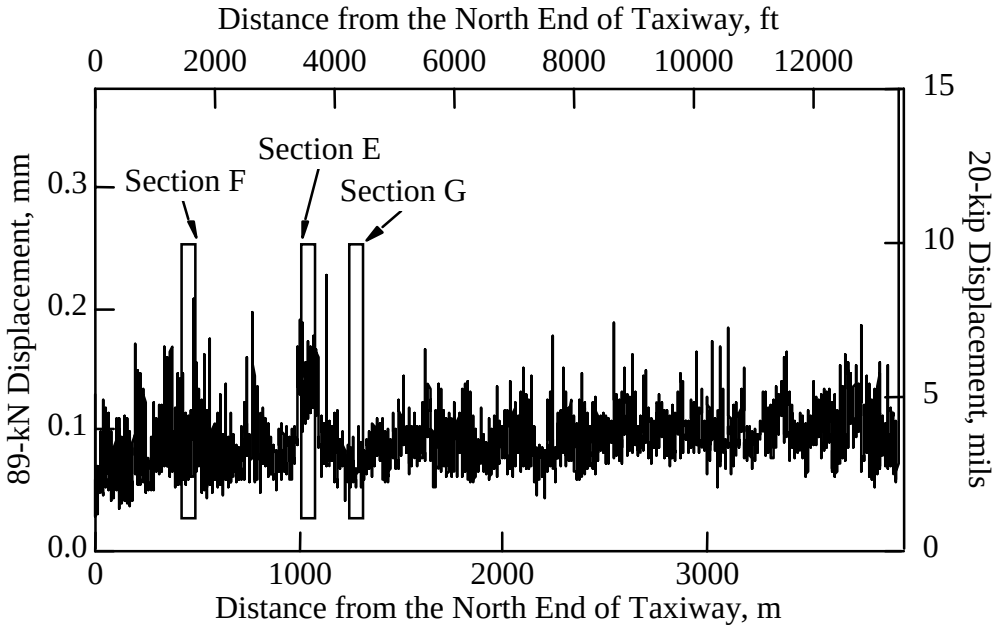

Figure 10.13 Continuous Displacement Profile Measured with the Centerline-in-Line Sensor on Taxiway L at the DFW International Airport

RDD testing was also performed along transverse alignments at two locations on Taxiway L. These displacement profiles are presented in Figure 10.15. The transverse displacement profiles, like the longitudinal profiles, have large displacement peaks at the construction joints and smaller displacement peaks at the sawn joints at the centers of the slabs. The large displacements at the edges of the taxiway are caused by free pavement edges. Normalized midslab displacements were also calculated for the transverse displacement profiles measured on Taxiway L. These results are presented in Figure 10.16. The displacements near the center of the taxiway, where most aircraft traffic occurs, are about 37 percent higher than they are near the edges of the taxiway. The effect of aircraft traffic on displacement on Taxiway L is similar to that found on Runway 17R-35L.

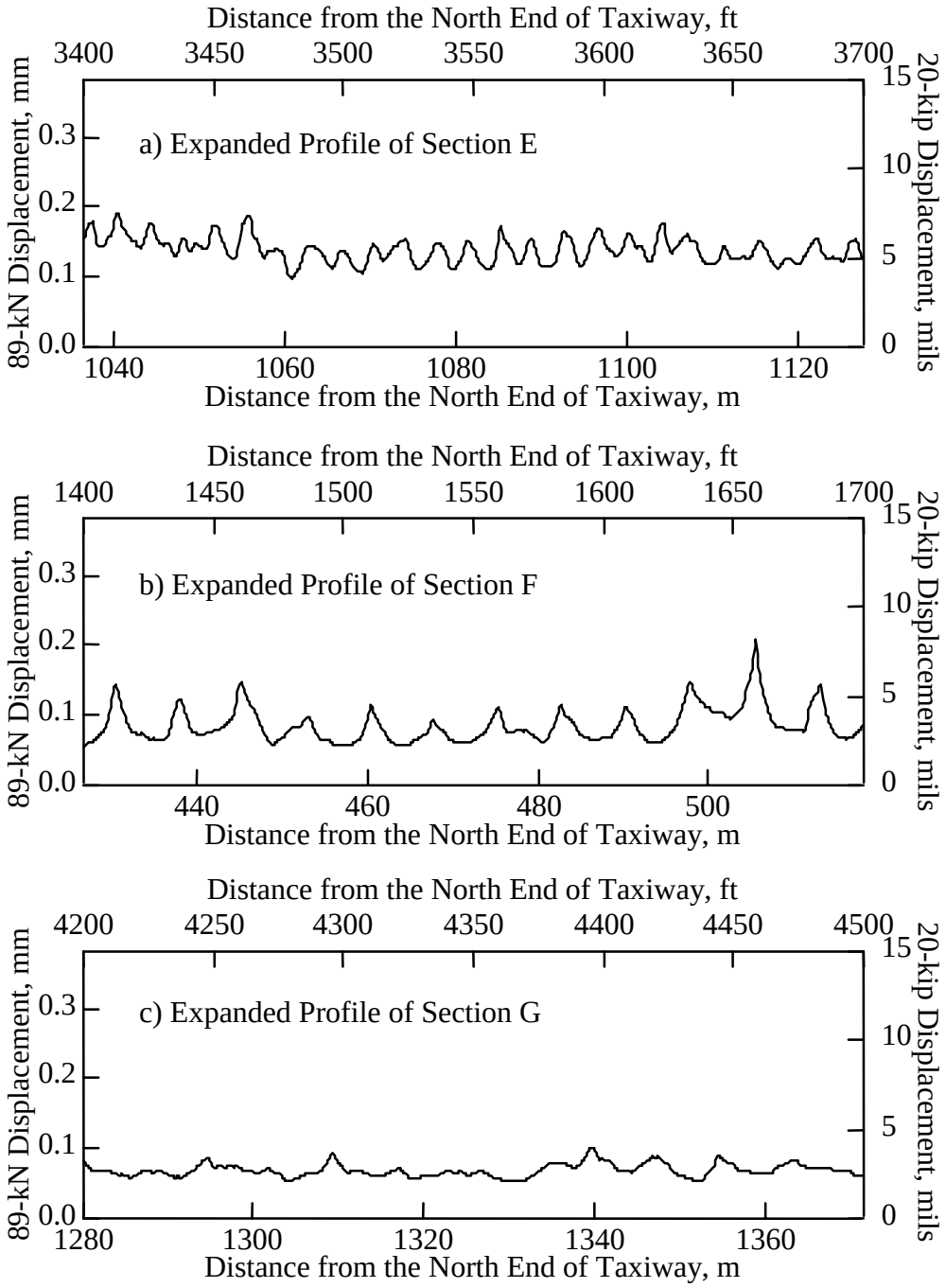

Figure 10.14 Expanded Displacement Profiles from Taxiway L, DFW International Airport

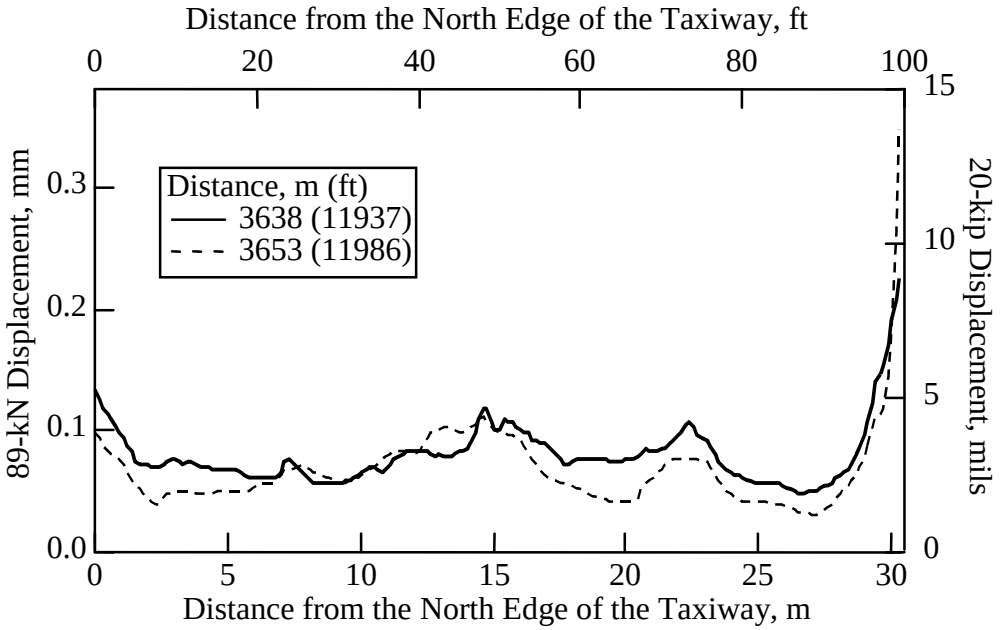

Figure 10.15 Displacement Profiles along Transverse Alignments of Taxiway L at the DFW International Airport

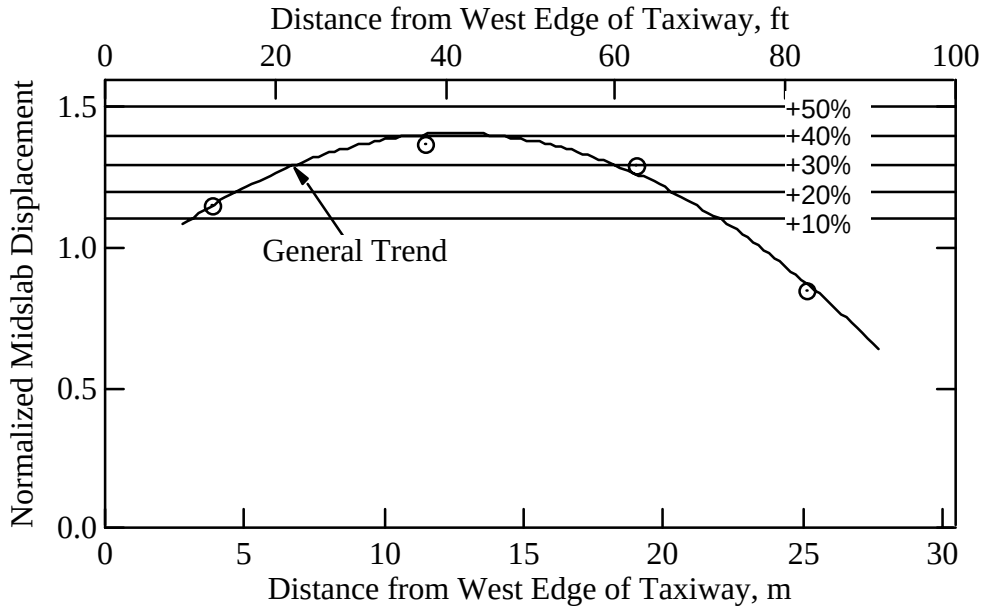

Figure 10.16 Normalized Midslab Displacements Measured at Taxiway L at the DFW International Airport

10.3.3 New Runway

At the time this testing was performed, a new runway had been constructed at the DFW airport but was not yet open to aircraft traffic. Owing to construction activities, only a small section of the new runway (about 1,525 m [5,000 ft] long) was available for RDD testing. The cross-section of the new runway is very similar to that of Runway 17R-35L, which makes these results a good comparison of trafficked and untrafficked runways.

The displacement profile for the tested section is shown in Figure 10.17. Generally, the displacements are much lower for the new runway than for Runway 17R-35L. The average displacement for the section tested is about 30 percent of the average displacement measured on Runway 17R-35L

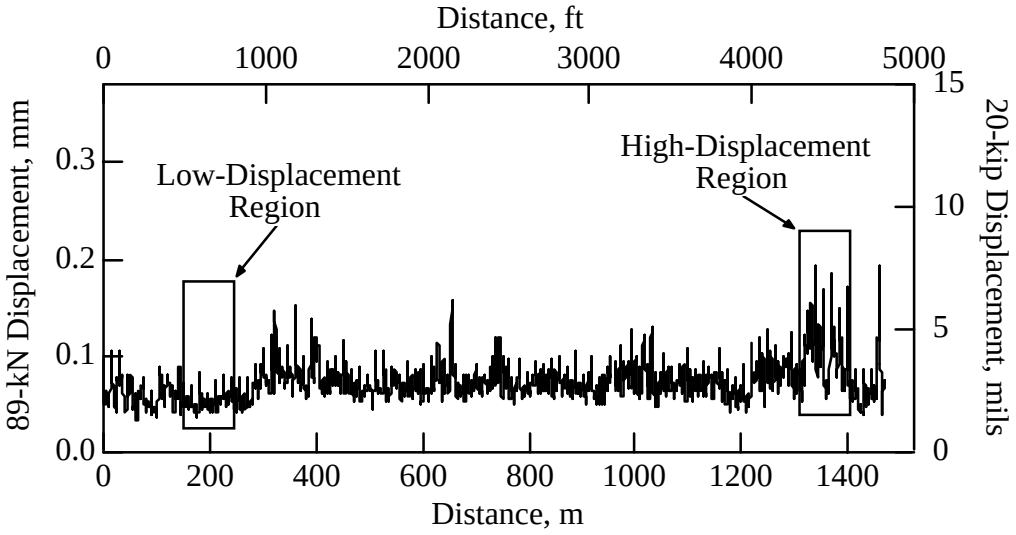

Figure 10.17 Continuous Displacement Profile Measured with the Centerline-in-Line Sensor on the New Runway at the DFW International Airport

Two sections of the taxiway displacement profile are expanded for more detailed review: the section with the lowest measured displacements and the section with the highest. These expanded sections are shown in Figure 10.18. The displacement profile from the section exhibiting the lowest deflections is shown in Figure 10.18a. Both midslab and joint displacements are very low for this section and, overall, are much lower than any displacements measured on Runway 17R-35L. Many cracks and joints had no significant influence on the magnitude of the displacements measured at this section. Those cracks and joints that do influence displacements influence only a very small region. The displacement profile from the section that exhibited the highest deflections is shown in Figure 10.18b. These displacements are also lower than most displacements on Runway 17R-35L. The cracks and joints influence the displacements over a region that extends an average of 2.3 m (7.4 ft) either side of the crack or joint over this section of pavement.

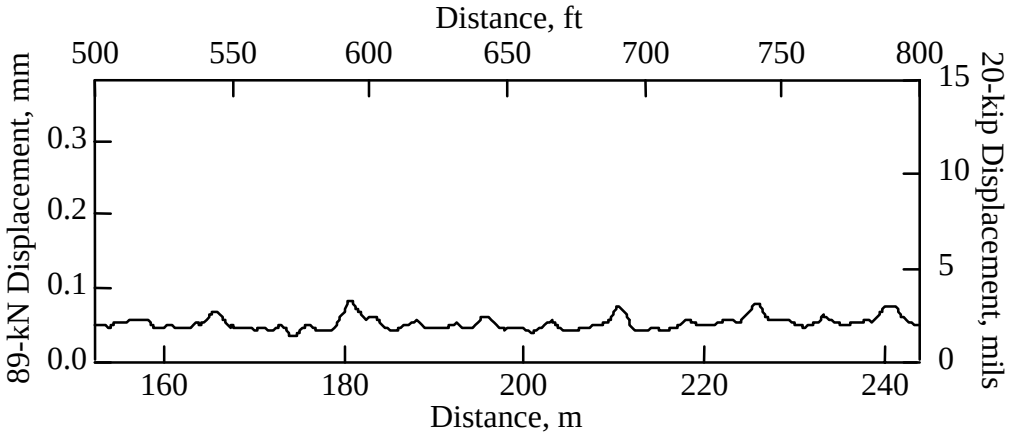

a) Expanded Profile of Region with Lowest Displacements

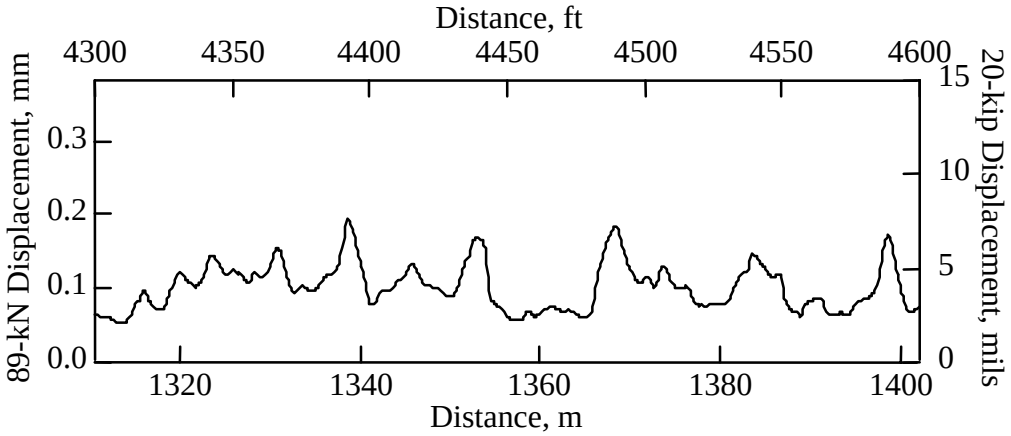

b) Expanded Profile of Region with Highest Displacements

Figure 10.18 Expanded Displacement Profiles from New Runway at DFW International Airport

Two transverse displacement profiles were measured on the new runway. These are plotted in Figure 10.19. Again, these displacement levels are lower than those displacements on runway 17R/35L, but more interestingly, higher displacements are not seen near the center of the runway. This is shown more clearly in the plot of normalized midslab displacements presented in Figure 10.20. The average midslab displacements are generally all within ±15 percent, and there is no strong trend with higher displacements near the center of the runway. The lack of high displacements at the center of the runway is consistent with the fact that the center of the new runway has not experienced increased distress at its center as a result of aircraft traffic.

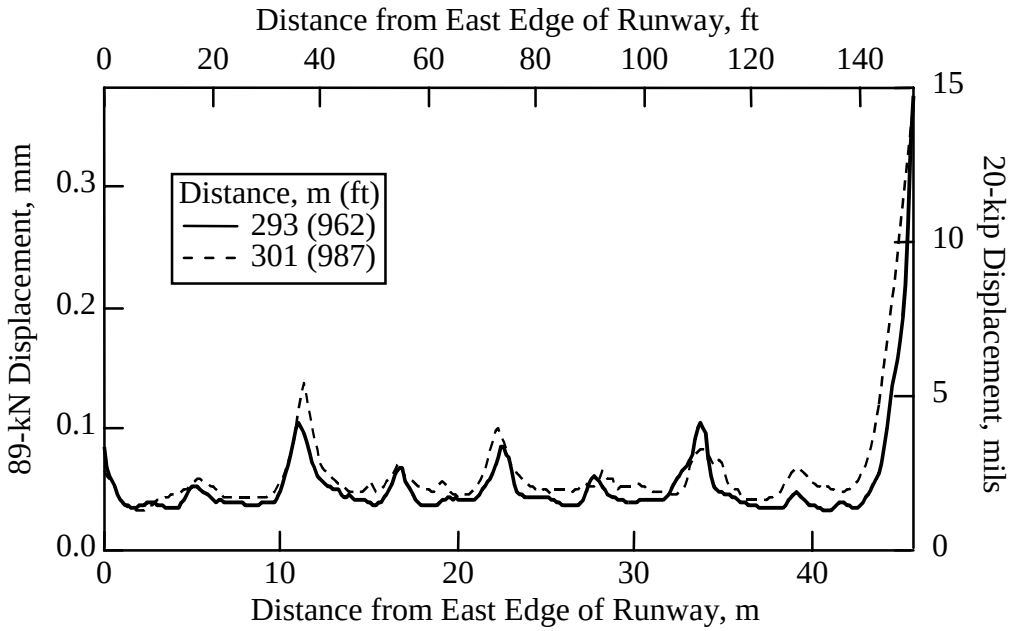

Figure 10.19 Displacement Profiles along Transverse Alignments of New Runway at the DFW International Airport

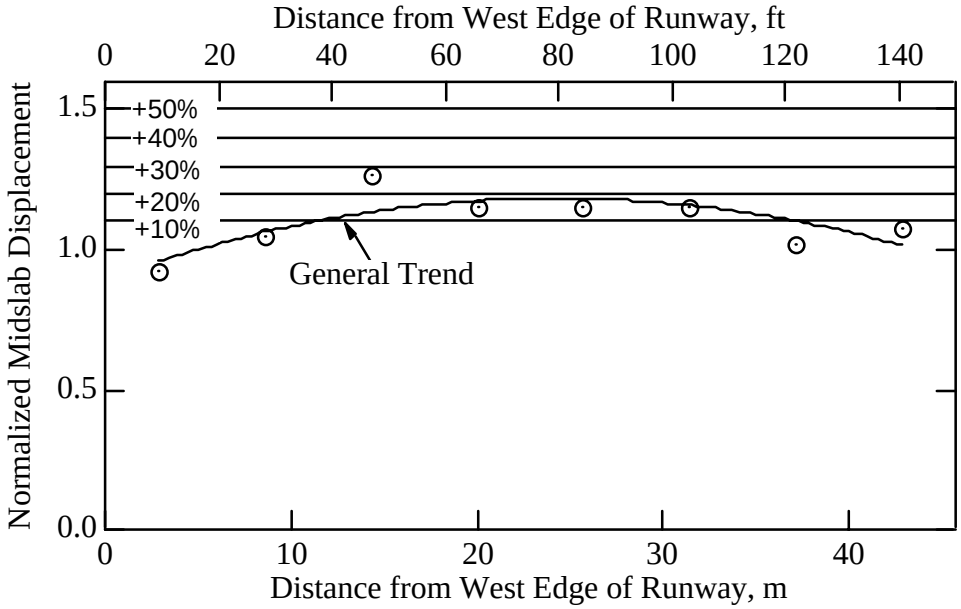

Figure 10.20 Normalized Midslab Displacements Measured on New Runway at the DFW International Airport

10.4 SUMMARY

Continuous displacement profiles measured with the RDD provide valuable information about airport pavement systems (McNerney et al., 1997[1]). This point is demonstrated by testing on two runways and one taxiway at the DFW Airport. These displacement profiles can be used to differentiate soft pavement regions, which exhibit high displacements, from stiffer regions. With continuous deflection profiles, joints and their zones of influence can easily be differentiated from the intact midslab behavior. The effects of distress caused by aircraft traffic can be seen in the displacement profiles. This effect was demonstrated in two ways: first, by comparing the displacements at less trafficked runway and taxiway edges with the heavily trafficked central area, and, second, by comparing the displacements on a newly constructed runway with the displacements on an older, heavily trafficked runway. Displacements measured at the edges of a heavily trafficked runway and a heavily trafficked taxiway were 66 percent to 70 percent as high as displacements measured at the center of the structures. The displacements measured on the new, untrafficked runway were about 30 percent as high as the displacements measured on the heavily trafficked runway. Displacements measured near the edge of both runways are of similar magnitudes. Surprisingly, one relatively new section of runway showed displacements higher than those generally experienced on the aging runway. An explanation advanced by personnel at DFW is that this area is where a 4.6 m (15 ft) trench was dug and backfilled across the current runway location.

The cracks and joints generally influence regions of pavement that extend 2 to 2.6 m (6.5 to 8.5 ft) either side of the joint or cracks on the pavements tested. Joints and cracks that exhibit higher displacements generally influence a larger region than those with smaller displacements. The region influenced by cracks and joints on the airport pavements tested tends to extend about twice as far each side of the joint as the highway pavements tested and discussed in Chapter 9.

Repeated RDD measurements would give airport administrators an accurate and detailed assessment of changing pavement conditions and an accurate prediction of the remaining life of the pavements. RDD testing can also be used to identify poorly performing pavement sections that may require remedial measures. These tests can be performed quickly and during time periods when aircraft traffic is light.

CHAPTER 11. SUMMARY, CONCLUSIONS, AND RECOMMENDATIONS FOR FUTURE IMPROVEMENTS TO THE ROLLING DYNAMIC DEFLECTOMETER

11.1 SUMMARY

The rolling dynamic deflectometer (RDD), developed at The University of Texas at Austin, is a new tool for nondestructive testing of pavements. RDD testing has one major advantage over other nondestructive testing methods: It provides a continuous profile of pavement behavior while all other commonly used nondestructive (and destructive) testing techniques provide information only at discrete pavement locations. Discrete testing methods provide no assurance that critical, or even typical, pavement locations have been tested. The advantage of a continuous method is that the entire pavement is characterized, resulting in a very informative picture of the behavior of the pavement. With continuous testing, the behavior of every joint and crack is easily determined, and the regions affected by joints and cracks are distinguishable from intact slab regions.

The RDD determines continuous profiles expeditiously and robustly, even in the presence of traffic in adjacent lanes. The RDD applies a large sinusoidal dynamic load to the pavement surface through loading rollers as the RDD travels along the pavement. The deflections induced by this sinusoidal dynamic load are measured with rolling sensors that are towed along the pavement by the RDD. Continuous measurements are made of the forces applied to the pavement, the displacements at each rolling sensor, and the position of the RDD along the pavement. These measurements are used to generate continuous displacement profiles.

The RDD was constructed by modifying a Vibroseis truck. Vibroseis trucks are used as seismic wave sources in geophysical surveys for oil exploration. The RDD uses the hydraulic system and some of the electronic control components of the Vibroseis loading system in its dynamic loading system. The modifications to the Vibroseis required to construct the RDD included: 1) reworking the dynamic loading electronic control system, 2) adding a structural loading frame, 3) adding a support system to resist lateral forces and tipping in the dynamic loading system, 4) adding bearings and loading rollers to apply forces to the pavement, and 5) adding a servo-valve and electronic controls to regulate static forces applied to the pavement. Construction of the RDD required the design and construction of: 1) rolling sensors to measure dynamic displacements, 2) a distance measuring system to track the position of the RDD during testing, and 3) a data acquisition system to record all pertinent data.

The RDD can apply dynamic forces to the pavement from 4.45 to 310 kN (1 to 70 kip) peak-to-peak at frequencies from 5 to 100 Hz. The static hold-down force applied by the RDD can be varied from 4.45 to 195 kN (1 to 44 kip). RDD testing can be performed at speeds along the pavement of 0.2 to 0.46 m/s (0.67 to 1.5 ft/sec) or 0.7 to 1.6 km/hr (0.4 to 1 mph).

Displacement measurements made with the RDD are subject to noise caused by the movement of the loading rollers and the rolling sensors over rough pavement, and by vibrations from nearby traffic. An analysis procedure has been developed to digitally filter

the noise from the final results. A statistical approach was employed to predict the confidence interval for any displacement measurement. The parameters used in data analysis can be varied to decrease the confidence interval (increase the accuracy) of a displacement measurement while decreasing the spatial resolution of the displacement profile; alternatively, the spatial resolution of the profile can be increased with an associated decrease in the accuracy of the measurement due to an increased impact of noise in the final result. Analysis parameters can be selected to tailor the RDD results to the needs of a given survey.

The effectiveness of the RDD has been demonstrated in testing on highway and airport pavements. The RDD has demonstrated its ability to obtain high-quality measurements reasonably quickly and very cost effectively. The RDD significantly out-performed the falling weight deflectometer (FWD) in simultaneous testing, generating much more pavement information in significantly less time. In the most recent work, the RDD measurements have been used by pavement engineers to make detailed assessments of the condition and remaining life of the pavements tested.

11.2 CONCLUSIONS

The following conclusions may be drawn from the research described in this report.

1. The RDD can be used to obtain continuous displacement profiles of pavement systems. These measurements are very robust; good results are obtained in the presence of such adverse conditions as heavy traffic in adjacent lanes and rough pavements. These conclusions have been demonstrated by RDD tests performed on about 38.4 km (24 mi) of highway pavements and on about 8 km (5 mi) of airport pavements.

2. Continuous displacement profiles obtained with the RDD provide valuable information about the condition and deflection behavior of pavement systems. Sections of pavement can be characterized according to the displacement level the sections exhibit under dynamic loading. The behavior of joints and cracks can be characterized by absolute displacement levels and by relative displacements on both sides of the joint or crack. Displacements in pavement sections that have been subjected to heavy traffic can be compared to those obtained from similar but less-trafficked sections to determine degradation in the pavement resulting from traffic.

3. Regions of the pavement influenced by joints, cracks, and free edges are readily identified in continuous displacement profiles obtained with the RDD. This picture is important because most models used in backcalculating pavement profiles from deflection data assume that all layers have infinite lateral extent. Backcalculations performed on deflections measured in regions influenced by joints, cracks, and free edges will be in error. Because these regions are not readily identified in conventional field testing procedures, their influence is not apparent in the results of discrete testing methods. Of course, the attempt is made in all discrete tests to be outside the zone of influence of these features.

4. In addition to collecting continuous displacement measurements, the RDD has the potential to predict the depth to bedrock at a site, to measure the nonlinear response of a pavement, and to determine the fatigue resistance of a pavement by quickly applying a large number of loading cycles.

5. The RDD's loading frame and lateral force support systems safely resist the large forces generated during RDD testing. The RDD loading rollers are a critical component of this system and must withstand very high cyclic forces that are applied at high frequencies. The latest loading roller design, composed of stiff urethane cast to a slotted aluminum hub with steel retaining plates on both sides, withstands the combined static and dynamic forces applied by the RDD.

6. The modified Vibroseis hydraulic system provides the continuous sinusoidal force output required for RDD testing. The RDD static loading system, which utilizes a proportional pressure-flow (P-Q) servo-valve and electronic controls, provides adequate control and regulation of static force for RDD operation.

7. The RDD load cells provide accurate measurements of static and dynamic forces applied by the RDD while withstanding the extreme loading to which they are subject to during testing. Inertial force measurement systems, used in prior stages of RDD development, do not provide a sufficiently accurate dynamic force measurement for RDD testing.

8. The RDD rolling sensors with three 15.2 cm (6 in.) diameter wheels provide optimal rolling noise reduction within practical space and construction constraints. Increasing the diameter of the rolling sensor wheels decreases the amplitude of the rolling noise and shifts it to lower frequencies. Increasing the number of rolling sensor wheels decreases the rolling noise amplitude. To obtain the full benefit of multiple wheels on the rolling sensor, the wheels should be positioned so that no two wheels encounter joints or other features perpendicular to the sensor's path simultaneously.

9. The RDD data analysis procedure isolates the applied forces and displacements from the noise associated with rolling over rough pavement. This procedure demodulates RDD force and displacement signals about the operating frequency. This simplifies data analysis by allowing the use of the same digital filter for any operating frequency selected for testing.

10. The accuracy of an RDD measurement can be quantified with statistical confidence intervals. RDD data analysis can be customized to provide an optimal combination of accuracy and spatial resolution. The accuracy of the displacements measured with the RDD can be increased by decreasing the spatial resolution of the measurement; conversely, the spatial resolution of the measurement can be increased at the expense of displacement accuracy.

11.3 RECOMMENDATIONS FOR FUTURE IMPROVEMENTS TO THE ROLLING DYNAMIC DEFLECTOMETER

The following recommendations are suggested for improving the RDD.

1. The rolling sensors should be modified to provide a hold-down force to keep the sensors in contact with the pavement. This modification will allow RDD testing to be performed while traveling at somewhat higher speeds. Additionally, it will allow testing to be performed at higher frequencies where there is less traffic and rolling noise.

2. The servo-controls of the dynamic loading system should be modified to include a dynamic force feedback from the load cell. This feedback would provide for more accurate control of the forces applied to the pavement and less variation in dynamic force owing to roughness in the pavement and to changes in pavement stiffness.

3. Accelerometers should be attached to the loading roller bearings to allow an inertial correction to be applied to the measured dynamic forces. Current dynamic measurements are slightly erroneous owing to the vertical movement of the loading rollers. This error is assumed to be quite small in the testing already performed, but it can be corrected with this additional measurement in future tests.

4. Additional rolling sensors could be employed to obtain more lateral coverage during testing. This would allow the determination of the behavior of different lateral regions of pavement while profiling longitudinally.

5. Real-time data analysis should be incorporated into the RDD data acquisition system. The latest computer technology should provide data processing that is sufficiently fast for real-time data analysis. Real-time displacement profiles would be useful in making decisions regarding subsequent testing and would, overall, be worthwhile to pavement managers.

6. Video images of the pavement undergoing testing could be recorded. This would allow pavement managers to quickly correlate features in the continuous displacement profile with physical features of the pavement.

7. Global positioning system (GPS) technology should be incorporated into the RDD position tracking system. This would provide for accurate RDD position tracking, even when good position references are not present near the pavement.

REFERENCES

American Institute of Steel Construction (AISC) (1980), *Manual of Steel Construction*, AISC, Chicago, Illinois.

Anstey, N. A. (1991), *Vibroseis*, Prentice-Hall, Inc., Englewood Cliffs, New Jersey.

Baeten, G., and Ziolkowski, A. (1990), *The Vibroseis Source*, Elsevier Science Publishing Co. Inc., Amsterdam.

Bay, J. A., Stokoe, K. H., II, and Jackson, J. D. (1995), "Development and Preliminary Investigation of a Rolling Dynamic Deflectometer," *Transportation Research Record 1473*, Transportation Research Board (TRB), Washington, D.C., pp. 43–54.

Bedenbender, J. W. (1994), of Heavyquip, Ponca City, Oklahoma; personal communication.

Bedenbender, J. W., and Kelly, G. H. (1985), "Force or Pressure Feedback Control for Seismic Vibrators," U.S. Patent 4519053.

Black, H. S. (1953), *Modulation Theory*, D. Van Nostrand Co., New York, New York.

Bohn, A., Ullidtz, P., Stubstad, R., and Sorensen, A. (1972), "Danish Experiments with the French Falling Weight Deflectometer," *Proceedings*, The University of Michigan Third International Conference on Structural Design of Asphalt Pavements, Volume 1, September 1972, pp. 1119–1128.

Bracewell, R. N. (1986), *The Fourier Transform and Its Applications*, McGraw-Hill Book Co., New York, New York.

Carneiro, F. B. L. (1966), "Benkelman Beam — Auxiliary Instrument of the Maintenance Engineer," *Transportation Research Record 129*, TRB, Washington, D.C., pp. 28–59.

Foinquinos, R., Roesset, J. M., and Stokoe, K. H., II (1995), "Response of Pavement Systems to Dynamic Loads Imposed by Nondestructive Tests," *Transportation Research Record 1504*, TRB, Washington, D.C., pp. 57–671.

Hoffman, M. S., and Thompson, M. R. (1982), "Comparative Study of Selected Nondestructive Testing Devices," *Transportation Research Record 852*, TRB, Washington, D.C., pp. 32–41.

Ifeachor, E. C., and Jervis, B. W. (1993), *Digital Signal Processing, A Practical Approach*, Addison-Wesley Publishing Co., Wokingham, England.

Johnson, R. F., and Rish, J. W., III (1996), "Rolling Weight Deflectometer with Thermal and Vibrational Bending Compensation," presented at TRB annual meeting, January 1996, Washington, D.C.

Kim, S-M. (1996), *Dynamic Response of Pavement Systems to Moving Loads*, doctoral dissertation, The University of Texas at Austin, August 1996.

McCullough, B. F., Nelson, R., Trevino, M., and Gräter, S. (1997), "Rehabilitation of IH-10 and IH-610 with Concrete Overlays," Research Project LOA 96-05, Texas Department of Transportation (TxDOT).

McNerney, M. T., McCullough, B. F., Stokoe K. H., II, Wilde, J., Bay, J. A., and Lee, N-J. (1997[1]), "Analysis of Remaining Life for Runway 17R-35L and Taxiway L at Dallas/Fort Worth International Airport," Vols. I-III, Research Report Number ARC-702, Center for Transportation Research (CTR), The University of Texas at Austin.

McNerney, M. T., McCullough, B. F., Stokoe, K.H., II, Lee, N-J., Bay, J. A., and Wilde, J. (1997[2]), "Prediction of Remaining Life of Airport Pavements," *Proceedings*, Aircraft Pavement Technology: In the Midst of Change, edited by F. Hermann, Aircraft Pavement Committee, ASCE, Seattle, Washington, August 1997, pp. 77–93.

National Instruments (1996), *Instrumentation Reference and Catalogue*, National Instruments Corporation.

Paquet, J. (1978), "The CEBTP Curviameter — A New Instrument for Measuring Highway Pavement Deflection," Centre Experimental de Recherches et d'Etudes du Batiment et des Travaux Publics, Paris, France, pp. 1–22.

Pelton (1980), *Pelco Advance I, Model 5 Vibrator Electronics Manual*, Pelton Company, Inc., Ponca City, Oklahoma.

Reust, D. K. (1993), "Enhanced Servovalve Technology for Seismic Vibrators," *Geophysical Prospecting*, Vol. 41 No. 1, pp. 43–60.

Richart, F. E., Jr., Hall, J. R., Jr., and Woods, R. D. (1970), *Vibrations of Soils and Foundations*, Prentice-Hall, Inc., Englewood Cliffs, New Jersey.

Roesset, J. M., Stokoe, K. H., II, and Seng, C-R. (1995), "Determination of Depth to Bedrock from Falling Weight Deflectometer Test Data," *Transportation Research Record 1504*, TRB, Washington, D.C., pp. 68–78.

Scrivner, F. H., Swift, G., and Moore, W. M. (1966), "A New Research Tool for Measuring Pavement Deflection," *Transportation Research Record 129*, TRB, Washington, D.C., pp. 1–11.

Smith, R. E., and Lytton, R. L. (1985), "Operating Characteristics and User Satisfaction of Commercially Availability NDT Equipment," *Transportation Research Record 1007*, TRB, Washington, D.C., pp. 1−10.

Stanley, W. D. (1984), *Operational Amplifiers with Linear Integrated Circuits*, Charles E. Merrill Publishing Co., Columbus, Ohio.

Sunstrand (1980), *Service Manual for Heavy Duty Transmissions*, Bulletin 9630 Rev. E, Sunstrand Hydro Transmission, Ames, Iowa.

Tholen, O., Sharma, J., and Terrel, R. L. (1985), "Comparison of the Falling Weight Deflectometer with Other Deflection Testing Devices," *Transportation Research Record 1007*, TRB, Washington, D.C., pp. 12−20.

Timoshenko, S. P., and Goodier, J. N. (1970), *Theory of Elasticity*, McGraw-Hill Book Co., New York, New York.

Walpole, R. E., and Myers, R. H. (1985), *Probability and Statistics for Engineers and Scientists*, Macmillan Publishing Co., New York, New York.

Waters, K. H. (1981), *Seismic Reflection Seismology, a Tool for Energy Resource Exploration*, John Wiley and Sons, Inc., New York, New York.

Zube, E., and Forsyth, R. (1966), "Flexible Pavement Maintenance Requirements as Determined by Deflection Measurement," *Transportation Research Record 129*, TRB, Washington, D.C., pp. 60−75.